THULIUM IONS IN A YTTRIUM ALUMINUM GARNET HOST FOR QUANTUM COMPUTING APPLICATIONS: MATERIAL ANALYSIS AND SINGLE QUBIT OPERATIONS

by

Ijaz Zafarullah

A dissertation submitted in partial fulfillment
of the requirements for the degree

of

Doctor of Philosophy

in

Physics

MONTANA STATE UNIVERSITY
Bozeman, Montana

May 2008

APPROVAL

of a dissertation submitted by

Ijaz Zafarullah

This dissertation has been read by each member of the dissertation committee and has been found to be satisfactory regarding content, English usage, format, citation, bibliographic style, and consistency, and is ready for submission to the Division of Graduate Education.

Dr. Wm. Randall Babbitt

Approved for the Department of Physics

Dr. William Hiscock

Approved for the Division of Graduate Education

Dr. Carl A. Fox

STATEMENT OF PERMISSIONTO USE

In presenting this dissertation in partial fulfillment of the requirements for a doctoral degree at Montana State University, I agree that the Library shall make it available to borrowers under rules of the Library. I further agree that copying of this dissertation is allowable only for scholarly purposes, consistent with “fair use” as prescribed in the U.S. Copyright Law. Requests for extensive copying or reproduction of this dissertation should be referred to ProQuest Information and Learning, 300 North Zeeb Road, Ann Arbor, Michigan 48106, to whom I have granted “the exclusive right to reproduce and distribute my dissertation in and from microform along with the non-exclusive right to reproduce and distribute my abstract in any format in whole or in part.”

Ijaz Zafarullah

May 2008

To my wife Samina,
Thanks for prayers, patience, and support

ACKNOWLEDGEMENTS

First of all I would like to thank Physics Department for supporting me as a graduate student. I especially thank Professor Wm. Randall Babbitt, my advisor, whose support, encouragement, and helpful discussions, allowed me to complete my research work. This research work would not be possible without his constant support. I also like to thank Professor William Hiscock, head of the Physics Department, for providing a wonderful environment in the department for graduate students.

I like to thank Dr. Mingzhen Tian for her dedication and constant help. Her expertise and dedication were invaluable for the successful completion of this work. I also like to thank Dr. Charles Thiel for helpful discussions and his help in understanding and interpreting the experimental results. I also want to thank him for his helpful comments on dissertation write up. I also thank Dr. Krishna Rupavatharam for his help in refining the material in the dissertation. He went beyond the duties of a committee member and helped me to improve the content of the dissertation. I want to thank Professor Rufus Cone for loaning the key equipments and his helpful comments. I also want to thank all my committee members for their help. I also thank Ariana Paliobagis for proofreading the dissertation.

I would also like to thank Margaret Jarrett, Jeannie Gunderson, Jeremy Gay, Rose Waldon, Sarah Barutha, and Norm Williams for taking care many administrative and technical matters. I also want to thank my family members for their support and prayers throughout my life.

TABLE OF CONTENTS

TABLE OF CONTENTS – CONTINUED

TABLE OF CONTENTS – CONTINUED

TABLE OF CONTENTS – CONTINUED

LIST OF TABLES

Table Page

LIST OF FIGURES

Figure Page

LIST OF FIGURES – CONTINUED

Figure Page

LIST OF FIGURES – CONTINUED

Figure Page

LIST OF FIGURES – CONTINUED

Figure Page

LIST OF FIGURES – CONTINUED

Figure Page

LIST OF FIGURES – CONTINUED

Figure Page

LIST OF FIGURES – CONTINUED

Figure Page

LIST OF FIGURES – CONTINUED

Figure Page

LIST OF FIGURES – CONTINUED

Figure Page

LIST OF FIGURES – CONTINUED

Figure Page

ABSTRACT

Rare-earth-doped crystals have been used for optical signal processing and storage applications. In this dissertation, their potential for quantum computing applications is explored. In one quantum computing scheme, information is stored in nuclear spin states and this information is then processed by using optical pulses through the coupling of these nuclear spin states to a common electronic level. To implement this scheme, nuclear spin states and coupling of these nuclear spin states to a common electronic level is required. Preliminary work in rare-earth materials like Pr^{3+} and Eu^{3+} has shown promising results regarding their suitability for quantum computing applications. One particular problem with these materials is that their transition wavelengths are only accessible with dye lasers. These lasers are inherently unstable, and currently few available systems exhibit the stability required for quantum computing applications.

An alternative choice was to investigate other rare-earth ions like thulium. Thulium has a transition wavelength that can be accessed with diode lasers, which are commercially available, easy to stabilize, and compact. This dissertation is based on our investigations of Tm^{3+}:YAG for quantum computing applications.

Investigations involved a detailed characterization of the material. Nuclear spin states, in Tm^{3+}:YAG, were obtained by applying an external magnetic field to the sample. First, interaction of an external magnetic field with the thulium ions at various sites in the crystal was analyzed. This analysis was used to measure the magnetic anisotropy in the material. These results show that it is possible, with the suitable choice of the magnetic orientation and the site in the crystal, to build a working 3-level quantum system.

In the demonstration of single qubit operations in Tm^{3+}:YAG, we first theoretically studied the effect of Gaussian spatial beam on the single qubit operations. Later on, we experimentally prepared a single isolated ensemble of ions in the inhomogeneously broadened absorption profile of the medium. This single isolated ensemble of ions was used as a test-bed to implement the single qubit operations. We also isolated two ensembles of ions in the inhomogeneous absorption profile of the medium. The interaction between these two isolated ensembles of ions was also studied.

CHAPTER ONE

INTRODUCTION

The main purpose of this work is to investigate the rare-earth-doped material, Tm^{3+}:YAG, for its suitability in quantum computing applications. These investigations include characterizing the thulium-doped crystal and tailoring the operating conditions for quantum computing applications. This work provides enhanced insight into the material properties and suitability of the material as a test-bed for implementation of basic quantum computing schemes. In this chapter, an introduction to classical and quantum computing and the dissertation outline are presented.

Classical Computing

Classical computing and its implementation in modern computers started with the groundbreaking work by A. M. Turing in 1936 [(1)] when he developed an abstract model of a programmable computer. This programmable computer is known as a Turing machine in honor of this pioneer of modern computer science. He also developed the notion of a universal computing machine that can simulate any other computing machine. Turing showed that an algorithm can be implemented in this universal Turing machine to perform a task. In general, any algorithmic process can be implemented using a universal Turing machine. This assertion is known as the Church-Turing thesis, in honor of Turing and Alonzo Church, another pioneer of modern computing [(2)].

In the modern era, progress achieved in computer hardware has been phenomenal. The rate of computer hardware growth was predicted by Gordon Moore in 1956 and is known as Moore's law. Moore estimated that computing power will double for constant cost roughly once every two years.

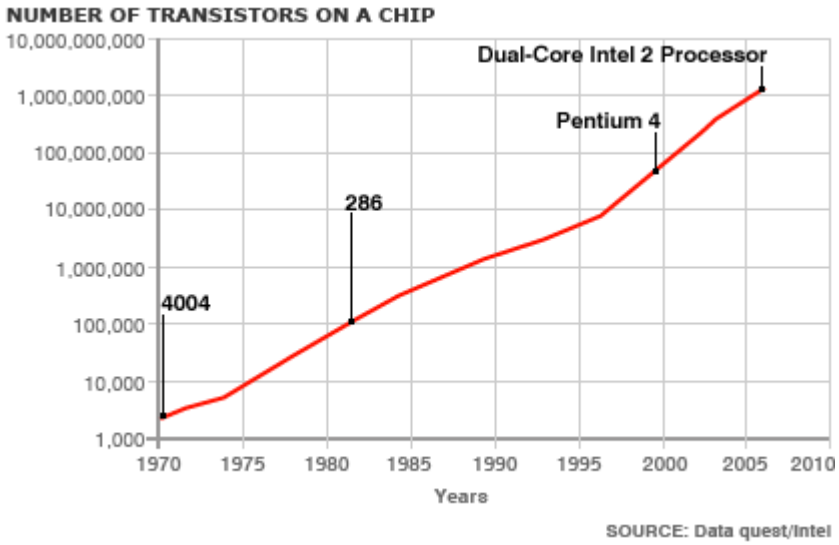

Figure 1: Growth of components on a computer chip per year.

Current growth in hardware has followed Moore's law (Figure 1), but it is believed that hardware growth will cease to follow Moore's law as conventional fabrication techniques encounter the problem of stacking increased number of components on a computer chip. One way to increase the computing power without using additional resources on the computer chip is to use a different computing technique: one that is more efficient in using the available computing resources.

In an efficient computing technique, the resources needed for computing grow polynomially with the size of the problem. On the other hand, in the case of an inefficient

programming technique, computing resources grow exponentially with the size of the problem. The conventional computation model defined in the Church-Turing thesis can still be applied with a slight modification.

In mid-1970s, the Church-Turing thesis faced a new challenge. At that time it was discovered that probabilistic algorithms are more efficient than the deterministic algorithms. In probabilistic algorithms, the solution is not a definite answer; rather it determines the probability of a certain outcome. This led to another modification in the Church-Turing thesis: "Any algorithm process can be simulated efficiently using a probabilistic Turing machine." This prompted many to think that there may be some other computation model that can be used to simulate any physical system. This line of thinking prompted using a computational model based on the laws of physics [(3)]. Since these laws of physics are best described in quantum mechanics, this led David Deutsch in 1985 to propose the "Universal Quantum Computer" that was based upon the principles of quantum mechanics [(4)].

Quantum Computing

The building block in quantum computing is called a qubit, and any 2-level system can serve as a qubit. The lower energy level, $|0\rangle$, of the two levels can be thought of as the "0" state of the qubit, and the higher energy level, $|1\rangle$, of the two levels can be thought of as the "1" state of the qubit. This definition of a qubit is analogous to the definition of a classical bit where information is stored as 0's and 1's.

However, a qubit, in addition to these two states, can also exist in a superposition of these two states. Thus, in general, a qubit state will be $a|0\rangle + b|1\rangle$, where a and b are complex numbers. A qubit is best described by a coherent superposition of two states. This property of the qubit lies at the heart of quantum computation. This means that a qubit is performing two parallel computations at any given time. If there are two interacting qubits, then each qubit can exist in the superposition of four states. Thus, it can perform four parallel computations at any given time. The computation power of a quantum computer thus increases exponentially with the increase in the number of qubits. To realize the full potential of the superposition state of the qubits, one has to use special algorithms, sometimes called quantum algorithms, which incorporate quantum parallelism. Currently few quantum algorithms exist, thus limiting the use of quantum computation [(5), (6), (7), (8), (9)]. Apart from the scarcity of efficient quantum algorithms, there is also the challenging task of building a practical quantum computer. A physical system has to fulfill certain conditions in order for it to be considered a candidate for quantum computer hardware. These conditions are described in the next section.

Quantum Computing and DiVincenzo Requirements for a Physical System

David DiVincenzo put forward five basic requirements for a physical system. The physical system has to fulfill these conditions to be considered for quantum computing applications [(10)]. These conditions are

1. A scalable physical system with well-characterized qubits.

2. The ability to initialize the state of the qubits to a simple initial state, such as $|000...\rangle$.
3. A coherence time much longer than the gate operation time.
4. A “universal” set of quantum gates.
5. A qubit-specific measurement capability

The first condition requires the preparation of a qubit that has two well characterized states, for example, two spin levels of a spin ½ particle, the ground and excited states of an atom/molecule/ion, or two distinct polarization states of a single photon.

The second condition requires that the state of a qubit can be controlled, so that it can be initialized to a known value before the start of computation.

The third condition deals with the ability of the qubit to store information without much loss. This requires the qubit to have minimal contact with the environment, but it should also be able to interact with other qubits, as per condition 4, and with the measurement apparatus, as per condition 5. Condition 3, coupled with conditions 4 and 5; highlights the fundamental difficulty in building a quantum computer.

A quantum gate can be thought of as a unitary transformation that acts on a qubit and transforms its current state to a new state. A set of quantum gates will be universal if any unitary transformation of a qubit state can be realized by combinations of these quantum gates.

A number of physical systems are being investigated by others in order to assess how well they fulfill these requirements. They include Nuclear Magnetic Resonance (NMR) [(11)], Ion traps [(11)], Superconducting circuits made with Josephson junctions [(11)], Linear optics quantum computing [(11)], Solid state (quantum dot and spin

qubits) [(11)], Cavity quantum electrodynamics (Cavity QED) [(11)], and Neutral atoms [(11)]. The Roadmap document, [(11)], describes each approach and compares progress for implementation of quantum computing in each physical system for each of the DiVincenzo criteria [(10)]. The reader is referred to this document and further references in it for greater detail on these systems.

Reference (11) also includes new approaches for quantum computing applications, one of which is called the spectral hole-burning approach in rare-earth-doped crystals. Rare-earth-doped crystals rate favorably against the five requirements outlined by DiVincenzo. In the rare-earth-doped crystals, dopant ions are randomly distributed, with each dopant residing in a unique, shielded environment. This inhomogeneously broadened absorber, at low temperature, can provide a significant number of potential candidates for qubits. In the current study, the thulium-doped material, Tm^{3+}:YAG, is investigated for its application in quantum computing as outlined in the next section.

Dissertation Outline

The dissertation is divided into two main parts with the first part dealing with the material characterization of Tm^{3+}:YAG and the second part giving results for ensemble selection for qubit preparation and implementation of single qubit operations on this selected ensemble in Tm^{3+}:YAG.

The dissertation starts with the basic theory necessary for characterizing the material. Note that, two main techniques are employed to characterize the material: one

uses the coherence effects in the medium while the other relies on absorption spectroscopy.

In Chapter 2, results for coherent transient effects arising from coupling of the optical field with the two and three levels are summarized. These results provide the framework needed to investigate the material's coherence properties. In Chapter 3, theoretical results for hyperfine splitting in a spin ½ system are presented and transition probabilities for various transitions are defined.

Chapter 4 includes the experimental results for characterization of the material. The characterization of the material for quantum computing applications essentially required us to optimize the conditions for cross-transition probabilities, the population lifetime of hyperfine levels, and the hyperfine coherence time. The theoretical results in Chapter 3 are used extensively to characterize the material for these three parameters. First, we characterize the hyperfine splitting for Tm^{3+} ions at different sites in the thulium-doped crystal. Characterizing the hyperfine levels includes a study of the population lifetime of these levels and variation in the population lifetime with the orientation of the applied magnetic field. We also investigated the splitting of hyperfine levels for ions at different sites. Results from Chapter 3 are also used to study the transition probabilities for ions at these sites for different magnetic field orientations. These results mapped the hyperfine splitting and transition probabilities for ions at different sites in the crystal. We also studied the effect of the misalignment of the applied magnetic field on the hyperfine splittings and the transition probabilities. Various decay rates for the material were modeled theoretically, and this model was used to

experimentally study these relaxation mechanisms in the material. The effect of the sample temperature on these relaxation parameters was also studied. Later, we experimentally investigated the hyperfine coherence times for ions at different sites in the crystal and for various orientations of the magnetic field.

Introductory work describing the relevant theory for a single qubit operation is given in Chapter 5. It deals with the single qubit operation under ideal conditions and also extends the operation to non-ideal conditions. These non-ideal conditions include non-uniformity in the optical beam intensity. Predictions for operations on a single qubit for a Gaussian spatial optical beam are also presented.

In Chapter 6, a method to select an ensemble of ions for demonstrating a single qubit operation is described. This was followed by a description of this method for implementation in the experiment. This method provided us a selected ensemble of selected ions. The properties of this ensemble were studied using coherence and absorption spectroscopy. The selected ensemble of ions was used as a test-bed to implement the basic qubit operations. Experimental results from these single qubit rotations were compared with the theoretical predictions for the uniform and non-uniform (Gaussian) excitations. Finally, two ensembles at two different locations in the absorption spectrum of the medium were selected. The interaction between these two selected ensembles was investigated using photon echo experiments.

In Chapter 7, a summary of all the results is presented. This chapter also contains the future directions, one should pursue to implement the multi-qubit operations in Tm^{3+}:YAG.

CHAPTER TWO

COHERENT INTERACTION OF LIGHT WITH MULTI-LEVEL SYSTEMS

Introduction

A quantum computing scheme relies on the multi-level system. In the multi-level system some levels are used to store and manipulate the population and the other levels are used to store and manipulate the coherences in the system. The detailed information regarding the system will be presented in Chapter 6. In this chapter, we consider the interaction of such a multi-level system with an optical field. The primary purpose here is to describe the interaction of an optical field with two and three optical levels in 2- and 4-level atomic systems. The description is carried out using the density matrix formalism with the introductory theory presented in the next section. When an optical field, $\vec{E}_0 = \vec{x}E_0 \cos(\omega t - kz)$, interacts with these systems, it not only redistributes population but it also creates coherences in the system [(12)]. In density matrix formalism, the population density of each of these energy levels is given by the diagonal elements of the density matrix, and the optical coherence in the system is given by

$$\langle \mu \rangle = Trace(\rho\mu) \tag{2.1},$$

where μ is the transition dipole matrix and ρ is the density matrix.

In an inhomogeneously broadened medium, the macroscopic polarization consists of contributions from atoms/ions at different detunings. Therefore, the macroscopic polarization for such a system will be

$$P(t,z)=\int_{-\infty}^{\infty}\langle\mu\rangle g(\Delta)d\Delta \qquad (2.2),$$

where Δ is the frequency detuning, and $g(\Delta)$ is the line shape of inhomogeneous profile such that $\int_{-\infty}^{\infty} g(\Delta)d\Delta=1.$

The output optical field from the medium can be obtained from the Maxwell equation

$$\vec{\nabla}\times\vec{\nabla}\times\vec{E}_{rerad}(t,z)+\frac{1}{c^2}\frac{\partial^2}{\partial t^2}\vec{E}_{rerad}(t,z)=-\frac{1}{c^2\varepsilon_0}\frac{\partial^2}{\partial t^2}P(t,z) \qquad (2.3),$$

where c is the speed of light in a vacuum and ε_0 is the permittivity of free space.

Equation (2.3) is quite complicated and has no analytical solution in general, but it is possible to get an approximate result for the special case considered here. Here, we consider a case for which macroscopic polarization, $\vec{P}$, is solely created by an incident field, $\vec{E}_0$. If the amplitudes of the incident fields, the polarization, and the output field are slowly varying in time, then the total optical field emitted from the system is given by [(12)]

$$\vec{E}_T(t,L)=(E_o+\varepsilon_c)\cos(\omega t-kL)+\varepsilon_s\sin(\omega t-kL) \qquad (2.4),$$

where $\varepsilon_c(t,L)=-\frac{\omega L}{2\varepsilon_0 c}P_s(t-L/c), \varepsilon_s(t,L)=-\frac{\omega L}{2\varepsilon_0 c}P_c(t-L/c),$

$\vec{P}(t,L)=\vec{x}[P_c\cos(\omega t-kL)+P_s\sin(\omega t-kL)]$, and L is the length of medium.

For this particular case, if the macroscopic polarization, $\vec{P}$, is given, then the reradiated field can be easily calculated using equation (2.4). Thus, the focus in the rest of the chapter will be to find the macroscopic polarization for different systems. This in turn

involves finding density matrices for these systems. Note that the population redistribution manifests itself as a change in the absorption profile of the medium.

Interaction of a Single Pulse with a 2-Level System

First consider a 2- level system as shown in Figure 2. The wave function in the $|0\rangle = \begin{pmatrix} 1 \\ 0 \end{pmatrix}$ and $|1\rangle = \begin{pmatrix} 0 \\ 1 \end{pmatrix}$ basis is written as $\psi(t) = \begin{pmatrix} \psi_0(t) \\ \psi_1(t) \end{pmatrix}$.

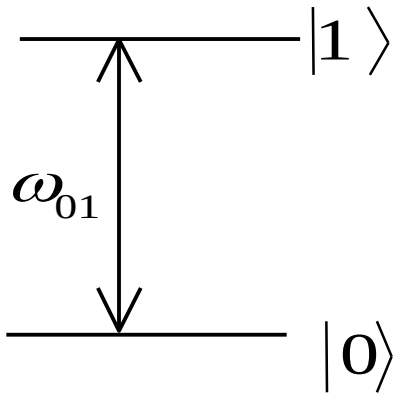

Figure 2: A 2-Level System

The evolution of this state of the system is governed by the Schrodinger equation as

$$i\hbar \frac{\partial}{\partial t}\psi(t) = H_0 \psi(t) \qquad (2.5),$$

where H_0 is the Hamiltonian of the system and, for a 2-level system, is given as $H_0 = \hbar \begin{pmatrix} 0 & 0 \\ 0 & \omega_{10} \end{pmatrix}$, where $\hbar\omega_{10}$ is the energy difference between the two levels. For this situation it is straightforward to solve the Schrodinger equation (2.5) and thus find the evolution of the system. In this case, each level will oscillate in time with an oscillation frequency ω_{10}.

Now, if this system interacts with the external electric field via dipole interaction, then the Schrodinger equation will also have an interaction term, and the system evolution in time will be given by the Schrodinger equation as

$$i\hbar \frac{\partial}{\partial t}\psi(t) = (H_0 + H_I)\psi(t) \tag{2.6}$$

where H_I is the interaction Hamiltonian and is given by $H_I = -\begin{pmatrix} 0 & \mu_{01} \\ \mu_{10} & 0 \end{pmatrix} E_0 \cos(\omega_L t + \varphi)$. Here the external field, $E(t) = E_0 \cos(\omega_L t + \varphi)$ for $t \geq t_0$ and $E(t) = 0$ for $t \leq t_0$, is assumed parallel with the dipole moment and E_0 is constant in time; μ_{10} is the coupling of the two states and is assumed real, i.e. $\mu_{10} = \mu_{01}^*$, [Note, if μ_{10} is assumed complex, then it just introduces a phase factor]; ω_L is the laser frequency; and φ is the phase of the laser pulse. In this discussion, the optical coherence decay, the population decay, and the propagation effects are ignored.

In order to solve the Schrodinger equation (equation (2.6)), the wave function is transferred to a new frame that is rotating with the laser frequency as $\psi'(t) = e^{iAt}\psi(t)$, where $A = \begin{pmatrix} 0 & 0 \\ 0 & \omega_L \end{pmatrix}$. Therefore, the Schrodinger equation in the new frame will be

$$i\hbar \frac{\partial}{\partial t}\psi'(t) = H'\psi'(t) \tag{2.7}$$

where $H' = e^{iAt}(H_0 + H_I - \hbar A)e^{-iAt}$.

Using the rotating wave approximation and ignoring terms oscillating at twice the laser frequency in equation (2.7), we get $H' = \hbar \begin{pmatrix} 0 & -\frac{\Omega_0}{2} e^{i\varphi} \\ -\frac{\Omega_0}{2} e^{-i\varphi} & \Delta \end{pmatrix}$, where $\Delta = \omega_{10} - \omega_L$ and $\Omega_0 = \frac{\mu E_0}{\hbar}$. In the new frame, H' is independent of time. Thus equation (2.7) can be solved and the wave function would be $\psi'(t) = e^{-i\frac{H'}{\hbar}t}\psi'(0)$. Here $u = e^{-i\frac{H'}{\hbar}(t-t_0)}$ can be written as

$$u(\Omega_0, t-t_0, \Delta, \varphi) = S e^{-i\frac{S^{-1}H'S}{\hbar}t} S^{-1}$$
$$= e^{-i\frac{\Delta(t-t_0)}{2}} \begin{pmatrix} \cos\left(\frac{\Omega(t-t_0)}{2}\right) + i\frac{\Delta}{\Omega}\sin\left(\frac{\Omega(t-t_0)}{2}\right) & i\frac{\Omega_0}{\Omega}e^{i\varphi}\sin\left(\frac{\Omega(t-t_0)}{2}\right) \\ i\frac{\Omega_0}{\Omega}e^{-i\varphi}\sin\left(\frac{\Omega(t-t_0)}{2}\right) & \cos\left(\frac{\Omega(t-t_0)}{2}\right) - i\frac{\Delta}{\Omega}\sin\left(\frac{\Omega(t-t_0)}{2}\right) \end{pmatrix} \quad (2.8),$$

where the matrix S diagonalizes H' and $\Omega = \sqrt{\Omega_0^2 + \Delta^2}$. Therefore, the density matrix is

$$\rho'(t \geq t_0) = \begin{pmatrix} \rho'_{00}(t \geq t_0) & \rho'_{01}(t \geq t_0) \\ \rho'_{10}(t \geq t_0) & \rho'_{11}(t \geq t_0) \end{pmatrix} \quad (2.9),$$

where $\rho'_{00}(t \geq t_0) = \Omega^2 \cos^2\left(\frac{\Omega(t-t_0)}{2}\right) + \Delta^2 \sin^2\left(\frac{\Omega(t-t_0)}{2}\right) / \Omega^2$,

$\rho'_{01}(t \geq t_0) = -i\Omega_0 e^{i\varphi}\left(\Omega\cos\left(\frac{\Omega(t-t_0)}{2}\right) + i\Delta\sin\left(\frac{\Omega(t-t_0)}{2}\right)\right)\sin\left(\frac{\Omega(t-t_0)}{2}\right)/\Omega^2$,

$\rho'_{10}(t \geq t_0) = i\Omega_0 e^{-i\varphi}\left(\Omega\cos\left(\frac{\Omega(t-t_0)}{2}\right) - i\Delta\sin\left(\frac{\Omega(t-t_0)}{2}\right)\right)\sin\left(\frac{\Omega(t-t_0)}{2}\right)/\Omega^2$,

$\rho'_{11}(t \geq t_0) = \Omega_0^2 \sin^2\left(\frac{\Omega(t-t_0)}{2}\right)/\Omega^2$, the initial population is in the ground state, and no initial coherences are present in the system.

Next, we use the results given in this section and present the results for interaction of a single optical pulse and multiple optical pulses with a 2-level system.

Rabi Oscillations

We follow the derivation given in [(12)] and consider the interaction of a single pulse with a 2-level system. We use equations (2.9) and (2.1) to obtain the coherence created in a 2-level system with a single optical pulse as

$$\langle \mu \rangle = \mu\left(\rho'_{01}e^{-i\omega_L t} + \rho'_{10}e^{i\omega_L t}\right)$$

$$= -\mu\frac{\Omega_0}{\Omega^2}\left(\Omega \sin\left(\Omega(t-t_0)\right)\sin\left(\omega_L t-\varphi\right) + i\Delta \sin^2\left(\frac{\Omega(t-t_0)}{2}\right)\cos\left(\omega_L t-\varphi\right)\right) \quad (2.10),$$

First, consider the case when an optical field is interacting with atoms/ions on resonance i.e., $\Delta = 0$. In this case, the optical field coherently drives the population between ground state and excited state with frequency Ω_0. This frequency is often referred to as the resonant Rabi frequency, owing its name to I. I. Rabi who first calculated the results to describe the magnetic field interactions with the nuclear spin systems [(13)].

For the case where each ion/atom in the system is occupying a unique environment and ions/atoms in the material are randomly distributed with the energy level of each ion perturbed by the residual strain of the crystal, the absorption profile of the system is typically Gaussian. For this case, the macroscopic polarization can be obtained from equation (2.2) by using the expressions for the absorption profile of the

system, $g(\Delta) = \frac{1}{\sqrt{\pi}\,\Delta_0} e^{-\left(\frac{\Delta}{\Delta_0}\right)^2}$, and the coherence in the system, is given by equation (2.10). Resultant integral in equation (2.2) is easy to evaluate if low bandwidth excitation, i.e., the bandwidth of the pulse is smaller than the inhomogeneous broadening of the system, is considered. For this case, the absorption profile of the system is assumed to be flat, and the second term in (2.10) will integrate to zero as it is an odd function of the detuning, Δ . Then the surviving term in equation (2.2) will be the in-quadrature component, P_s, of macroscopic polarization and is given by [(12)]

$$P_s(t \geq t_0) = -\frac{\sqrt{\pi}\,\mu\Omega_0\omega_L}{\Delta_0} e^{-\frac{(t-t_0)}{T_2'}} J_0\left(\Omega_0(t-t_0)\right) \qquad (2.11),$$

where J_0 is the first order Bessel function and T_2' depends on the bandwidth of the excited ions and on the inhomogeneous dephasing time of the material.

The output intensity from the system will be

$$I(t \geq t_0) = \frac{1}{2} c\varepsilon_0 E_0^2 + \frac{\sqrt{\pi}\hbar L\Omega_0^2\omega_L}{2\Delta_0} e^{-\frac{(t-t_0)}{T_2'}} J_0\left(\Omega_0(t-t_0)\right) \qquad (2.12),$$

where c is the speed of light in a vacuum and ε_0 is the permittivity of free space.

The result in equation (2.12) is valid for an optical field with spatially uniform intensity and it can be generalized to an optical beam with a Gaussian intensity profile as [(12)]

$$I(t \geq t_0) = \pi w_0^2 \left(I_0 + \frac{\sqrt{\pi}\hbar L\Omega_0\omega_L}{\Delta_0(t-t_0)} e^{-\frac{(t-t_0)}{T_2'}} J_1\left(\Omega_0(t-t_0)\right) \right) \qquad (2.13),$$

where w_0 is the full width of 1/e maximum of intensity, $I_0 = c\varepsilon_0(E_0)^2 / 2$, and J_1 is the first order Bessel function.

Free Induction Decay (FID)

Now we follow derivations in references [(14), (12)] and present the response of the system after it was excited with an optical pulse. In the free induction decay study, the system is first excited with an optical field. The evolution of the ensemble of ions/atoms in the system is studied at a later time. Therefore, in the FID study, the evolution of an ensemble of atoms/ions is studied after the field is turned off. The optical free induction is very similar to the NMR free induction decay that was first observed by Hahn in 1949 [(15)]. Following the derivations in [(14), (12)] we present the results for two cases.

FID after the Interaction with a Short Optical Pulse: In this case, a short optical pulse of duration $\tau = t_e - t_0$ and Rabi frequency Ω_0 such that $\tau^{-1} > \Delta \text{ and } \Omega_0 > \Delta$ is applied to the system starting at t = t_0. Therefore, in this case, the inhomogeneous broadening of the system is assumed to be smaller than the bandwidth of the pulse. Hence the detuning is neglected during the pulse and the density matrix, using equation (2.8), just after the pulse will be

$$\rho'\left(t = t_e\right) = u\left(\Omega_0, t_e - t_0, \Delta = 0, \varphi = 0\right)\rho'\left(t = t_0\right)u^*\left(\Omega_0, t_e - t_0, \Delta = 0, \varphi = 0\right) \quad (2.14a).$$

The system is now allowed to evolve freely, and the evolution of the system at a later time $t > t_e$ will be given by

$$\rho'(t > t_1) = u(0, t - t_e, \Delta, 0)\rho'(t = t_e)u^*(0, t = t - t_e, \Delta, 0) \quad (2.14),$$

where u^* is the Hermitian conjugate of u.

The macroscopic polarization can be calculated using equations (2.1, 2.2) and the expression for the Gaussian absorption profile of the system. In this case, the in-phase component, P_c, will vanish and the in-quadrature component, P_s, will be given by

$$P_s(t > t_e) \propto \mu e^{-\frac{(t-t_e)}{T_2}} e^{-\frac{\Delta_0^2}{4}(t-t_e)^2} \sin(\Omega_0 \tau) \quad (2.15).$$

In this case, the decay of the FID signal will depend on the combination of the bandwidth, Δ_0, of the sample being excited, and the material coherence time, T_2, as shown in Figure 3.

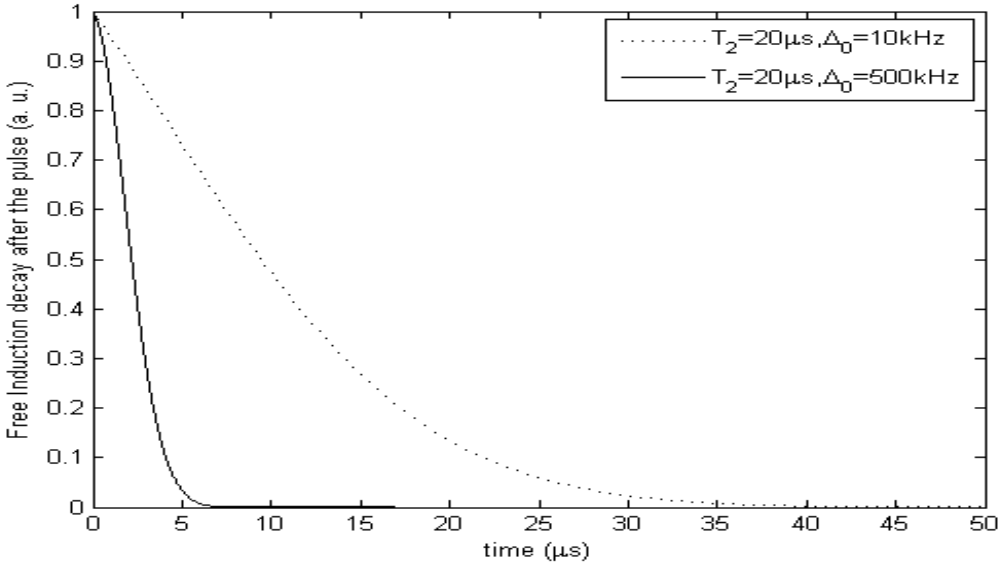

Figure 3: FID after excitation with a short laser pulse with dephasing, detuning, and population decay neglected during the pulse.

The plots in Figure 3 show that the FID signal from the system having a narrowband absorption profile, given by dotted line, will last longer than the FID signal from the system having a broadband absorption profile with the same material dephasing time, T_2. Therefore, the FID signal provides a tool to characterize the inhomogeneous width of the ensemble of ions.

FID after the Interaction with a Long Optical Pulse: Now consider the interaction of a 2-level system with a long optical pulse such that the system is in a steady state at the end of the pulse. In the case of steady state, the elements of the density matrix reach a constant value and do not change with time. In this case, again following the derivation in [(12)], the in-phase macroscopic polarization will vanish and the in-quadrature component will be

$$P_s\left(t > t_e\right) = \frac{\sqrt{\pi}\,\mu\Omega_0}{\Delta_0} e^{-\frac{(t-t_e)}{T_2}} \left(1 - \frac{1}{\Gamma}\right) e^{-\Gamma\frac{(t-t_e)}{T_2}} \qquad (2.16),$$

where $\Gamma = \sqrt{1+\Omega_0^2 T_1 T_2}$, T_2 is the coherence time of the system, T_1 is the population decay time of the system, and the inhomogeneous profile of the system is assumed to be flat. Equation (2.16) shows that the decay of the coherent emission is exponential and it depends on the combination of the coherence time and the population decay time.

Interaction of Two Brief Pulses with a 2-Level System

In the previous section, results for the interaction of one pulse with a 2-level system were presented and relevant phenomena arising from the interaction were briefly

discussed. Here, the interaction of two brief pulses with a 2-level system is presented. In this discussion, the pulses are considered to be sufficiently brief so that the detuning and any other decay processes (coherence decay and population decay) during the pulse are ignored. In this study we again follow the derivation given in references [(14), (12)].

The first brief pulse is assumed to be applied around time t_1, from t_1^- to t_1^+. Assuming that the initial population is in the ground state and there are no coherences in the system, the density matrix just after the pulse can be written from equation (2.9) as

$$\rho'\left(t = t_1^+\right) = \begin{pmatrix} \cos^2\left(\frac{\theta_1}{2}\right) & -i0.5e^{i\varphi_1}\sin\left(\theta_1\right) \\ i0.5e^{-i\varphi_1}\sin\left(\theta_1\right) & \sin^2\left(\frac{\theta_1}{2}\right) \end{pmatrix} \quad (2.17),$$

where $\theta_1 = \Omega_1\tau_1$, $\tau_1 = t_1^+ - t_1^-$ is the duration, φ_1 is the phase of the pulse, and it is assumed that $\Omega_1 > \Delta$, $\tau_1 << T_2$, and $\tau_1 << \Delta^{-1}$. The coherence created in the system with pulse 1 is given by the off diagonal elements of the density matrix in equation (2.17). After the application of pulse 1, the system will evolve in time and the density matrix at time $t > t_1$ will be

$$\rho'\left(t > t_1\right) = e^{-(t-t_1)/T_2}\begin{pmatrix} \cos^2\left(\frac{\theta_1}{2}\right) & -i0.5e^{i\varphi_1}\sin\left(\theta_1\right)e^{-i\Delta(t-t_1)} \\ i0.5e^{-i\varphi_1}\sin\left(\theta_1\right)e^{i\Delta(t-t_1)} & \sin^2\left(\frac{\theta_1}{2}\right) \end{pmatrix} \quad (2.18).$$

Now apply a second pulse of pulse area θ_2 and phase φ_2 from t_2^- to t_2^+. Then the density matrix just after the second pulse will be

$$\rho'\left(t = t_2^+\right) = \left(u\left(\Omega_2\tau_2, \Delta = 0, \varphi_2\right)\rho'\left(t = t_2^-\right)u^*\left(\Omega_2\tau_2, \Delta = 0, \varphi_2\right)\right) \quad (2.19),$$

where the detuning and the coherent dephasing during the pulse are neglected because the pulse duration, $\tau_2 = t_2^+ - t_2^-$, is assumed to be smaller than the coherence time and $\tau_2 < (\Delta^{-1})$.

The interest here is to find the output field created by the interaction of two optical pulses applied to the system at different times. As noted earlier, the reradiated field from the system can be obtained using off diagonal elements of the density matrix. Therefore, just after the second pulse, the off diagonal element of the density matrix will be

$$\rho'_{01}\left(t = t_2^+\right) \propto e^{-\frac{(t_2 - t_1)}{T_2}} \begin{pmatrix} \cos(\theta_1)\sin(\theta_2)\, e^{i\varphi_2} \\ -\sin(\theta_1)\sin^2\left(\frac{\theta_2}{2}\right) e^{i\Delta(t_2 - t_1) + i(2\varphi_2 - \varphi_1)} \\ +\sin(\theta_1)\cos^2\left(\frac{\theta_2}{2}\right) e^{-i\Delta(t_2 - t_1) + i\varphi_1} \end{pmatrix} \quad (2.20),$$

where $\theta_2 = \Omega_2 \tau_2$, τ_2 is the duration, and φ_2 is the phase of the second pulse.

The coherence set-up by these two optical pulses in the system will dephase and the coherence at a later time will be

$$\rho'_{01}(t > t_2) \propto e^{-\frac{(t - t_1)}{T_2}} \begin{pmatrix} \cos(\theta_1)\sin(\theta_2)\, e^{i\varphi_2 - i\Delta(t - t_2)} \\ -\sin(\theta_1)\sin^2\left(\frac{\theta_2}{2}\right) e^{-i\Delta(t - 2t_2 + t_1) + i(2\varphi_2 - \varphi_1)} \\ +\sin(\theta_1)\cos^2\left(\frac{\theta_2}{2}\right) e^{-i\Delta(t - t_1) + i\varphi_1} \end{pmatrix} \quad (2.21).$$

The analysis of the evolution of coherence, equation (2.21), in the system at a later time shows that the second term in $\rho'_{01}(t > t_2)$ will perfectly rephase at $t = 2t_2 - t_1$ independent of the detuning of the individual atom/ion in the system. Hence, the coherent

emission from the system will yield an optical echo at this rephasing time, which is usually called the 2-pulse echo [(12)].

Interaction of a Single Optical Pulse with Three Levels in a 4-Level System

Consider a 4-level system as shown in Figure 4. The theory of the electric field interaction with a 4-level system is well-known, and for a detailed description the reader is referred to the literature in references [(16), (17)]. Here we will just present relevant results from these references. Consider Figure 4, where levels 3 and 4 are optically coupled to level 1 or level 2, while there is no direct optical coupling between levels 3 and 4 or levels 1 and 2. Consider an optical pulse given by $E(t) = E_0 \cos(\omega_L t + \varphi_1)$, for $\varphi_1 = 0$ and $t_1^- < t < t_1^+$ and zero elsewhere such that $\tau_1 = t_1^+ - t_1^- < |\omega_1 - \omega_2|^{-1}$. Thus, another case, where $\tau_1 = t_1^+ - t_1^- > |\omega_1 - \omega_2|^{-1}$, is discussed in the next section. Note in this case the bandwidth of the excitation pulse is smaller than the energy difference between levels 1 and 2. This single optical pulse will excite three levels in the 4-level system. Again, decay processes in the material and the dephasing time during the pulse are ignored and this problem is solved using similar techniques, as in the case of a 2-level system [(16)].

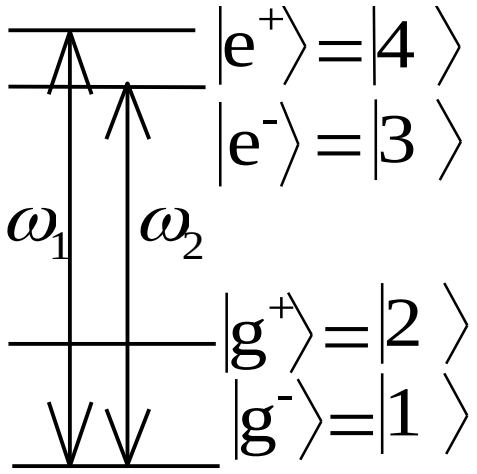

Figure 4: A V-type system in a 4-level system and few marked optical transitions. All optical transitions are not marked for simplicity.

This optical pulse will create coherence not only between the optical transitions but also between levels 3 and 4. Assume that the initial population is in level 1. Then the coherence created between levels 3 and 4 with this single optical pulse is given by the matrix element of density matrix in the reference [(18)] as

$$\rho'_{34}\left(t = t_1^+\right) = \mu_{14}\mu_{13}\left(\frac{\sin^2\left(\frac{\theta_1}{2}\right)}{\left(\mu_{13}^2 + \mu_{14}^2\right)}\right) \qquad (2.22),$$

where $\theta_1 = \sqrt{\left(\mu_{13}^2 + \mu_{14}^2\right)}\frac{E_0}{\hbar}\left(t_1^+ - t_1^-\right)$, $\Delta = \omega_1 - \omega_L$, μ_{13} is transition dipole for transition from level 1 to level 3, and μ_{14} is the transition dipole for transition from level 1 to level 4. Note that the coherences created between optical transitions are similar to those given in equation (2.9) and those cases are not discussed here. Here the aim is to discuss the coherence created between non-optical transitions.

Note that a single pulse can only create a coherence between levels 3 and 4, as given in equation (2.22), if both of the optical transition dipoles are non-zero. In the laboratory frame, the coherence between levels 3 and 4 after the pulse 1 will be [(18)]

$$\rho_{34}(t > t_1) = \mu_{13}\mu_{14} e^{-\frac{(t-t_1)}{T_2'}} \left(\frac{\sin^2\left(\frac{\theta_1}{2}\right)}{\left(\mu_{14}^2 + \mu_{13}^2\right)} \right) e^{-i(\omega_1 - \omega_2)(t-t_1)} \quad (2.23),$$

where T_2' is the coherence time for coherence between levels 3 and 4. In this case, dephasing and detuning during the pulse are ignored as $\tau_1 < T_2$ and $\tau_1 < \Delta^{-1}$.

The coherence given in equation (2.23) is the maximum if the applied pulse has pulse area π. Note that levels 3 and 4 are not optically coupled. Therefore, we cannot optically detect the coherence given in equation (2.23).

In order to probe this coherence and detect an optical signal, the Raman forward scattering method is used [(16), (19)]. In this method another narrowband optical pulse with the bandwidth smaller than the separation between levels 3 and 4 is applied between any of the optically allowed levels. First assume for our calculations that the optical pulse is applied between levels 1 and 4. Then this optical pulse will convert the non-optical (RF) coherence to the optical coherence. Using this method, the macroscopic polarization created in the system for optimum, $\theta_1 = \pi$, first pulse will be

$$P_{13}\left(\Delta_1, t > t_1^+\right) \propto \left\{ \begin{array}{l} \dfrac{\mu_{14}^2 \mu_{13}^2}{\left(\mu_{14}^2 + \mu_{13}^2\right)} e^{-\left(\frac{t-t_1^+}{T_2}\right)} \left(\dfrac{\sin\left(\dfrac{\left(\sqrt{\left(\Delta_1^2+\Omega_2^2\right)}\right)}{2}\left(t-t_1^+\right)\right)}{\sqrt{\left(\Delta_1^2+\Omega_2^2\right)}} \right) \dfrac{E_2}{\hbar} e^{i\omega_2\left(t-t_1^+\right)+i\frac{\Delta_1}{2}\left(t-t_1^+\right)} \\ \\ + c.c. \end{array} \right\} \quad (2.24),$$

where Δ is the detuning defined earlier, E_2 is the amplitude, and Ω_2 is the Rabi frequency of the second optical pulse. Here, the second pulse is assumed to start just after the end of the first pulse.

The reradiated field obtained from equation (2.24) will have frequency ω_2 while the frequency of the second pulse is ω_1. Thus, the total field will be the sum of these two fields, and hence, a beat note of frequency $\omega_2 - \omega_1$ will be observed. This beat signal is often referred to as a coherent Raman beat or quantum beat signal and is often used to measure Stark splitting, hyperfine splitting, etc. [(20), (21)].

Optical Rephasing in a 4-Level System with Multiple Optical Pulses

In the previous section, the FID signal from the interaction with a single optical pulse was used to explore the coherences in a 4-level system. In the current section multiple pulses are used to study the coherences in the 4-level system. Here we follow the derivation given in the reference [(22)]. The interaction of multiple optical pulses with a 4-level system can result in the rephasing phenomenon similar to the case in the 2-level system. In current section we present the results and conditions to observe a rephased

signal, known as Raman echo, from a 4-level system using three optical pulses. Later limitations on the rephasing with the three optical pulses are presented. We present a well-known alternate technique [(23)] to achieve a perfect rephasing with more than three optical pulses. The disadvantage in using the co-propagating beams is discussed and a modified scheme to avoid the problem with the detection of the coherence, is also presented.

Consider the level diagram in Figure 5. Here, the optical pulses do not couple simultaneously to three levels. Instead each pulse couples to just two optically allowed transitions in the 4-level system. In Figure 3, some optically allowed transitions are marked with transition frequencies ω_1 and ω_2. Since each pulse interacts only with two levels at a time, the effect of a single pulse (ignoring detuning during the pulse and decay processes in the system) can be calculated using the results given for the interaction of the optical field with a 2-level system. Therefore, the density matrix will be the same as in equation (2.8) and the evolution matrix for a 4-level system, where an optical pulse is applied between levels 1 and 3, can, in general, be written as [(22)]

$$u_{1\to 3}\left(\Omega_{01},\tau_1,\Delta_1,\varphi_1\right)$$

$$= e^{-i\frac{\Delta_1\tau_1}{2}}\begin{pmatrix} \cos\left(\frac{\Omega_1\tau_1}{2}\right)+i\frac{\Delta_1}{\Omega_1}\sin\left(\frac{\Omega_1\tau_1}{2}\right) & 0 & i\frac{\Omega_{01}}{\Omega_1}e^{i\varphi_1}\sin\left(\frac{\Omega_1\tau_1}{2}\right) \\ 0 & 1 & 0 \\ i\frac{\Omega_{01}}{\Omega_1}e^{-i\varphi_1}\sin\left(\frac{\Omega_1\tau_1}{2}\right) & 0 & \cos\left(\frac{\Omega_1\tau_1}{2}\right)-i\frac{\Delta_1}{\Omega_1}\sin\left(\frac{\Omega_1\tau_1}{2}\right) \end{pmatrix} \quad (2.25),$$

where $E_1(t) = E_{01}\cos(\omega_{1L}t + \varphi_1)$ for $t_1^- < t < t_1^+$ and zero elsewhere, $\tau_1 = t_1^+ - t_1^-$, $\Omega_{01} = \frac{\mu_{13}E_{01}}{\hbar}$, $\Delta_1 = \omega_1 - \omega_{1L}$, $\Omega_1 = \sqrt{\Omega_{01}^2 + \Delta_1^2}$, and φ_1 is the phase of the laser pulse.

Now, consider the particular case of an application of the first pulse that is resonant with levels 1 and 3, at $t = t_1$. We ignore detuning and any other decay processes during the pulse. Therefore, the density matrix just after the pulse will be

$$\rho'(t = t_1^+) = u_{1\to 3}(\Omega_{01}, \tau_1, 0, \varphi_1)\rho'(t = t_1^-)u_{1\to 3}^*(\Omega_{01}, \tau_1, 0, \varphi_1) \quad (2.26),$$

where $\rho'(t = t_1^-)$ is the density matrix of the system just before the application of the optical pulse.

The density matrix will evolve after the first optical pulse and the evolution will be given as

$$\rho'(t > t_1) = u_D(\Delta_1, \Delta_2, t - t_1)\rho'(t = t_1)u_D^*(\Delta_1, \Delta_2, t - t_1) \quad (2.27),$$

where u_D is the evolution matrix governing evolution of the system just after the optical pulse and is given by [(22)] as

$$u_D(\Delta_1, \Delta_2, t - t_n) = \begin{pmatrix} 1 & 0 & 0 \\ 0 & e^{-i\Delta_2(t-t_n)} & 0 \\ 0 & 0 & e^{-i\Delta_1(t-t_n)} \end{pmatrix} \quad (2.28),$$

where $\Delta_1 = \omega_1 - \omega_{1L}$ and $\Delta_2 = \omega_2 - \omega_{2L}$. Here it is assumed that the detunings for both optical transitions are not correlated.

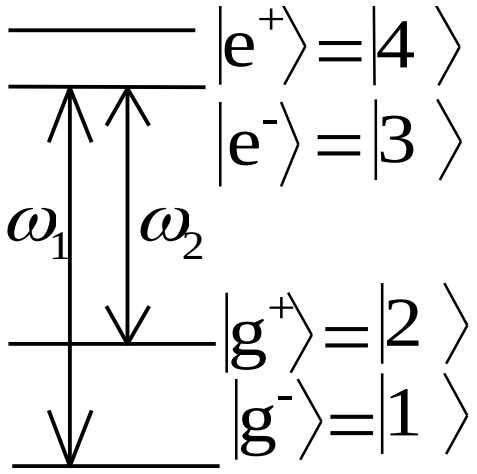

Figure 5: A Λ-type system in a 4-level system and few marked optical transitions. All optical transitions are not marked for simplicity.

Now we use equations (2.25-2.28) to obtain the density matrix element that gives the coherence between levels 1 and 3 at a later time for the case where levels 1 and 2 are equally populated, as

$$\rho'_{13}\left(t > t_1\right) \propto e^{-\left(\frac{t-t_1}{T_2}\right)}\left(\sin\theta_1\right) e^{i\varphi_1 + i\Delta_1\left(t-t_1\right)} \qquad (2.29),$$

where $\Delta_1 = \omega_1 - \omega_{1L}$, $\theta_1 = \Omega_{01}\left(t_1^+ - t_1^-\right)$ is the pulse area, ω_{1L} is the frequency of the optical beam from the center of level 1 to the center of level 3, and φ_1 is the phase of pulse 1. Note that coherence dephasing (equation (2.29)) is very similar to the case of a 2-level system (see off diagonal elements in equation (2.9)). Maximum coherence between levels 1 and 2 is created if $\theta_1 = \frac{\pi}{2}$ and thus this fixes the pulse area of pulse 1.

Now at time $t = t_2^-$, another optical pulse resonant with levels 2 and 3 is applied. The evolution matrix for this case will be [(22)]

$$u_{2\to 3}\left(\Omega_{02},\tau_2,\Delta_2,\varphi_2\right)$$

$$= e^{-i\frac{\Delta_2(\tau_2)}{2}}\begin{pmatrix} 1 & 0 & 0 \\ 0 & \cos\left(\frac{\Omega_2(\tau_2)}{2}\right)+i\frac{\Delta_2}{\Omega_2}\sin\left(\frac{\Omega_2(\tau_2)}{2}\right) & i\frac{\Omega_{02}}{\Omega_2}e^{i\varphi_2}\sin\left(\frac{\Omega_2(\tau_2)}{2}\right) \\ 0 & i\frac{\Omega_{02}}{\Omega_2}e^{-i\varphi_2}\sin\left(\frac{\Omega_2(\tau_2)}{2}\right) & \cos\left(\frac{\Omega_2(\tau_2)}{2}\right)-i\frac{\Delta_2}{\Omega_2}\sin\left(\frac{\Omega_2(\tau_2)}{2}\right) \end{pmatrix}$$

(2.30),

where $E_2(t) = E_{02}\cos\left(\omega_{2L}t+\varphi_2\right)$ for $t_2^- < t < t_2^+$ and zero elsewhere,

$\tau_2 = t_2^+ - t_2^-$, $\Omega_{02} = \frac{\mu_{23}E_{02}}{\hbar}$, $\Delta_2 = \omega_2 - \omega_{2L}$, $\Omega_2 = \sqrt{\Omega_{02}^2+\Delta_2^2}$, and φ_2 is the phase of the laser pulse.

The density matrix of the system just after pulse 2 will be

$$\rho'\left(t=t_2^+\right) = u_{2\to 3}\left(\Omega_{02},\tau_2,0,\varphi_2\right)\rho'\left(t=t_2^-\right)u_{2\to 3}^*\left(\Omega_{02},\tau_2,0,\varphi_2\right) \quad (2.31).$$

Pulse 2 transfers coherence between levels 1 and 3 to the coherence between levels 1 and 2, as given in equation (2.31). Thus the evolution of the system just after the second pulse will be given by

$$\rho'\left(t>t_2\right) = u_D\left(\Delta_1,\Delta_2,t-t_2,\Delta_1\right)\rho'\left(t=t_2^+\right)u_D^*\left(\Delta_1,\Delta_2,t-t_2\right) \quad (2.32).$$

Thus, using equation (2.32), the coherence between levels 1 and level 2, for $t > t_2$, just after the application of pulse 2, is

$$\rho_{12}'\left(t>t_2\right) \propto e^{-\left(\frac{t-t_1}{T_2}\right)}\left(\sin\left(\frac{\theta_2}{2}\right)\right)e^{-i(\varphi_2-\varphi_1)+i\Delta_1(t_2-t_1)+i\Delta_2(t-t_2)}$$

(2.33),

where T_2 is the coherence time, $\Delta_2 = (\omega_2 - \omega_{2L})$, $\theta_2 = \Omega_{02}(t_2^+ - t_2^-)$ is the pulse area of pulse 2, ω_{2L} is the frequency of optical beam from the center of level 2 to the center of level 3, and φ_2 is the phase of pulse 2.

For maximum coherence (see equation (2.33)) between levels 1 and 2, pulse 2 needs to have pulse area π. Note that the coherence has an extra dephasing term that depends on the inhomogeneous broadening of the non-optical levels (levels 1 and 2). To detect this coherence optically, another optical pulse is needed. If this pulse is applied from $t = t_3^-$ to $t = t_3^+$ between levels 1 and 3, then this pulse will transfer the coherence between levels 1 and 2 back to levels 2 and 3. Afterwards, the coherence between levels 2 and 3 will be given by the following density matrix element

$$\rho'_{23}(t > t_3) \propto e^{-\left(\frac{(t-t_1)}{T_2}\right)}(\sin(\theta_3))e^{-i(\varphi_3+\varphi_2-\varphi_1)+i\Delta_2(t-t_3-t_2+t_1)-i\Delta_1(t-t_2)} \qquad (2.34),$$

where $\theta_3 = \Omega_1(t_3^+ - t_3^-)$ is the area, φ_3 is the phase of pulse 3, and optimal areas of pulse 1 $(\pi/2)$ and pulse 2 (π) are used to obtain the maximum coherence in the system. It is not possible to achieve perfect rephasing with just three optical pulses in a system that has non-correlated transitions. In the case of a system with uncorrelated transitions, the detunings Δ_1 and Δ_2 are independent of each other and thus the coherence in equation (2.34) will not rephase for any time for non-zero Δ_1 and Δ_2. The detailed discussion, about the detunings Δ_1 and Δ_2, is given in Chapter 4.

However, perfect rephasing in a case similar to the one considered here was achieved experimentally with six co-propagating optical pulses [(23)]. In that case a

series of six optical pulses with optimized pulse areas (the pulses areas creating the maximum coherence in the system) were applied, alternating between optical transitions as shown in Figure 6. Following the scheme outlined in reference (23), the coherence between levels 1 and 3 after pulse 6 will be

$$\rho'_{13}\left(t > t_6\right)$$

$$\propto e^{-\left(\frac{t-t_1}{T_2'}\right)} e^{i\left(\varphi_6+\varphi_5-2\varphi_4+\varphi_3+\varphi_2-\varphi_1\right)+i\Delta_2\left(t-t_6-t_5+2t_4-t_3-t_2+t_1\right)+i\Delta_1\left(t_6-2t_4+t_2\right)} \quad (2.35),$$

where φ_1, φ_2, φ_3, φ_4, φ_5, and φ_6 are phases of six pulses, t_1, t_2, t_3, t_4, t_5, and t_6 are positions in time of each pulse in the sequence of six pulses.

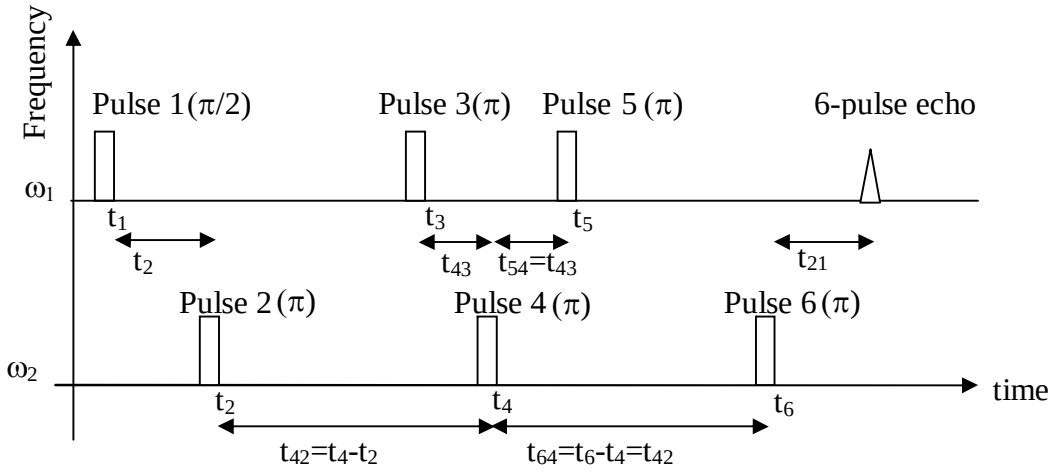

Figure 6: A six pulse sequence to achieve a rephasing in a 4-level system to measure the coherence between non-optical levels.

The perfect rephasing of coherence in the system was achieved by choosing the appropriate timing of these six pulses. Now if we analyze the equation (2.35), it shows that the perfect rephasing will occur at a time $t_{rephase} = t_5 + t_3 - t_1$ with $t_6 = 2t_4 - t_2$. The phase of the rephased radiation, also called the 6-pulse echo, will be $\varphi_{rephase} = \varphi_6 + \varphi_5 - 2\varphi_4 + \varphi_3 + \varphi_2 - \varphi_1$. The rephased radiation will be emitted in the direction, $\vec{k}_{rephase}$, which depends on the propagation direction of each pulse in the sequence and is given by $\vec{k}_{rephase} = \vec{k}_6 + \vec{k}_5 - 2\vec{k}_4 + \vec{k}_3 + \vec{k}_2 - \vec{k}_1$, where $\vec{k}_i, i = 1..6$, represent the propagation directions of these pulses. Note that if all pulses are co-propagating then the rephased radiations will be emitted in the same direction as the pulses. However, in general the direction of rephased radiation may not be the same as any of the propagation directions of the pulses.

Note that in calculating the coherence given in equation (2.35), optimized pulse areas were used. These optimized pulse areas not only create the maximum coherence to produce the 6-pulse echo but also null out other possible coherence signals. However, for practical implementation of this scheme, a laser beam is used and its spatial profile is typically Gaussian unless converted to a uniform intensity beam using spatial beam shaper [(24)]. In most experimental implementations, it is not possible to get rid of all the non-uniformity in the beam intensity. Therefore, in the case of co-propagating optical beams there is always a chance of interference between 6-pulse echo and the echoes produced by other optical pulses in the sequence. This is especially true if the intensities of the beams have Gaussian spatial profiles. For example in the case of non-uniform co-propagating optical pulses, equation (2.35) contains additional terms with each term

rephasing at different times. In these additional terms there is one term from pulses 1, 3, and 5 that rephases exactly at the same time as the 6-pulse echo. This will contaminate 6-pulse echo signal..

However, the contamination of the 6-pulse echo signal from unwanted echoes can be avoided by choosing appropriate propagation direction of each pulse in the 6-pulse echo sequence. If two different propagation directions are chosen such that the propagation direction for pulse 2 is $\vec{k}_2$ and the propagation direction for all other pulses is $\vec{k}_1$, then the 6-pulse echo will propagate along $\vec{k}_2$ and the 3-pulse echo from pulses 1, 3, and 5 will propagate along $\vec{k}_1$. This will thus give us an unadulterated 6-pulse echo without any contamination by other echo signals. In the next section we describe another technique that is also used in certain cases to study the coherence in multi-level systems.

Interaction of Temporally Overlapped Pulses with a 4-Level System

A different technique can be used to excite a 4-level system [(25), (26)]. Here we summarize the results in reference [(25)]. To study the Raman echo phenomenon, narrowband double frequency pulses are used. This technique has some advantages in terms of isolating the desired signal from the unwanted signals. In this section the interaction of multiple bi-frequency pulses with a 4-level system is discussed and conditions are presented for achieving the maximum rephased signal, i.e., the Raman echo.

The analysis is very similar to the case of interaction of a single pulse with a 4-level system, and those results can be used here. First consider a bi-frequency pulse of a

duration τ containing frequencies ω_{1L} and ω_{2L} such that the bi-frequency pulse satisfies the condition of two photon resonance with levels 1, 2, and 3 as shown in Figure 7. Now ignore the phase of each pulse and consider interaction of this pulse at time $t = t_1^-$ with the system having transition frequencies ω_1 and ω_2 as shown in Figure 7.

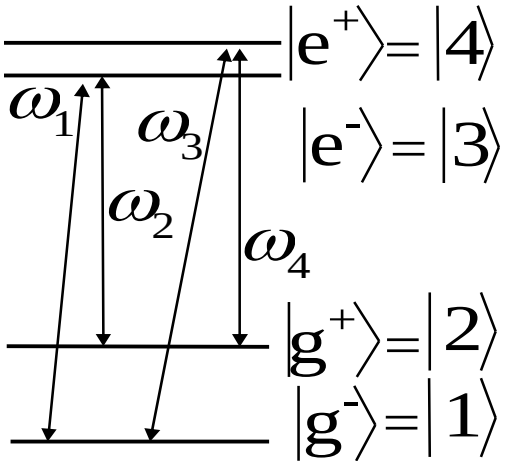

Figure 7: A 4-level system with marked optical transitions.

In this analysis both lower levels (levels 1 and 2) are assumed to be equally populated. The detuning during the pulse and any decay processes, coherence and population decay, during the pulses' duration are ignored. This pulse creates the coherence between levels 1 and 2. The coherence at a time $t > t_1$ is given by the density matrix element [(25)] as

$$\rho'_{12}\left(t > t_1\right) \propto e^{-\left(\frac{t-t_1}{T_2^*}\right)}\left(\frac{\Omega_1\Omega_2}{\Omega_1^2 + \Omega_2^2}\right)\sin^2\left(\frac{\theta_{12}}{2}\right)e^{i\Delta_1(t-t_1)} \qquad (2.36),$$

where $\Delta_1 = (\omega_2 - \omega_1) - (\omega_{2L} - \omega_{1L})$, Ω_1 is the Rabi frequency of the pulse resonant with levels 1 and 3, Ω_2 is the Rabi frequency of the pulse resonant with levels 2 and 3,

$\theta_{12} = \sqrt{\Omega_1^2 + \Omega_2^2}\tau_1$ is the pulse area and τ_1 is the duration of the pulse with $\left(\left|\omega_2 - \omega_1\right|^{-1} < \tau_1 < T_2\right)$. Equation (2.36) gives the maximum value of the coherence for $\theta_{12} = \pi$ and $\Omega_2 = \Omega_1$. Here we choose the area of the first pulse such that we have the maximum coherence in the system (equation (2.36)). Later, at time $t = t_2$ we apply a second bi-frequency pulse of duration τ_2 containing frequencies ω_{3L} and ω_{4L}, such that the bi-frequency pulse satisfies the condition of two photon resonance with levels 1, 2, and 4 as shown in Figure 7. Again the coherence between levels 1 and 2 at a later time, $t > t_2$, will be

$$\rho'_{12}(t > t_2) \propto \tfrac{1}{2} e^{-\left(\frac{t-t_1}{T_2'}\right)}\left(2e^{i\Delta_1(t-t_2)} + e^{i\Delta_1(t-t_1)} + e^{i\Delta_1(t-2t_2+t_1)}\right) \quad (2.37),$$

where $\Delta_1 = (\omega_4 - \omega_3) - (\omega_{4L} - \omega_{3L})$ and the area of the second pulse in the sequence is π with the same Rabi frequencies for each frequency in the pulse. Note that the equation (2.37) implies that there is a time, $t = 2t_2 - t_1$, when the last term in equation (2.37) will perfectly rephase for all detunings Δ_1. To probe the coherence at the rephasing time, a single frequency pulse with frequency ω_{1L} is used, which converts the coherence between levels 1 and 2 to the coherence between optical levels 2 and 3. This coherence produces an optical field with the frequency ω_2, which is observed as a beat signal on the detection pulse as discussed previously. Note that in this scheme, both bi-frequency pulses are shifted in frequency and are separated in time. The application of this scheme in the context of avoiding the temporal overlap of the Raman echo and the 2PE will be discussed in Chapter 4.

Summary

We summarize the results for the coherence phenomena resulting from the interactions of various optical fields with 2- and 4-level systems. These results provide theoretical tools that will be used to characterize the material later in Chapter 4. It was noted that the interaction of a single optical pulse with two optical levels can be used to obtain information about the characteristics of the ions. This provides a useful method in measuring the bandwidth of the ensemble of ions. This method can also be used to measure the state of an ensemble of ions, which will be discussed in Chapter 5. The phenomenon of the 2-pulse echo, arising from the interaction of two time-delayed pulses with two optical levels, will be used to study the coherence properties of the material and of the selected ensemble of ions.

We also presented the results for interaction of a single optical pulse with three levels in a 4-level system. In this case, an expression for the coherent Raman beat was presented. Later, results for the interaction of multiple optical pulses with two levels in a 4-level system were also presented. It was noted that, for the general case where the detunings of the energy levels are uncorrelated, perfect rephasing with three optical pulses may not be possible. In such a system, a modified pulse sequence containing six optical pulses can be used to achieve perfect rephasing in a 4-level system. Finally, another method to achieve perfect rephasing in 4-level system is presented. This method uses bi-frequency pulses to achieve perfect rephasing in a 4-level system. Results of these

studies will be extensively used in Chapter 4 to study the hyperfine coherence time in a 4-level system.

CHAPTER THREE

SPECTRAL HOLE BURNING AND ENERGY LEVEL STRUCTURE OF THULIUM IONS IN A YTTRIUM ALUMINUM GARNET HOST (YAG)

Introduction

Rare-earth-doped crystals at low temperatures (less than 4K) exhibit a narrow absorption line for each individual ion in the crystal. The rare-earth ions, like Pr^{3+} and Eu^{3+} doped into a host material like Y_2SiO_5, which have very weak magnetic fluctuations, can have a 100Hz line-width at low temperatures (less than 2K) [(27), (28)]. The line-width of each absorption line measured in Tm^{3+} doped in YAG can be as narrow as 4kHz [(29)]. In rare-earth-doped crystals, each dopant ion occupies a different environment in the crystal. Thus, the frequency of each dopant ion will be slightly shifted from the neighboring dopant ion. Therefore, in the material absorption spectrum, there are a range of frequencies within which a material can absorb light. The width of the material absorption spectrum is called the inhomogeneous width while the width of absorption spectrum of each ion is called the homogeneous width. The inhomogeneous width is due to the random shifts introduced by the inhomogeneous static environment.

Spectral Hole Burning

One technique used to probe the material absorption is known as spectral hole burning [(30), (31), (32)]. In hole burning, as the name suggests, a spectral hole is burned with a narrowband laser in an inhomogeneously broadened medium by burning

away or modifying the ground state population at a specific frequency in a spectral window in the medium.

Spectral hole burning phenomena can be divided into two broad categories. One is known as a 2-level saturation hole burning, and the other is known as a multi-level persistent hole burning. In saturation hole burning, a resonant field excites the population from the ground state to the excited state. The resultant saturation of the absorbers creates a spectral hole in the absorption profile at that frequency. The hole lifetime in this case is limited by the excited state lifetime. In the case of persistent hole burning, the population of absorbers at the laser frequency is removed from the resonant two levels and is stored in a non-resonant storage level. The lifetime of the spectral hole in this case can be much longer than the lifetime of the excited state. Initially, the phenomenon of saturation hole burning was observed in NMR [(33)] where the spin lattice relaxation was studied. Later on, the phenomenon of saturation hole burning was also observed in an optical system with a HeNe laser [(34)]. The first solid state system investigated using saturation hole burning technique was ruby. In this system, the ruby laser was used to study the cross relaxation parameters in ruby [(35)]. Observation of the phenomenon of persistent hole burning in organic mixed crystals with a dye laser opened a new door for the analysis of other temperature dependent parameters [(36)]. The spectral hole burning technique is also used to measure magnetic moments, Stark coefficients, temperature dependent line-widths, and relaxation times [(37)].

The first rare-earth ion studied using a spectral hole burning technique was Pr^{3+} doped in LaF_3 [(38)]. The main reason for studying Pr^{3+} was the availability of dye lasers

to match the transition wavelength in the material. Later, diode lasers made it possible to study other rare-earth ions, such as Tm^{3+}. The spectral hole burning technique was successfully used in Tm^{3+} doped in LaF_3 to study the relaxation parameters and Stark coefficients [(39)]. In this dissertation the hole burning technique is used to characterize rare-earth ions (Tm^{3+}:YAG) and it is also used to select the ensemble of ions for qubit preparation.

Energy Level of the Tm^{3+}:YAG without the External Magnetic Field

Rare-earth ions such as Pr^{3+}, Eu^{3+} and Tm^{3+} doped into crystals have been extensively studied for optical signal processing [(40), (41), (42), (43)] and more recently for quantum computing applications [(44), (45), (46)]. All of these rare-earth ions have an even number of electrons in their partially filled f shells and exhibit long optical coherence times [(27)]. The reason for long coherence times between f-f transitions is due to the nature of optical dephasing in these ions. The f-f transitions are very well shielded from the environment. One mechanism limiting the dephasing is magnetic in nature [(29)]. The dephasing in these materials is usually due to magnetic spin fluctuations of the host ions. Thus, the rare-earth ions doped in a host with very weak magnetic moment can have long coherence times [(47)]. In the case of thulium-doped in YAG, experimental data has shown that the fluctuating nuclear spin fields of aluminum ions contribute towards reduction in the coherence time [(29)].

Preliminary studies for quantum computing applications in Pr^{3+} and Eu^{3+} have shown promising results [(48), (49), (50)]. However, one problem with these systems is

the transition wavelengths. Transition wavelengths in both of these materials can only be accessed with dye lasers, and these lasers are notoriously hard to stabilize, without elaborate apparatus, to the level of stability needed for quantum computing applications. Currently, very few systems exist in the world that can achieve the kHz stability required for quantum computing applications.

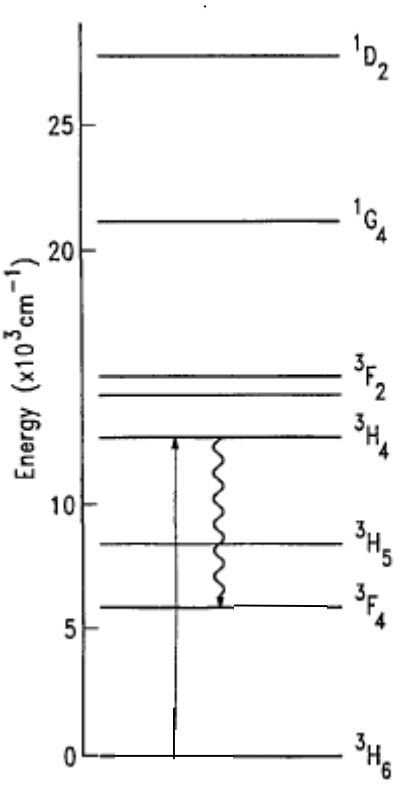

Figure 8: Energy level structure of Tm^{3+} [(39)] without an external magnetic field. Here transition at 793nm and decay from excited state to the intermediate level are marked.

On the other hand Tm^{3+} has an f-f transition at 793nm that can be accessed with the commercially available diode lasers. These diode laser systems are cheap, compact, and can be easily stabilized to sub kHz line-width with the spectral hole locking techniques [(51)]. The transition of interest between the lowest crystal field level of

ground state multiplet, $^3H_6$, and the lowest crystal field level of an excited state multiplet, $^3H_4$, in Tm^{3+} ion doped in YAG is shown in Figure 8.

Now consider the interaction of a narrowband laser with levels $^3H_6$ and $^3H_4$ in Figure 8. Then the hole burning spectrum from the medium will be similar as given in Figure 9. Note that there will be just the absorption change at the burning frequency. The hole burning spectrum provides a tool for absorption spectroscopy of the medium.

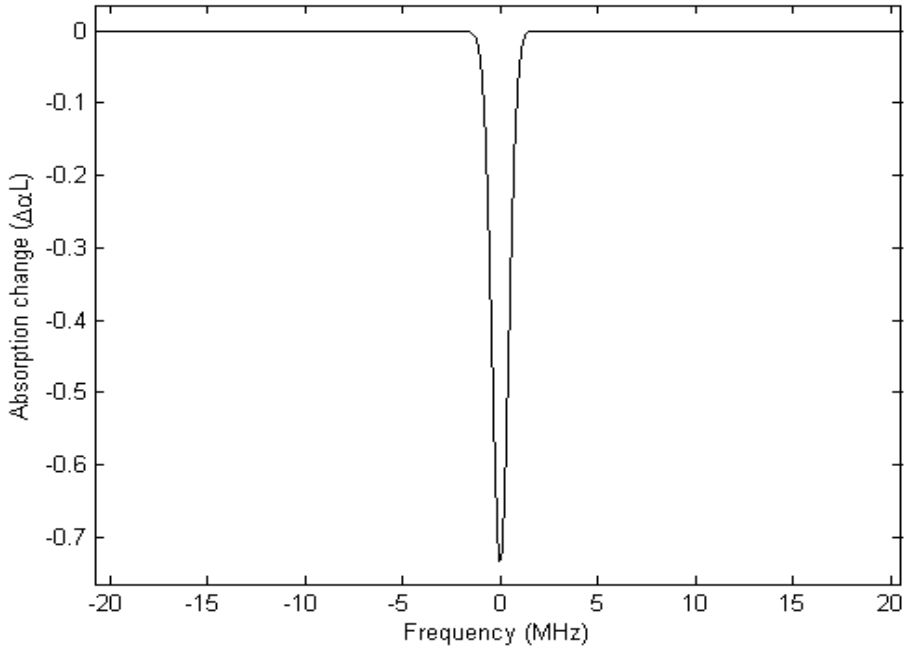

Figure 9: Simulation of the hole burning spectrum for a 2-level system. The horizontal axis is referenced with respect to the burning frequency.

Now again we switch back to the task at hand. Our aim for the material study is to optimize the conditions in Tm^{3+}:YAG for quantum computing applications. Most of these schemes require more than two accessible levels. In these schemes, usually the hyperfine structure is used to store the qubit. But the Tm^{3+}:YAG has no hyperfine structure at zero

applied field external magnetic field. In the next section we give an overview of a method for obtaining appropriate hyperfine structure in the Tm^{3+}:YAG by applying an external magnetic field.

Energy Level of the Tm^{3+}:YAG with the External Magnetic Field

Here we skip details about the structure of the crystal and description of thulium ions at different sites in the crystal. The detailed treatment is given in Chapter 4. Here we just note that if Tm^{3+} doped in YAG is placed in the external magnetic field, then each electronic level splits into two spin states, and the degeneracy in the spin states is lifted. This creates a hyperfine structure that can be used for qubit storage in quantum computing applications. Hence, the external magnetic field gives us a 4-level system in Tm^{3+}:YAG as depicted in Figure 10.

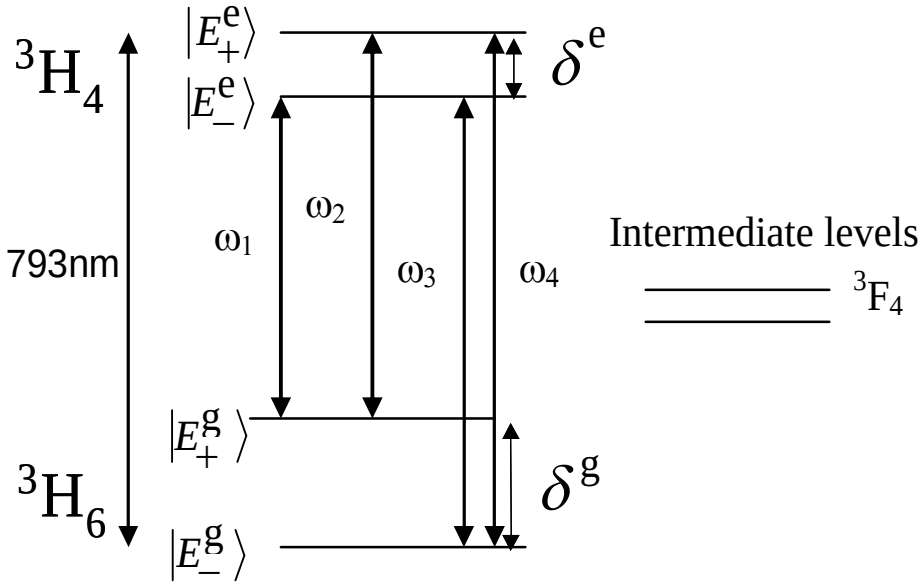

Figure 10: Selected energy levels of Tm:YAG with the external magnetic field

In an earlier study, the hyperfine structure in Tm^{3+}:YAG has been used as a way for long term population storage for signal processing applications [(52)]. Our aim is to tailor a 3-level system within the 4-level Tm^{3+}:YAG system for quantum computing applications. Before we present the quantitative analysis for the interaction of magnetic field with Tm^{3+}:YAG; we first consider an interaction of a narrowband laser pulse with the 4-level system. In this case even though the burning pulse is resonant with two levels in the 4-level system, it will result in a change in the absorption at other frequencies as well. The hole burning spectrum of such an interaction is shown in the Figure 11. The hole burning spectrum shows the absorption changes at nine different frequencies due to population redistribution among hyperfine levels.

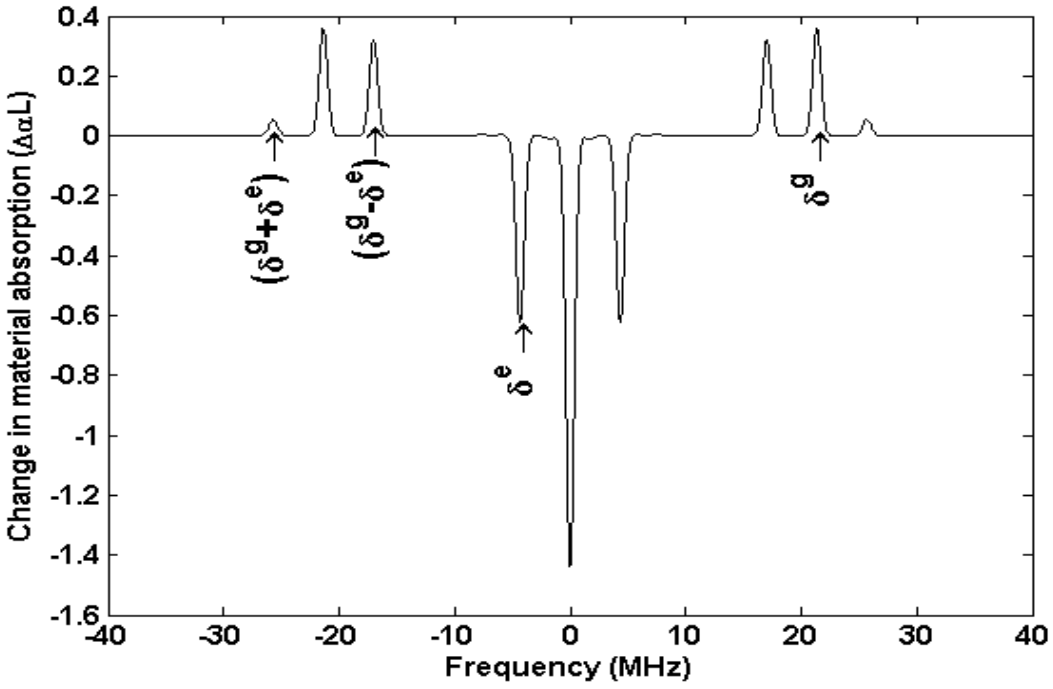

Figure 11: The hole burning spectrum from a 4-level system. Again the horizontal axis is referenced with respect to the burning frequency.

Here the absorption changes, due to the burning frequency, at 0MHz and at other frequencies, are marked relative to the burning frequency. Note the hyperfine splittings [Figure 10] and the locations of the changes in absorption in the hole burning spectrum [Figure 11]. This hole burning spectrum can also be used to obtain the values for the hyperfine splittings in the medium. We can also use this hole burning spectrum to study the relaxation dynamics of the 4-level system. Now we qualitatively analyze the interaction of a magnetic field with Tm^{3+}:YAG.

For qualitative analysis, consider the general Hamiltonian in the presence of an external magnetic field as [(53), (54)]

$$\hat{H} = \left[\hat{H}_{FI} + \hat{H}_{CF}\right] + \left[\hat{H}_{HF} + \hat{H}_{Q} + \hat{H}_{EZ} + \hat{H}_{NZ}\right] \qquad (3.1),$$

where $\hat{H}_{FI}$ is the free ion, $\hat{H}_{CF}$ is the crystal field, $\hat{H}_{HF}$ is the hyperfine interaction, $\hat{H}_{Q}$ is the nuclear-electric quadrupole interaction, $\hat{H}_{EZ}$ is the electron Zeeman interaction, and $\hat{H}_{NZ}$ is the nuclear Zeeman interaction in the Hamiltonian.

The first two terms in the Hamiltonian, equation (3.1), are dominant terms, and they determine the structure of electronic levels while other terms have much smaller contribution to the energy level structure. The Eigen-functions obtained using the first two terms are used to obtain the hyperfine splitting and the splitting due to magnetic interaction. In the case of Tm^{3+}:YAG, for zero external applied magnetic field, the hyperfine interaction and magnetic effects appear in second order. The quadrupole interactions also vanish in Tm^{3+}:YAG, as thulium is a spin ½ system. Therefore, the effective Hamiltonian is comprised of the last four terms in the total Hamiltonian [(37)]

$$\hat{H}_{eff} = \sum_{\alpha\beta=(x,y,z)} \gamma_{\alpha\beta} B_\alpha I_\beta \qquad (3.2),$$

where $\gamma_{\alpha\beta} = -g_N \mu_N - 2 g_J \mu_e \Lambda_{\alpha\beta}$, $\Lambda_{\alpha\beta} = A_J \sum_{n=1}^{2J+1} \frac{\langle 0|J_\alpha|n\rangle\langle n|J_\beta|0\rangle}{E_n - E_0}$, $g_N (g_J)$ is the nuclear (electronic) g-value, $\mu_N (\mu_e)$ is the nuclear (electronic) Bohr magneton, A_J is the hyperfine coupling constant, J is the total angular momentum, $|n\rangle$ are the crystal field levels with $|0\rangle$ being the lowest level, I is the nuclear spin, and B is the applied external magnetic field. The effective Hamiltonian is [(53), (37)]

$$\hat{H}_{eff} = \gamma_x B_x I_x + \gamma_y B_y I_y + \gamma_z B_z I_z \qquad (3.3),$$

where $\gamma_\alpha = -g_N \mu_N - 2 g_J \mu_e \Lambda_{\alpha\alpha}$ give principal values of the gyromagnetic tensor along the principal axis.

For a spin ½ system, the spin Hamiltonian (equation (3.3)) in $|-\tfrac{1}{2}\rangle$, $|+\tfrac{1}{2}\rangle$ basis can be written as

$$H_{eff} = \frac{1}{2}\begin{pmatrix} -\gamma_z B_{0z} & \gamma_x B_{0x} + i\gamma_y B_{0y} \\ \gamma_x B_{0x} - i\gamma_y B_{0y} & \gamma_z B_{0z} \end{pmatrix} \qquad (3.4),$$

which shows that for $\gamma_x B_{0x} - i\gamma_y B_{0y} = 0$, the external magnetic field, $\vec{B}_0 = (B_{0x}, B_{0y}, B_{0z})$, will be parallel to the z-axis and there will be no mixing of spin states in the energy levels for ground and excited states.

However, note that if the magnetic field is not parallel to the z-axis, i.e., $\gamma_x B_{0x} - i\gamma_y B_{0y} \neq 0$, then there will always be mixing in spin states. Thus the energy Eigen-states and energy Eigen values will be

$$\left|E_{+}\right\rangle = a_1\left|+\tfrac{1}{2}\right\rangle + a_2\left|-\tfrac{1}{2}\right\rangle \tag{3.5}$$

$$\left|E_{-}\right\rangle = a_3\left|+\tfrac{1}{2}\right\rangle + a_4\left|-\tfrac{1}{2}\right\rangle \tag{3.6}$$

where $a_1 = \sqrt{\frac{\left(E-\gamma_z B_{0z}\right)}{2E}}$, $a_2 = \frac{\gamma_x B_{0x} - i\gamma_y B_{0y}}{\sqrt{2E\left(E-\gamma_z B_{0z}\right)}}$, $a_3 = -\frac{\gamma_x B_{0x} - i\gamma_y B_{0y}}{\sqrt{2E\left(E+\gamma_z B_{0z}\right)}}$,

$a_4 = \sqrt{\frac{\left(E+\gamma_z B_{0z}\right)}{2E}}$, $E_{+} = +\frac{E}{2}$, $E_{-} = -\frac{E}{2}$, and $E = \sqrt{\left(\gamma_x^2 B_{0x}^2 + \gamma_y^2 B_{0y}^2 + \gamma_z^2 B_{0z}^2\right)}$.

Since Tm^{3+} is a spin ½ system, for the general orientation of the magnetic field, each of its electronic level will split into two sub-levels as shown in Figure 10, and the energy differences for excited and ground state manifolds will be

$$\delta^e = \left(E_{+}^e - E_{-}^e\right) = \sqrt{\left(\gamma_x^e B_{0x}\right)^2 + \left(\gamma_y^e B_{0y}\right)^2 + \left(\gamma_z^e B_{0z}\right)^2} \tag{3.7}$$

$$\delta^g = \left(E_{+}^g - E_{-}^g\right) = \sqrt{\left(\gamma_x^g B_{0x}\right)^2 + \left(\gamma_y^g B_{0y}\right)^2 + \left(\gamma_z^g B_{0z}\right)^2} \tag{3.8}$$

where index e denotes the excited state and index g denotes the ground state.

Thus instead of absorption at a single frequency as is the case in Figure 8, there will be a possibility of optical absorption at four distinct frequencies as shown in Figure 10. The absorption probabilities at these frequencies are directly related to the probability of cross-transition between any of the two electronic energy levels.

Note that the optical field cannot flip the spin; i. e., cross-transition probability is zero for pure spin states. In the current situation, each spin state is mixed, as can be seen in equations (3.5, 3.6), and this makes the transition probability non-zero for cross-transitions in thulium. The transition probabilities are defined as

$$R_{+-} \propto \left|\left\langle E_{+}^g \left|\mu\right| E_{-}^e \right\rangle\right|^2 \tag{3.9}$$

$$R_{++} \propto \left| \left\langle E_{+}^{g} \left| \mu \right| E_{+}^{e} \right\rangle \right|^{2} \qquad (3.10),$$

where $R_{++} = R_{--}$, $R_{+-} = R_{-+}$, and μ is the optical transition dipole. In the next chapter, the transition strengths [(3.9-3.10)] and hyperfine splittings [(3.7-3.8)] for thulium ions at different sites in the YAG crystal are studied using the spectral hole burning technique.

CHAPTER FOUR

CHARACTERIZATION AND OPTIMIZATION OF THULIUM IONS IN A YTTRIUM ALUMINUM GARNET HOST (YAG) FOR QUANTUM COMPUTING APPLICATIONS

Introduction

In this chapter, thulium-doped YAG is investigated for building a 3-level system where a qubit can be stored and manipulated. The storage space for the qubit is provided in the two levels of the thulium hyperfine manifold of either the ground state or the excited state. The operation on the qubit is implemented by the optical pulses that couple these two hyperfine levels to a common electronic level. The hyperfine structure of Tm^{3+}:YAG is obtained with an applied external magnetic field.

The objective of the analysis in this chapter is to optimize conditions for qubit storage and manipulation in the system. Therefore, there are three main objectives. One is to optimize the conditions for the optical coupling of the two hyperfine levels with a single common level (known as a Λ or V system as shown in Figure 12). The second objective is to optimize the conditions for long term population storage in the hyperfine levels. And the third is to optimize the conditions in the material for long term coherence storage in the hyperfine levels. The first objective is critical for the storage and manipulation of the qubit. The second objective plays a critical role for the selection of the ensemble of ions for the qubit preparation. The third objective provides the optimal conditions for the storage time in the hyperfine levels for the qubit.

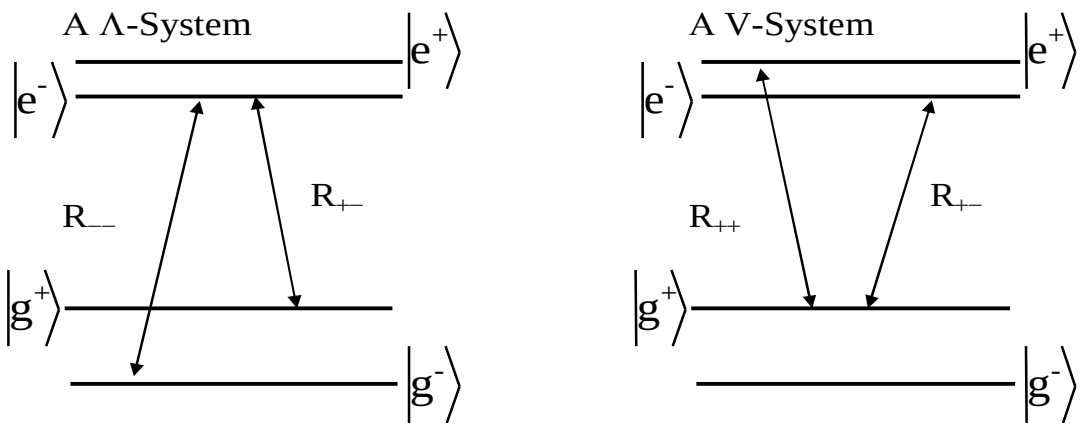

Figure 12: Two different 3-level systems for quantum computing applications. Here the cross-transition is given by R_{+-}, and the direct transitions are given by R_{++} and R_{--}.

The organization of this chapter is as follows. First, the details of the experimental set-up and the introduction about the material are presented. Then, the basic theory given in Chapter 3 is used to identify the hyperfine splittings from the thulium ions at each site in the crystal. In order to optimize the coupling of the two hyperfine levels with the common electronic level, we need to optimize the cross-transition probabilities. The first step to achieve this goal is to use the basic theory and find the probabilities of optical transitions between each level for the thulium ions at all different sites in the crystal. The definition for the transition probabilities is the same as was defined in the reference (55). The cross-transition probabilities critically depend on the magnetic anisotropy in the medium. The magnetic anisotropy in the medium was determined by measuring the components of the gyromagnetic tensors. We initially used the theoretical results of reference [(55)], for the values of components of the gyromagnetic tensors to gain insight into the cross-transition probabilities for the thulium ions at different sites in the

crystal. The theoretical results in the reference [(55)] also provided us with the estimate for the hyperfine splittings for thulium ions at different sites in the crystal. The effects of the misalignment of the magnetic field on the transition probabilities and the hyperfine splittings are also presented. This background knowledge was applied to the experimental results to study the hole burning spectra from the medium.

The components of the gyromagnetic tensor were measured by mapping the hyperfine splitting for various orientations of the magnetic field. The mapping was obtained using the spectral hole burning experiment. In the recent experimental study, the hole burning technique was used and the y-components of the gyromagnetic tensors were obtained [(56)]. Partial information was gained about the other components (x and z) of the gyromagnetic tensors [(56)]. Our hope in the experiment was to gain more information about the x, and z components of the gyromagnetic tensors by using the full mapping of the hyperfine splitting and the magnetic field orientation. These two components (x and z) of the gyromagnetic tensor are important because they significantly affect the transition probabilities for the thulium ions at each site. The information gained from these measurements was used to select the orientations of the magnetic field for the optimal transition probabilities. In Tm^{3+}:YAG optimal orientations of the magnetic field are being studied. The optimal orientations of the magnetic field are chosen as the orientations for which the direct [R_{++}, R_{--}] and cross-transition [R_{+-}, R_{-+}] probabilities are comparable to each other.

The second objective was to maximize the population lifetime of hyperfine levels. To fulfill this objective, we investigated the population lifetime of the hyperfine levels for

two optimal orientations. This task will maximize the population lifetime of the hyperfine levels. Previous results indicate that the population lifetime of the hyperfine levels for the thulium ions in the crystal can be more than a second [(52)]. Recently, the population lifetime of the hyperfine levels was again measured for a non-optimal orientation of the magnetic field, and more than a minute of population lifetime of hyperfine levels was observed [(57)]. In both of these experiments, the population lifetime of hyperfine levels was measured by observing the decay of the central hole. Those past studies have drawn contradictory conclusions about the population lifetime of the hyperfine levels and its dependence on the strength of the magnetic field. In one study, the lower applied magnetic field resulted in a longer population lifetime of the hyperfine levels [(52)], while in the other study, the opposite was true [(57)]. Thus, our goals were to observe the decay of the absorption features arising specifically from the interaction of the ions at each site in the crystal and to investigate both claims of the past investigations [(52), (57)]. This method should provide direct and unambiguous results for the population lifetime of both excited and ground state hyperfine levels. We also investigated the dependence of the population lifetime on the orientation of the magnetic field. This investigation should also shed the light on the population lifetimes of hyperfine levels for ions at different sites in the crystal and their dependence on the local environment in the crystal and orientation of the magnetic field.

In the next step, two optimal orientations of the magnetic field were selected for the investigation of the coherence time of the hyperfine levels. This investigation will choose the orientation of the magnetic field for the maximum coherence time as required

by one of the objectives outlined earlier. In this study, two different methods were used to explore the hyperfine coherence time. This study will provide information about the hyperfine coherence time for ions at different sites in the crystal and also about the dependence of the hyperfine coherence time on the orientation of the magnetic field.

In this chapter, a theoretical model describing the population excitation and relaxation in Tm^{3+}:YAG is also developed. This model describes the relaxation mechanism in thulium under an applied magnetic field. The theoretical results of the model in conjunction with the time-dependent experimental data for the spectral hole burning experiment will be used to obtain the excitation and relaxation parameters. This theoretical model will also be used to tailor the medium for qubit preparation.

Sample and Experimental Set-up

For all of the characterization experiments, 0.1% atm. doped thulium in YAG was used and was vapor-cooled in a liquid helium cryostat.

Magnetic Field and the Design of the Helmholtz Coil

The static magnetic field was supplied with a home-made Helmholtz coil. The Helmholtz coil is often used to provide the uniform magnetic field over the interaction region in the crystal. The Helmholtz coil consists of a parallel pair of two identical circular coils, where the separation between the two coils equals the radius of the coil. The windings on these coils are such that the current flows through both coils in the same direction. The winding of the coils and the separation between the coils result in a uniform magnetic field in a large volume between the coils. The resultant uniform

magnetic field is along the common axes of the two coils. The strength of the magnetic field is directly proportional to the number of turns on each coil and the applied current.

In the current design, the heat generated from each coil and the efficiency of the cooling system dictated the maximum number of turns for each coil. Thus, the current design has 50 layers of 14 turns for each coil that amounts to 700 turns for each coil. The design of the coil was based on the design being used by the Cone Lab in Physics, MSU, Bozeman. The outer radius of the cryostat has restricted the inner radius of each coil to about 60mm. The current system can handle a maximum current of about 7.5 A in each coil without overheating. However, the typical operating current was about 5 A, well below the maximum current. The data set in Figure 13 shows the measured values of the magnetic field along the common axes of these two coils at the midpoint between the coils for the applied current in each coil. The measured data set for the magnetic field was obtained using a Hall probe. The Hall probe was borrowed from the Idzerda Lab in Physics, MSU, Bozeman. The diameter of the sensitive area of the Hall probe was 4.8mm. Thus, the uncertainty in the position was $\pm 2.4\text{mm}$ in the data for Figure 14. The data set in Figure 13 shows a linear dependence on the magnetic field with the applied current varying as $B_0 = (80.82 \pm 0.83)I$ Gauss, where I is the current in amperes in each coil.

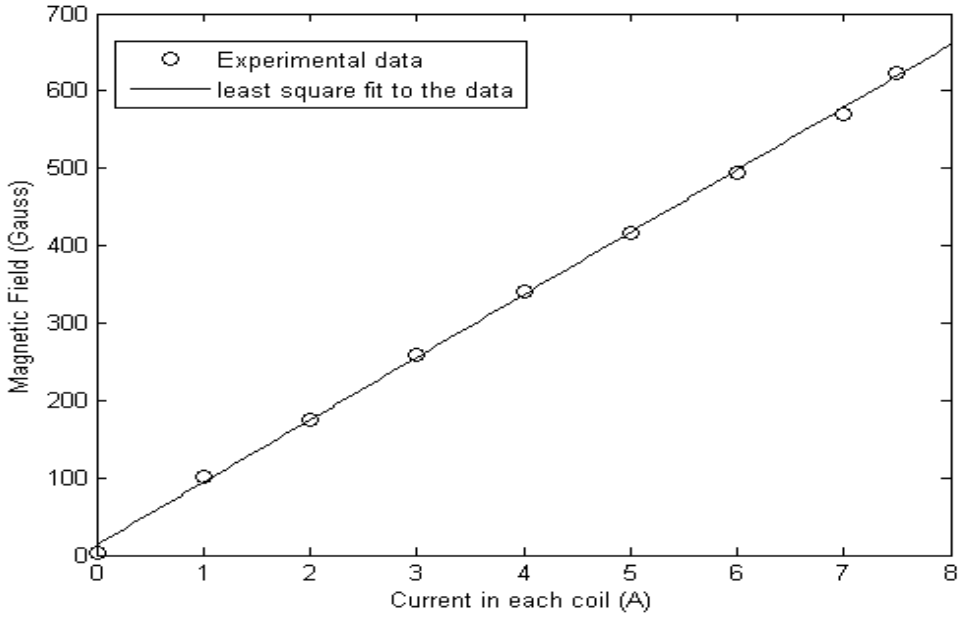

Figure 13: Experimental values of the magnetic field along the common axis of two coils at the midpoint between two coils.

The inhomogeneity in the magnetic field is measured using the position-dependent measurements of the magnetic field. We again used the above-mentioned Hall probe. The biggest error in these measurements was the uncertainty in the position, and in this case, the uncertainty in the position was $\pm 2.4\text{mm}$. The data set in Figure 14 shows the magnetic field and its dependence on the position. In the first part of this experiment, the current in each coil was fixed, and the magnetic field was measured as a function of the distance from the midpoint between the coils along the coil axis. The normalized measurements of the magnetic field along the axis of these coils are shown in Figure 14 as stars. This data set shows that the magnetic field is fairly uniform over $\pm 20\text{mm}$ with the maximum change in the magnetic field about 0.3% over $\pm 10\text{mm}$.

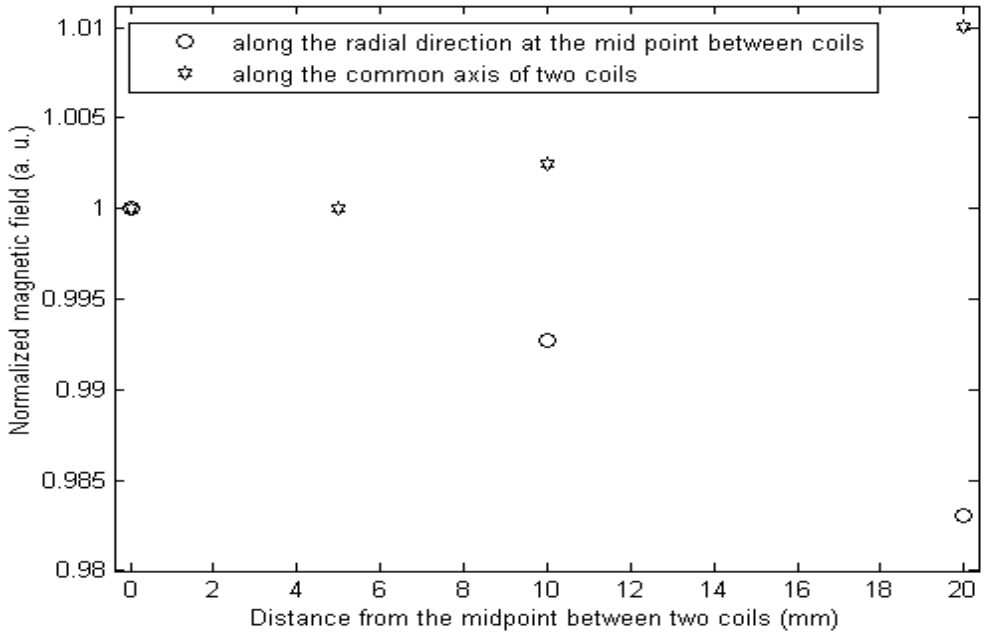

Figure 14: Magnetic field as measured with the magnetic probe at different positions away from the midpoint at the common axis between coils.

In the second part of the experiment, the magnetic field is traced along the radial direction in the plane containing the midpoint between the coils. The data for this part of the experiment again show the uniform magnetic field with the maximum change in the magnetic field about 0.3% over the $0-10\text{mm}$ distance from the midpoint in the center. This set-up thus provided a homogeneous $(\pm 0.3\%)$ magnetic field over the sample interaction length of $\leq 20\text{mm}$. The vertical and the horizontal positioning of the interaction volume were maintained to be within $\pm 10\text{mm}$ of the center of the coil.

The Stabilized Laser Source, RF Electronics, and the Detector

The laser source used in all the experiments was a New Focus Vortex Laser, an external cavity diode continuous wave laser operated at 793.380 nm. The output from the laser was amplified with an Eagleyard semiconductor tapered amplifier. The tapered amplifier, when driven at 1.5A, provided a 13dB gain to the input laser power at 793nm at room temperature. A maximum output laser power of 500 mW was obtained on amplification.

The frequency of the laser was stabilized to 10kHz over a second with the spectral hole locking [(51)]. In the spectral hole locking, the Pound-Drever-Hall locking technique [(58), (59)] is used to stabilize the frequency of the laser by locking the frequency of the laser to the spectral hole instead of locking the laser to the high finesse cavity. This method provides a frequency stabilized laser with 10kHz drift in the laser frequency over a second [(50)].

The phase, the amplitude, and the temporal duration of each optical pulse were controlled digitally using two acousto-optics modulators (AOM 1, AOM 2). Each acousto-optic modulator was driven by an arbitrary waveform generator (Tektronix AWG 520). Each AOM had a center frequency of 125MHz with 40 MHz bandwidth.

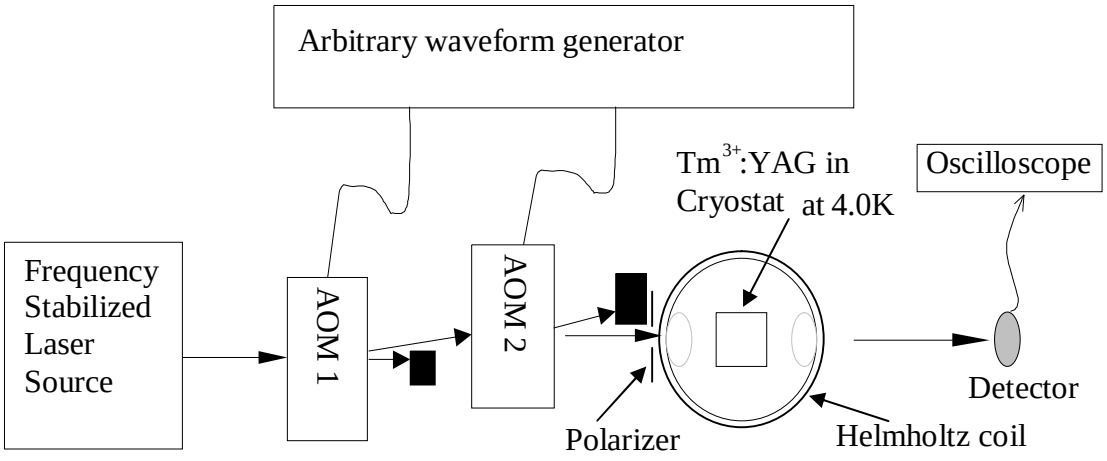

Figure 15: Experimental set-up for spectral hole burning, free induction decay, and photon echo experiments

The output signals were detected with a Thorlabs amplified silicon detector, PDA155, of 50 MHz bandwidth and 2.5×10^{-11} W/$\sqrt{\text{Hz}}$ noise equivalent power (NEP) at 793 nm. Each data set was collected with a four channel digital oscilloscope (Tektronix TDS 3054) having 500 MHz bandwidth and 5 GS/s maximum sample rate. The complete experimental set-up is shown in Figure 15.

The Alignment of the Optical Beam and the Magnetic Field

In this experiment, the optical beam was kept parallel to the optical bench, which contains all the optics. The level of the optical table was checked with a bubble level, and it was found to be leveled with the floor (earth) within the accuracy, 0.1mm/M or $\pm 0.006^{o}$, of the bubble level [(60)].

Here, we investigate the misalignment introduced in the experimental set-up due to the misalignment of the optical set-up and due to the misalignment of the Helmholtz

coil. This analysis will provide us the upper bound on the misalignment in the experimental set-up. Later, we will see that any misalignment in the experimental set-up is insignificant as compared to the error in the axes of the crystal. We start with the polarizer. It was calibrated using a polarized beam, with the zero on the dial marking the horizontal polarization with respect to the optical table. The dial on the polarizer has markings 1.0^{o} apart and thus has 0.5^{o} error for polarization of the optical beam. The optical beam was aligned to propagate along the $[1-10]$direction of the crystal with the polarization of the optical beam oriented in the (1-1 0) plane. The plane (1 -1 0) was perpendicular to the optical table. The alignment of the optical beam in the required orientation was achieved by overlapping the incident beam on the (1-10) plane with the reflected beam from the surface of the (1 -1 0) plane (the front surface of the crystal).

In the experiment a 1 mm diameter optical beam was overlapped with the back reflected beam. The maximum separation between the two beams was 0.5 mm at a 600 mm distance away from the front surface of the crystal. This misalignment introduced an error of about 0.02^{o} in the tilt of the optical beam with respect to the (1 -1 0) plane of the crystal.

Another factor contributing to the error in the optical beam alignment is the position of the optical beam with respect to the optical bench. In order to quantify the error, the vertical position of the optical beam was measured with respect to the optical table before and after the crystal. The two positions were 1200 mm apart and the difference in the vertical positions of the optical beam at these two locations was 0.5 mm. This introduced an additional uncertainty of 0.02^{o} in the beam tilt with respect to the

optical table and the magnetic field axis. Thus, the total error in the alignment of the optical beam with the $[1-10]$ direction was 0.03^{o}. This error is too small to have any significant effect on the measurements and can be ignored.

Another possible source of an error is in the centering of the optical sample at the midpoint between the two Helmholtz coils. The magnetic field from the Helmholtz coils is uniform around the midpoint, as shown in Figure 14. Thus, this error analysis will help in establishing the inhomogeneity of the magnetic field being experienced by the optical sample. The error discussed earlier was critical in establishing the interaction of the optical and the magnetic fields with the thulium ions at various sites in the crystal, as interactions of these ions critically depend on the direction of the applied optical and magnetic fields. The inhomogeneity in the applied magnetic field usually contributes to the inhomogeneous broadening of the hyperfine levels.

In the experiment, our aim is to have minimal effect from the inhomogeneity in the magnetic field. This can be achieved by centering the beam at the midpoint between the coils of the Helmholtz coil, which will make the inhomogeneity in the applied magnetic field negligibly small, $\pm 0.3\%$ (Figure 14). Results (Figure 14) for the mapping of the magnetic field around the midpoint show that the magnetic field has less than 1% inhomogeneity in the magnetic field for 20 mm radius around the midpoint.

In the drawing in Figure 16, the Helmholtz coil will have negligibly small inhomogeneity, $\pm 0.3\%$, in the applied magnetic field in the spherical region of radius 10mm centered at $(60\text{mm}, 60\text{mm}, 25.90\text{mm})$. In the laboratory, we were able to adjust the

Helmholtz coil around the cryostat so that the sample is within 1mm of an ideal vertical height, 25.90mm , the height needed for the uniform magnetic field.

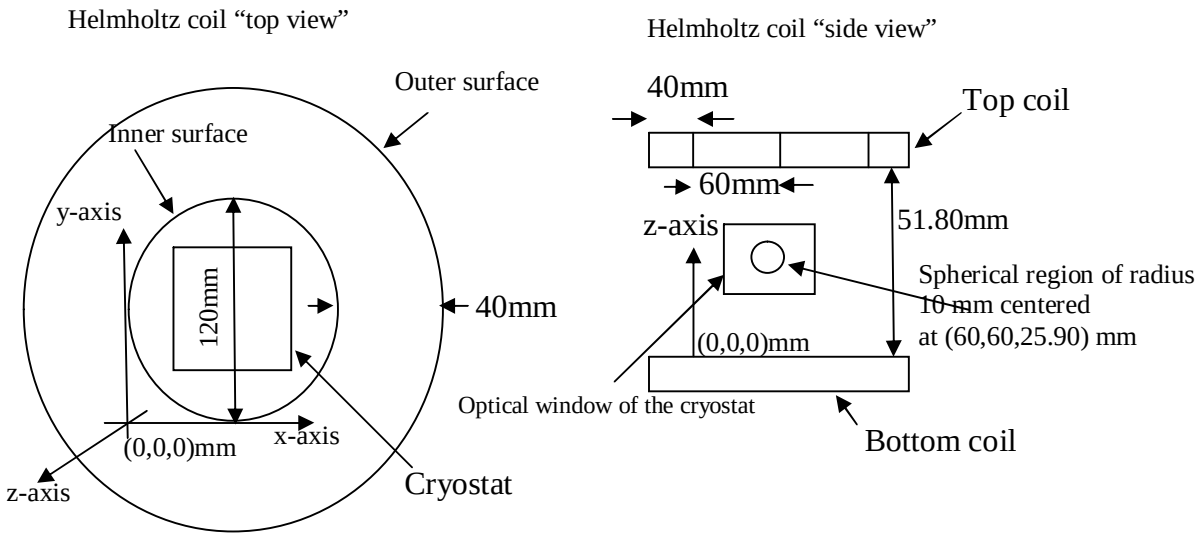

Figure 16: Helmholtz coil as arranged around the cryostat for application of uniform magnetic field to the sample in the cryostat.

The vertical position of the optical beam passing through the crystal was measured with reference to the upper surface of the bottom coil, and the height of the Helmholtz coil is adjusted to achieve the required height of 25.90 mm. However, the horizontal adjustment was tricky as there was less room to maneuver the Helmholtz coil around the cryostat. Note that the distance between the inner surface of the coil and the closest point of the outer surface of the cryostat is 10mm. The design of the optical mount was such that the sample, and hence the optical beam, were not centered in the optical window. This resulted in our inability to align the optical beam exactly at

$(60\text{mm}, 60\text{mm}, 25.90\text{mm})$. In the end, the optical beam was 5.0 mm away from the center in the plane containing the midpoint between the coils. Thus, the sample was centered at $(55\text{mm}, 55\text{mm}, 25.90\text{mm})$. These two errors introduced less than 1% inhomogeneity in the sample, as can be seen from the data in Figure 14.

Now consider an error in setting up the Helmholtz coil along the normal to the optical table. The heights of the two coils in the Helmholtz coil were adjusted with respect to the table so that each coil is parallel with each other, and they are also parallel to the table. The error in these adjustments is the error in measuring the heights. The smallest division (1mm) on the scale defined the error in our measuring the heights. Therefore, this measurement error will introduce $\pm 0.06^{o}$ error in the alignment of the magnetic field. This error again is small as compared to the error in determining the crystal axis which may be $\pm 3^{o}$ or more. The crystal manufacturer, Scientific Materials, Bozeman, MT, quoted $\pm 3^{o}$ error in measuring the plane of the crystal axis for the cutting.

In our alignment procedure, we also used the bubble level in measuring the level of the polarizing beam cube. This polarizing beam cube was used to calibrate the dial on the polarizer. The bubble level was also used to measure the level of the optical table. The accuracy of these levels is about 0.1 mm/M [(60)]. Thus, the error introduced in the polarizer dial will be less than a degree. The accuracy of the bubble level was also measured. The bubble in the bubble level moved 2.0 mm from the center with 1.0^{o} inclination from the level surface. Thus, the error in the analysis is less than $1^{o} - 2^{o}$.

The Crystal Structure of YAG

The host material is yttrium aluminum garnet (YAG),$Y_3Al_5O_{12}$. The host has cubic space group symmetry with eight formula units per unit cell as shown in Figure 17 [(61)]. The yttrium ions, Y^{3+}, occupy c sites in the crystal, which have D_2 local symmetry. The aluminum ions, Al^{3+}, are found in two different sites, a and d, in the crystal. The aluminum ions at a-site experience the crystal field of C_{3i} symmetry, and the aluminum ions at d-site experience a crystal field of S_4 symmetry. When Tm^{3+} is doped in YAG, it substitutes for some of the Y^{3+} in dodecahedral sites and experiences the same crystal field of D_2 symmetry.

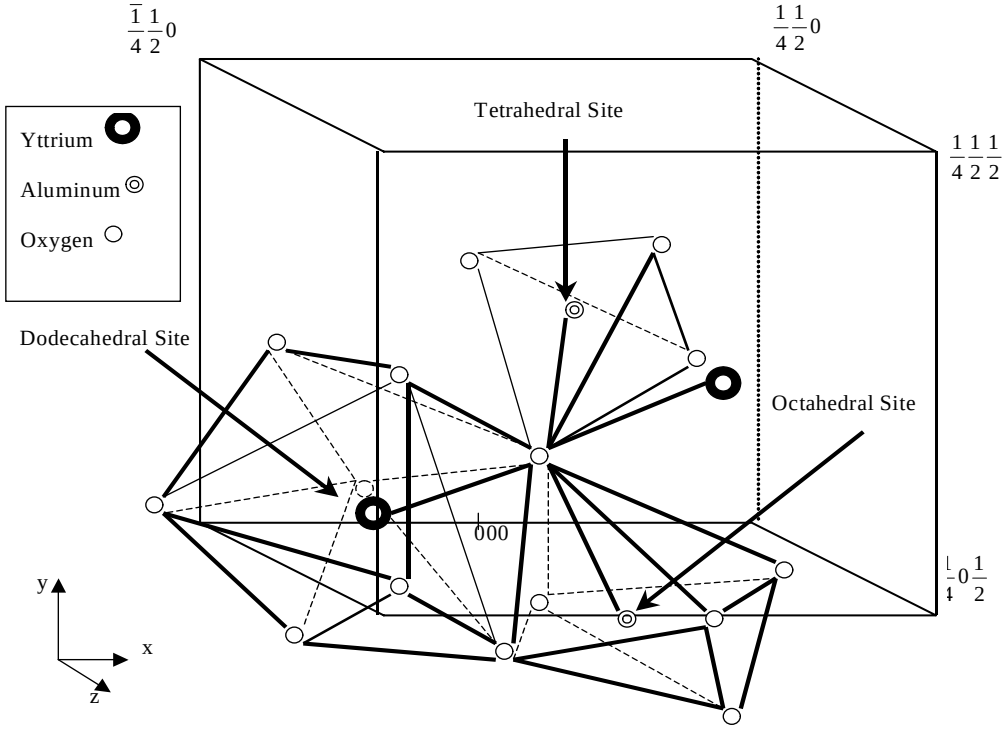

Figure 17: One octant of the unit cell of YAG lattice is shown [(61)].

Since thulium ions reside in the c-site with D_2 symmetry, it is instructive to focus on the c-sites in the crystal. In garnet (YAG) crystal there are twenty-four c-sites in a unit cell. These c-sites are divided into three groups with eight c-sites in each group. One of these three groups has a local z-axis parallel to a <001> axis of the crystal. Each of these groups of eight sites is further subdivided into two groups. The axes of these two groups are rotated 90^o from each other with the common z-axis, as shown in Figure 18. These six groups, with each group containing four sites, are called six magnetically inequivalent sites.

The Electronic and the Magnetic Dipole Directions in the Crystal

In Tm^{3+}:YAG, the electronic levels are non-degenerate, as the crystal field lifts the degeneracy in the electronic levels. These non-degenerate electronic levels, known as Stark levels, are hundreds of GHz apart [(62), (63)]. In these transitions between Stark levels, the lowest crystal field level of the ground multiplet, $^3H_6(1)$, and the lowest crystal field level of the excited multiplet, $^3H_4(1)$, are 793nm apart. This transition is accessible with diode lasers and is the focus of the study in this dissertation.

The transition at 793nm is an f-f transition. An f-f optical transition is not allowed in first order, but in this case, due to wave function mixing with 5d levels, the transition rule is relaxed, and thus, the f-f transitions here are weakly allowed. As the thulium ion has partially filled a 4f shell with an even number of electrons, it is called a non-Kramer ion [(64)].

Six crystallographically equivalent, but orientationally inequivalent, sites are pictured in Figure 18. They occupy D_2-symmetry sites; the electronic and magnetic transition dipole necessarily will be along either of the local axes (x, y, z) of the site [(65)].

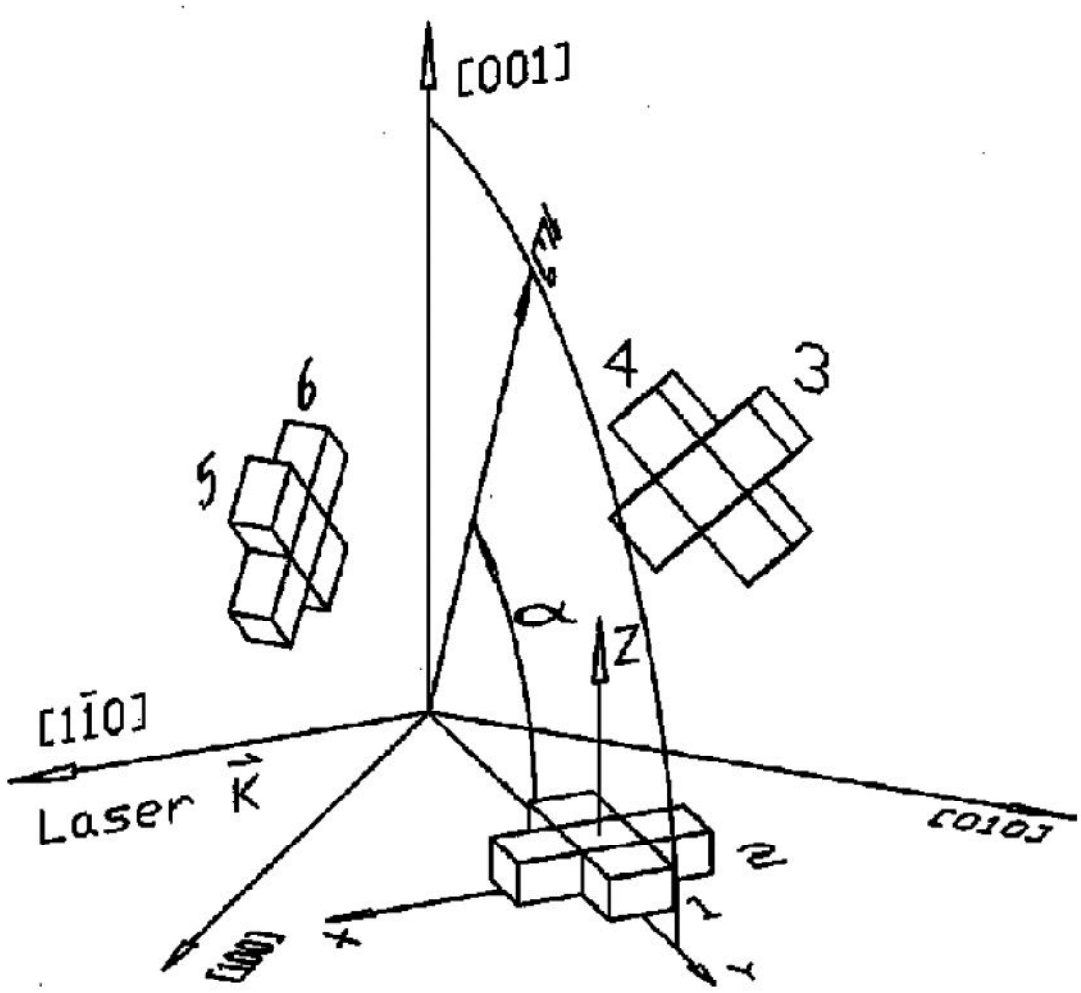

Figure 18: Trivalent thulium ions at different sites in YAG crystal. Each site is assigned a unique local axis which is related to the crystal axis. The axes are identified using Miller indices, where square brackets refer to directions and angular brackets to axes, as is defined on page 132 of Ref. [(66)]. Picture is reproduced from Sun, et. al.[(67)].

For this case, Gruber, et. al. [(62)] noted that the magnetic transition dipole between electronic levels is much weaker than the electric transition dipole. Note that no two types of the sites have the same local axis. Thus, the ions at each site will have a unique transition dipole orientation. In the case of Tm^{3+}:YAG, the directions of electric transition dipoles are studied, but there is still ambiguity about the exact direction of the electric transition dipoles [(67)]. The results in reference (67) show that the transition dipoles lie along the local x or y-axes for these sites.

Interaction of Thulium Ions with the Optical Field

For the current analysis the electric dipole is considered to lie along the y-axis in the local frame, which is a reasonable choice as both (x or y) directions are equivalent. We follow the approach given in reference [(67)]. If the electric field lies in the (1-10) plane and makes an angle θ_E with the <001>, then ions at each site in the crystal will interact with the electric field and contribute to the Rabi frequency as $\Omega_i = \vec{\mu}_i \cdot \vec{E} \big/ \hbar$, where $\vec{\mu}_i$ is the transition dipole moment for ions at a particular site and $i = 1,2,3,4,5,6$. In this case, the Rabi frequency for ions at each site will be different as given below

$$\left.\begin{aligned} \Omega_1(\theta_E) &= 0 \\ \Omega_2(\theta_E) &= \Omega_0 \left|\sin(\theta_E)\right| \\ \Omega_{4,6}(\theta_E) &= \frac{\Omega_0}{\sqrt{2}}\left|\left(\frac{\sin(\theta_E)}{\sqrt{2}} + \cos(\theta_E)\right)\right| \\ \Omega_{3,5}(\theta_E) &= \frac{\Omega_0}{\sqrt{2}}\left|\left(\frac{\sin(\theta_E)}{\sqrt{2}} - \cos(\theta_E)\right)\right| \end{aligned}\right\} \qquad (4.1),$$

where each index corresponds to the ions at a particular site in the crystal, as shown in Figure 18, $\Omega_0 = \frac{\mu E_0}{\hbar}$, μ is the magnitude of the electric transition dipole moment, and E_0 is the magnitude of the electric field.

It can be seen from equation (4.1) that the interaction of ions with the electric field can be switched on or off by the choice of the direction of the applied optical field. For example, $\Omega_2(\theta_E)$ is zero when $\theta_E = 0^o$, $\Omega_{4,6}(\theta_E)$ is zero, when $\theta_E = -54.7356^o$, or $\Omega_{3,5}(\theta_E)$ is zero when $\theta_E = 54.7356^o$. This is an important property and will be used to identify ions at each site in the crystal.

Now we will modify the results in the equation (4.1) and consider a few degrees tilt in the crystal axis. This is important to consider, as in our analysis, a few degrees tilt in the crystal axes will have a significant effect on the interpretation of the spectral hole burning data. Thus, we assume that the electric field is not in the (1-10) plane and, instead, is tilted such that it makes a tilt angle θ_{tE} with the (1-10) plane. In this case, the electrical field interacting with the medium will be

$$\vec{E}(\theta_E, \theta_{tE}) = E_0\left(\frac{1}{\sqrt{2}}(\cos(\theta_{tE})\sin(\theta_E) + \sin(\theta_{tE}))\hat{X} + \frac{1}{\sqrt{2}}(\cos(\theta_{tE})\sin(\theta_E) - \sin(\theta_{tE}))\hat{Y} + \cos(\theta_E)\cos(\theta_{tE})\hat{Z}\right) \quad (4.1a),$$

where $(\hat{X}, \hat{Y}, \hat{Z})$ are crystal axes as defined in Figure 18.

The interaction with the electric field given in equation (4.1) will be modified, and the resultant expression will involve a tilt angle, θ_{tE}. This will cause a non-zero interaction of the optical field with ions at site 1. The modified expressions for the interaction of thulium ions at each site with the optical field will be

$$\left.\begin{aligned}
\Omega_1(\theta_E,\theta_{tE}) &= \Omega_0\left|\sin(\theta_{tE})\right| \\
\Omega_2(\theta_E,\theta_{tE}) &= \Omega_0\left|\sin(\theta_E)\cos(\theta_{tE})\right| \\
\Omega_3(\theta_E,\theta_{tE}) &= \frac{\Omega_0}{\sqrt{2}}\left|\left(\frac{(\sin(\theta_E)\cos(\theta_{tE})-\sin(\theta_{tE}))}{\sqrt{2}}-\cos(\theta_E)\cos(\theta_{tE})\right)\right| \\
\Omega_4(\theta_E,\theta_{tE}) &= \frac{\Omega_0}{\sqrt{2}}\left|\left(\frac{(\sin(\theta_E)\cos(\theta_{tE})-\sin(\theta_{tE}))}{\sqrt{2}}+\cos(\theta_E)\cos(\theta_{tE})\right)\right| \\
\Omega_5(\theta_E,\theta_{tE}) &= \frac{\Omega_0}{\sqrt{2}}\left|\left(\frac{(\sin(\theta_E)\cos(\theta_{tE})+\sin(\theta_{tE}))}{\sqrt{2}}-\cos(\theta_E)\cos(\theta_{tE})\right)\right| \\
\Omega_6(\theta_E,\theta_{tE}) &= \frac{\Omega_0}{\sqrt{2}}\left|\left(\frac{(\sin(\theta_E)\cos(\theta_{tE})+\sin(\theta_{tE}))}{\sqrt{2}}+\cos(\theta_E)\cos(\theta_{tE})\right)\right|
\end{aligned}\right\} \qquad (4.1b).$$

Now we will consider the interaction of the magnetic field with the thulium ions at these sites in the crystal.

Interaction of Thulium Ions with the Magnetic Field

Recall that in a qubit the information is stored in the hyperfine levels. Thus, in order to use the hyperfine structure for ions at certain sites in Tm^{3+}:YAG, we need to characterize the hyperfine structure of ions at these sites in Tm^{3+}:YAG. For characterization of hyperfine splittings, recall the general form of the Hamiltonian given in equation (3.3). It was mentioned in Chapter 3, that, due to the external magnetic field, the degeneracy in the energy levels is lifted, and the resultant level structure is shown in Figure 10 (Chapter 3). Thus each electronic level of each thulium ion in the crystal will split into two sublevels. The hyperfine splitting will be the same for magnetically equivalent ions and will be different for magnetically inequivalent ions for a general orientation of the magnetic field. Taking into account the cut of the sample used and the

mounting scheme for the sample, we restrict our analysis to the situation where the magnetic field is in the (1 -1 0) plane or the magnetic field is tilted from the (1-10) plane.

First, consider an external magnetic field in the (1 -1 0) plane making an angle θ_B with the <0 0 1> axis. The ions at each site in the crystal will experience a magnetic field in their local coordinates as

$$\vec{B}_1(\theta_B) = B_0(\sin(\theta_B), 0, \cos(\theta_B)) \tag{4.2},$$

$$\vec{B}_2(\theta_B) = B_0(0, \sin(\theta_B), \cos(\theta_B)) \tag{4.3},$$

$$\vec{B}_{3,5}(\theta_B) = \frac{B_0}{\sqrt{2}}\left(\frac{\sin(\theta_B)}{\sqrt{2}} + \cos(\theta_B), -\frac{\sin(\theta_B)}{\sqrt{2}} + \cos(\theta_B), \sin(\theta_B)\right) \tag{4.4},$$

$$\vec{B}_{4,6}(\theta_B) = \frac{B_0}{\sqrt{2}}\left(-\frac{\sin(\theta_B)}{\sqrt{2}} + \cos(\theta_B), -\frac{\sin(\theta_B)}{\sqrt{2}} - \cos(\theta_B), \sin(\theta_B)\right) \tag{4.5}.$$

This magnetic field will interact with ions at all six sites and induce hyperfine splitting in each electronic level of these ions. The hyperfine splittings for ions at each site are obtained using equations (3.7, 3.8) and equations (4.2-4.5) as

$$\delta_1^{e,g}(\theta_B, \gamma_x^{e,g}, \gamma_y^{e,g}, \gamma_z^{e,g}) = B_0\sqrt{(\gamma_x^{e,g}\sin(\theta_B))^2 + (\gamma_z^{e,g}\cos(\theta_B))^2} \tag{4.6},$$

$$\delta_2^{e,g}(\theta_B, \gamma_x^{e,g}, \gamma_y^{e,g}, \gamma_z^{e,g}) = B_0\sqrt{(\gamma_y^{e,g}\sin(\theta_B))^2 + (\gamma_z^{e,g}\cos(\theta_B))^2} \tag{4.7},$$

$$\delta_{3,5}^{e,g}(\theta_B, \gamma_x^{e,g}, \gamma_y^{e,g}, \gamma_z^{e,g}) = B_0\sqrt{0.5\left(\left(\gamma_x^{e,g}\left(\frac{\sin(\theta_B)}{\sqrt{2}} + \cos(\theta_B)\right)\right)^2 + \left(\gamma_y^{e,g}\left(\frac{\sin(\theta_B)}{\sqrt{2}} - \cos(\theta_B)\right)\right)^2 + (\gamma_z^{e,g}\sin(\theta_B))^2\right)} \tag{4.8},$$

$$\delta_{4,6}^{e,g}(\theta_B, \gamma_x^{e,g}, \gamma_y^{e,g}, \gamma_z^{e,g}) = B_0\sqrt{0.5\left(\left(\gamma_x^{e,g}\left(\frac{\sin(\theta_B)}{\sqrt{2}} - \cos(\theta_B)\right)\right)^2 + \left(\gamma_y^{e,g}\left(\frac{\sin(\theta_B)}{\sqrt{2}} + \cos(\theta_B)\right)\right)^2 + (\gamma_z^{e,g}\sin(\theta_B))^2\right)} \tag{4.9}.$$

where numeric indices correspond to the ions in crystallographically equivalent and rotationally/magnetically inequivalent sites, while indices e and g correspond to the excited and the ground states, respectively.

For this particular orientation of the magnetic field, ions at sites 3 and 5 are magnetically equivalent, with the same hyperfine splitting (cf. equation (4.8)). Similarly, ions at sites 4 and 6 are magnetically equivalent (cf. equation (4.9)) and, thus, have the same hyperfine splitting. The ions at other two sites, sites 1 and 2, are not magnetically equivalent, and their hyperfine splittings are not the same.

Therefore, for this particular magnetic field orientation, there are four magnetically inequivalent groups of ions. However, this statement is not true if the magnetic field is not in the (1-10) plane. If the magnetic field is not in (1-10) plane but instead is in a plane that is tilted from the (1-10) plane with a tilt angle θ_{tB} with respect to the plane (1-10), then the expressions in equations (4.2-4.5) for the magnetic field experienced by ions at different sites of the crystal will be modified as

$$\vec{B}_l\left(\theta_B,\theta_{tB}\right)=\left(\vec{B}\left(\theta_B,\theta_{tB}\right)\cdot\hat{x}_l\right)\hat{x}_l+\left(\vec{B}\left(\theta_B,\theta_{tB}\right)\cdot\hat{y}_l\right)\hat{y}_l+\left(\vec{B}\left(\theta_B,\theta_{tB}\right)\cdot\hat{z}_l\right)\hat{z}_l \qquad (4.10),$$

where $\left(\hat{x}_l,\hat{y}_l,\hat{z}_l\right)$ represents the orientation of the local axis for each site in the crystal, as defined in Figure 18, with $l=1,2,3,4,5$ and the external applied magnetic field is

$$\vec{B}(\theta_B,\theta_{tB})=B_0\left(\frac{1}{\sqrt{2}}(\cos(\theta_{tB})\sin(\theta_B)+\sin(\theta_{tB}))\hat{X}+\frac{1}{\sqrt{2}}(\cos(\theta_{tB})\sin(\theta_B)-\sin(\theta_{tB}))\hat{Y}+\cos(\theta_B)\cos(\theta_{tB})\hat{Z}\right),$$

where $\left(\hat{X},\hat{Y},\hat{Z}\right)$ represents the crystal axis as defined in Figure 18.

The hyperfine splittings for ions at all six sites can be obtained using equations (3.7, 3.8) with the magnetic field given above. In this case, the hyperfine splittings will be

$$\delta_l^e\left(\gamma_x^e,\gamma_y^e,\gamma_z^e,\theta_B,\theta_{tB}\right)=\sqrt{\left(\gamma_x^e B_{lx}\right)^2+\left(\gamma_y^e B_{ly}\right)^2+\left(\gamma_z^e B_{lz}\right)^2} \quad (4.11),$$

$$\delta_l^g\left(\gamma_x^g,\gamma_y^g,\gamma_z^g,\theta_B,\theta_{tB}\right)=\sqrt{\left(\gamma_x^g B_{lx}\right)^2+\left(\gamma_y^g B_{ly}\right)^2+\left(\gamma_z^g B_{lz}\right)^2} \quad (4.12),$$

where B_{lm} with $l=1,2,3,4,5$ and $m=x,y,z$ are components of the applied magnetic field in the local frame of each site in the crystal.

Measurement of the Magnetic Anisotropy in the Medium

Introduction

Now we have basic expressions for the interaction of thulium ions at different sites in the crystal with the optical and magnetic fields. The next step will be to map the hyperfine splittings for thulium ions at each site in the crystal. Note that the hyperfine splittings (4.11-4.12) depend on the strength and the orientation of the magnetic field. These hyperfine splittings also depend on the components of the gyromagnetic tensors. Therefore, in order to measure the magnetic anisotropy in the medium, we need to map the hyperfine splitting for different orientations of the magnetic field. Before we proceed to the experiment, we will first review the recent theoretical results [(55)]. The relevant definitions of the terms used later in the dissertation are also given.

Theory

Following the analysis in [(55)] we define the cross-transition probabilities for ions at each site. Now we use the equations (3.9, 3.10) and write the expressions of the cross-transitions for thulium ions at each site in the crystal as

$$R_l^{+-}\left(\gamma_x^{e,g},\gamma_y^{e,g},\gamma_z^{e,g},\theta_B,\theta_{tB}\right)=R_l^{-+}\propto\left|\left(a_l^g\right)^* c_l^e+\left(b_l^g\right)^* d_l^e\right|^2=\left|\left(c_l^g\right)^* a_l^e+\left(d_l^g\right)^* b_l^e\right|^2$$

(4.13),

and the probability for direct transition for ions at each site will be

$$R_l^{--}\left(\gamma_x^{e,g},\gamma_y^{e,g},\gamma_z^{e,g},\theta_B,\theta_{tB}\right)=R_l^{++}\propto\left|\left(a_l^g\right)^* a_l^e+\left(b_l^g\right)^* b_l^e\right|^2=\left|\left(c_l^g\right)^* d_l^e+\left(c_l^g\right)^* d_l^e\right|^2$$

(4.14),

where

$$a_l^{g,e}=\left(-\gamma_x^{g,e}B_{lx}+i\gamma_y^{g,e}B_{ly}\right)\Big/\sqrt{\left(2\delta_l^{g,e}\left(\delta_l^{g,e}+\gamma_z^{g,e}B_{lz}\right)\right)},\qquad b_l^{g,e}=\sqrt{\left(\delta_l^{g,e}+\gamma_z^{g,e}B_{lz}\right)/\left(2\delta_l^{g,e}\right)},$$

$$c_l^{g,e}=\left(\gamma_x^{g,e}B_{lx}-i\gamma_y^{g,e}B_{ly}\right)\Big/\sqrt{\left(2\delta_l^{g,e}\left(\delta_l^{g,e}-\gamma_z^{g,e}B_{lz}\right)\right)},\ d_l^{g,e}=\sqrt{\left(\delta_l^{g,e}-\gamma_z^{g,e}B_{lz}\right)/\left(2\delta_l^{g,e}\right)},$$

and $l=1,2,3,4,5,6$.

Now following the earlier analysis [(55)], we define the cross-transition ratio with respect to the direct transition as

$$R_l\left(\gamma_x^{e,g},\gamma_y^{e,g},\gamma_z^{e,g},\theta_B,\theta_{tB}\right)=\frac{R_l^{-+}\left(\gamma_x^{e,g},\gamma_y^{e,g},\gamma_z^{e,g},\theta_B,\theta_{tB}\right)}{R_l^{++}\left(\gamma_x^{e,g},\gamma_y^{e,g},\gamma_z^{e,g},\theta_B,\theta_{tB}\right)}\qquad(4.15),$$

where $l=1,2,3,4,5,6$.

Now we analyze the results for the cross-transition ratio in equation (4.15) for ions at each site in the crystal. First, we plot the cross-transition ratio as a function of the orientation of the magnetic field for thulium ions at each site in the crystal. In this plot, theoretical estimates for the components of the gyromagnetic tensor in the reference (55) are used. The approach adopted here (equation (4.15)) to compare the cross-transition probability, $R_l^{-+,+-}\left(\gamma_x^{e,g},\gamma_y^{e,g},\gamma_z^{e,g},\theta_B,\theta_{tB}\right)$, with the direct transition probability,

$R_l^{++,--}\left(\gamma_x^{e,g},\gamma_y^{e,g},\gamma_z^{e,g},\theta_B,\theta_{tB}\right)$, only makes sense if the direct transition probability is non-zero for all the orientations of the magnetic field.

In order to investigate the direct transition probability dependence on the orientation of the applied magnetic field, we first plot the normalized direct probability as a function of the orientation of the magnetic field in Figure 19. Results in Figure 19 show that the direct transition probability changes with the orientation of the magnetic field with the maximum decrease being less than 20%. Note that the direct transition probability is non-zero for all the orientations of the magnetic field.

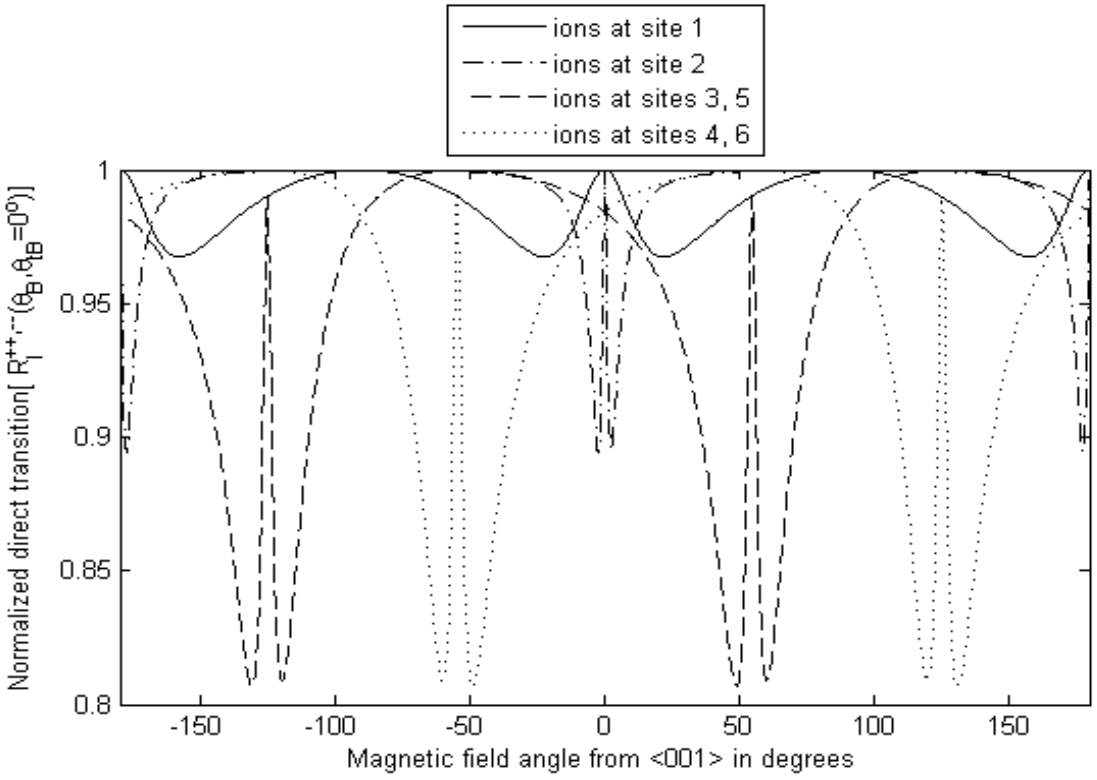

Figure 19: Theoretical plot for direct transition probability for ions in the Tm^{3+}:YAG at different sites in the crystal. In this plot the theoretical values, [(55)], of the components of the gyromagnetic tensor for the ground state, $\vec{\gamma}^{\,g}=(18.9,559.6,11.2)^{MHz}/_{Tesla}$, and the excited state, $\vec{\gamma}^{\,e}=(22.3,75.2,6.3)^{MHz}/_{Tesla}$, manifolds are used in equation (4.13).

As the direct transition probability is non-zero for all the orientations of the magnetic field, we are justified in analyzing the cross-transition ratios as defined in the equation (4.15). The theoretical results in Figure 20 for cross-transition ratios as a function of the magnetic field orientation show that even though ions at sites 2, 4, and 6 have equal interaction with the electric field, their cross-transition ratios are not the same. This plot also shows that the magnetically equivalent sites, e.g., ions at sites 4 and 6, have similar cross-transition ratios, and the magnetically inequivalent sites, e.g., ions at sites 2 and 4, have quite different cross-transition ratios.

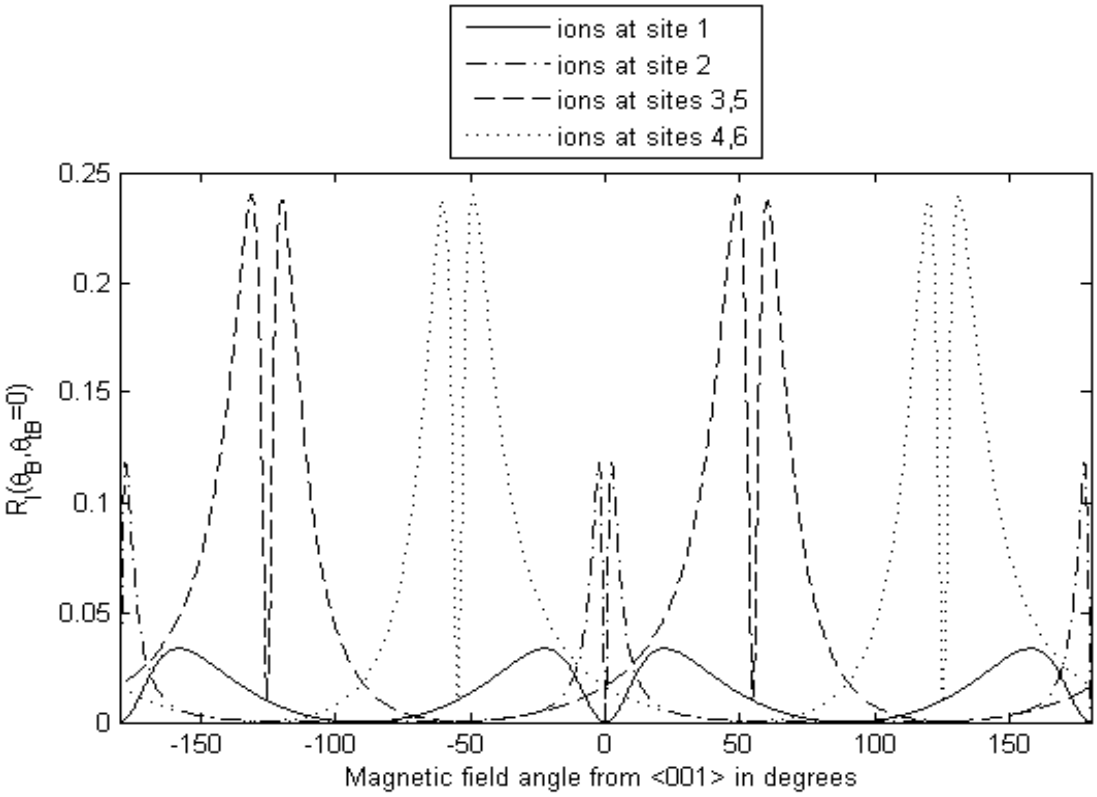

Figure 20: Theoretical results for cross-transition ratios for ions at various sites in Tm^{3+}:YAG and their dependence on magnetic field orientation. The values chosen for $\vec{\gamma}^{\,e,g}$ are the same as in Figure 19.

If the magnetic field is not confined in the (1-10) plane, and is instead tilted, then the cross-transition ratio $R_l\left(\gamma_x^{e,g},\gamma_y^{e,g},\gamma_z^{e,g},\theta_B,\theta_{tB}\right)$ will be modified, as ions at sites 3 and 5 (ions at sites 4 and 6) will not be magnetically equivalent.

In our experiment, it is quite possible to have $\pm 3^o$ misalignment of the plane, as this is the accuracy quoted by the manufacturer of the crystal (Scientific Materials, Bozeman, MT). Now, if we assume an approximately 3^o misalignment of (1-10) plane, then the cross-transition ratios will be modified as shown in Figure 21. The results in Figure 21 show that the orientations for maximum cross-transition ratios will be shifted, and ions at all the six sites in the crystal will be magnetically inequivalent.

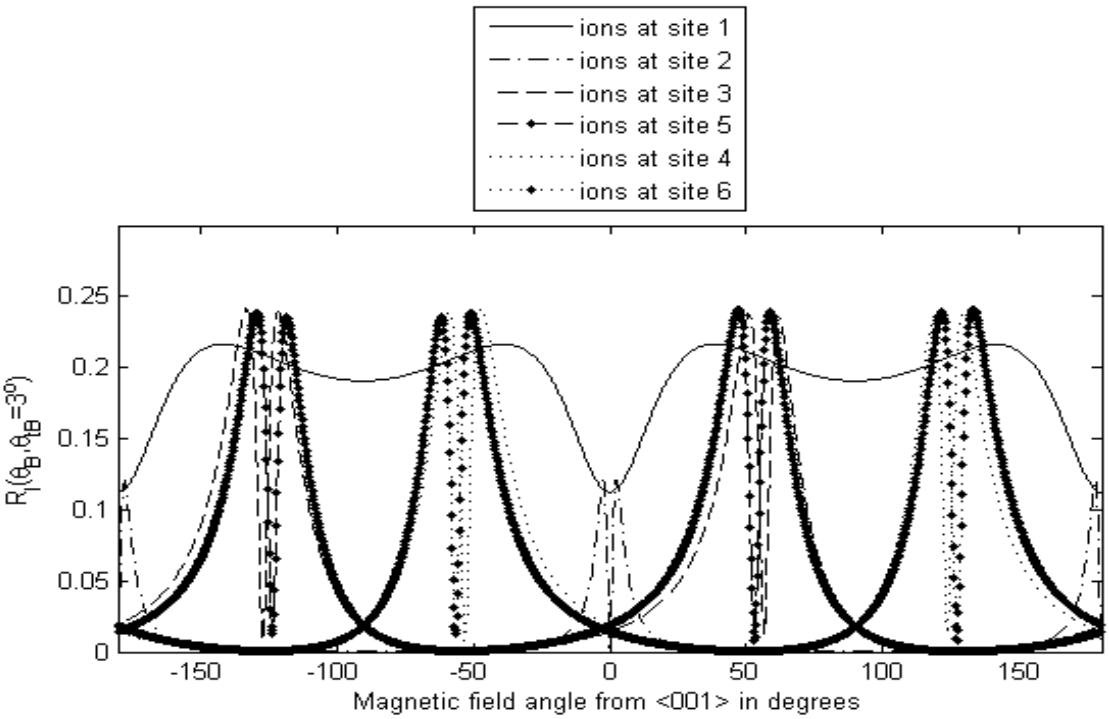

Figure 21: Theoretical results for cross-transition ratios for ions at various sites in Tm^{3+}:YAG and their dependence on magnetic field orientation. The components of gyromagnetic tensors are the same as in Figure 19. The magnetic field is tilted from (1-10) plane, with the tilt angle as $\theta_{tB} = 3^o$.

These theoretical results in Figure 21 also show that the ions at site 1 will have a non-zero cross-transition ratio instead of a zero cross-transition ratio as was the case for a zero tilt with the magnetic field in the (1-10) plane. Another interesting feature is the maximum value of the cross-transition ratio for ions at site 1. The results in Figure 21 show that ions at site 1 will have the highest cross-transition ratio for quite a wide range of the magnetic field orientations. A question one might ask is, why not select the ions at site 1? The answer lies in the fact that ions at site 1 have almost zero hyperfine splittings for these particular orientations (Figure 22), thus making this choice not suitable for quantum computing applications.

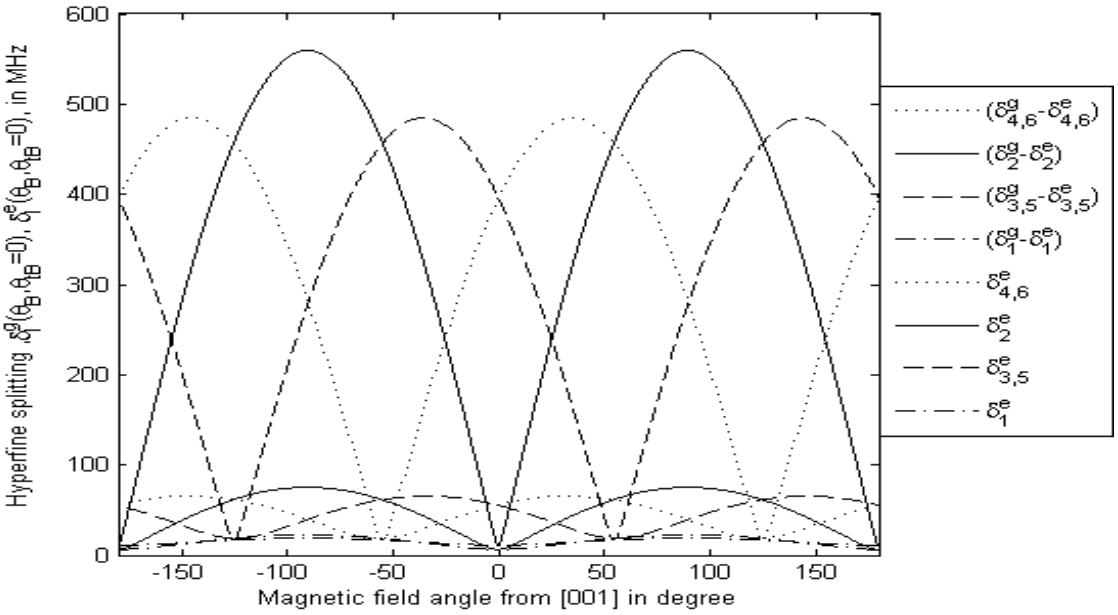

Figure 22: Theoretical results for the hyperfine splittings for ions at all six sites in the crystal when an external magnetic field of hypothetical 1 Tesla is applied to the sample. The plot uses the theoretical values (55) of the components of the gyromagnetic tensor for the ground state, $\vec{\gamma}^{\,g} = (18.9,559.6,11.2)^{MHz}/_{Tesla}$, and the excited state, $\vec{\gamma}^{\,e} = (22.3,75.2,6.3)^{MHz}/_{Tesla}$, manifolds in equation (4.13).

Before we proceed to the experiment, consider the hyperfine splittings for these two cases, the one involving a zero tilt and the other involving a 5^{o} tilt in the orientation of the magnetic field from the (1-10) plane. One can use equations (4.11-4.12) and plot the hyperfine splittings for thulium ions at all these six sites in the crystal. First, assume that the magnetic field is restricted in the (1-10) plane. For this case, results in Figure 22 show that the ions at sites 2, 3, 4, 5, and 6 have higher hyperfine splittings in the ground state manifold and smaller splittings in the excited state manifold. The hyperfine splittings for ions at site 1 is the smallest (22MHz/Tesla (maximum value of the hyperfine splittings)) for both of the manifolds and ions at site 2 have the largest splittings among all the ions (550 MHz/Tesla (maximum value of the hyperfine splittings)). Now if the magnetic field is not restricted to the (1-10) plane, but is tilted a few degrees from the plane, then the results plotted in Figure 23 show that the ions at site 2 still have the largest hyperfine splitting, and the ions at site 1 have the smallest hyperfine splitting among all the thulium ions at different sites in the crystal. Also note that ions at all the six sites have different hyperfine splittings, and the ions at sites 4 and 6 (ions at sites 3 and 5) are no longer magnetically equivalent.

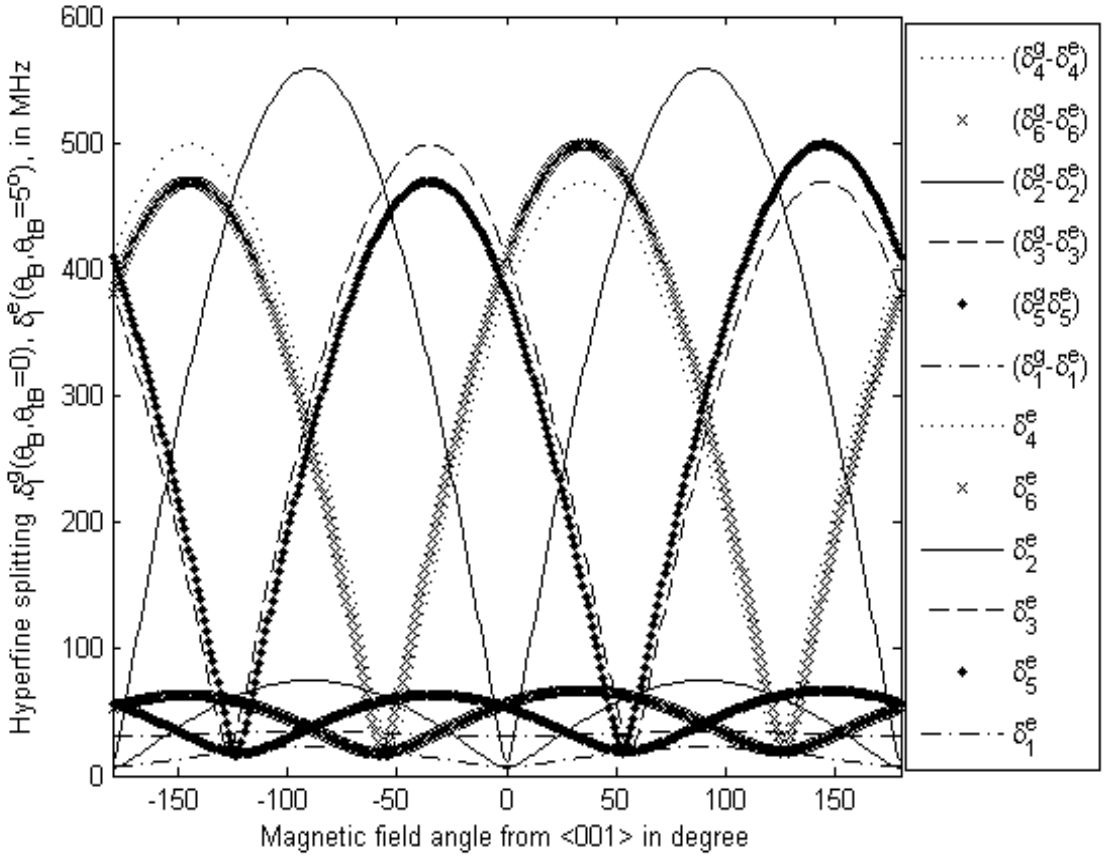

Figure 23: Theoretical results for hyperfine splittings for ions at all six sites in the crystal when an external magnetic field of 1 Tesla is applied to the sample. Here, the magnetic field is not restricted to (1-10) plane and is tilted from the plane by tilt angle, θ_{tB}, fixed at 3^o. The values of the components of the gyromagnetic tensor are the same as in Figure 22.

Thus, the hole burning spectrum for the case when the magnetic field is restricted in the (1-10) plane and for the case when the magnetic field is tilted will be quite different. In general, the hole burning spectrum will depend on the tilt angle (orientation of the magnetic field) and the strength of the magnetic field. To analyze the effect of the tilt angle on the hole burning spectrum, consider the excitation of the medium with an optical pulse of bandwidth 500kHz that is interacting with the ions at sites 4 and 6. The

simulation results of the spectra for the cases of zero tilt and 3^o tilt are given in Figure 24. The analysis of these particular spectra shows that the shift in the excited state splittings is not large enough to see another peak. On the other hand, the difference in the hyperfine splittings in the ground state for ions at each site is twice as large as compared to the bandwidth of the excited ions. Thus, the double hump appears in the absorption features for the ground state hyperfine splittings in the spectrum in Figure 24 for 3^o tilt.

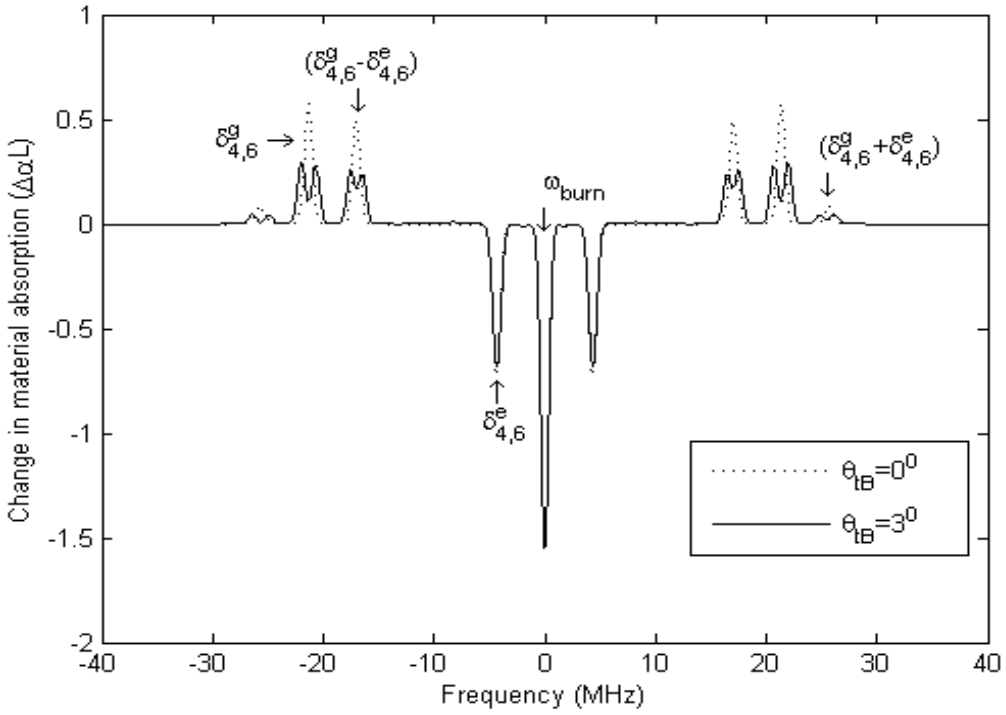

Figure 24: Simulation of the hole burning spectrum of the ions at sites 4 and 6 for the orientation, $\theta_B = 34^o$, of magnetic field giving maximum hyperfine splittings with an applied magnetic field fixed at 567 Gauss. The spectrum shows that the widths of absorption features other than at $0, \pm\delta_e$ are increased, as double humps appear for these absorption features which signify contributions from ions at two different sites in the crystal.

The important insight gained in this analysis will be used to study and interpret the hole burning spectra obtained experimentally. The analysis in this section will be extensively used to identify the ions at different sites in the crystal, to identify the orientation of the crystal, and to approximate the orientations for optimal cross-transition ratios.

Experiment

The experimental set-up for the anisotropy measurement was the same as given in Figure 15. The sample, 0.1% atm. Tm^{3+}:YAG crystal, was mounted on a rotating mount (the sample rotating mount, the Helmholtz coil, and the cryostat were provided by the Prof. Cone's Lab) in the cryostat, and it was vapor-cooled to $4 \pm 0.5K$ with liquid helium. The external magnetic field was kept fixed at 175 Gauss during the experiment. The crystal was rotated along the [-1 1 0] axis of the crystal, and the propagation direction of the laser beam was kept aligned along the [-1 1 0] axis of the crystal. The polarization of the electric field was oriented such that the optical field addresses ions at sites 2, 4, and 6 equally and does not interact with the ions at sites 1, 3, and 5 in the crystal, as noted in equation (4.1).

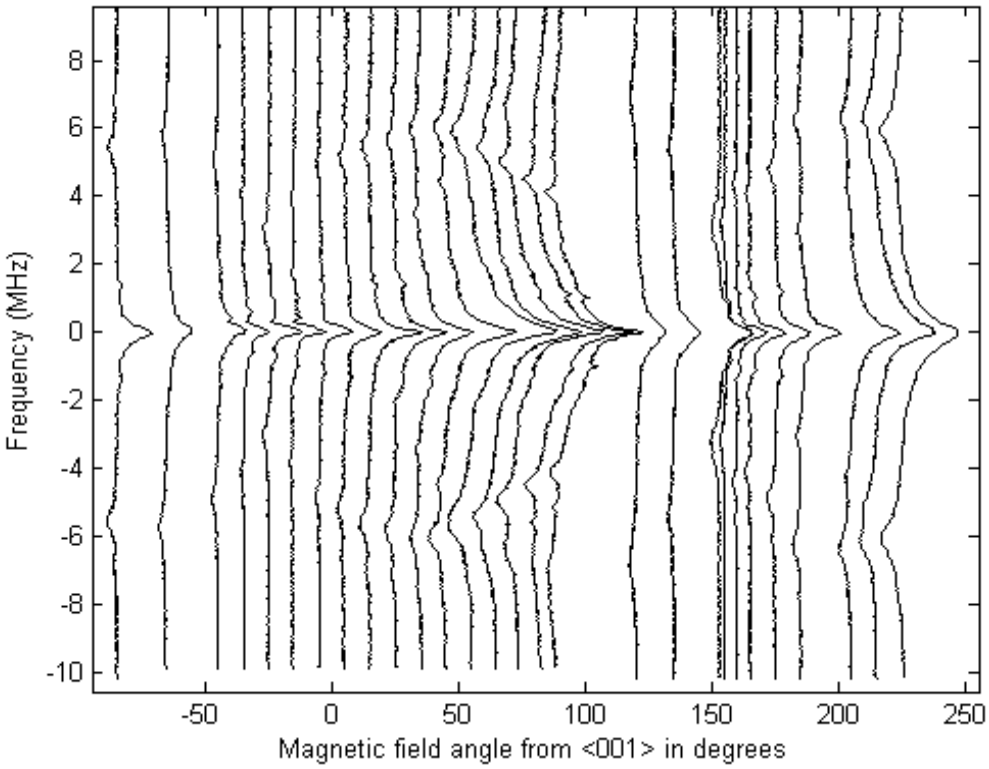

Figure 25: Experimental results for the hole burning spectrum obtained for the Tm^{3+}:YAG sample at $4 \pm 0.5K$. A fixed magnetic field of 175 Gauss applied to the sample. The orientation of the sample with respect to the magnetic field was varied in (1 -1 0) plane by rotating the sample in that plane. The optical field orientation was fixed along the [111] direction.

The hyperfine splittings in the ground and the excited states as a function of the magnetic field orientation are mapped using the experimental hole burning data. In this experiment, five repetitions of a narrowband pulse of $100\,\mu s$ duration and 1ms repetition time were applied to the medium. The medium was 0.1% atm. Tm^{3+}:YAG sample and was vapor-cooled to $4 \pm 0.5K$ with the liquid helium. The sample, after the excitation with the pulse, was scanned with a weak broadband chirp having 20MHz bandwidth and $500\,\mu s$ duration. This slow and weak chirp allowed us to map out the spectrum of the

medium without changing the absorption profile of the medium as was mentioned in the hole burning technique (Chapter 3). The optical beam, in this experiment, was not focused in the medium, which allowed us to obtain a better signal-to-noise ratio for the output signal from the medium. The spectrum for each magnetic field orientation was collected as shown in Figure 25. In this experiment, the strength of the magnetic field was fixed at 175 Gauss. Thus, for 3^{o} misalignment of the magnetic field, the maximum difference for hyperfine splittings for ions at sites 4 and 6 (ions at sites 3 and 5) will be 500kHz. In the current spectral hole burning data, we were unable to resolve the peaks with this frequency separation. The positions of the absorption features, other than at the burning frequency, 0 MHz, were measured using data in Figure 25. The resultant experimental data (circles) are shown in Figure 26.

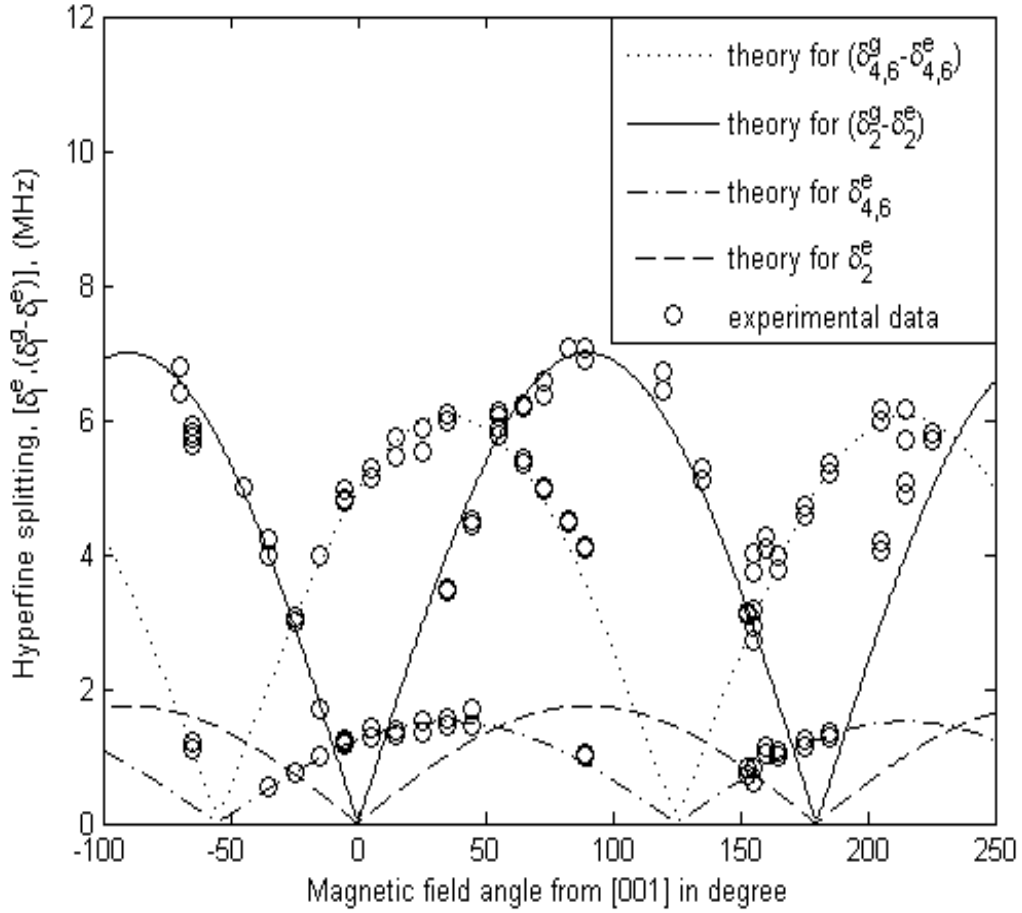

Figure 26: Experimental data (circles) and theoretical results (lines). The components of the gyromagnetic tensor for the ground and the excited state manifolds are obtained by fitting experimental data using equations (4.11-4.12) for different values of the components of the gyromagnetic tensor.

We used the data in Figure 26 to find the experimental values for the components of the gyromagnetic tensors. The process of finding the components of the gyromagnetic tensors is as follows. The theoretical (equations (4.11-4.12)) results for the hyperfine splittings for ions at each site are fitted to the experimental data. The values for the components of the gyromagnetic tensors for the ground and the excited states, giving us the best fit with trial and error to the experimental data, are plotted (lines). During the

fitting process, it is anticipated, based on the theoretical results, that y-components of the gyromagnetic tensors will be dominant. Thus, for the initial fit, $\gamma_x^{e,g}, \gamma_z^{e,g}$ are set to zero and $\gamma_y^{e,g}$ is varied in equations (4.11-4.12). This provides us with an initial estimate for the components of the gyromagnetic tensors. Later, $\gamma_y^{e,g}$ is kept fixed, and other components, $\gamma_x^{e,g}, \gamma_z^{e,g}$, are varied in equations (4.11-4.12), and the best fit to the experimental data with the trial and error is obtained.

The major error in this experiment is due to the misalignment in the orientation of the magnetic field. We estimated the angular error due to the misalignment in the magnetic field orientation to be about $\pm 5^o$. The value of this error was based on the combination of the data provided by the manufacturer of the crystal and the limit in the resolution of the experimental data. Thus, fit by trial and error (solid lines) to the experimental data gives us the values for the components of the gyromagnetic tensor for the ground state ($\gamma_y^g = 480 \pm 4\, {}^{MHz}\!/_{Tesla}$, $\gamma_x^g = 13 \pm 6\, {}^{MHz}\!/_{Tesla}$, $\gamma_z^g = 4 \pm 2\, {}^{MHz}\!/_{Tesla}$) and the excited state ($\gamma_y^e = 95 \pm 1\, {}^{MHz}\!/_{Tesla}$, $\gamma_x^e = 25 \pm 6\, {}^{MHz}\!/_{Tesla}$, $\gamma_z^e = 5 \pm 3\, \frac{MHz}{Tesla}$). Note that, there is a large uncertainty in the x and the z components of the gyromagnetic tensors. The uncertainty is particularly large in the z components of the gyromagnetic tensors. The uncertainty arises from the relative size of the components of the gyromagnetic tensors and the difficulty in obtaining the data for very small cross-transition ratio and for small splittings with the hole burning experiment.

Components of g-tensors	$\gamma_y^g\left(MHz/Tesla\right)$	$\gamma_x^g\left(MHz/Tesla\right)$	$\gamma_z^g\left(MHz/Tesla\right)$	$\gamma_y^e\left(MHz/Tesla\right)$	$\gamma_x^e\left(MHz/Tesla\right)$	$\gamma_z^e\left(MHz/Tesla\right)$
Theory [(55)]	559.6	18.9	11.2	75.2	22.3	6.3
Experiment [(56)]	403 ± 3			82 ± 3		
Experiment	480 ± 4	13 ± 6	4 ± 2	95 ± 1	25 ± 6	5 ± 3

Table 1: The components of the gyromagnetic tensors for the excited state and for the ground state manifolds.

The value for the y-component of the gyromagnetic tensor for the ground state, 480 MHz/Tesla, obtained here is smaller than the predicted value, 559.6MHz/Tesla, while the y-component of the gyromagnetic tensor for the excited state, 95MHz/Tesla, is a bit higher than the predicted value, 75.2MHz/Tesla [(55)]. The error in these experimental data is due to the uncertainty in the orientation of the magnetic field and the calibration of the magnetic field value for the Helmholtz coil. In recent experimental measurements [(56)], the values for the y-components of both the ground state, $\gamma_y^g = 403\pm3\frac{MHz}{Tesla}$, and the excited state, $\gamma_y^e = 82\pm3\frac{MHz}{Tesla}$, were smaller than the values of these components obtained in our experiment. The difference in the y-components of the gyromagnetic tensors in the two experiments may be attributed to the difference in the calibration of the applied external magnetic fields. This can be seen from the same percentage difference, 17%, for both the ground and the excited states components of the gyromagnetic tensors in two experiments. This implies that either we are underestimating

the strength of the applied magnetic field, or earlier investigation has overestimated the strength of the applied magnetic field. In the experimental investigation in reference (56), the values for other components of the gyromagnetic tensor were not given, and only the combinations of x and z-components were obtained. In our experiment, we were able to put some constraints on the x and z-components even though error in these values is large.

Now we revisit the cross-transition ratios and study their dependence on the orientation of the applied magnetic field using the experimental values of the gyromagnetic tensors. Using equation (4.15), one can plot the cross-transition ratios for ions at each site in the crystal with the experimentally-obtained values of the components of the gyromagnetic tensors. The results of that plot are shown in Figure 27.

First, consider thulium ions at site 1 in the crystal. These ions have the maximum cross-transition ratios of 0.042 ± 0.04, which have large error bars and their lower value is well below the predicted value of 0.03 (cf. theoretical results in Figure 20). The reason for the large difference in the predicted and the experimental values for the cross-transition ratios for ions at site 1 is its strong dependence on the alignment of the magnetic field, as can be seen from the results in Figure 21. Thus, minor misalignment in the orientation of the magnetic field causes significant change in the cross-transitions for ions at site 1.

There is no significant difference in the maximum cross-transition ratios for ions at sites 3, 4, 5, and 6, with the maximum estimated to be 0.26 ± 0.06. The theoretically

predicted value of the maximum cross-transition ratios for these ions is 0.24 (cf. theoretical results in Figure 20) which is in excellent agreement.

The experimental results give the maximum cross-transition ratio for ions at site 2 as 0.15 ± 0.04. The theoretically predicted value of the cross-transition ratio for ions at site 2 is 0.12 (Figure 20). Note that for ions at site 2, the theoretically predicted result gave a value smaller than the mean value obtained from the experimental result. It is important to note that the experimental results just give the range of possible values for the cross-transition ratios, and in this case the theoretically predicted value happens to fall in the lower end of the experimental results.

The error bars in these measured values of the cross-transition ratios are due to the error in measuring the components, $\left(\gamma_x^{e,g}, \gamma_y^{e,g}, \gamma_z^{e,g}\right)$, of gyromagnetic tensors. The error bounds on components of gyromagnetic tensors give us the maximum and the minimum possible values of the cross-transition ratios. It is interpreted that the theoretical values of cross-transition ratios fall within the error bound of the experimental values of cross-transition ratios.

Now we can use these experimental results for the components of the gyromagnetic tensors and estimate the orientations of the magnetic field that can give us the optimal cross-transition ratios for thulium ions at a particular site in the crystal.

The Magnetic Field Orientations for Optimal Material Performance

The results of the cross-transition ratios in Figure 27 show that ions at sites 3, 4, 5 and 6 have the highest cross-transition ratio of 0.26 ± 0.06 for particular orientations of

the magnetic field. For example, the highest values of the cross-transition ratios for ions at sites 3 and 5 can be accessed by aligning the magnetic field along $\theta_B = 50^o$, or $\theta_B = 60^o$. While the highest cross-transition ratios for thulium ions at sites 4 and 6 can be accessed by aligning the magnetic field along $\theta_B = -50^o$, or $\theta_B = -60^o$. Similarly, the maximum cross-transition ratios for ions at sites 1 and 2 can be accessed by aligning the magnetic field along a particular direction. Also note that the ions at site 2 have the second highest and the ions at site 1 have the third highest cross-transition ratios.

Our goal here is to optimize the conditions in Tm^{3+}:YAG for quantum computing applications. One quantum computing scheme requires that the candidate material should have an efficient coupling of the two hyperfine levels to a common optical level. Thus, one needs to choose the orientation of the magnetic field and ions at the site in Tm^{3+}:YAG that give the highest cross-transition ratios. Now we use the results in Figure 27 and identify the orientations of the magnetic field and corresponding sites that fulfill above mentioned requirement that requires an efficient coupling of a single optical level to the two hyperfine levels. We can identify that ions at either sites 4 and 6 or sites 3 and 5 will be good candidates for the quantum computing applications for a particular orientation of the magnetic field. Another interesting magnetic field orientation, $\theta_B = \pm 2^o$, is the one giving the maximum cross-transition ratio, about 0.14, for ions at site 2. However, the cross-transition ratio for ions at site 1 is 0.042 ± 0.04, which is too small to be useful for quantum computing applications. The small cross-transition ratio coupled with the very small hyperfine splittings for ions at site 1 render them not useful for further exploration.

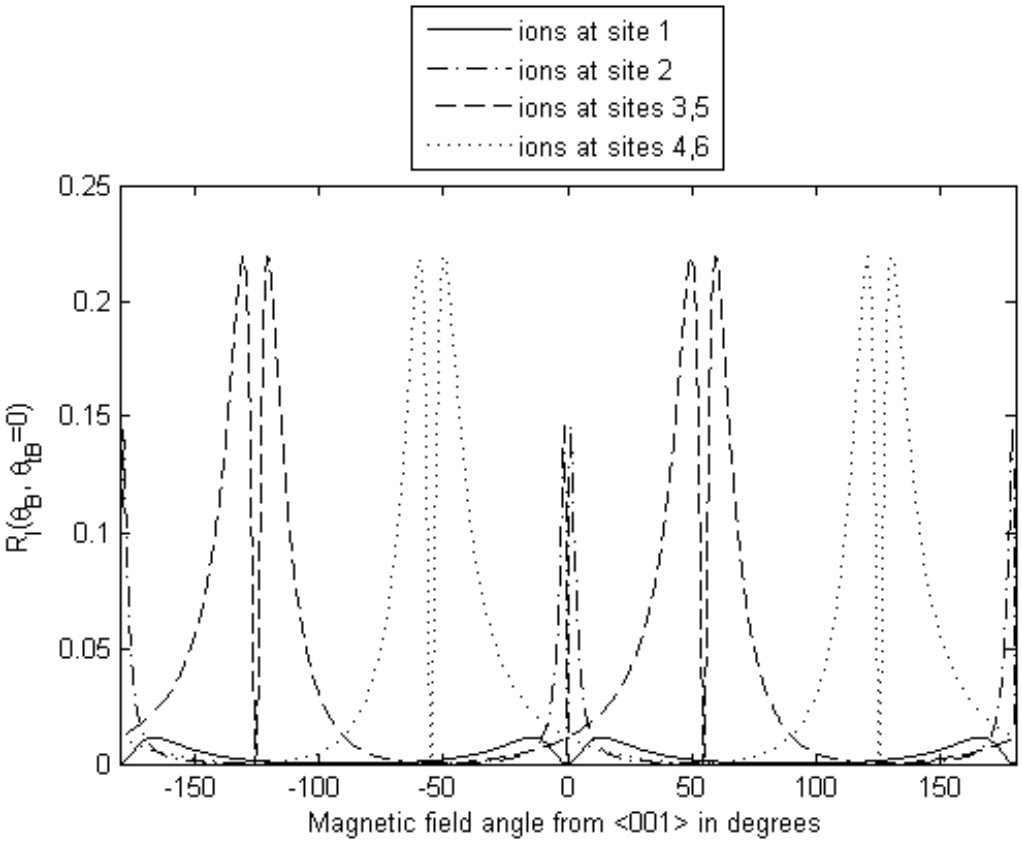

Figure 27: Theoretical cross-transition ratios for ions at various sites in Tm^{3+}:YAG and their dependence on magnetic field orientation. In this plot, our experimentally-obtained values of gyromagnetic tensors are used in equation (4.15).

In the current study it seems sufficient to focus attention on the ions at sites 3 and 5 or the ions at sites 4 and 6. The experimental results in Figure 26 and Figure 27 show that the orientations of the magnetic field that provide the highest cross-transition ratios for ions at a particular site are also the orientations for the minimal hyperfine splittings for ions at that particular site. Thus some sort of balance needs to be achieved so that there is reasonable hyperfine splitting and reasonable cross-transition ratios for ions at that particular site. The minimum hyperfine splitting, $\delta_l^{e,g}$, needs to be bigger than the

bandwidth of the pulse, τ_p^{-1}, being used to address ions in the medium, with $\tau_p < T_2$, where τ_p is the pulse duration and T_2 is the material dephasing time. If a pulse with 1.0MHz Rabi frequency and 500ns duration is used to excite the system, then the minimum splitting, $\delta_l^{e,g}$, needs to be more than 2MHz. For the current set-up in the lab, a peak magnetic field of 567 Gauss can be achieved without overheating the Helmholtz coils. Thus, the ions at site 1 and all the orientations for ions at other sites where splittings more than 2MHz cannot be achieved with a 560 Gauss magnetic field are ruled out. In the current study, we explored two different orientations of the magnetic field. In one orientation, the magnetic field was aligned along the orientation giving close to the maximum cross-transition ratio for ions at sites 4 and 6. We say "close to" because at the maximum cross-transition ratio, the hyperfine splittings are too small (less than 1MHz) for the available magnetic field in the lab. In the second orientation, the magnetic field was aligned to the direction of the near maximum cross-transition ratio for ions at site 2. Therefore, in the current study only, two orientations of the magnetic field, one giving near maximum cross-transition ratio for ions at sites 4 and 6, and other giving near maximum cross-transition ratios for ions at site 2, are explored.

The Hyperfine Splittings and the Interacting Thulium Ions

The theoretical calculations, equations (4.11-4.12), show that all the hyperfine splittings change linearly with the applied magnetic field. This section presents the experimental results for the hyperfine splittings for ions at different sites for the orientations of the magnetic field giving the maximum cross-transition ratios for ions at

these sites (Figure 18). This analysis will also help to accurately identify the orientation of the crystal.

Experiment

The experimental set-up in Figure 15 was required to measure the hyperfine splittings. In this experiment, the hole burning technique is used to map the hyperfine splittings and their dependence on the value of the magnetic field in 0.1% atm. Tm^{3+}:YAG.

The sample was vapor-cooled to $4 \pm 0.5K$ and the optical field was aligned along the particular orientation needed to address ions at that particular site. For example, the optical field was aligned along the [111] direction to address ions at sites 2, 4, and 6. Similarly, other alignments of the optical field were chosen to address ions at other sites in the crystal. There is always some error in the alignment of the optical field, and in this case, the polarizer in conjunction with the half-wave plate was used to align the optical field along the particular direction in the (1-10) plane. The accumulated error due to the polarizer and half-wave plate misalignment was about $\pm 0.7^0$, for collimated normal incident beam. This amount of the misalignment in the orientation of the optical field should not affect the experimental results presented here. The value of the hyperfine splittings should not be affected due to this misalignment. The results in equations (4.11-4.12) show that the values of the hyperfine splittings depend critically on the magnitude and the orientation of the magnetic field. The hyperfine splittings are independent of the orientation of the optical field.

The magnetic field for the sample was supplied with the Helmholtz coils. In this experiment, the magnetic field was varied from 0 Gauss to 567 Gauss. In this experiment, the medium, Tm^{3+}:YAG, was excited by repeatedly applying an optical pulse of $100\,\mu s$ duration with a repetition rate of 1kHz. The spectrum of the medium was obtained by scanning the medium after $200\,\mu s$ with broadband of 40 MHz bandwidth and $500\,\mu s$ duration chirp.

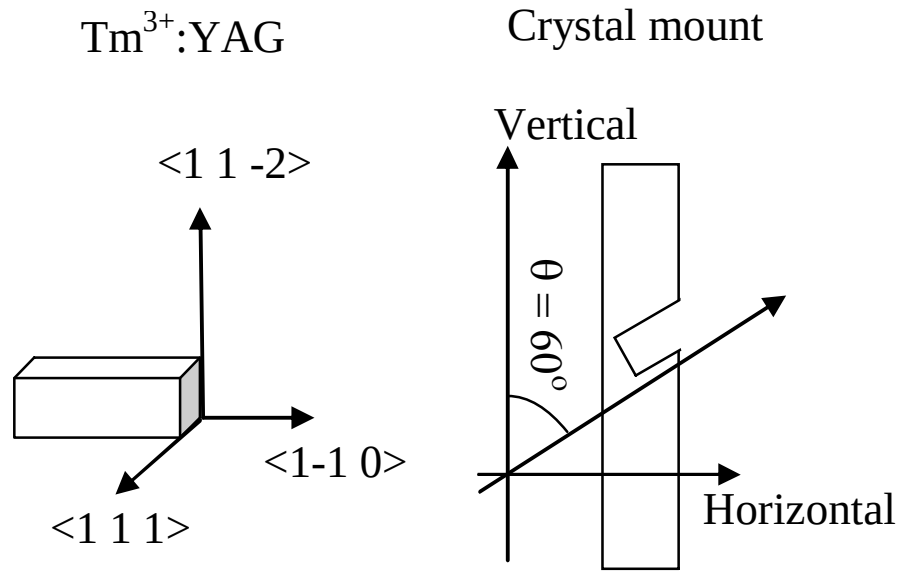

Figure 28: The geometry of the Tm^{3+}:YAG crystal and the home-made mount for the crystal.

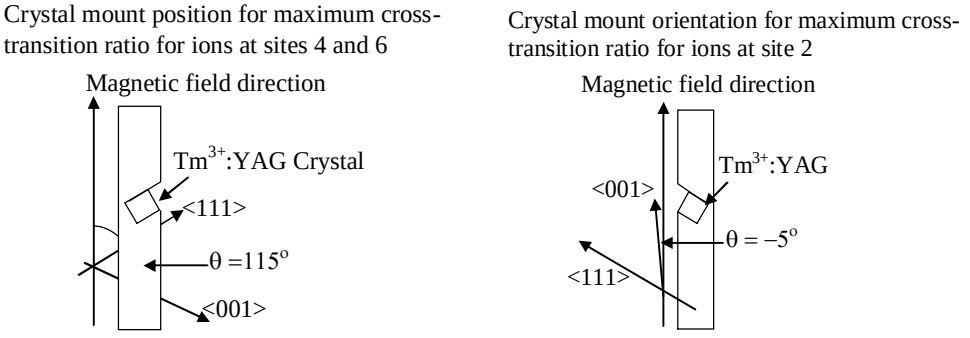

Figure 29: Positions of the crystal mount for various orientations.

The geometry of the crystal and of the home-made mount is shown in Figure 28. To study the ions at site 2 in the crystal, the magnetic field should have been oriented in the direction giving the maximum cross-transition ratio for ions at site 2, i. e., $\theta_B = -2^o$, but our home-made mount limited us to a direction of $\theta_B = -5^o \pm 1^0$ (Figure 29 (right side)) which does not give the maximum cross-transition ratio. However, the cross-transition ratio for ions at site 2 is still non-zero.

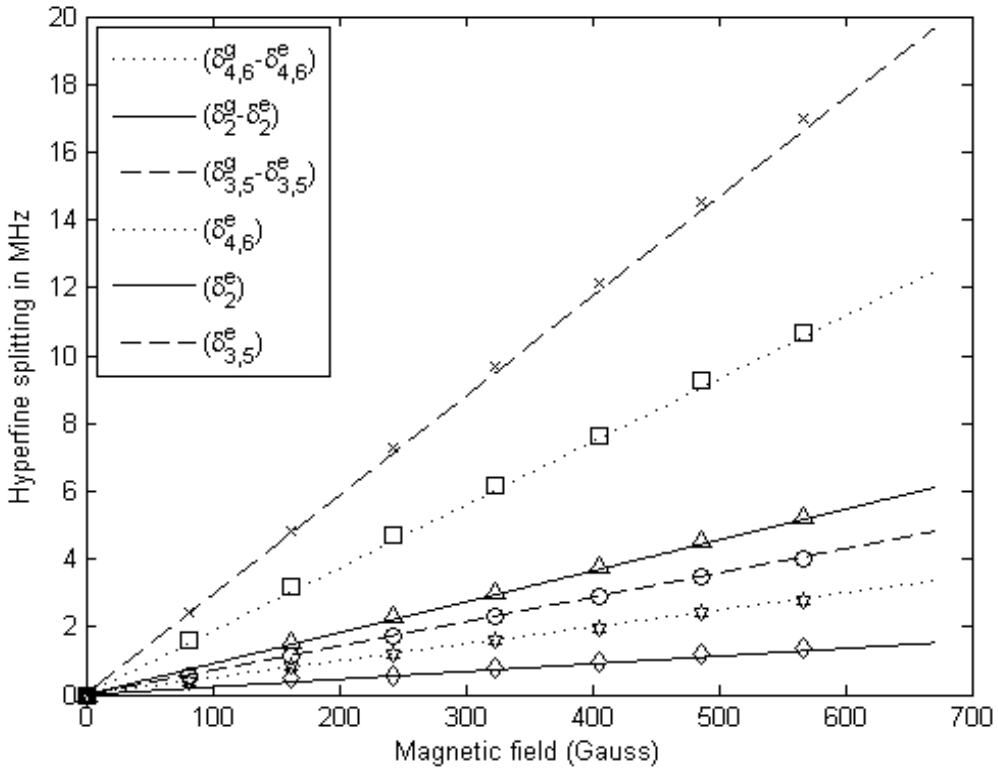

Figure 30: Experimental data (squares, diamonds, stars, circles, triangles, and crosses) showing hypefine splittings for $\theta_B = -5^0$. Lines are the theoretical results for hyperfine splittings for ions at each site with $\theta_B = -15^0$ obtained using equations (4.11-4.12) and experimentally calculated components of the gyromagnetic tensor.

The experimental data set in Figure 30 shows the linear dependence of the hyperfine splittings on the magnitude of the external magnetic field for both the excited and the ground states. For this particular orientation of the crystal, the cross-transition ratio is non-zero for ions at sites 2, 3, 4, 5, and 6, and by repeatedly applying the excitation pulse, we were able to see contributions from ions at all these sites.

All the absorption features in the hole burning spectrum are plotted and matched with the expected results using equations (4.11-4.12). Here, the experimentally-determined values of the components of the gyromagnetic tensors were used. In the fitting routine, the orientation of the magnetic field was varied, and a match to the experimental data was obtained for certain orientations of the magnetic field. The match gave us the correct orientation of the magnetic field. In this case, the theoretical results for the hyperfine splittings matched with the experimental data for $\theta_B = -15^o \pm 1^o$ and zero tilt angle, $\theta_{tB} = 0$. This means that the actual orientation of the crystal is about 10^o off from the nominal orientation.

Now each data set is fitted to a line with the assumption of equally weighted error in each data point using a least square fit routine in Matlab. Each fit gave more than 99% confidence for a linear fit to the data. This linear fit to experimental data gave us the hyperfine splitting for ions at site 2 for the ground state as $(115.85 \pm 1.5)^{MHz}/_{Tesla}$ and for the excited state as $(23.45 \pm 0.90)^{MHz}/_{Tesla}$. The experimental results for the hyperfine splittings compare well with the predicted splitting for ions at site 2. The predicted result for the hyperfine splitting for the ground state is $116.44^{MHz}/_{Tesla}$ and for the excited state is $23.98^{MHz}/_{Tesla}$. For ions at sites 4 and 6, the experimental result for the hyperfine

splitting for the ground state is $(237.60 \pm 3.20)^{MHz}/_{Tesla}$ and for the excited state is $(49.25 \pm 1.8)^{MHz}/_{Tesla}$. The predicted hyperfine splitting for ions at sites 4 and 6 for the ground state is $239.35^{MHz}/_{Tesla}$ and for the excited state is $47.82^{MHz}/_{Tesla}$. Now, for ions at sites 3 and 5 the experimental values for the hyperfine splittings for the ground state is $(370.34 \pm 2.5)^{MHz}/_{Tesla}$ and for the excited state is $(71.10 \pm 1.5)^{MHz}/_{Tesla}$. The predicted hyperfine splitting for ions at sites 3 and 5 for the ground state is $371.20^{MHz}/_{Tesla}$ and for the excited state is $71.10^{MHz}/_{Tesla}$. The experimental and the theoretical values for the hyperfine splittings agree very well within the error bounds of the experimental results.

$\theta_B = -15^o$	$\delta_2^e\left({}^{MHz}/_{Tesla}\right)$	$\delta_{3,5}^e\left({}^{MHz}/_{Tesla}\right)$	$\delta_{4,6}^e\left({}^{MHz}/_{Tesla}\right)$	$\delta_2^g\left({}^{MHz}/_{Tesla}\right)$	$\delta_{3,5}^g\left({}^{MHz}/_{Tesla}\right)$	$\delta_{4,6}^g\left({}^{MHz}/_{Tesla}\right)$
Theory	23.98	71.10	47.82	116.44	371.20	239.35
Experiment	23.45 ± 0.9	71.10 ± 1.5	49.25 ± 1.8	115.85 ± 1.5	370.34 ± 2.5	234.6 ± 3.2

Table 2: The fixed orientation, $\theta_B = -15^o$, of the applied magnetic field and the hyperfine splitting values for thulium ions in YAG.

In the second experiment, the sample is positioned such that the cross-transition ratio is the maximum for ions at sites 4 and 6, i. e., $\theta_B = 120^0$. Our orientation was $\theta_B = 115^o \pm 1^0$(Figure 29 (left)) which is 5 degrees off from the orientation for the maximum cross-transition ratio. This misalignment did not affect our analysis since ions at sites 4 and 6 still have the highest cross-transition ratios among the ions at all other sites in the crystal for this orientation. The experiment was repeated as described before,

and the data was collected for different values of the magnetic field. The data set in Figure 31 also shows that the hyperfine splitting linearly changes with the strength of the applied magnetic field. Again, an equally weighted error in each data point is assumed and a Matlab routine (APPENDIX A) based on least square fit is used to fit a line to the experimental data.

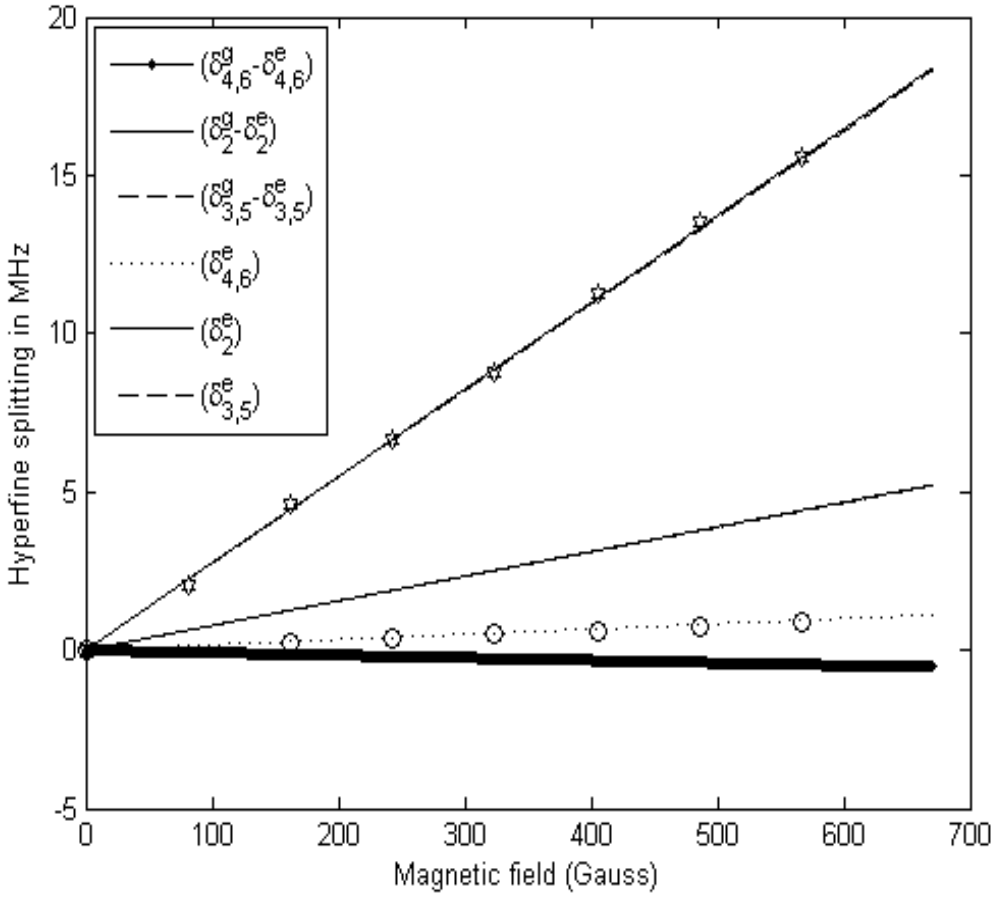

Figure 31: Experimental data (circles and stars) showing hypefine splitting for the orientation giving $\theta_B = 115^0$. Lines are plotted using theoretical results in equations (4.11-4.12) for $\theta_B = 125^0$.

Each least square fit gave more than 99% confidence for a linear fit to the data, and the values for hyperfine splittings in the ground and the excited states were obtained. This linear fit to the experiment data (circles, stars) using the least square fit in Matlab (APPENDIX A) gave us the desired hyperfine splitting. For ions at site 2 (sites 3 and 5), the difference between the hyperfine splitting in the ground and the excited states, $\delta^{g}_{2,3,5} - \delta^{e}_{2,3,5}$, was obtained as $(277.29 \pm 2.5)^{MHz}/_{Tesla}$. However, we could not get separate values for the hyperfine splittings for the excited and the ground states. Inability to get data for these splittings was due to the weak cross-transition ratios for ions at these sites for this particular orientation of the magnetic field. The predicted value for the difference in the hyperfine splittings, $\delta^{g}_{2,3,5} - \delta^{e}_{2,3,5}$, for ions at sites 2, 3 and 5 is $278.44^{MHz}/_{Tesla}$ and for excited state splitting, $\delta^{e}_{2,3,5}$, is $79.515^{MHz}/_{Tesla}$. The predicted values for $\delta^{g} - \delta^{e}$ are well within the experimentally-obtained values for $\delta^{g} - \delta^{e}$. The experimentally-measured hyperfine splitting for the excited state for ions at sites 4 and 6 is $(15.30 \pm 1.30)^{MHz}/_{Tesla}$. The predicted value for the hyperfine splitting for ions at sites 4 and 6 in the excited state is $16.70^{MHz}/_{Tesla}$. For ions at sites 4 and 6, the predicted value for hyperfine splitting for the ground state is $16.3^{MHz}/_{Tesla}$, which we could not obtain experimentally. A possible reason may be the fast population relaxation for hyperfine levels. The reason for the fast relaxation is the small splitting for ions at sites 4 and 6 for this orientation. The small splitting could be more prone to the environment. In the current case, the random flip-flop of spins due to aluminum in the host crystal and phonon coupling can shorten the population lifetime of these hyperfine levels. The

population lifetimes of the excited and the ground hyperfine levels may be different due to the difference in the wave functions for these hyperfine levels. Again, the experimental results for excited state splitting agree very well with the predicted results for the hyperfine splittings.

$\theta_B = 125^o$	$\left(\delta^g_{2,3,5} - \delta^e_{2,3,5}\right)\left(MHz/Tesla\right)$	$\delta^e_{4,6}\left(MHz/Tesla\right)$
Theory	278.44	16.70
Experiment	277.29 ± 2.5	15.30 ± 1.3

Table 3: The fixed orientation, $\theta_B = 125^o$, of the applied magnetic field and the hyperfine splitting values for thulium ions in YAG.

In another measurement, the crystal was oriented along $\theta_B = -65^0$. Again, the hyperfine splitting is obtained by monitoring the hyperfine splitting versus the magnetic field. The experimental data (triangle, circles, diamonds, and stars) are shown in Figure 32. The theoretical results are matched with the experimental data by varying the orientation of the magnetic field. In this orientation, again, the theoretical results matched with the experimental data for $\theta_B = -50^0$. This again implies that the orientation of the crystal axis is more than 10^o off from the nominal direction. The linear fit to the experimental data using the least square fit in Matlab (program given in APPENDIX A) gave us the hyperfine splitting for ions at site 2 for the ground state as $\left(370.96 \pm 13.77\right) MHz/Tesla$ and for the excited state as $\left(72.26 \pm 1.0\right) MHz/Tesla$. The predicted hyperfine splitting for ions at site 2 for the ground state is $365.95\, MHz/Tesla$ and for the excited state is $73.67\, MHz/Tesla$. The

experimental results give the hyperfine splittings for ions at sites 3 and 5 for the ground state as $(327.17 \pm 2)^{MHz}/_{Tesla}$ and for the excited state as $(65.60 \pm 1)^{MHz}/_{Tesla}$. The predicted hyperfine splittings for ions at sites 3 and 5 for the ground state as $328.30^{MHz}/_{Tesla}$ and for the excited state is $66.53^{MHz}/_{Tesla}$. All the experimental data for the hyperfine splittings agree with the theoretically predicted results within the error bounds. The error in the splittings may be due to the error in the orientation of the applied external magnetic field.

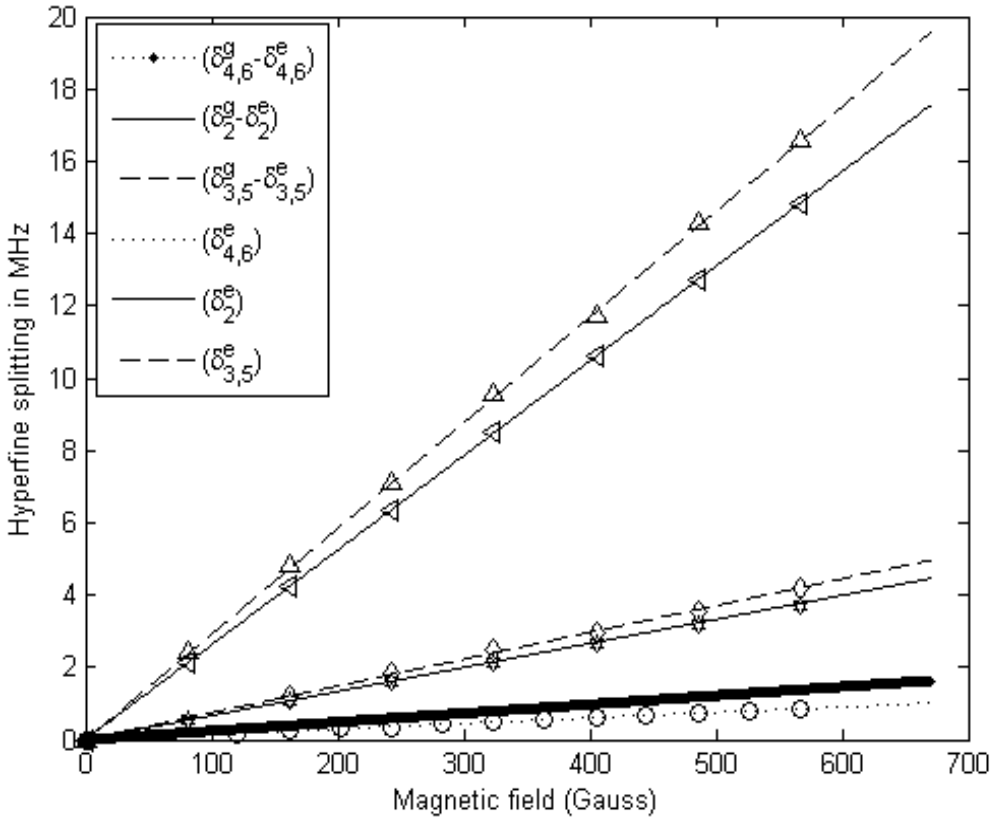

Figure 32: Experimental data (triangles, diamonds, stars, and circles) showing hypefine splitting for the orientation of the magnetic field along $\theta_B = -65^0$. Lines are the theoretical results obtained using $\theta_B = -50^0$ in equations (4.11-4.12).

$\theta_B = -50^o$	$\delta_2^e \left({}^{MHz}/_{Tesla} \right)$	$\delta_{3,5}^e \left({}^{MHz}/_{Tesla} \right)$	$\delta_2^g \left({}^{MHz}/_{Tesla} \right)$	$\delta_{3,5}^g \left({}^{MHz}/_{Tesla} \right)$
Theory	73.67	66.53	365.95	328.30
Experiment	72.26 ± 1	65.60 ± 1	370.96 ± 13.77	327.17 ± 2

Table 4: The fixed orientation, $\theta_B = -50^o$, of the applied magnetic field and the hyperfine splitting values for thulium ions in YAG.

Again, our inability to get any data for ground state splitting for ions at sites 4 and 6 may be attributed to the fast population relaxation for the hyperfine levels in the excited state and the ground state manifolds. Another point that needs mention is the difference in the orientation of the crystal versus the orientation obtained by matching the experimental data for the hyperfine splitting with the theoretically predicted results for the hyperfine splittings. The difference in the orientation of the magnetic field is about 10^0. The hyperfine splitting data indicate that the orientation of the (1-10) plane is within the accuracy quoted by the manufacturer. However, the errors in the orientations of the other planes are not within the accuracy of 3^o. In the rest of the dissertation, we will quote the orientations obtained by matching the experimental data for the hyperfine splittings with the predicted theoretical results for the hyperfine splittings.

The Hole Burning Spectrum and the Interacting Thulium Ions

Introduction

Here, the results of the effect of the optical field orientation on the hole burning spectrum are presented. This method provides another technique to identify ions at different sites in the Tm^{3+}:YAG crystal. Analysis of the theoretical results in equation

(4.1) shows that the optical field does not interact equally with the thulium ions at various sites in the crystal. The property of unequal interaction with the optical field can be used to identify ions at different sites in the medium contributing to the absorption in the hole burning spectrum. The results from the equation (4.1) just deal with the direct optical transition, and it is possible to have maximum direct transition strength and zero cross-transition ratio. This is important because in the hole burning spectrum, apart from the absorption feature at the burning frequency, all other absorption features critically depend on the strength of the cross-transition ratio.

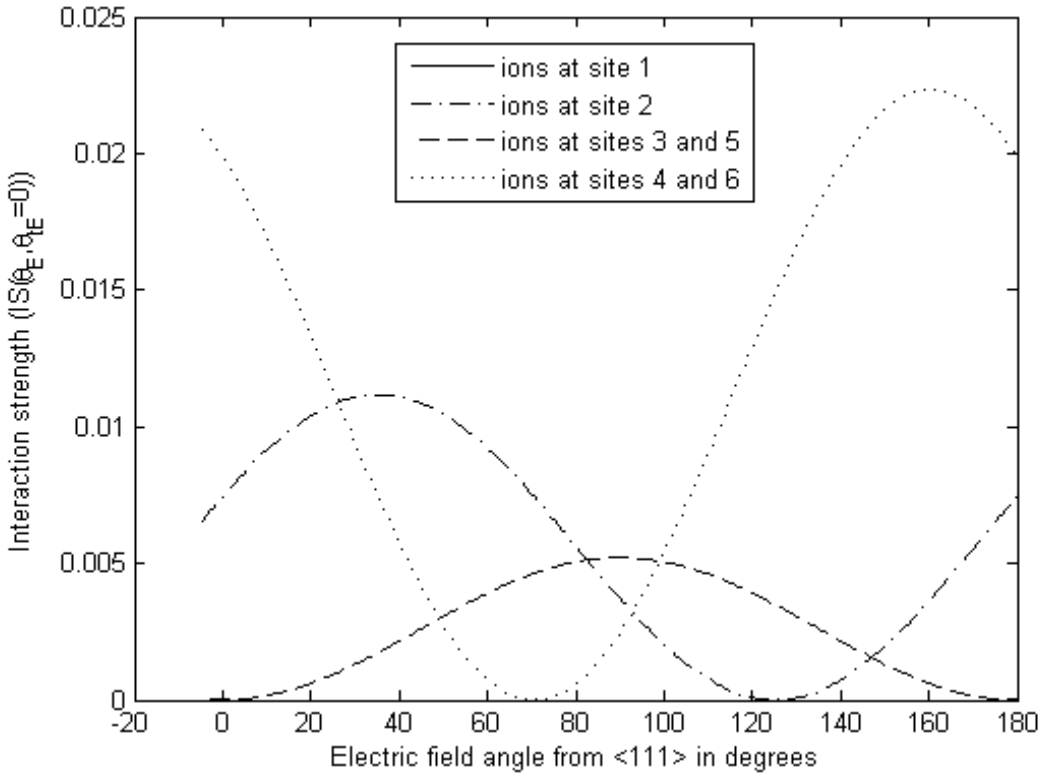

Figure 33: Theoretical plot for absorption strength of ions at different sites contributing to the absorption features in the hole burning spectrum. The magnetic field is along the direction that is -15 degree away from <001>. The results are obtained with the experimental values of the gyromagnetic tensor.

Careful analysis of the results in Figure 27 shows that for the orientation of the magnetic field along $\theta_B = \theta_{0B} = -15^o$ and $\theta_{tB} = 0^o$, the cross-transition ratios for ions at each site in the crystal have non-zero values. Now, define the absorption strength for ions at each site as the combination of the cross-transition ratio and the interaction with the optical field. Then, use equations (4.1, 4.15) and write the absorption strength, IS, of ions at each site as

$$IS_l\left(\gamma_x^{e,g},\gamma_y^{e,g},\gamma_z^{e,g},\theta_{tE},\theta_E\right) = R_l\left(\gamma_x^{e,g},\gamma_y^{e,g},\gamma_z^{e,g},\theta_{tB},\theta_B\right)\Omega_l^2\left(\theta_{tE},\theta_E\right) \tag{4.16}$$

where $l = 1,2,3,4,5,6$.

Now, we use the equation (4.16) to plot the absorption strength for ions at each site. The resultant plots are shown in Figure 33. Results show that there are certain orientations of the electric field for which the absorption strengths for ions at sites 3, 4, 5, and 6 are non-zero. Therefore, there is a possibility to see the contributions from ions at sites 3, 4, 5, and 6 in addition to the contribution from ions at site 2. Note that for these particular orientations of magnetic and electric fields, there is no possibility to see any contribution from ions at site 1. The ions at site 1 have zero absorption strength with the optical field as given by equation (4.1) for all the orientations of the optical field in the (1-10) plane.

Experiment

The experimental set-up for the identification of ions at different sites in the crystal was the same as given in Figure 15. The sample, 0.1% atm. Tm^{3+}:YAG, was vapor-cooled to 4K, and the hyperfine structure was obtained with the external magnetic

field. A pulse sequence similar to the one discussed in the previous section, containing a burning pulse and a very weak scanning chirp pulse, was used. The sample was mounted along $\theta_B = -15^o$. The fixed magnetic field of 560 Gauss was applied to the sample. As mentioned earlier, if the optical field is aligned along the [111] direction, then most of the contribution in the hole burning spectrum, other than at the burning frequency, will be from ions at sites 4 and 6. This is due to the fact that they have a much higher cross-transition ratio for these particular orientations of magnetic and optical fields.

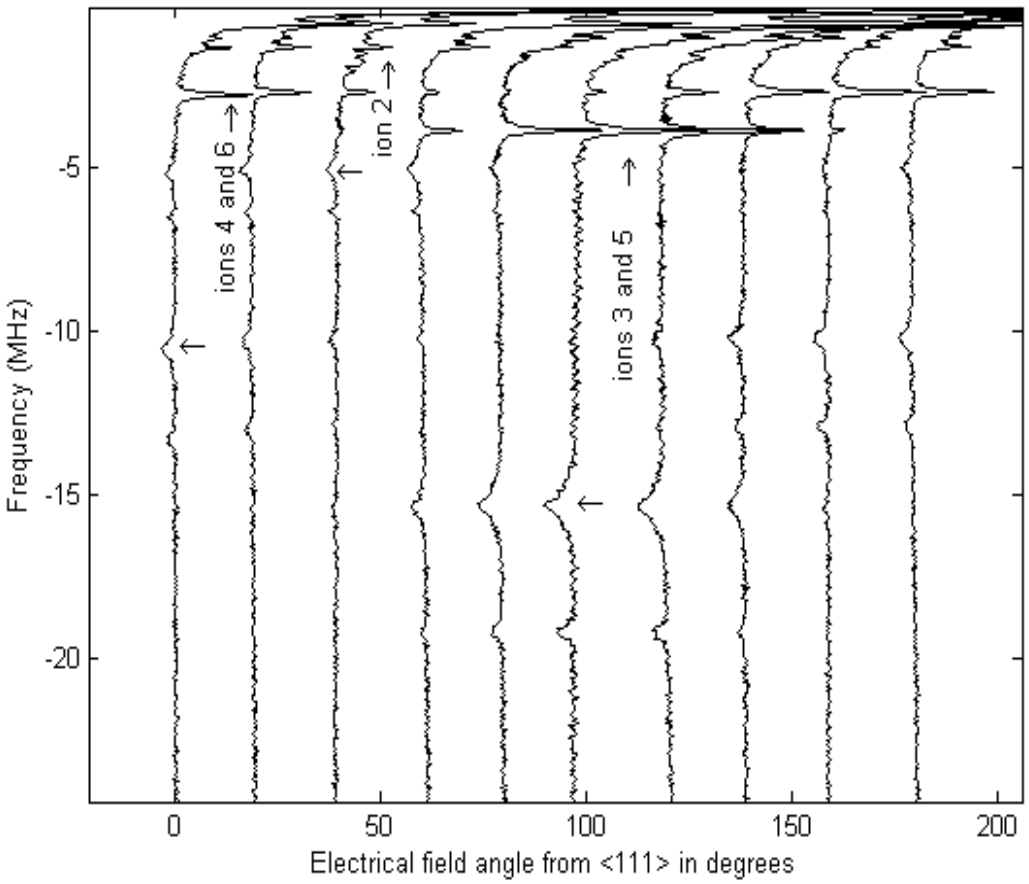

Figure 34: Experimental results showing the hole burning spectrum from ions at different sites in the crystal. Here the 560 Gauss magnetic field was aligned along $\theta_B = -15^o \pm 1^o$ relative to <001> and the orientation of the electric field was varied in the (1-10) plane.

In the experiment, the direction of the optical field was varied in the (1 -1 0) plane using the polarizer. The hole burning spectra for different orientations of the optical field were collected. The spectra presented in Figure 34 show the contribution from ions at sites 2, 3, 4, 5, and 6. Ions at each site were identified using the results of full rotation of the electric field and the values of the hyperfine splitting for this orientation of the magnetic field (Figure 22). The results shown in Figure 34 confirm that, for the electric field orientation along the direction that is 55^{o} away from the <111> direction, the ions at sites 2, 3, 4, 5, and 6 have non-zero coupling. The ions from these five sites contribute to the change in the absorption at the position other than at the burning frequency in the hole burning spectrum (Figure 34). Thus, we can clearly identify the contributions from thulium ions at each of these sites.

Population Lifetime of the Hyperfine Levels at 4K

Introduction

We now focus on another parameter, the population lifetime of the hyperfine levels, for the optimization of the conditions in the material for quantum computing application. We will see later in the dissertation that the population lifetime plays a significant role in the ensemble selection for the qubit preparation. In this experiment, the hyperfine structure in Tm^{3+}:YAG is obtained by applying a 400 G magnetic field. In order to measure the population lifetime of hyperfine levels, the medium is first excited with a laser pulse, and the population relaxation in the hyperfine levels is monitored at different times. The population in the hyperfine levels is monitored by scanning the

medium with a weak chirp laser pulse. The scan of the absorption with the weak chirp provides the hole burning spectrum. The hole burning spectrum gives information about the absorption change due to the ions at various sites in the crystal. Note that the absorption change, apart from the absorption change at the burning frequency, is unique to ions at each magnetically equivalent site in the crystal. Thus, the time-dependent scan of the medium, after the burning pulse and tracking of the each individual absorption feature, can provide us with the population lifetime of each site in the crystal.

In the previous experiments [(52), (57)], the population lifetime was measured by monitoring the absorption change at the burning frequency. However, that particular absorption change is usually due to thulium ions at multiple sites in the crystal. If the population relaxation between the hyperfine levels for these ions at multiple sites is not the same, then multiple decays might be observed, thus complicating the assignment of the hyperfine population lifetime to ions at any particular site in the crystal. In our approach, as we are monitoring the absorption change particular to ions at a certain site in the crystal, the assignment of the population lifetime to the ions at each particular site will be straightforward.

Experiment

The experimental set-up was the same as outlined in Figure 15. In the first experiment, the Tm^{3+}:YAG sample with 0.1% atm. thulium was positioned in the cryostat so that $\theta_B = -15^o \pm 1^o$. This direction roughly corresponds to the highest cross-transition ratios for ions at sites 4 and 6 in the crystal while ions at other sites have smaller non-zero cross-transition ratios. Any residual interactions of the laser field with ions at sites 1, 3,

and 5 were turned off by choosing the appropriate direction of the optical field, which in this case was along [111]. The sample was vapor-cooled with the liquid helium to 4K, and the spectral hole burning technique was used to measure the population lifetime of hyperfine levels. Any accumulation effects from the prior pulse were avoided by setting the trigger rate on the arbitrary waveform generator (AWG) to 0.25Hz.

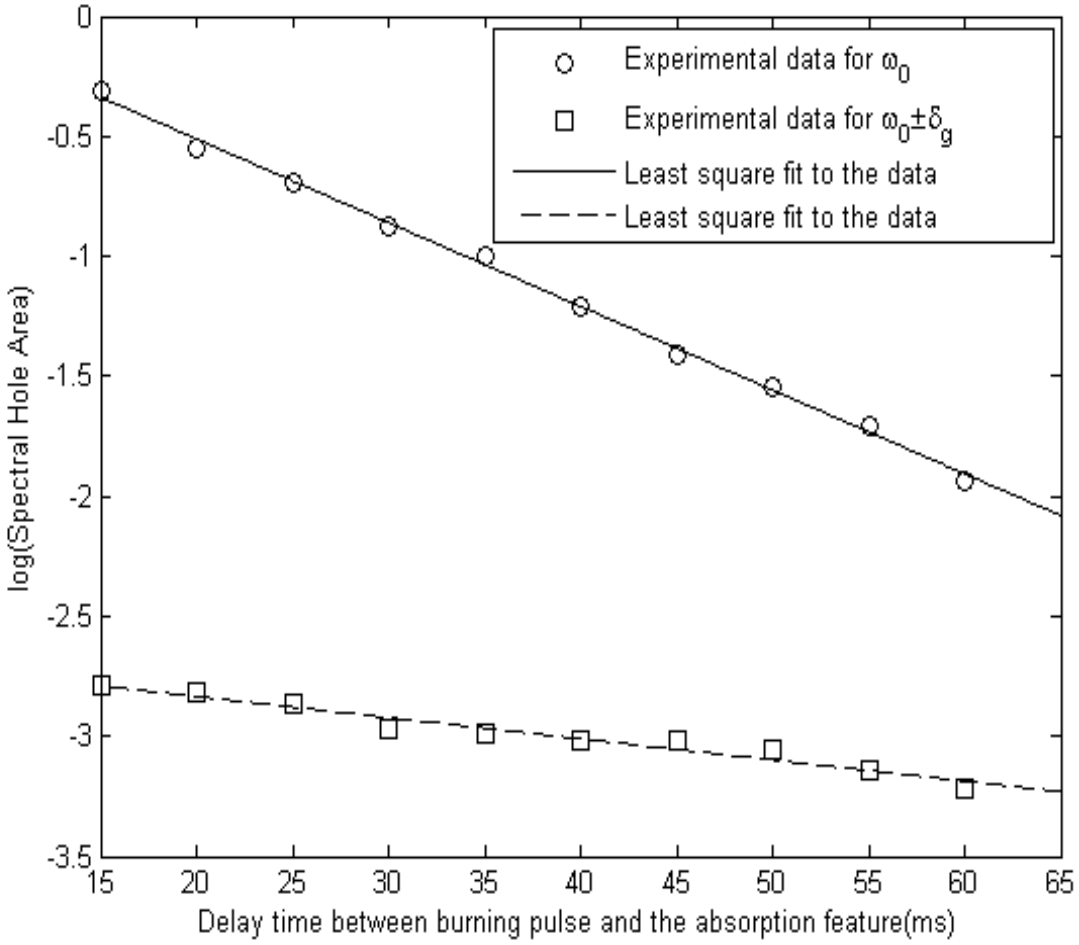

Figure 35: Experimentally-measured population relaxation between hyperfine levels for ions at sites 4 and 6 in the crystal. The crystal was oriented along $\theta_B = -15^o \pm 1^o$. Least square fits, shown as straight lines to the experimental data sets (circles and squares), gave us the hyperfine population lifetimes.

Figure 35 shows the data for the log of the spectral hole area of different absorption features in the hole burning spectrum and corresponding probe time. Here, the decay of the change in the features from ions at sites 4 and 6 are shown. The data set shows the linear dependence on the log scale of the spectral hole area with the probe time. Thus, the decay of each absorption feature in the hole burning spectrum is a single exponential. For this orientation, the population relaxation time between hyperfine levels of the excited state manifold is $28.5 \pm 0.5\text{ms}$. The population relaxation time for the ground state manifold is $114 \pm 9\text{ms}$.

In the next experiment, the crystal is oriented such that $\theta_B = 125^o \pm 1^o$, as this direction corresponds to the direction of the maximum cross-transition ratios for ions at sites 4 and 6 with the minimal cross-transition ratios for ions at other sites (2, 3, and 5). The orientation of the optical field was adjusted such that the interactions with ions at sites 1, 3, and 5 are turned off. So the focus will be on ions at sites 2, 4, and 6. In this case, even though ions at sites 4 and 6 have the highest cross-transition ratios, we were unable to get data for the population lifetimes for the hyperfine levels for these ions. The reason, as mentioned earlier is the fast population relaxation for ions at sites 4, and 6. However, we were able to get the population relaxation time for ions at site 2. Recall the experimental data for the hyperfine splitting for ions at site 2 in the crystal (Figure 31). Note that, the data for hyperfine splitting in the excited state is absent in that hyperfine splitting data. As mentioned earlier, the ions at site 2 have a minimal cross-transition ratio, and any absorption change in the hole burning spectrum attributed to ions at site 2 is mostly due to the accumulation. For this orientation of the magnetic field, we were

only able to monitor the absorption change at the burning frequency and the absorption change at $\delta_2^g - \delta_2^e$ from ions at site 2 in the crystal. This still provides an unambiguous population lifetimes for the hyperfine levels of ions at site 2 because other ions (ions at sites 4 and 6) contributing to the absorption change at the burning frequency have shorter population decay times (~ 20 ms). Now, we proceed to the experimental results.

In this experiment, we again avoid any accumulation effects from the prior pulse sequence by setting the trigger rate on the AWG to 0.25 Hz. The experimental results (circles and squares) for the time-dependent measurements of the absorption scan are plotted in Figure 36. The results in Figure 36 show the log plot of the spectral hole area at different probe times. It can be seen that the spectral area has a linear dependence on logarithmic scale on the probe time. This again implies that the population decay process is a single exponential. The population relaxation times for relaxation between hyperfine levels of electronic ground state and the electronic excited state manifolds are obtained using the least square fit to all the data sets in Figure 36. The lines are fitted to the data using the least square fit. The least square fits give relaxation time for ground state manifold as $1157 \pm 34\text{ms}$ and for excited state manifold as $822 \pm 12\text{ms}$.

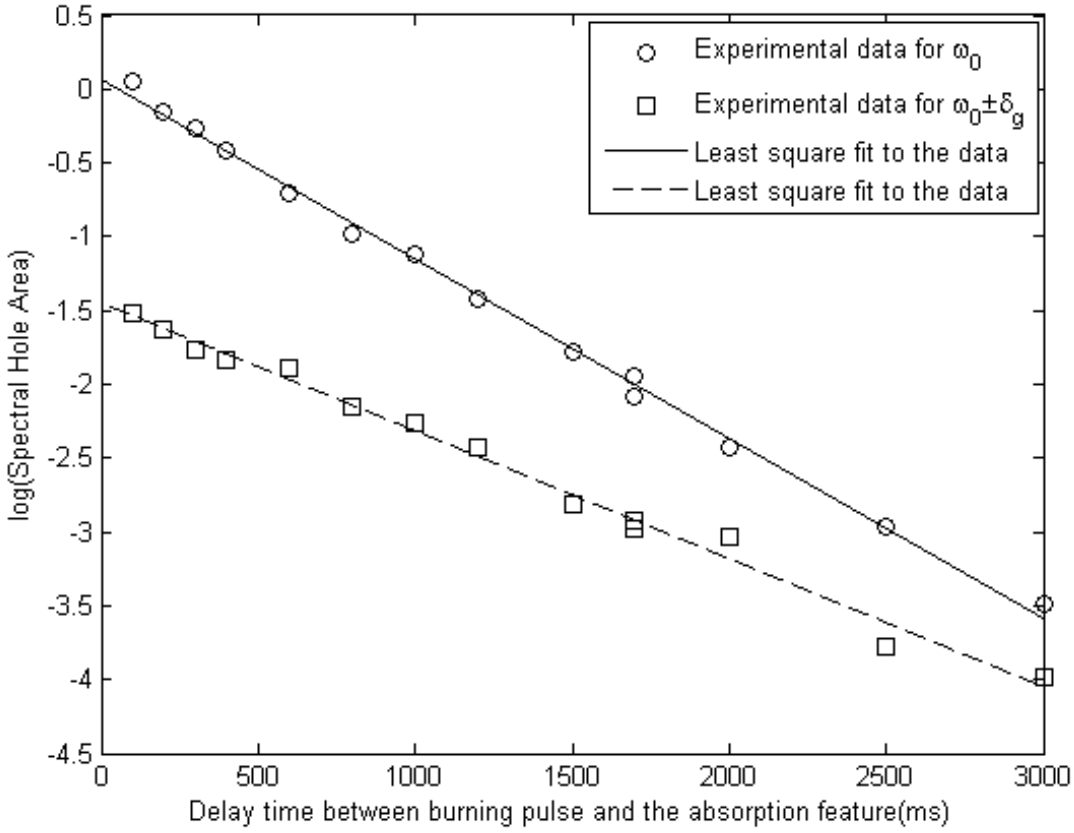

Figure 36: Experimentally-measured population relaxation between hyperfine levels for ions at site 2 in the crystal for a fixed magnetic field orientation at $\theta_B = 125^o \pm 1^o$. The least square fits represented by lines to the data sets (circles and squares) gave us the hyperfine population lifetimes.

Note that the hyperfine population lifetime in this case is significantly higher than in the previous case. This means that the population lifetime of hyperfine levels critically depends on the orientation of the magnetic field. These results also imply that the phonon interaction is anisotropic. Thus, as far as population lifetime is concerned, this orientation is clearly superior. Further investigations were carried out to study the effect of a sample temperature on the population relaxation rates for these two orientations.

Population Lifetime of the Hyperfine Levels at 5K

For practical applications, it is always desirable to have a minimal effect of temperature on the system. Using both orientations, $\theta_B = 125^o$ and $\theta_B = -15^o$, of the magnetic field, the effect of the sample temperature on the population lifetime is studied. In this experiment, the external magnetic field used to obtain the hyperfine structure in the medium is kept fixed at 400 Gauss, and the sample temperature is increased from $4 \pm 0.5K$ to $5 \pm 0.5K$.

The population lifetime of the hyperfine levels is expected to decrease with the increase in sample temperature. The goal here is to find how much reduction in the population lifetime is caused by the increase in the sample temperature. The major effect contributing to the decrease in the population lifetime is the phonon coupling. As the temperature of the sample is increased, there are more phonons available that can couple to the hyperfine levels. This results in an increase in the population relaxation rate between the hyperfine levels [(68), (69), (70),].

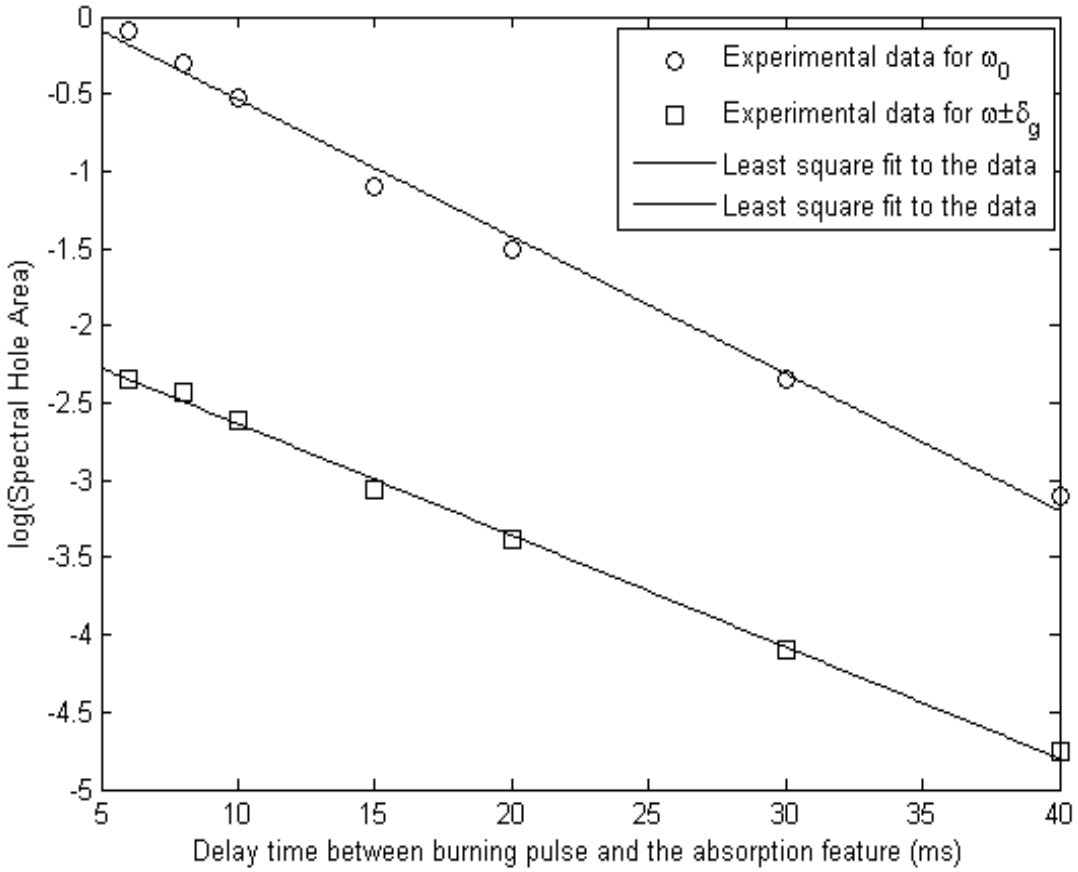

Figure 37: Experimentally-measured population relaxation between hyperfine levels at $5 \pm 0.5K$ for ions at sites 4 and 6 with crystal oriented at $\theta_B = -15^o \pm 1^o$. The experimental data (circles and squares) and the least square fits to these data sets are lines giving us the hyperfine population lifetimes.

In this experiment, the same technique as described above was used to obtain the experimental data for population lifetime measurements for two orientations of the magnetic field. Experimental data (circles and squares) in Figure 37 show the area of each absorption feature measured at a different probe time for ions at sites 4 and 6. The decay times for the ground state, $14 \pm 0.4\text{ms}$, and the excited state, $11.30 \pm 0.4\text{ms}$, manifolds are about the same. These relaxation times of these hyperfine levels are about

the same as the relaxation time, 12ms, of the intermediate electronic level. The hyperfine lifetimes are considerably shorter than the measured population lifetime at 4K for the same orientation of the magnetic field ($\theta_B = -15^o \pm 1^o$ for ions at sites 4 and 6).

In the second experiment, the crystal orientation with respect to the external magnetic field is adjusted such that the cross-transition ratios are highest for ions at sites 4 and 6, in the medium, with the largest splitting for ions at sites 2, 3, and 5. In this case, the magnetic field is oriented such that $\theta_B = 125^o \pm 1^o$, and the hyperfine population lifetime was measured for ions at site 2. Again, we could not observe any absorption features for ions at sites 4 and 6. We could only obtain the population lifetimes of hyperfine levels for ions at site 2. Again, one expects to see an increase in the relaxation rate between the hyperfine levels in the ground state and in the excited state manifolds.

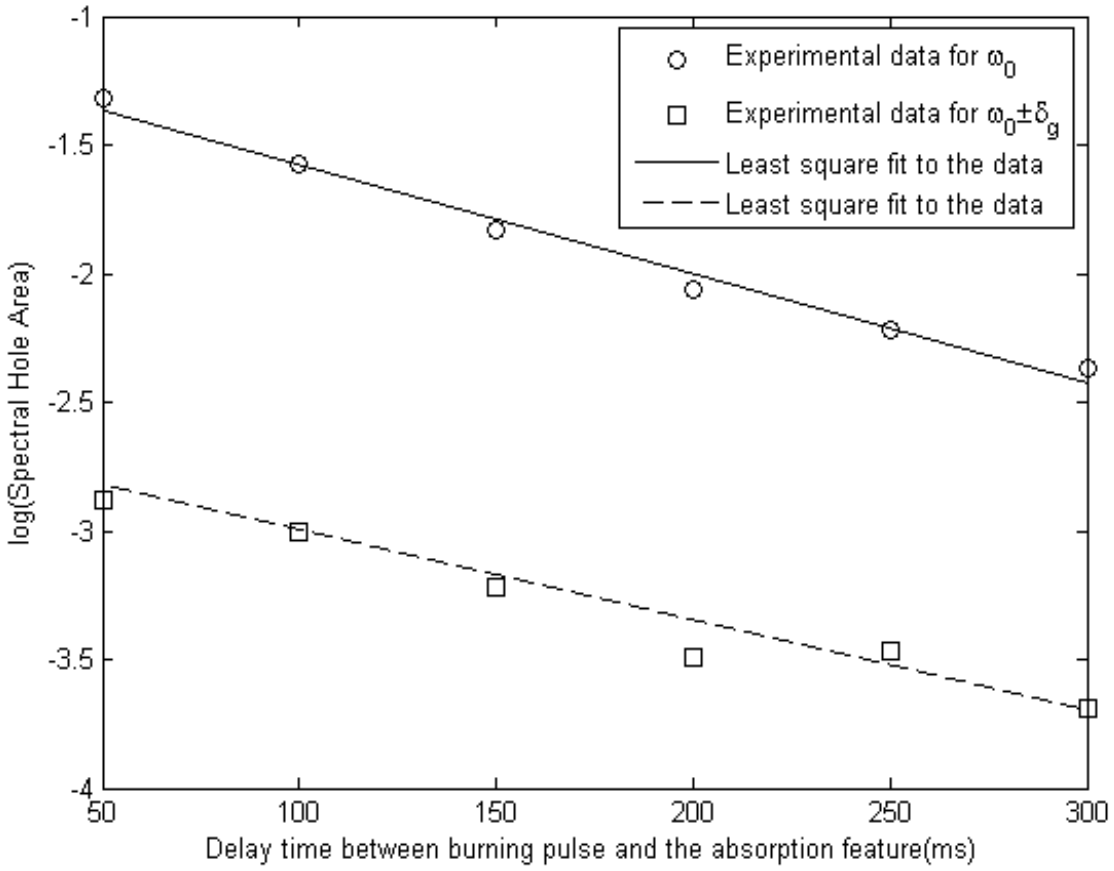

Figure 38: Experimentally-measured population relaxation between hyperfine levels at 5K for ions at site 2 with crystal oriented along the direction $\theta_B = 125^o \pm 1^o$. Each experimental data is shown as a point (circle and square). The least square fit to the experimental data sets are represented with lines. These lines were used to obtain the hyperfine population lifetimes.

The experimental data (circles and squares) for this case are shown in Figure 38. The absorption features again decayed as a single exponential. The least squares fit were used to extract the population lifetime for the ground and the excited state hyperfine manifolds. In this case, the population relaxation time between the ground state hyperfine levels was decreased to about 310 ± 33ms, which is still much higher than the population lifetime observed for ions at sites 4 and 6 at this temperature. For excited state hyperfine

levels a population lifetime of 237 ± 14.50ms was observed which is also higher than the population lifetime observed for ions at sites 4 and 6 at this temperature.

We have described the relaxation mechanism in the hyperfine levels for ions at different sites in the crystal. Now, the aim is to model the full relaxation dynamics in Tm^{3+}:YAG and measure the relaxation parameters governing the excitation and relaxation just after the excitation pulse. The theoretical description and application of the relaxation model is described in the next section.

Modeling the Relaxation Dynamics in the Medium

Introduction

In the previous section, it was shown that the population relaxation times for the hyperfine level in the ground state manifold are reasonably long (>100ms at 4K). The corresponding orientations of the magnetic field also have non-zero cross-transition ratios. The population relaxation time can be increased further by lowering the sample temperature. Thus, there is a possibility of a working with a 3-level system for quantum computing applications.

Now, the focus will be to directly measure the cross-transition ratios for these orientations and also to measure the other relaxation parameters shown in Figure 39. The mapping of the relaxation and excitation parameters in Tm^{3+}:YAG will also help us decide the best method for ensemble selection during the qubit preparation process. Thus, the goals of this investigation are twofold. One is to theoretically model the relaxation dynamics for the system given in Figure 39. The second goal is an experimental

investigation of the excitation and the relaxation parameters for the orientation of the magnetic field that will give us the maximum cross-transition ratios.

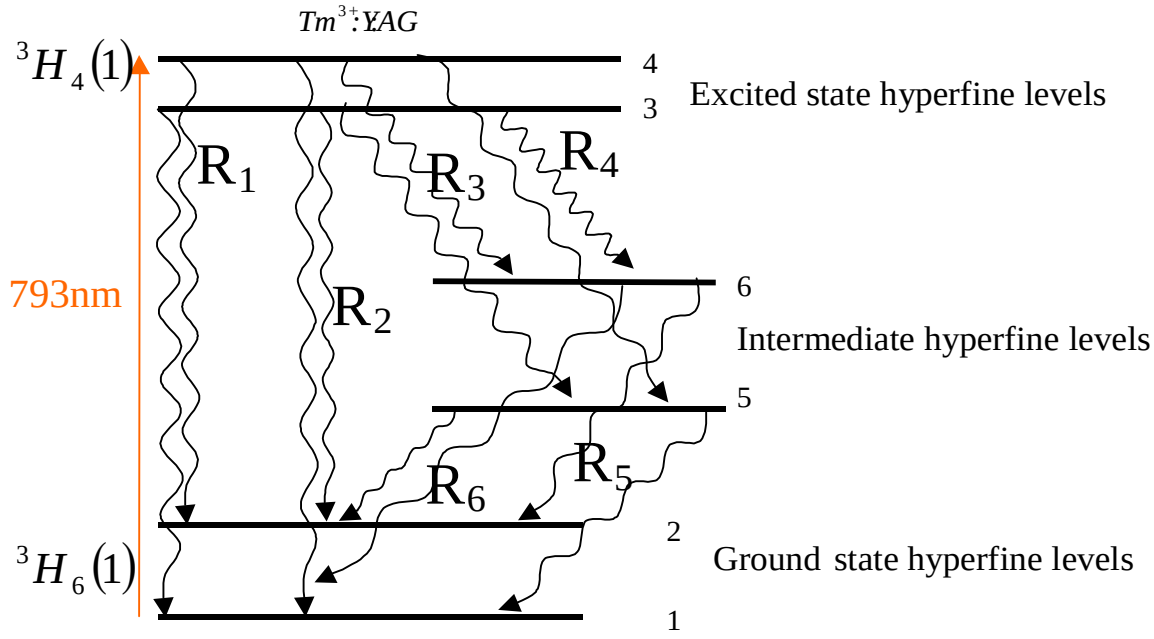

Figure 39: Energy level diagram of Tm^{3+}:YAG with an external magnetic field applied to the sample at 4K showing the hyperfine levels.

A recent theoretical (55) study predicted that it is possible to get non-zero cross-transition ratios in Tm^{3+}:YAG for certain orientations of the magnetic field. Later, the cross-transition ratio was experimentally-measured [(57)] for a certain orientation of the magnetic field. In the current study, we not only measure the cross-transition ratio, but we also measure other relaxation parameters. The results in Figure 20 show the orientation of the magnetic field and the corresponding cross-transition ratios for thulium ions at different sites in the crystal. There are three particularly interesting magnetic field orientations that predict maximum cross-transition ratios for ions at sites 2, 3, 4, 5, and 6.

In the current experimental study, the results are presented only for one of the orientations of the magnetic field. However, the theoretical framework can be applied to study any other orientation of the magnetic field.

In this section, we first present the theoretical framework governing the relaxation dynamics. In the experiment, we align the crystal with respect to the magnetic field along the orientation $\theta_B = -15^o \pm 1^o$, giving us a non-zero cross-transition ratio for ions at sites 4 and 6. We apply the theoretical model to the spectral hole data from the experiment and obtain the excitation and the relaxation parameters for the system in Figure 39.

Theoretical Model

In the spectral hole burning measurements, the medium is first excited. Then, the relaxation of the excited population is mapped by monitoring the absorption profile of the medium at different times using another weak chirp pulse. Thus the focus of the theoretical study will be on three basic mechanisms: the population excitation, the population relaxation, and the probing of the absorption profile of the medium.

Excitation with a Narrowband Pulse: As noted earlier, in Chapter 3, each thulium ion will have four possible optical transitions for excitation and relaxation as an external magnetic field is applied to the medium. In these four optical transitions, two optical transitions will be allowed, and the other two will be weakly allowed due to some mixing of the spin states. Now, we assign the value μ_a for the transition dipole moment for optically allowed transitions and the value μ_u for transition dipole moment for weakly allowed optical transition for each ion in the medium.

Consider the excitation of energy levels in the medium in Figure 39 with a narrowband optical pulse at time *t=0*, such that the bandwidth and the Rabi frequency of the excitation pulse are smaller than the smallest hyperfine splitting in the group of ions being addressed, i.e., $\left(\tau_p, \frac{1}{\Omega_p}\right) >> \frac{1}{Min(\delta_e, \delta_g)}$, as shown in Figure 40. In this calculation, we ignore any relaxation process during the pulse. In other words, the population relaxation time for these levels is assumed to be much larger than the duration of the applied pulse. Figure 40 shows the coupling of a narrowband optical pulse at ω_0 with the energy levels in the sub-group of ions A, B, C, and D for thulium ions at sites 4 and 6.

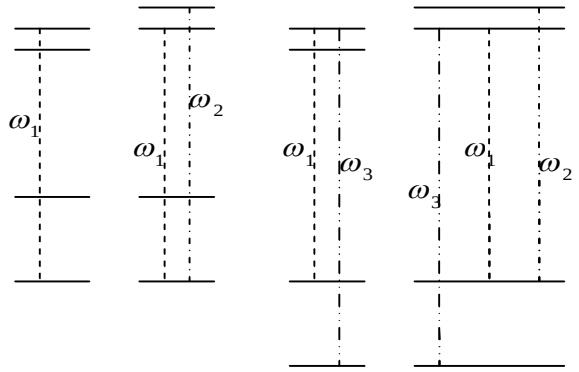

Figure 40: Sub-group of ions considered for the analysis. Here, $\omega_1 = \omega_0$, $\omega_2 = \omega_0 + \delta_e$, $\omega_3 = \omega_0 + \delta_g$, δ_e is the hyperfine splitting for the excited state, and δ_g is the hyperfine splitting for the ground state for each ion. In this figure, for simplicity, other possible optical transitions are not shown.

For a medium with a small absorption, i.e., $\alpha L << 1$, the population density for each level after the excitation will be (cf. Figure 39 for labels)

$$\left.\begin{aligned} n_1 &= \frac{n_0}{4}\left(1+\cos\theta_u\right) \\ n_2 &= \frac{n_0}{2} \\ n_3 &= 0 \\ n_4 &= \frac{n_0}{4}\left(1-\cos\theta_u\right) \end{aligned}\right\} \qquad (4.17),$$

$$\left.\begin{aligned} n_1 &= \frac{n_0}{4}\left(1+\cos\theta_a\right) \\ n_2 &= \frac{n_0}{2} \\ n_3 &= \frac{n_0}{4}\left(1-\cos\theta_a\right) \\ n_4 &= 0 \end{aligned}\right\} \qquad (4.18),$$

$$\left.\begin{aligned} n_1 &= \frac{n_0}{2} \\ n_2 &= \frac{n_0}{4}\left(1+\cos\theta_a\right) \\ n_3 &= 0 \\ n_4 &= \frac{n_0}{4}\left(1-\cos\theta_a\right) \end{aligned}\right\} \qquad (4.19),$$

$$\left.\begin{aligned} n_1 &= \frac{n_0}{2} \\ n_2 &= \frac{n_0}{4}\left(1+\cos\theta_u\right) \\ n_3 &= \frac{n_0}{4}\left(1-\cos\theta_u\right) \\ n_4 &= 0 \end{aligned}\right\} \qquad (4.20),$$

where n_0 is the initial population before the pulse was applied, with equally populated ground state hyperfine levels, and where θ_a, θ_u are the pulse areas defined as

$$\theta_a = \frac{\mu_a}{\hbar}\int_0^{\tau_p}\varepsilon(t)dt\,,\ \theta_u = \frac{\mu_u}{\hbar}\int_0^{\tau_p}\varepsilon(t)dt.$$

In the next section the evolution, from these initial populations, of this excited system will be discussed.

Relaxation Dynamics of the Excited Population: In this section, the relaxation dynamics of the excited population given in equations (4.17-4.20) is modeled. Note that the population excitation and relaxation in this system involves cross-transitions, as can be seen from equations obtained after excitation with a narrowband pulse and which will also be evident from the results for the relaxation dynamics.

Several pathways for relaxation of the excited ion are shown in Figure 39 where all short-lived relaxations are ignored and only the long-lived levels are considered. It is assumed that the cross and direct transition probabilities are independent of the particular hyperfine state. They only depend on the particular electronic state involved. Explicitly, in the modeling of the relaxation dynamics, it is assumed that direct, R_1, and cross, R_2, relaxations from level 4 to the ground state levels 1, 2 are equal to the direct and cross relaxations from level 3 to the ground state levels 1, 2. Similarly direct, R_3, and cross, R_4, relaxations from level 4 to the intermediate levels 5, 6 are equal to the direct and cross relaxations from level 3 to the intermediate levels 5, 6 and also direct, R_5, and cross, R_6, relaxations from level 5 to the ground state levels 1, 2 are equal to the direct

and cross relaxations from level 6 to the ground state levels 1, 2 as shown in Figure 39. We assume that the relaxation rate between the ground state hyperfine levels is given by κ_2 and the relaxation rate between excited state hyperfine levels is given by κ_1.

If we assume that the population density in each level is $n_i, i = 1 \cdots 6$ (cf. Figure 39), then the population density in each level after some time later, $t > 0$, will be described by

$$\frac{d}{dt} n_3 = \kappa_1 (n_4 - n_3) - \left(\frac{1}{T_1} \right) n_3 \tag{4.21},$$

$$\frac{d}{dt} n_4 = -\kappa_1 (n_4 - n_3) - \left(\frac{1}{T_1} \right) n_4 \tag{4.22},$$

$$\frac{d}{dt} n_1 = \kappa_2 (n_2 - n_1) + \frac{R_1}{T_1} n_3 + \frac{R_2}{T_1} n_4 + \frac{R_5}{T_3} n_5 + \frac{R_6}{T_3} n_6 \tag{4.23},$$

$$\frac{d}{dt} n_2 = -\kappa_2 (n_2 - n_1) + \frac{R_2}{T_1} n_3 + \frac{R_1}{T_1} n_4 + \frac{R_6}{T_3} n_5 + \frac{R_5}{T_3} n_6 \tag{4.24},$$

$$\frac{d}{dt} n_5 = \frac{R_3}{T_1} n_3 + \frac{R_4}{T_1} n_4 - \left(\frac{1}{T_3} \right) n_5 \tag{4.25},$$

$$\frac{d}{dt} n_6 = \frac{R_3}{T_1} n_4 + \frac{R_4}{T_1} n_3 - \left(\frac{1}{T_3} \right) n_6 \tag{4.26},$$

where T_1 is the population lifetime of the excited state and T_3 is the population lifetime of the intermediate level.

Equations (4.21) and (4.22) can be solved and the population in levels 3 and 4 will be

$$n_3(t) = \tfrac{1}{2}\left(\left(n_4(0) + n_3(0)\right) - \left(n_4(0) - n_3(0)\right)e^{-2\kappa_1 t}\right)e^{-a_1 t} \tag{4.27}$$

$$n_4(t) = \tfrac{1}{2}\left(\left(n_4(0) + n_3(0)\right) + \left(n_4(0) - n_3(0)\right)e^{-2\kappa_1 t}\right)e^{-a_1 t} \tag{4.28}$$

where $a_1 = \left(\frac{1}{T_1}\right)$.

Subtracting equation (4.25) from (4.26) we get

$$\frac{d}{dt}(n_6 - n_5) = a_2(n_4 - n_3) - a_3(n_6 - n_5) \tag{4.29},$$

where $a_2 = \left(\frac{R_3 - R_4}{T_1}\right)$ and $a_3 = \left(\frac{1}{T_3}\right)$.

Adding equations (4.25) and (4.26) yields

$$\frac{d}{dt}(n_6 + n_5) = a_4(n_4 + n_3) - a_3(n_6 + n_5) \tag{4.30},$$

where $a_4 = \left(\frac{R_3 + R_4}{T_1}\right)$.

Subtracting equation (4.23) from (4.24) we get

$$\frac{d}{dt}(n_2 - n_1) = -2\kappa_2(n_2 - n_1) + a_5(n_4 - n_3) + a_6(n_6 - n_5) \tag{4.31},$$

where $a_5 = \left(\frac{R_1 - R_2}{T_1}\right), a_6 = \left(\frac{R_5 - R_6}{T_3}\right)$.

Adding equations (4.23) and (4.24) gives

$$\frac{d}{dt}(n_2 + n_1) = a_7(n_4 + n_3) + a_3(n_6 + n_5) \tag{4.32},$$

where $a_7 = \left(\frac{R_1 + R_2}{T_1}\right)$.

Equations from (4.29-4.32) can be solved exactly and the resultant expressions will be

$$\left(n_6(t)+n_5(t)\right)=\left(\left(n_6(0)+n_5(0)\right)+\left(\frac{a_4}{a_1-a_3}\right)\left(n_4(0)+n_3(0)\right)\left(1-e^{-(a_1-a_3)t}\right)\right)e^{-a_3t} \quad (4.33),$$

$$\left(n_6(t)-n_5(t)\right)=\left(\left(n_6(0)-n_5(0)\right)+\left(\frac{a_2}{a_1+2\kappa_1-a_3}\right)\left(n_4(0)-n_3(0)\right)\left(1-e^{-(a_1+2\kappa_1-a_3)t}\right)\right)e^{-a_3t} \quad (4.34),$$

$$\begin{aligned}\left(n_2(t)+n_1(t)\right) &= \left(n_2(0)+n_1(0)\right)\\ &+\left(\left(n_6(0)+n_5(0)\right)+\left(\frac{a_4}{a_1-a_3}\right)\left(n_4(0)+n_3(0)\right)\right)\left(1-e^{-a_3t}\right)\\ &+\left(\frac{a_7}{a_1}-\frac{a_3a_4}{a_1(a_1-a_3)}\right)\left(n_4(0)+n_3(0)\right)\left(1-e^{-a_1t}\right)\end{aligned} \quad (4.35),$$

$$\left(n_2(t)-n_1(t)\right)=\left(\begin{array}{l}\left(n_2(0)-n_1(0)\right)\\ +\left(\left(n_6(0)-n_5(0)\right)+\left(\frac{a_2}{a_1+2\kappa_1-a_3}\right)\left(n_4(0)-n_3(0)\right)\right)\left(\frac{a_6}{(a_3-2\kappa_2)}\right)\left(1-e^{-(a_3-2\kappa_2)t}\right)\\ +\left(\frac{a_5}{(a_1+2\kappa_1)}-\frac{a_2a_6}{(a_1+2\kappa_1-2\kappa_2)(a_1+2\kappa_1-a_3)}\right)\left(n_4(0)-n_3(0)\right)\left(1-e^{-(a_1+2\kappa_1-2\kappa_2)t}\right)\end{array}\right)e^{-2\kappa_2t} \quad (4.36).$$

Results obtained here provide a complete description of the relaxation processes governing the population decay. The results given here have six independent parameters. These independent parameters will be measured experimentally using the spectral hole burning technique.

Scanning the Medium with a Weak Chirp Pulse: The relaxation parameters are measured experimentally using time-dependent measurements. In this technique, the

excited medium is scanned at different times with a weak broadband chirp pulse. Each scan with the chirp will provide the absorption profile of the medium. The scanned absorption profile will give the information about the population in each level at a certain time. This, in turn, will be used to study the relaxation dynamics of the medium. The broadband chirp pulse will interact with all four levels of these four ions (A, B, C, and D) in the medium as it scans the medium.

Therefore, the absorption for each transition, as measured with a weak broadband chirp pulse, will be

$$\alpha_{ij}(t) = \sigma\left(\frac{\mu_{ij}^2}{\mu_{ij}^2+\mu_{lm}^2}\right)\left(n_i(t) - n_j(t)\right), i = 1,2;\ j = 3,4; l(\neq i) = 1,2; m(\neq j) = 3,4,$$

where σ is the absorption cross-section, and μ_{ij} are the dipole matrix elements, and they are either μ_a for allowed transitions or μ_u for weakly allowed transitions, and $n_i(t)$ is the population of each level at time, *t*, as given by the equations (4.27, 4.28, 4.33-4.36).

The total absorption for each transition will be $\alpha(t) = \sum_{i=1,2:\, j=3,4} \alpha_{ij}(t)$. The absorption change as compared to the initial absorption can be obtained as $\Delta\alpha(t) = \sum \alpha_{ij}(t) - \alpha(0)$, where $\alpha(0) = \sigma n_0$ is the absorption of the medium in a fully relaxed state. The normalized absorption can be calculated as $\frac{\Delta\alpha(t)}{\alpha(0)}$.

Now, consider all of the transitions for ions A, B, C, and D in Figure 40 in the sub-group of ions that are excited with a narrowband laser pulse at ω_0. It is important to consider all the transitions for the analysis, as population relaxation in the medium involves all of these transitions. In Figure 40, the transitions at $\omega_0 + \delta_e, \omega_0 + \delta_g$ for

these four ions are shown, where hyperfine splitting for upper electronic levels is δ_e and hyperfine splitting in lower electronic levels is δ_g for each ion. There are also other transitions at $\omega_0 - \delta_e, \omega_0 - \delta_g$, and $\omega_0 \pm \left(\delta_g \pm \delta_e\right)$ that are not drawn in Figure 40. These transitions will be considered for the study of population relaxation in the system. Therefore, for each excitation, there are nine possible transitions for which an absorption change would result and, hence, nine absorption features in each scan. However, note that the strength of these absorption features will critically depend on the transition dipole for each transition.

Now using the energy level diagram in Figure 40 for four types of these ions, the absorption profile at nine different frequencies will be

$$\alpha\left(\omega_0, t\right) = \sigma\left(\left(\frac{\mu_u^2}{\mu_u^2 + \mu_a^2}\right)\left(n_1^A(t) - n_4^A(t)\right) + \left(n_1^D(t) - n_3^D(t)\right) + \left(\frac{\mu_a^2}{\mu_u^2 + \mu_a^2}\right)\left(n_1^B(t) - n_3^B(t)\right) + \left(n_1^C(t) - n_3^C(t)\right)\right) \tag{4.37},$$

$$\alpha\left(\omega_0 - \left(\delta_g + \delta_e\right), t\right) = \sigma\left(\frac{\mu_u^2}{\mu_u^2 + \mu_a^2}\right)\left(n_2^A(t) - n_3^A(t)\right) \tag{4.38},$$

$$\alpha\left(\omega_0 - \left(\delta_g - \delta_e\right), t\right) = \sigma\left(\frac{\mu_a^2}{\mu_u^2 + \mu_a^2}\right)\left(n_2^B(t) - n_4^B(t)\right) \tag{4.39},$$

$$\alpha\left(\omega_0 - \delta_e, t\right) = \sigma\left(\left(\frac{\mu_a^2}{\mu_u^2 + \mu_a^2}\right)\left(n_1^A(t) - n_3^A(t)\right) + \left(\frac{\mu_u^2}{\mu_u^2 + \mu_a^2}\right)\left(n_2^C(t) - n_3^C(t)\right)\right) \tag{4.40},$$

$$\alpha\left(\omega_0 - \delta_g, t\right) = \sigma\left(\left(\frac{\mu_a^2}{\mu_u^2 + \mu_a^2}\right)\left(n_2^A(t) - n_4^A(t)\right) + \left(\frac{\mu_u^2}{\mu_u^2 + \mu_a^2}\right)\left(n_2^B(t) - n_3^B(t)\right)\right) \tag{4.41},$$

$$\alpha\left(\omega_0 + \delta_e, t\right) = \sigma\left(\left(\frac{\mu_u^2}{\mu_u^2 + \mu_a^2}\right)\left(n_1^B(t) - n_4^B(t)\right) + \left(\frac{\mu_a^2}{\mu_u^2 + \mu_a^2}\right)\left(n_2^D(t) - n_4^D(t)\right)\right) \tag{4.42},$$

$$\alpha(\omega_0+\delta_g,t)=\sigma\left(\left(\frac{\mu_u^2}{\mu_u^2+\mu_a^2}\right)\left(n_1^C(t)-n_4^C(t)\right)+\left(\frac{\mu_a^2}{\mu_u^2+\mu_a^2}\right)\left(n_2^D(t)-n_3^D(t)\right)\right) \quad (4.43),$$

$$\alpha\left(\omega_0+(\delta_g-\delta_e),t\right)=\sigma\left(\frac{\mu_a^2}{\mu_u^2+\mu_a^2}\right)\left(n_1^C(t)-n_3^C(t)\right) \quad (4.44),$$

$$\alpha\left(\omega_0+(\delta_g+\delta_e),t\right)=\sigma\left(\frac{\mu_u^2}{\mu_u^2+\mu_a^2}\right)\left(n_1^D(t)-n_4^D(t)\right) \quad (4.45).$$

Analysis of the Theoretical Results: First, we will examine a simple case. We assume that the burning pulse is applied at $t=0^-$ and the medium is scanned at $t=0^+$ such that the population decay from the upper electronic levels can be neglected. Then the absorption change for the transitions $\omega_0\pm(\delta_g-\delta_e)$ and $\omega_0\pm(\delta_g+\delta_e)$ will be zero. However, transitions at other frequencies will result in an absorption change with $\Delta\alpha(\omega_0,t=t_0)\le 0,\ \Delta\alpha(\omega_0\pm\delta_e,t=t_0)\le 0,$ and $\Delta\alpha(\omega_0\pm\delta_g,t=t_0)\le 0.$ Therefore, just after the burning pulse, there will be five absorption features. These absorption features will appear as a reduction in the absorption at these frequencies in the hole burning spectrum. These features are usually called holes in the absorption spectrum as there are fewer ions left who can absorb light at these particular frequencies. However, in general, there will be a change in absorption at nine different locations in the hole burning spectrum.

It should be noted that there are twelve variables $\kappa_1,\kappa_2,\mu_a,\mu_u,R_1,R_2,R_3,R_4,R_5,R_6,$ $T_1,\ T_3$. However, these twelve variables are not independent. They reduce to nine independent variables and still pose a significant challenge to measure experimentally. The number of these variables can be further reduced by noting the electronic upper state lifetime, $T_1=0.6ms,$ and the intermediate state lifetime, $T_3=10ms$, for Tm^{3+}:YAG [(71),

(72), (51)]. Therefore, unknown variables are further reduced to seven variables, which will be measured using the experimental data as described in the next section.

Experimental Results for Excitation and Relaxation Parameters at 4K

The experimental set-up is the same as given in Figure 15. For this experiment, the orientation of the rectangular crystal of 0.1% atm. thulium-doped in YAG is chosen such that the cross-transition ratio is the highest for ions at sites 4 and 6, i.e., $\theta_B = -15^o \pm 1^o$. The sample length was chosen to give an absorbance of 0.5, and the sample was cooled to $4 \pm 0.5K$. The magnetic field was fixed at 400 Gauss. Time-dependent population changes in the hyperfine levels of the electronic ground and excited state manifolds were measured by monitoring the change in absorption at different times. The method used here is very similar to the technique used to measure the population lifetimes of the hyperfine levels of the excited and the ground state manifolds.

In the previous experiment, the excited medium was scanned after most of the population between electronic levels was relaxed. The population relaxation process between hyperfine levels was measured. In the current experiments, the population relaxation is monitored just after the burning pulse. In the previous experiments, it was shown that at $4 \pm 0.5K$, the population relaxation process between hyperfine levels is much slower than the population relaxation between electronic levels. Therefore, the population relaxation, between the hyperfine levels for the time scale being considered here, is neglected. Therefore, it is assumed that $\kappa_1 = 0, \text{and } \kappa_2 = 0$ and the unknowns are further reduced to five independent variables. The hyperfine structure has $\delta_e = 2.0MHz$

and $\delta_g = 10.0MHz$ for the current orientation ($\theta_B = -15^o \pm 1^o$) and the strength (400 Gauss) of the magnetic field.

In the experiment, a narrowband (bandwidth = 100kHz) burning pulse excites the medium at the transition frequency ω_0. At the later time, the absorption profile of the medium is mapped using a weak chirp pulse of 20MHz bandwidth. The scanning weak chirp pulse does not modify the absorption profile of the medium. The data set is collected for the absorption features at frequencies ω_0, $\omega_0 \pm \delta_e$, and $\omega_0 \pm \delta_g$. The signal-to-noise ratio of the absorption data for the absorption features at other frequencies was too small to yield any useful information. Normalized absorption for each absorption feature is shown in Figure 41 with each point obtained at a particular time.

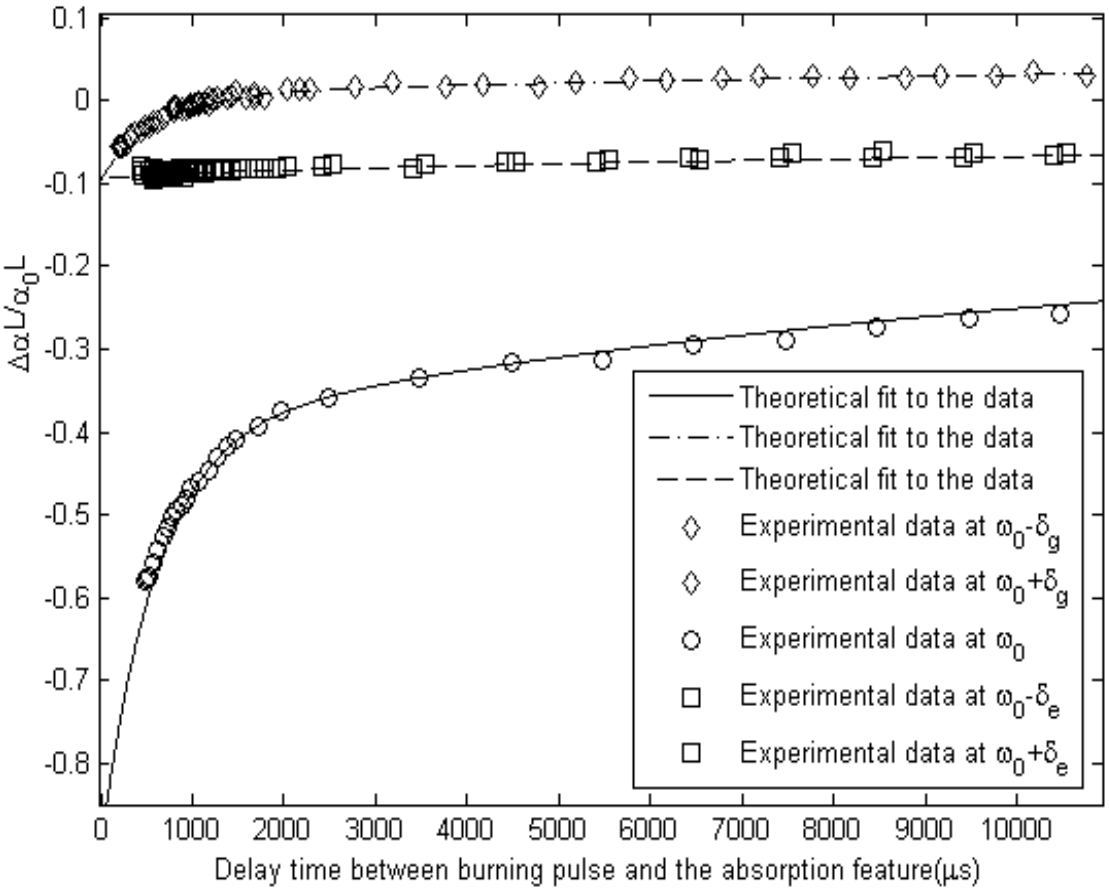

Figure 41: Experimental measurements of absorption change at a sample temperature of $4 \pm 0.5K$. Theoretical results (lines) are obtained using equations (4.37 and 4.40 - 4.43).

Now, we compare the experimental data set with the theoretical results, and the particular values of unknown parameters are obtained. But before we proceed to that comparison, we first define the new variables $\beta = \frac{\mu_u^2}{\mu_u^2 + \mu_a^2}, r_{21} = \frac{R_2}{R_1}, r_{43} = \frac{R_4}{R_3},$ and $r_{65} = \frac{R_6}{R_5}$. These parameters, combined with R_1, make up the five independent variables. The experimental data set is fitted to the theoretical results (4.37, 4.40, 4.41, 4.42, and 4.43) with the assumption that direct population relaxations between the hyperfine levels are ignored.

The unknown parameters, $\beta, R_1, r_{21}, r_{43}, \text{and } r_{65}$, in the theoretical results (4.37, 4.40, 4.41, 4.42, and 4.43) are varied until a match with the experimental results is obtained. Note that the variation in the excitation parameter, β, changes the relative sizes of the absorption features at ω_0, $\omega_0 \pm \delta_e$, and $\omega_0 \pm \delta_g$ and at initial time $t = 0$. Therefore, in the initial run, only the excitation parameter is varied, and the other four relaxation parameters are set to zero. This run gives an initial value for the excitation parameter. Later, other relaxation parameters are varied. It was noticed that each parameter has a strong contribution at different times. Note that, initially, r_{21} has a higher contribution than that of the other relaxation parameters. Thus, the systematic variation of these relaxation parameters with trial and error provides the best fits to the experimental data. The best fit, lines in Figure 41, to the experimental data are obtained with $\beta = 0.155 \pm 0.015$, $R_1 = 0.21 \pm 0.01$, $r_{21} = 0.2 \pm 0.05$, $r_{43} = 0.7 \pm 0.2$, and $r_{65} = 0.7 \pm 0.2$. Note that there is a significant error in the values of r_{43} and r_{65}. The error in these two parameters has no significant effect on other parameters, especially the excitation parameter β.

These results show about 75% of the total population decay through the intermediate levels. The population is essentially randomized in the manifold of hyperfine levels of the intermediate electronic state. In the case of direct relaxation, 84% of the population follows the direct relaxation path and decays back to the same hyperfine level. Note that the value of the excitation ratio, $\frac{\beta}{1-\beta}$, agrees very well with the ratio of relaxation value, r_{21}, for the direct relaxation, and it is also consistent with the results plotted in Figure 20. Recently, the excitation parameter was measured by another group

using a different approach, and a smaller value for the cross-transition ratio was obtained [(56), (57)]. The difference in these values may be due to some misalignment of the direction of the magnetic field. Another possibility may be that the other group might have measured the value of the cross-transition ratio for ions at site 2 instead of ions at sites 4 and 6. Note that the ions at site 2 have a lower cross-transition ratio than the ions at sites 4 and 6. Another interesting result is the one that shows that 75% of the total population decays through the intermediate levels. The value we obtained is significantly different than the value, 54%, obtained without the application of the external magnetic field [(71)]. The next step would be to study how the excitation and relaxation parameters change with the sample temperature.

Experimental Results for Excitation and Relaxation Parameters at 5K

In this experiment, the effect of the sample temperature on the previously measured excitation and relaxation parameters is studied. The full solution of the rate equations is used, as the relaxation time between hyperfine levels is comparable to the decay time, T_3, of the intermediate level to the ground state. In the experiment, the external magnetic field value, 400 Gauss, and other experimental parameters were similar to the previous case. The difference here is the sample temperature, which is increased from $4 \pm 0.5K$ to $5 \pm 0.5K$. Again, the experimental data is analyzed using unknowns in equations (4.37, 4.40, 4.41, 4.42, and 4.43) with the relaxation rate between hyperfine levels set to the experimentally measured value of $\frac{1}{12}\text{ms}^{-1}$(cf. population lifetimes of hyperfine levels in the earlier section). Similar approach as outlined in the previous

section is adopted to compare the experimental data with the theoretical results in (4.37, 4.40, 4.41, 4.42, and 4.43). The experimental (diamonds, circles, and squares) and theoretical (solid, dashed, and dot-dashed lines) results are shown in Figure 42.

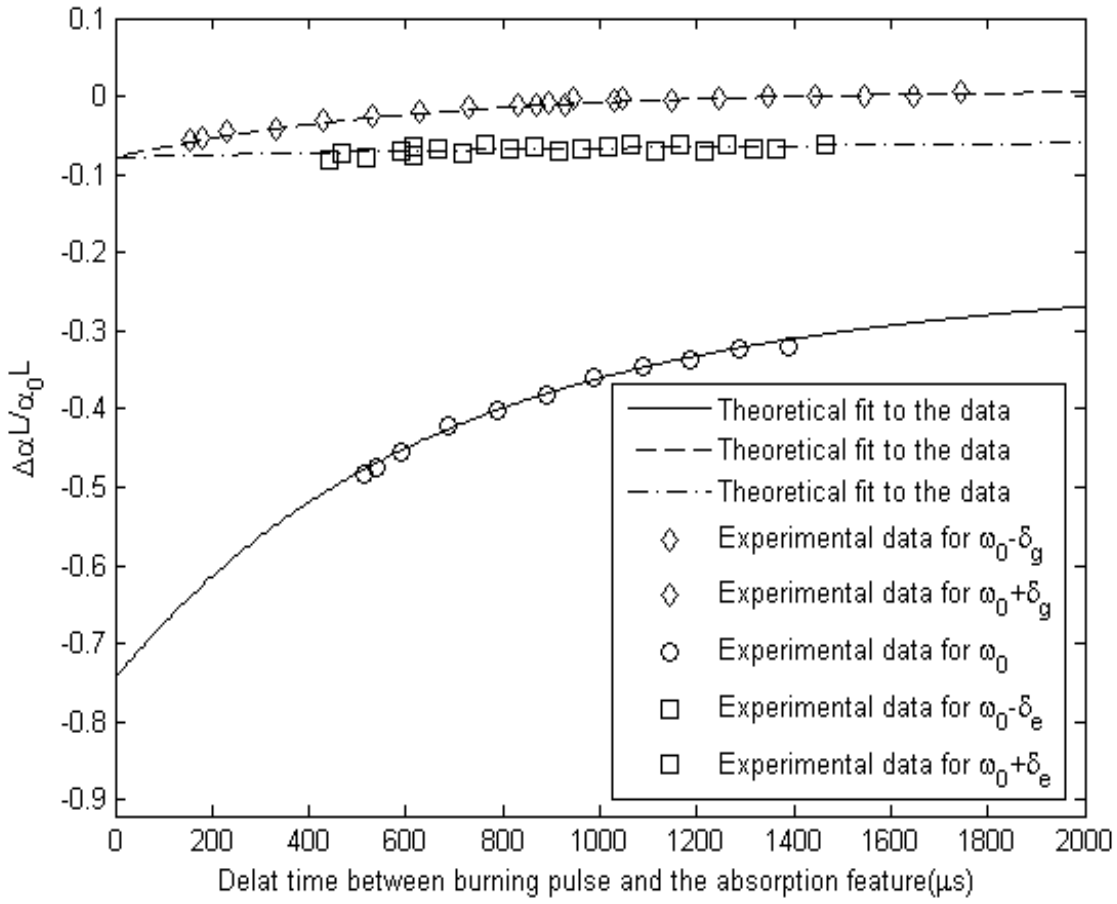

Figure 42: High sample temperature, $5 \pm 0.5K$, time-dependent measurements for spectral hole burning experiment, points, and the theoretical results obtained using equations (4.37, 4.40, 4.41, 4.42, and 4.43). The magnetic field orientation was $\theta_B = -15^o \pm 1^o$, that gave the highest cross-transition ratio for ions at sites 4 and 6.

The theoretical results (lines) are matched by trial and error to the experimental data (diamonds, circles, and squares in Figure 42) with the process outlined previously. The match provides the values for excitation and relaxation parameters as $\beta = 0.13 \pm 0.02$, $R_1 = 0.21 \pm 0.01$, $r_{21} = 0.2 \pm 0.05$, $r_{43} = 0.7 \pm 0.2$, and $r_{65} = 0.7 \pm 0.2$. The excitation parameter

obtained here falls within the error bars of the previous results. Hence, it can be said that there is no significant change in the excitation parameter as expected. Note again that there is a significant error in the values of r_{43} and r_{65}. Again, the error in these relaxation parameters has no significant effect on the other parameters, especially the excitation parameter β. These results again show that 75% of the total population decays through the intermediate levels. Again, it shows that the population is randomized in the manifold of the hyperfine levels of the intermediate electronic state. Again, for direct relaxation, 84% of the population decays back to the same level following the direct relaxation path. This concludes the study of the medium for excitation and relaxation dynamics. The next step would be to experimentally explore the hyperfine coherence time for this medium (Tm^{3+}:YAG).

Experiments to Explore the Hyperfine Coherence Time

In the previous experimental data, it was shown that dipole strength for cross-transition is about 0.45 times the dipole strength for direct transition, as $\beta = 0.155$. As such it makes an ideal choice for tailoring a 3-level system from Tm^{3+}:YAG for quantum computing applications [(73), (74), (75)].

Now the hyperfine coherence time is explored to optimize the 3-level system for quantum computing applications. This study will allow us to select the best orientation to store the qubit in the hyperfine levels. In this study, first, the coherence between hyperfine levels is created using optical or RF pulses. Then, the coherence is probed at different times. These time-dependent measurements are used to measure the coherence

time. There are generally two different methods used to measure the hyperfine coherence time. One method involves a combination of optical and radio frequency pulses [(76), (77), (78)] while the other method uses just optical pulses [(79), (23)].

The method used in this dissertation to measure coherence time involves only optical pulses. In the case of all optical pulses, the simplest scheme involves three optical pulses where the first two optical pulses create coherence between hyperfine levels, and the third pulse probes the coherence [(79)]. This scheme was successfully implemented in the atomic-Yb vapor [(80)]. However, this scheme fails to create perfect rephasing if there is inhomogeneity in the hyperfine levels as was seen in equation (2.34). The medium considered here is Tm^{3+}:YAG with the magnetic field applied along the direction giving the highest cross-transition ratio for ions at sites 4 and 6.

In the first experiment, a pulse sequence involving three optical pulses with optimized pulse areas, $\theta_1 = 0.5\pi, \theta_2 = \pi, \text{and}\, \theta_3 = \pi$ was implemented as shown in Figure 43. In this case, we were unable to observe an echo, suggesting that there is enough inhomogeneity in the hyperfine levels that it prevented any rephasing at a later time as was discussed in equation (2.25).

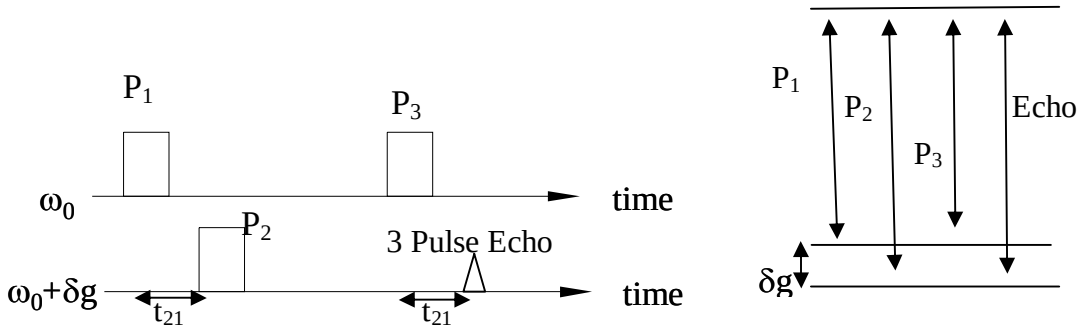

Figure 43: Three pulse sequence for hyperfine coherence time measurements.

To circumvent this problem, we need to use more than three optical pulses as suggested in the discussion of Chapter 2 following equation (2.35). This method was successfully implemented recently in another rare-earth-doped crystal containing Eu^{3+} [(23)]. We repeated the experiment using six optical pulses with the optimized pulse areas $\theta_1 = 0.5\pi$, $\theta_2 = \pi$, $\theta_3 = \pi$, $\theta_4 = \pi$, $\theta_5 = \pi$, and $\theta_6 = \pi$ with all pulses propagating collinearly as described in Chapter 2. These six pulse sequence produced an echo signal at the rephasing time. The decay of this rephased signal suggested a single decay on the order of the optical dephasing time. But the experiment was inconclusive in establishing whether the observed echo was a 6-pulse echo or a 3-pulse optical echo from pulses 1, 3, and 5, as the rephasing time is the same for both rephased signals.

The ambiguity in the measurement arises because, in the case of six collinear optical pulses, the spatial and the temporal location of the 6-pulse echo and the 3-pulse echo is the same. One technique to spatially isolate two signals is to choose propagation directions of six pulses such that two rephased signals are spatially isolated. Note from the results in equation (2.35) that the rephased signal from the six pulse sequence will propagate in the same direction as the propagation direction of the second pulse in the 6-pulse echo sequence with the other pulses in the sequence propagating collinearly in another direction. This scheme thus makes unwanted rephased signals, especially 3-pulse echo from P_1, P_3, and P_5, spatially isolated from the desired 6-pulse echo signal.

We did not implement the technique involving non-collinear six pulses in the lab. This should be the next step for the exploration of the hyperfine coherence time. However, we implemented another technique which is described in the next section.

Excitation with Temporally Overlapped Bi-Frequency Pulses

The method implemented in the experiment to explore the coherence in the hyperfine levels involves two bi-frequency pulses. This technique has been successfully implemented in Tm^{3+}:YAG to measure the hyperfine coherence time [(26)]. In this method, two bi-frequency pulses separated in time with each pulse satisfying the two photon resonance condition are used to create a Raman echo as explained in Chapter 2. The two main advantages with this set-up are:

1. The Raman echo can be isolated from other unwanted signals, i.e., 2-pulse echo, by the appropriate choice of the frequency of each pulse in the Raman Echo sequence as shown in Figure 44.
2. It has the ability to drive transitions in a system that has a low cross-transition probability [(25)].

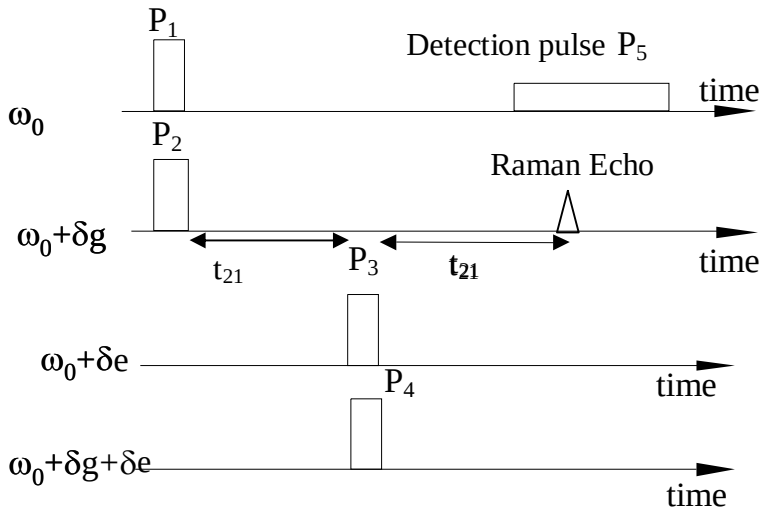

Figure 44: Sequence with two bi-frequency pulses used to study hyperfine coherence in the medium and for hyperfine coherence time measurements.

The complete pulse sequence for the experiment is shown in Figure 44, and the experimental set-up is shown in Figure 15. The optical signal is detected as a beat note using a detection pulse as given in equation (2.37). To avoid the frequency dependent shift in the position of each optical pulse, each AOM in the set-up was used in a double pass configuration. The output beams from AOMs were coupled to a single mode optical fiber, and the beam was focused to a 100 μm spot in the crystal. The polarization of the beam was adjusted so that the optical field is only addressing ions at sites 2, 4, and 6 as discussed earlier. The sample was cooled to 2K by pumping the LHe in a vapor-cooled cryostat. The magnetic field was aligned along $\theta_B = -15^o \pm 1^o$, and its strength was fixed at 200 Gauss.

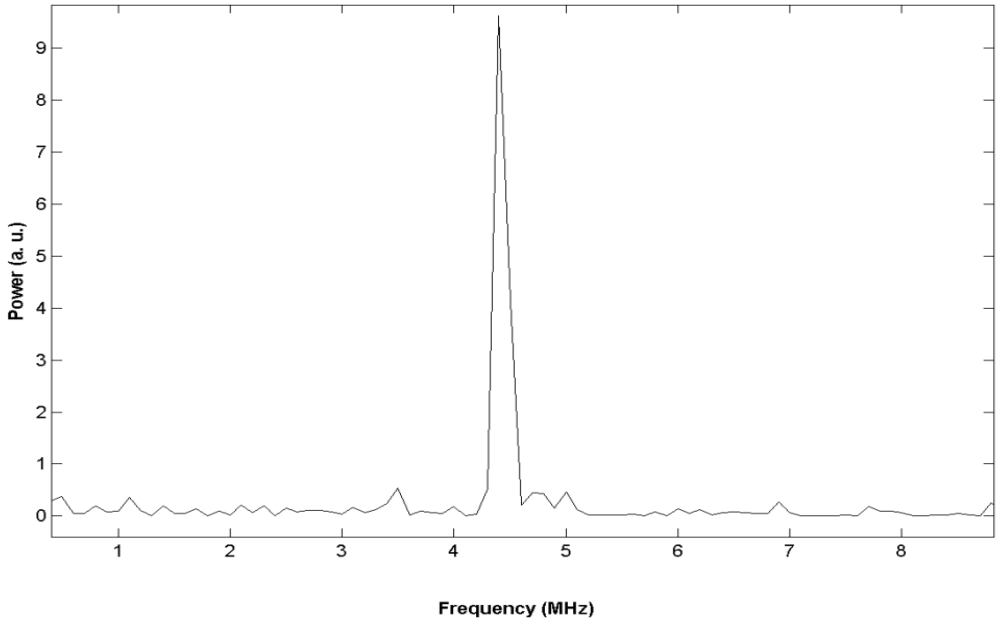

Figure 45: Fast Fourier transform (FFT) of an experimentally-obtained beat signal. The signal was obtained with two bi-frequency pulses using the pulse sequence given in Figure 44.

The resultant beat signal was detected with a 50 MHz detector. In the experiment, the frequency of each pulse was adjusted, as shown in Figure 44, and all the unwanted signals at the Raman echo location were avoided. The two bi-frequency pulses were 5 μs long and the Rabi frequency was 640kHz. The detection pulse was considerably weaker with a 20kHz Rabi frequency and 10μs duration.

The amplitude of the FFT signal of the beat signal is plotted in Figure 45 for 5MHz hyperfine splitting in the ground state. The decay of this beat amplitude is shown in Figure 46, which gives a hyperfine coherence time of $(68 \pm 6)\mu s$ for the least square fit to the experimental data (circles). This value for the hyperfine coherence time is about the same as the optical coherence time [(29)]. This is encouraging for qubit storage in the

hyperfine levels with the optical pulses as required for “all optical” quantum computing schemes.

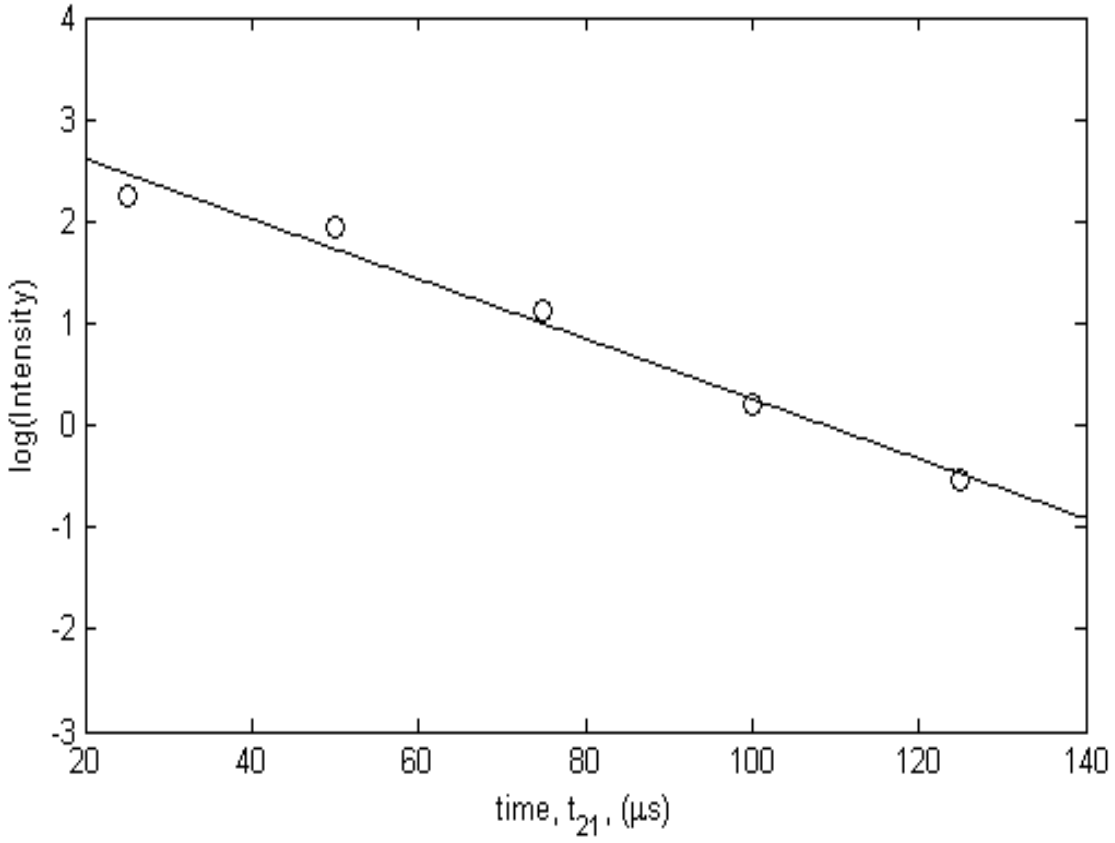

Figure 46: Decay of a Raman echo obtained from a Raman echo using two bi-frequency optical pulses as given in Figure 44. The least square fit (solid line) to the experimental data (circles) was used to obtain the hyperfine coherence time.

In order to achieve longer storage time in hyperfine levels for Tm^{3+}:YAG, more experimental explorations are needed to figure out the orientation of the magnetic field that can give a longer hyperfine coherence time. Note that in Figure 46, we did not have error bars on the data. The reason, for not including the bars, is the lack of the data for each point. In this experiment, the fluctuations, due to the vibrations from the mechanical pump directly connected with the cryostat, in the amplitude of the signal resulted in a

very low signal to noise ratio. It was meaningless to include the error bars with the insufficient data set for each point. Therefore, this experiment should be repeated with the apparatus that is well isolated from the external vibrations. In the next section, one of our explorations for the hyperfine coherence for another orientation of the magnetic field is presented. This exploration involves using a coherent Raman heterodyne technique.

Observation of a Coherent Raman Beat Signal

The coherent Raman beats (CRBs) were first observed experimentally in molecular vapors [(20)]. The CRBs were later also observed in the rare-earth, Pr, doped crystal [(21)]. Later, the coherent Raman beats were used to study the relative oscillator strengths of optical transitions in the rare-earth ions [(81)]. Apart from the detection of CRBs with all optical pulses, another method used a combination of optical and radio frequency pulses to detect the coherent Raman beats [(76)]. Later, the CRBs were extensively used to study rare-earth ions, Pr, Eu, and Tm doped crystals [(82), (83), (84), (85), (78), (86), (18), (87), (88), (89)]. In the current scheme, we used all optical pulses and studied the material properties of Tm^{3+}:YAG. In a recent study of Tm^{3+}:YAG, the CRBs have been observed [(89)]. Our aims in this experiment were to use the CRBs and estimate the coherence time and also to identify the ions at different sites contributing to the CRBs.

Experiment: The same sample of 0.1% atm. thulium-doped in YAG was used. The sample was vapor-cooled to 4K with a Janis cryostat system, and a static magnetic field was provided with the home-made Helmholtz coils. The New Focus laser at

793.380nm was amplified, and the frequency was stabilized with the spectral hole locking technique [(51)]. The basic experimental set-up is shown in Figure 15. In this experiment, the sample is aligned such that the cross-transition ratio is the highest for ions at sites 4 and 6, i.e., $\theta_B = 125^o \pm 1^o$, where the splitting for ions at each site is shown in Figure 31. The pulse sequence used and the energy levels addressed during the experiment are shown in Figure 47.

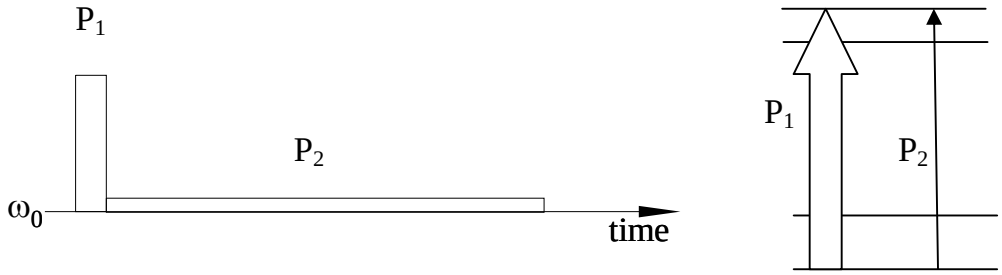

Figure 47: Pulse sequence applied to the medium for observing the coherent Raman beats in Tm:YAG.

In the experiment, a strong pulse of 1MHz Rabi frequency and 1μs length was used to create the coherence in the 4-level thulium with the hyperfine levels obtained with the external magnetic field. A second very weak optical pulse of 200kHz Rabi frequency and 100 μs in length was used to probe the coherence as shown in equation (2.24).

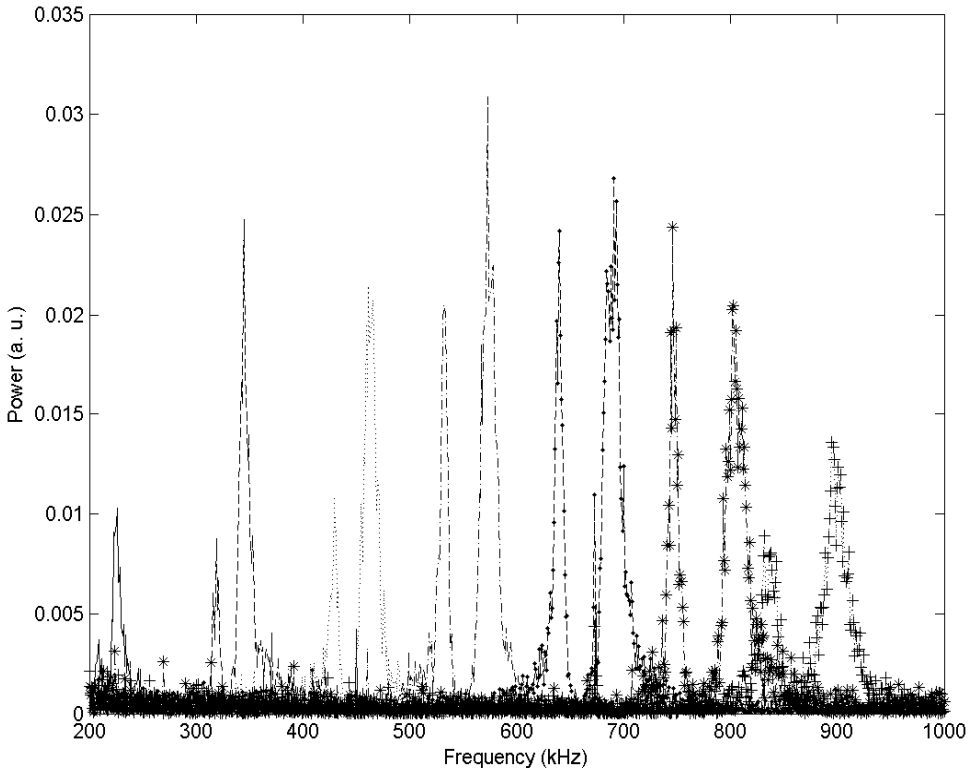

Figure 48: Experimental data for the coherent Raman signal observed at different magnetic fields from ions at sites 4 and 6. Each trace represents the Fourier transform of a beat signal at a different magnetic field.

Data were collected for various values of the magnetic fields, and the amplitude of the FFT signal of the beat signal is shown in Figure 48. Data from the beat signal were used to obtain the hyperfine splittings. In the FFT signal of the beat signal (Figure 48), there are two peaks for each value of the magnetic field. The second signal is comparatively weak, and it does not seem to correspond to any value of splitting for ions at different sites in the Tm^{3+}:YAG crystal. However, if we assume that it is due to a misalignment of the magnetic field, then this is only possible if the magnetic field is not

in the (1-10) plane and is tilted a few degrees from this plane. In the current experimental set-up, a misalignment of the magnetic field by a few degrees is quite possible.

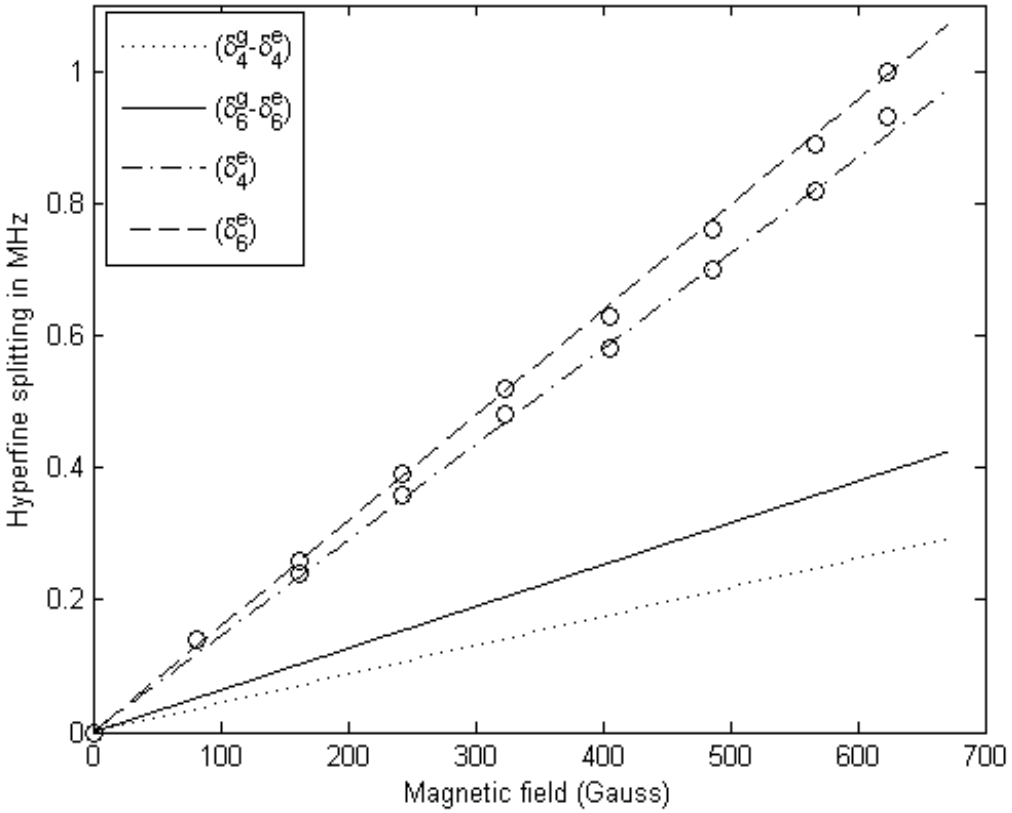

Figure 49: Experimental data (circles) for hyperfine splitting as obtained using coherent Raman beat with $\theta_B = 125^o \pm 1^o$. Theoretical results are represented by lines and are obtained using $\theta_B = 125^o$ and tilt angle $\theta_{tB} = 5^o$ in equations (4.11-4.12). Experimental data give the hyperfine splittings for the excited state as $(15.70 \pm 0.20)^{MHz}/_{Tesla}$ for ions at site 6 and $(14.60 \pm 0.15)^{MHz}/_{Tesla}$ for ions at site 4.

Now, we assume the misalignment in the magnetic field and plot the theoretical results for the hyperfine splittings for ions at sites 4 and 6. The results for the hyperfine splittings (circles) obtained using CRB data match with the theoretical results (dotted, solid, dashed, and dot-dashed) for hyperfine splittings for a 5^o misalignment in the

orientation of the magnetic field, as can be seen from Figure 49. Therefore, each peak in the FFT signal of the CRB data corresponds to ions at two different sites in the crystal. The results in Figure 49 also show that each peak in the FFT signal of the CRB data corresponds to the value of the hyperfine splittings for the excited state manifold. Note that, the experimental value for the hyperfine splitting obtained here agrees very well with the hyperfine splitting in the excited state manifold obtained with the spectral hole data. However, in the spectral hole data, the resolution was not high enough to observe the hyperfine splittings from ions at two different sites in the crystal. In other words, we were unable to resolve the 5^o misalignment in the orientation of the magnetic field with the spectral hole burning data for $\theta_B = 125^o \pm 1^0$.

Note the strength of each signal in Figure 48. The strength of each signal is not uniform for different values of the hyperfine splittings. Now, we plot the strength of the signal from one of the two sites observed for each value of the strength of the magnetic field. The data for the strength of each signal for the corresponding hyperfine splitting is shown as a circle in Figure 50. The non-uniformity in the strength of the FFT signal of the CRB signals can be explained by taking into account the finite duration of the strong excitation pulse (pulse 1). The pulse 1 has a 1MHz bandwidth and its Fourier transform is a “sinc” function with the nulls located 1MHz apart. The solid line in Figure 50 shows the theoretical results for the strength of the FFT of the beat signal and is obtained by taking into account the bandwidth of the excitation pulse. The theoretical results (solid line) for the strength of FFT of the beat signal agree very well with the experimental

results (circles) for the strength of the FFT signal of the beat signal as can be seen in Figure 50.

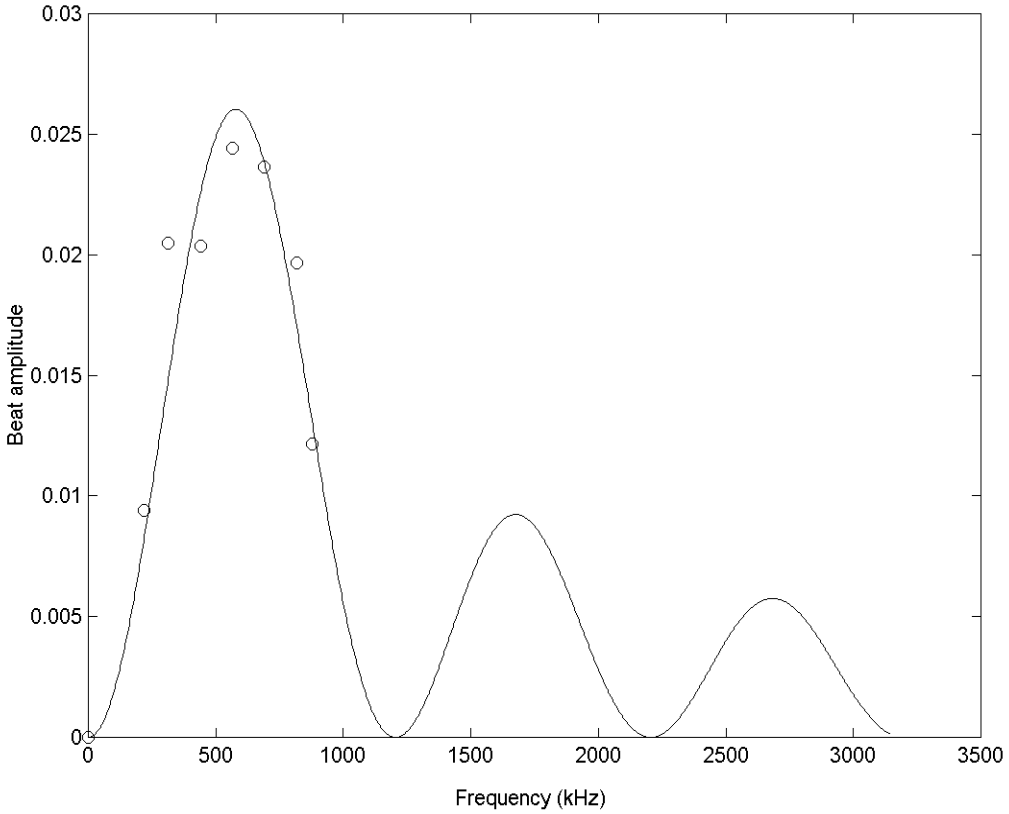

Figure 50: Experimental data (circles) and theoretical results (solid line) for the amplitude of the FFT signal in Figure 48. The plot shows the dependence of the signal amplitude on the separation of hyperfine energy levels in a 3-level system being excited with a 1μs long π-pulse. The probe pulse was 100μs long and about 50 times weaker than the excitation pulse.

The coherent Raman beat together with the results obtained using equation (2.23) show that, not only the cross-transition ratio is non-zero, but there is also a coherence created by pulse 1 in the hyperfine levels of the excited state manifold. The estimate from the data also shows that the coherence time between hyperfine levels is > 20μs.

The experiment was not successful in observing any beat signal from the hyperfine levels of the ground state manifold. There are a few reasons that may be preventing the observation of any beat signal from the hyperfine levels in the ground state manifold. One is the inhomogeneity in the hyperfine levels, which is much higher in the hyperfine levels of the ground state manifold than in the hyperfine levels of the excited state manifold. Another reason is that, in order to observe a coherent Raman beat signal from the hyperfine levels of the ground state manifold, the excitation pulse will be exciting all four levels instead of only three levels. This can result in the cancellation of a coherent Raman beat signal, as was the case in Europium-doped yttrium orthosilicate [(90)].

Conclusions

First, magnetic anisotropy in Tm^{3+}:YAG was experimentally measured. The anisotropy measurements were used to measure the cross-transition ratio of ions at various sites in the crystal. These measurements were also used to map the hyperfine splittings for thulium ions at different sites in the crystal. The selection of various sites in the crystal was achieved by controlling the polarization of the interacting optical field. The polarization control was used to identify and distinguish the contributions in the hole burning spectrum from thulium ions at different sites in the crystal.

The orientations of the magnetic field that give the highest cross-transition ratios for ions at different sites in the crystal were identified. These orientations were further selected to optimize other parameters such as population lifetime and the coherence time of the hyperfine levels. The spectral hole burning technique was used to measure the

population lifetime for hyperfine levels. The population lifetimes of hyperfine levels, for different sites in the crystal and for different orientations of the magnetic field, were measured. The population lifetime of hyperfine levels for ions at site 2 in the crystal was measured to be more than a second at 4K. The cross-transition ratio of ions at site 2 was very small for this orientation of the magnetic field. However, another orientation of the magnetic field gave us more than 100 ms population lifetime of the hyperfine levels for ions at sites 4 and 6. The cross-transition ratio of ions at sites 4 and 6 was reasonable, about 0.155, for this particular orientation of the magnetic field.

A theoretical model was developed to study the relaxation dynamics in the system. This theoretical model in conjunction with the spectral hole data was used to experimentally measure the excitation and relaxation parameters for Tm^{3+}:YAG. This technique directly measured the cross-transition ratio for one orientation of the magnetic field. The cross-transition ratio results demonstrated that there is a possibility of a 3-level system that could be used for qubit storage and manipulation. The theoretical model developed here will be used in Chapter 6 to investigate the material for an ensemble selection for qubit preparation.

Later, the hyperfine coherence times for the orientations of the magnetic field, giving the highest cross-transition ratios, were experimentally studied. This study, to probe the hyperfine coherence time, includes the use of the photon echo and the coherent Raman beat techniques. These studies revealed that the hyperfine coherence time (> 20μs) is about the same in magnitude as the optical coherence time (35μs). It is likely that the hyperfine coherence time is limited by the spin-spin interaction of the host ions,

especially those of the aluminum. Aluminum has a strong magnetic moment [(91)] and can induce random flip-flops on the thulium spin states. These interactions can shorten the hyperfine coherence time for certain orientations. Therefore, there may be some other orientations in the crystal that might have longer hyperfine coherence times. The point is reinforced when we look at the rare-earth ions like Eu^{3+} and Pr^{3+}, which exhibit extremely long optical and hyperfine coherence times. These materials are usually doped into materials, such as Y_2SiO_5, which have weak magnetic moments [(92), (93), (94), (95), (27), (28), (96)]. This led Wang [(29)] and co-workers to investigate the 0.1% atm. Tm^{3+} :$Y_2Si_2O_7$ in which the host ($Y_2Si_2O_7$) has a low nuclear magnetic moment. In this study, an optical coherence time of 23μs, at 2K, was obtained, which is lower than that of Tm^{3+}:YAG, 70μs [(29)], at the same temperature. This study also showed that the coherence time was strongly temperature dependent, and it was limited due to the short fluorescence lifetime, 68μs [(97)]. The hyperfine coherence time was not measured in the study [(97)].

CHAPTER FIVE

QUANTUM COMPUTING: THEORY FOR SINGLE QUBIT OPERATIONS

Introduction

In quantum computing, the information is stored in a qubit, which is analogous to the 'bit' in classical computing. A qubit can be represented by a 2-level quantum mechanical system. The quantum algorithms are usually implemented by applying the unitary operations on these qubits. These unitary transformations can be constructed by applying a specific sequence of pulses using optical or magnetic fields [(98)]. One such scheme, known as the geometric quantum computation, suggests using the geometric phase rotations to construct the unitary transformations and, hence, quantum logic gates [(99)]. This scheme presents an attractive option because the geometric phase depends on the geometric path and is independent of the details of the path [(100)]. In this scheme, relative phases of the optical pulses are used to construct the geometric phase gates. Extensive theoretical treatments exist for the implementation of the geometric phase rotations to construct the unitary operations in NMR [(101), (102)], trapped ions [(103)], neutral ions [(104)], optical systems [(105)], and superconducting nanocircuits [(106)]. Experimental demonstrations to construct the quantum logic gate using the geometric phase rotations have been successful in NMR systems [(99)], trapped ions [(107)], superconducting nanocircuits [(106)], and rare-earth ions doped crystals [(108)].

In this chapter, relevant theory for the experimental demonstration of a single qubit operation in rare-earth-doped crystals is presented. We follow the derivation given

in the reference [(98)]. In the first part of the chapter, we use a uniform intensity beam and present the method to realize the geometric phase gate in rare-earth-doped crystals. In the later part, we investigate the effect of non-uniformity in the laser beam on the geometric gate operations for single qubit rotations. These are relevant investigations because the intensity of the laser beams is usually non-uniform (Gaussian spatial profile). This spatial non-uniformity in the intensity of the laser beam results in a non-uniform interaction with the ions at different spatial locations in the rare-earth-doped crystal. The non-uniformity in the beam intensity cannot be solved completely by using a spatial beam shaper [(24)] or by expanding the beam size and using only the uniform core of the beam. This problem was not addressed in the earlier demonstration of one of the two rotations of the Bloch vector using the geometric phase [(108)**,** (109)**].** In these demonstrations, the effect of these rotations as a phase change on the echo was measured. This measurement alone is not sufficient to analyze the effect of non-uniform interaction. We will see later that non-uniform interaction contribute to the degradation in the operation fidelity. Here, the operation fidelity is the measure of the difference between actual state of the qubit and the desired state of the qubit after the quantum operation. In the end of the chapter, we analyze the fidelity of the quantum operation for uniform and non-uniform excitations.

Bloch Sphere and Pure State

In Bloch vector formalism, the qubit state on the Bloch sphere is represented by the position of the Bloch vector on the Bloch sphere. This can be seen by revisiting the 2-

level system as shown in Figure 51, where the ground state $|0\rangle = \begin{pmatrix} 1 \\ 0 \end{pmatrix}$ and the excited state $|1\rangle = \begin{pmatrix} 0 \\ 1 \end{pmatrix}$ are defined in a z-basis.

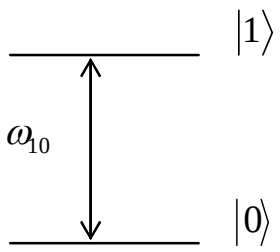

Figure 51: A 2 –Level system

Now if we imagine a qubit is in a state $|\psi\rangle$, then the position of the qubit on the Bloch sphere will be given by the position vector as

$$\hat{r}_{\psi} = (x_{\psi}, y_{\psi}, z_{\psi}) = \left(\langle\psi|\hat{X}|\psi\rangle, \langle\psi|\hat{Y}|\psi\rangle, \langle\psi|\hat{Z}|\psi\rangle\right) \quad (5.1),$$

where $\hat{X}$, $\hat{Y}$ and $\hat{Z}$ are Pauli operators and are defined as

$$\hat{X} = \begin{pmatrix} 0 & 1 \\ 1 & 0 \end{pmatrix} = |1\rangle\langle 0| + |0\rangle\langle 1|, \; \hat{Y} = \begin{pmatrix} 0 & i \\ -i & 0 \end{pmatrix} = -i\left(|1\rangle\langle 0| - |0\rangle\langle 1|\right), \text{ and}$$

$$\hat{Z} = \begin{pmatrix} -1 & 0 \\ 0 & 1 \end{pmatrix} = |1\rangle\langle 1| - |0\rangle\langle 0|.$$

These Pauli operators can be thought of as different operators for a qubit. These operators can map any arbitrary state of a qubit on a Bloch sphere. In order to get a one-to-one mapping of a qubit state on a Bloch sphere, we consider an arbitrary qubit state as

$$|\psi\rangle = \left(\langle 0|\psi\rangle\right)|0\rangle + \left(\langle 1|\psi\rangle\right)|1\rangle \quad (5.2),$$

where $\left|\left(\langle 0|\psi\rangle\right)\right|^2$ and $\left|\left(\langle 1|\psi\rangle\right)\right|^2$ are the probabilities of finding the atom/ion in the ground, $|0\rangle$, and the excited, $|1\rangle$, states, respectively. A point on the Bloch sphere can, in general, be specified by a position vector defined as

$$\vec{r}_{\psi} = \left(x_{\psi}, y_{\psi}, z_{\psi}\right) = \left(\cos(\varphi)\sin(\theta), \sin(\varphi)\sin(\theta), \cos(\theta)\right) \tag{5.2a}.$$

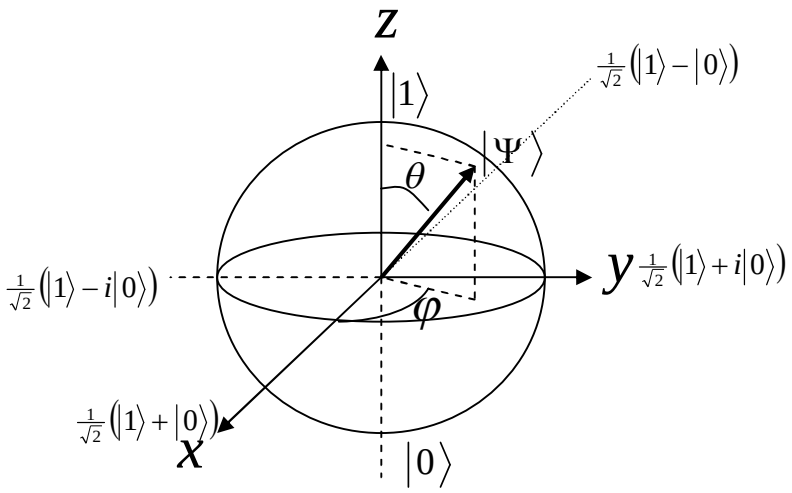

Figure 52: The Bloch sphere with different states of a 2-level system mapped on the sphere.

One can use equation (5.1) to find the qubit state that corresponds to the Bloch vector in equation (5.2a). Using equation (5.1) and (5.2), one finds that

$$\left.\begin{aligned} &\left(\langle 0|\psi\rangle\right)\left(\langle 1|\psi\rangle\right)^* + \left(\langle 0|\psi\rangle\right)^*\left(\langle 1|\psi\rangle\right) = \cos(\varphi)\sin(\theta) \\ &-i\left(\langle 0|\psi\rangle\right)\left(\langle 1|\psi\rangle\right)^* + i\left(\langle 0|\psi\rangle\right)^*\left(\langle 1|\psi\rangle\right) = \sin(\varphi)\sin(\theta) \\ &-\left(\langle 0|\psi\rangle\right)\left(\langle 0|\psi\rangle\right)^* + \left(\langle 1|\psi\rangle\right)^*\left(\langle 1|\psi\rangle\right) = \cos(\theta) \end{aligned}\right\} \tag{5.3}.$$

Solving the above system of equations, one obtains the following values

$$\left(\langle 0|\psi\rangle\right) = e^{i\varphi}\sin(\theta/2),\ \left(\langle 1|\psi\rangle\right) = \cos(\theta/2).$$

Thus, the qubit state would be

$$|\psi\rangle = \sin\left(\theta/2\right) e^{i\varphi} |0\rangle + \cos\left(\theta/2\right)|1\rangle \quad (5.4).$$

The result in equation (5.4) shows that any arbitrary state of a 2-level system can be mapped on a Bloch sphere. Thus, each point on a Bloch sphere can be thought of as a state of a qubit which is analogous to mapping the polarization on the Poincare's sphere. The idea of mapping a polarization of light on the sphere was conceived by Henri Poincare in about 1892.

Bloch Sphere and Mixed State

In the previous section, the results for mapping a pure state of a 2-level system onto the Bloch sphere were presented. However, in physical systems, the state of the system is a mixed state rather a pure state. We follow the density matrix formalism and present results for mapping a mixed state onto the Bloch sphere.

Density Matrix Formalism

The density matrix formalism is useful in studying the system in a mixed state. First, we define the density matrix in terms of the Eigen-states of the system as

$$\hat{\rho} = \sum_{i,j} p_{ij} |\psi_i\rangle\langle\psi_j| \quad (5.5),$$

where p_{ij} is the probability of finding the system in a particular state, and $|\psi_i\rangle$ is the state of the qubit. Note that the expectation value of an operator is defined as

$$\langle\hat{\theta}\rangle = Trace\left(\hat{\rho}\hat{\theta}\right) \quad (5.6).$$

Therefore, using equation (5.6), position operators will have the following expectation values:

$$\left.\begin{aligned} \left\langle \hat{X} \right\rangle &= Trace\ \left(\hat{\rho}\hat{X}\right) = r_x \\ \left\langle \hat{Y} \right\rangle &= Trace\ \left(\hat{\rho}\hat{Y}\right) = r_y \\ \left\langle \hat{Z} \right\rangle &= Trace\ \left(\hat{\rho}\hat{Z}\right) = r_z \end{aligned}\right\} \tag{5.7}.$$

Equation (5.1) can be modified for a mixed state/ensemble, and thus, the position of the Bloch vector on the Bloch sphere will be

$$\vec{r}_\rho = \left(Tr\ \left(\hat{\rho}\hat{X}\right), Tr\ \left(\hat{\rho}\hat{Y}\right), Tr\ \left(\hat{\rho}\hat{Z}\right)\right) \tag{5.8}.$$

The evolution of the density matrix in time can be obtained from the following equation

$$\frac{\partial}{\partial t}\hat{\rho} = -\frac{i}{\hbar}\left[\hat{\rho}, \hat{H}\right] \tag{5.9},$$

where $\hat{H}$ is the Hamiltonian of the system.

In order to show that any mixed state of a 2-level system can be mapped to the Bloch sphere, we first write the density matrix as

$$\hat{\rho} = \begin{pmatrix} \rho_{00} & \rho_{01} \\ \rho_{10} & \rho_{11} \end{pmatrix} = \rho_{11}|1\rangle\langle 1| + \rho_{10}|1\rangle\langle 0| + \rho_{01}|0\rangle\langle 1| + \rho_{00}|0\rangle\langle 0| \tag{5.10}.$$

Using equation (5.10) and the Pauli matrices, the expressions in equation (5.7) can be written as

$$\left.\begin{aligned} \left\langle \hat{X} \right\rangle &= Trace\ \left(\hat{\rho}\hat{X}\right) = r_x = \rho_{10} + \rho_{01} \\ \left\langle \hat{Y} \right\rangle &= Trace\ \left(\hat{\rho}\hat{Y}\right) = r_y = -i\left(\rho_{01} - \rho_{10}\right) \\ \left\langle \hat{Z} \right\rangle &= Trace\ \left(\hat{\rho}\hat{Z}\right) = r_z = \rho_{11} - \rho_{00} \end{aligned}\right\} \tag{5.11}.$$

To show that (r_x, r_y, r_z) can be mapped onto a unit sphere, we calculate the following:

$$r_x^2 + r_y^2 + r_z^2 = 4\rho_{01}\rho_{10} - 2\rho_{00}\rho_{11} + \rho_{11}^2 + \rho_{00}^2 = (Tr(\rho))^2 - 4\det(\rho) \quad (5.12).$$

Note $\det(\rho) \geq 0$ in the above expression, and write

$$\begin{aligned} &\tfrac{1}{4}\left((Tr\,(\rho))^2 - \left(r_x^{\,2} + r_y^{\,2} + r_z^{\,2}\right)\right) \geq 0 \\ &\Rightarrow \left(r_x^{\,2} + r_y^{\,2} + r_z^{\,2}\right) \leq (Tr\,(\rho))^2 \\ &\Rightarrow \left(r_x^{\,2} + r_y^{\,2} + r_z^{\,2}\right) \leq 1\,. \end{aligned}$$

Thus, we have a mixed state mapped onto a unit sphere. However, if $|r|^2 = 0$ then the state is maximally mixed, and the analogy of mapping a state on a unit sphere breaks down.

Again, we use equation (5.12) to find the degree to which a state is mixed, as described. First we rewrite equation (5.12) as

$$|r|^2 + 1 = 1 + 4\rho_{01}\rho_{10} - 2\rho_{00}\rho_{11} + \rho_{11}^2 + \rho_{00}^2.$$

Now we use the identity that $(Tr(\rho))^2 = 1$ and write

$$|r|^2 + 1 = (\rho_{11} + \rho_{00})^2 + 4\rho_{01}\rho_{10} - 2\rho_{00}\rho_{11} + \rho_{11}^2 + \rho_{00}^2.$$

After simplification and rearranging terms, we get $|r|^2 + 1 = 2Tr(\rho^2)$, which gives $Tr(\rho^2) = \dfrac{|r|^2 + 1}{2}$, and it describes the measure of a mixed state that will be 1 for a pure state and 0.5 for a maximally mixed state.

Evolution of the Bloch Vector of a 2-Level System

The basic theory dealing with the evolution of the Bloch vector of a 2-level system without any external interaction with the system is presented here. Consider the Hamiltonian, H_0, for a 2-level system as

$$\hat{H}_0 = \hbar\left(\omega_0 |0\rangle\langle 0| + \omega_1 |1\rangle\langle 1|\right) \tag{5.13}$$

It is useful to write this Hamiltonian in terms of the Pauli operators as $\hat{H}_0 = \hbar\left(\frac{\omega_1 - \omega_0}{2}\hat{Z} + \frac{\omega_1 + \omega_0}{2}\hat{I}\right)$. The last term in the expression can be ignored as it only causes global phase shift. Thus, the Hamiltonian for a freely evolving 2-level system will become

$$\hat{H}_0 = \hbar\frac{\omega_{10}}{2}\hat{Z} \tag{5.14}$$

where $\omega_{10} = \omega_1 - \omega_0$.

The task then is to find how Pauli operators, which are related to the components of the Bloch vectors, evolve under the Hamiltonian, H_0. Since any operator evolves as $\hat{O}(t) = e^{i\frac{\hat{H}_0}{\hbar}t}\hat{O}(0)e^{-i\frac{\hat{H}_0}{\hbar}t}$, the evolution of the Pauli matrices for a freely evolving system will yield the following expressions for these matrices [(98)]

$$\hat{X}(t) = \hat{X}(0)\cos(\omega_{10}t) - \hat{Y}(0)\sin(\omega_{10}t) \tag{5.15}$$

$$\hat{Y}(t) = -\hat{X}(0)\sin(\omega_{10}t) + \hat{Y}(0)\cos(\omega_{10}t) \tag{5.16}$$

$$\hat{Z}(t) = \hat{Z}(0) \tag{5.17}$$

This result shows that, without any external field applied to the 2-level system, the Bloch vector of the system will precess about the z-axis with a precession frequency of ω_{10}, known as the Larmor Precession first observed in NMR Systems [(110)].

Interaction with the Optical Field and Evolution of the Bloch Vector

In the previous section, the well-known formalism for Bloch vector evolution without any interaction with an external field was presented. We now discuss the interaction of a 2-level system with an external electric field, $\vec{E}$, that is resonant with two levels, $|0\rangle$ and $|1\rangle$. Now we ignore any decay processes in the medium and write the Hamiltonian for this system as $\hat{H} = \hat{H}_0 + \hat{H}_I$, where $\hat{H}_0$ is the Hamiltonian given in equation (5.14), and $\hat{H}_I$ is the interaction Hamiltonian given as $\hat{H}_I = -\hat{\vec{\mu}}.\vec{E}$, where $\hat{\vec{\mu}}$ is the transition dipole moment operator. In the $|0\rangle$ and $|1\rangle$ basis, it can be written as

$$\hat{\vec{\mu}} = \vec{\mu}_{01}|0\rangle\langle 1| + \vec{\mu}_{10}|1\rangle\langle 0| \qquad (5.18),$$

where $\vec{\mu}_{01} = \langle 0|\hat{\vec{\mu}}|1\rangle$, $\vec{\mu}_{10} = \langle 1|\hat{\vec{\mu}}|0\rangle$, $\vec{\mu}_{00} = \langle 0|\hat{\vec{\mu}}|0\rangle = 0$, and $\vec{\mu}_{11} = \langle 1|\hat{\vec{\mu}}|1\rangle = 0$.

Using equations (5.14) and (5.18), with the definition of the Pauli operator $\hat{X}$, and an expression for the optical field $\vec{E} = \vec{E}_0 \cos(\omega t + \varphi)$, for $t_1^- \le t \le t_1^+$, and zero elsewhere, one can write the Hamiltonian as

$$\left.\begin{aligned}\hat{H} &= \frac{\hbar}{2}\omega_{10}\hat{Z} - E_0\cos(\omega_l t+\varphi)\left(\mu|1\rangle\langle 0| + \mu^*|0\rangle\langle 1|\right)\\ \hat{H} &= \frac{\hbar}{2}\omega_{10}\hat{Z} - \mu E_0\cos(\omega_l t+\varphi)\hat{X}\end{aligned}\right\} \quad (5.19),$$

where ω_l is the frequency, φ is the phase, and E_0 is the amplitude of the applied optical field. Here we have assumed that the dipole is parallel to the applied field such that $\vec{\mu}\cdot\vec{E}_0 = \mu E_0$.

Now we choose a rotating frame and use the rotating wave approximation (RWA). Then the Hamiltonian, in equation (5.19), in the laser frame during the laser pulse can be written as

$$\hat{H}' = \hbar\left(\frac{\Delta}{2}\hat{Z} - \frac{\Omega_0}{2}\left(\hat{X}\cos(\varphi)+\hat{Y}\sin(\varphi)\right)\right) \quad (5.20),$$

where $\Delta = \omega_{10} - \omega_l$ is the detuning from the laser frequency and $\Omega_0 = \mu E_0/\hbar$ is the Rabi frequency.

The Hamiltonian in equation (5.20) in the z-basis can also be written as

$$\hat{H}' = -\frac{\hbar\Omega_0}{2}\begin{pmatrix}0 & e^{i\varphi}\\ e^{-i\varphi} & 0\end{pmatrix} \quad (5.21).$$

The choice of the laser frame and RWA allows us to write the Hamiltonian in an equation (5.20) which is independent of time. The evolution of the Bloch vector can be found by using the evolution operator $u(t\geq t_0) = Se^{-iS^{-1}\frac{H'}{\hbar}S(t-t_0)}S^{-1}$, where S diagonalizes the Hamiltonian in equation (5.21). We consider the case when the detuning during the pulse can be ignored, i.e., $(\Omega_0, \tau^{-1}) >> \Delta$, where τ is the pulse duration. The explicit

expression for the evolution matrix governing the evolution of the 2-level system just after the optical pulse will be

$$u(\theta,\varphi)=\begin{pmatrix}\cos\left(\frac{\theta}{2}\right) & i\sin\left(\frac{\theta}{2}\right)e^{i\varphi}\\ i\sin\left(\frac{\theta}{2}\right)e^{-i\varphi} & \cos\left(\frac{\theta}{2}\right)\end{pmatrix} \tag{5.22}$$

where φ is the phase, $\theta=\Omega_0\tau$ is the pulse area, and $\tau=\left(t_0^+-t_0^-\right)$ is the duration of the pulse being applied.

Therefore, the Pauli matrices after the application of an optical pulse will be

$$\hat{X}(\tau)=\left(\cos^2\left(\tfrac{\theta}{2}\right)+\sin^2\left(\tfrac{\theta}{2}\right)\cos(2\varphi)\right)\hat{X}(0)+\sin^2\left(\tfrac{\theta}{2}\right)\sin(2\varphi)\hat{Y}(0)+\sin(\theta)\sin(\varphi)\hat{Z}(0)$$

(5.23),

$$\hat{Y}(\tau)=\left(\cos^2\left(\tfrac{\theta}{2}\right)-\sin^2\left(\tfrac{\theta}{2}\right)\cos(2\varphi)\right)\hat{Y}(0)+\sin^2\left(\tfrac{\theta}{2}\right)\sin(2\varphi)\hat{X}(0)-\sin(\theta)\cos(\varphi)\hat{Z}(0)$$

(5.24),

$$\hat{Z}(\tau)=-\sin(\theta)\sin(\varphi)\hat{X}(0)-\sin(\theta)\cos(\varphi)\hat{Y}(0)+\cos(\theta)\hat{Z}(0) \tag{5.25}.$$

where $\theta=\Omega_0\tau$ is the area of the optical pulse and τ is the duration of the pulse as defined earlier. Note that the position of the Bloch vector on the Bloch sphere depends not only on the pulse area but also on the phase of the optical pulse. In geometric quantum computing schemes where the relative phase of the laser pulses is used, it is this phase that is being exploited to construct robust unitary transformations [(108)**,** (109)]. In the next section, we present the results showing the relations between components of the Bloch vector and coherent emission from the system.

Coherence in the Medium and Components of the Bloch Vector

The position of the Bloch vector on the Bloch sphere is detected using the coherent emission from the sample. In this section, a brief introduction is given that shows the relationship between the coherent emission from the system and the components of the Bloch vector. First, we use equation (5.6) and write the coherence in the medium as

$$\langle \hat{\mu} \rangle = Trace\ (\hat{\rho}\hat{\mu}) \tag{5.26},$$

where $\hat{\mu}$ is the transition dipole moment and is defined in Chapter 2.

The coherence in a 2-level system in the laser frame will be

$$\langle \hat{\mu} \rangle = \mu((\rho_{01} + \rho_{10})\cos(\omega_l t) + i(\rho_{01} - \rho_{10})\sin(\omega_l t)) \tag{5.27}.$$

Using the expression for the Pauli matrices and the expression for the ensemble averages in equations (5.7), one can write the coherence in the system as

$$\langle \hat{\mu} \rangle = \mu\left(\langle \hat{X} \rangle \cos(\omega_l t) - \langle \hat{Y} \rangle \sin(\omega_l t)\right) \tag{5.28}.$$

Thus the in-phase component of the coherent emission will give the x-component of the Bloch vector, while the y-component of the Bloch vector is given by the in-quadrature component of the coherent emission.

Single Qubit Operations Using the Geometric Phase Rotations

The mapping of the state vector on the Bloch sphere shows that any state of a 2-level system can be mapped with two parameters. In other words, there are two basic rotations that can be used to construct any arbitrary rotation of the Bloch vector. These

two rotations are the Bloch vector rotation about the z-axis and the Bloch vector rotation about either the y-axis or the x-axis.

The Bloch Vector Rotation about the Z-axis

The rotation matrix for achieving rotation, δ, about the z-axis can be written as $e^{-i\frac{\delta}{2}\hat{Z}}$ and in the z-basis can be written as

$$R_z = \begin{pmatrix} e^{i\frac{\delta}{2}} & 0 \\ 0 & e^{-i\frac{\delta}{2}} \end{pmatrix} \tag{5.29}$$

To show the effect of this rotation on a system in an arbitrary initial state, we start with a system in a state $|\psi\rangle = \sin(\theta/2)e^{i\varphi}|0\rangle + \cos(\theta/2)|1\rangle$, which corresponds to the position vector on the Bloch sphere $\bar{r}_\psi = (\cos(\varphi)\sin(\theta), \sin(\varphi)\sin(\theta), \cos(\theta))$. Then, the new state of the system, after the rotation about the z-axis, will be $|\psi\rangle' = \sin(\theta/2)e^{i(\varphi+\delta)}|0\rangle + \cos(\theta/2)|1\rangle$, and the position of the new state on the Bloch sphere will be

$$\bar{r}'_\psi = (\cos(\varphi+\delta)\sin(\theta), \sin(\varphi+\delta)\sin(\theta), \cos(\theta)),$$

which shows explicitly the rotation, δ, of the new state about the z-axis.

The aim here is to achieve the rotation about the z-axis with an optical pulse or a combination of optical pulses. In other words, we want to find an evolution operator that matches the rotation matrix in equation (5.29). Note that the evolution operator for a single optical pulse in equation (5.22) cannot be matched with the rotation matrix in the equation (5.29) for any values of the pulse area or the phase. However, if the detuning is

present, then the detuned ions/atoms will rotate around the z-axis. In the current study, resonant ions are being considered; thus, the Bloch vector will not rotate around the z-axis for these ions with a single optical pulse. Therefore, we need to look for an alternative. One option is to decompose the rotation matrix, R_Z, governing the rotation about the z-axis into sub-rotation matrices as

$$R_z = \begin{pmatrix} e^{i\frac{\delta}{2}} & 0 \\ 0 & e^{-i\frac{\delta}{2}} \end{pmatrix} = \begin{pmatrix} 0 & e^{i\frac{\delta}{4}} \\ e^{-i\frac{\delta}{4}} & 0 \end{pmatrix} \begin{pmatrix} 0 & e^{-i\frac{\delta}{4}} \\ e^{i\frac{\delta}{4}} & 0 \end{pmatrix} \tag{5.30}$$

Now we compare the sub-rotation matrices in equation (5.30) and the evolution operator in equation (5.22). The comparison shows that the rotation about the z-axis can be achieved by using two evolution matrices instead of using a single evolution matrix. Therefore, the Bloch vector of the resonant ions can be rotated around the z-axis using two optical pulses. Consequently, two successive pulses with the pulse areas of each pulse, π, and the phase difference, $\pi-\delta/2$, will rotate the Bloch vector of the resonant ions the required amount, δ, around the z-axis.

Detection of the Bloch Vector Rotation about the Z-axis: In order to measure the Bloch vector rotation, a measurement technique similar to the one outlined for a qubit state measurement [(98)] is used. We consider the initial position of the Bloch vector on the Bloch sphere as $\vec{r}_0 = \left(\left\langle \hat{X}\ (0)\right\rangle, \left\langle \hat{Y}\ (0)\right\rangle, \left\langle \hat{Z}\ (0)\right\rangle\right)$. Now we apply the pulse sequence needed for the realization of Bloch vector rotation around the z-axis. Then, the components of the Bloch vector after the pulse sequence will be

$$\left\langle \hat{X} \right\rangle = \left(\cos\left(\delta\right)\right)\left\langle \hat{X}\left(0\right)\right\rangle - \sin\left(\delta\right)\left\langle \hat{Y}\left(0\right)\right\rangle \tag{5.31},$$

$$\left\langle \hat{Y} \right\rangle = \left(\cos\left(\delta\right)\right)\left\langle \hat{Y}\left(0\right)\right\rangle + \sin\left(\delta\right)\left\langle \hat{X}\left(0\right)\right\rangle \tag{5.32},$$

$$\left\langle \hat{Z} \right\rangle = \left\langle \hat{Z}\left(0\right)\right\rangle \tag{5.33},$$

where the initial Bloch vector is known and can be prepared using optical pulses.

Therefore, the coherent signal just after the pulse sequence can be written, using equation (5.28), as

$$\left\langle \hat{\mu} \right\rangle = \mu\left(\left(\left(\cos(\delta)\right)\left\langle \hat{X}(0)\right\rangle - \sin(\delta)\left\langle \hat{Y}(0)\right\rangle\right)\cos\left(\omega_l t\right) - \left(\left(\cos(\delta)\right)\left\langle \hat{Y}(0)\right\rangle + \sin(\delta)\left\langle \hat{X}(0)\right\rangle\right)\sin\left(\omega_l t\right)\right) \tag{5.34}.$$

If, initially, the population is in the ground state, and the initial state is prepared with a $\pi/2$ pulse of zero phase, then the coherent signal in equation (5.34) will be

$$\left\langle \hat{\mu} \right\rangle = \mu\left(\left(-\sin\left(\delta\right)\right)\cos\left(\omega_l t\right) + \left(\left(\cos\left(\delta\right)\right)\right)\sin\left(\omega_l t\right)\right) \tag{5.35}.$$

The in-phase and in-quadrature components of the signal in equation (5.35) will give the rotation angle of the Bloch vector. But this coherent signal will dephase, and it can be rephased using another optical pulse. Now if the coherent signal in equation (5.35) is rephased using a π-pulse of zero phase, then the rephased coherent signal gives rise to a photon echo [(111)], which is similar to the spin echo [(112)]. This coherent rephased signal will be

$$\left\langle \hat{\mu} \right\rangle = \mu\left(\left(-\sin\left(\delta\right)\right)\cos\left(\omega_l t\right) - \left(\left(\cos\left(\delta\right)\right)\right)\sin\left(\omega_l t\right)\right) \tag{5.36}.$$

The coherent echo signal in equation (5.36) provides a measurement for the detection of the rotation angle of the Bloch vector. Note that the Bloch vector rotation angle is twice the phase of the control pulse sequence. Note that the measurement of the

phase of an echo provides a direct measurement of the rotation of the Bloch vector. The pulse sequence needed to realize the measurement scheme is given in Figure 53.

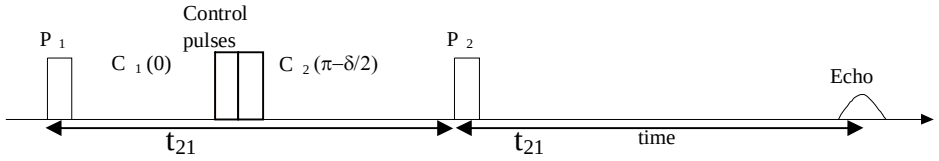

Figure 53: A pulse sequence to rotate and detect the rotation of the Bloch vector around the z-axis.

The Bloch Vector Rotation about the Y-axis

The second of the two rotations needed to construct any single qubit gate for the Bloch vector rotation is described here. In this rotation, the aim is to find a pulse sequence that can rotate the Bloch vector around the y-axis.

The rotation around the y-axis for an amount, δ, can be written as $e^{-i\frac{\delta}{2}\hat{Y}}$. In the z-basis, the rotation can be written as

$$R_Y = \begin{pmatrix} \cos\left(\frac{\delta}{2}\right) & \sin\left(\frac{\delta}{2}\right) \\ -\sin\left(\frac{\delta}{2}\right) & \cos\left(\frac{\delta}{2}\right) \end{pmatrix} \tag{5.37}$$

This rotation will rotate the Bloch vector of the resonant ions to a new position on the Bloch sphere, and the coordinates of the new position will be

$\bar{r}'_\psi = ((\cos(\theta)\sin(\delta) + \cos(\delta)\sin(\theta)\cos(\varphi)), \sin(\varphi)\sin(\theta), (\cos(\theta)\cos(\delta) - \sin(\theta)\sin(\delta)\cos(\varphi)))$ where the initial position of the Bloch vector is given as $\bar{r}_\psi = (\cos(\varphi)\sin(\theta), \sin(\varphi)\sin(\theta), \cos(\theta))$. If we choose the initial Bloch vector in the

x-z plane, then the new position of the Bloch vector will be $\vec{r}_{\psi}' = (\sin(\theta+\delta), 0, \cos(\theta+\delta))$, which again explicitly shows the rotation around the y-axis.

The Bloch Vector Rotation about the Y-axis with a Single Optical Pulse: Recall the evolution matrix in equation (5.22) and the rotation about the y-axis, equation (5.37). Note that this rotation of the Bloch vector can be achieved with a single optical pulse. If a single optical pulse of phase -0.5π is applied to the Bloch vector, then this pulse will rotate the Bloch vector of resonant ions around the y-axis. The angle of the rotation will be given by the area of the applied optical pulse. One drawback of this technique is the reliance of the rotation on the exact pulse area of the optical pulse. This technique thus requires perfectly matching the pulse area for the correct required rotation around the y-axis. Any spatial variation in the intensity across the interaction volume will compromise the operational fidelity, and thus, the operation will not be robust. The rotation of the resonant ions around the y-axis with a single optical pulse can be detected using a similar technique as outlined in the previous case. The details for this case are presented in the next section.

Detection of the Bloch Vector Rotation about the Y-axis: Let us consider the initial position of the Bloch vector on the Bloch sphere as $\vec{r}_0 = \left(\langle \hat{X}(0)\rangle, \langle \hat{Y}(0)\rangle, \langle \hat{Z}(0)\rangle\right)$. Now we apply the single optical pulse to achieve the Bloch vector rotation around the y-axis. The Bloch vector, after the application of a single optical pulse of pulse area θ and phase -0.5π, will be

$$\left\langle \hat{X} \right\rangle = \cos(\theta)\left\langle \hat{X}(0) \right\rangle - \sin(\theta)\left\langle \hat{Z}(0) \right\rangle \tag{5.38},$$

$$\left\langle \hat{Y} \right\rangle = \left\langle \hat{Y}(0) \right\rangle \tag{5.39},$$

$$\left\langle \hat{Z} \right\rangle = \sin(\theta)\left\langle \hat{X}(0) \right\rangle + \cos(\theta)\left\langle \hat{Z}(0) \right\rangle \tag{5.40},$$

where the initial Bloch vector is known and can be prepared using optical pulses. Note that the rotation angle of the Bloch vector in this case is the same as the pulse area of the pulse.

The coherent signal just after the first pulse can be written, using equation (5.28), as

$$\left\langle \hat{\mu} \right\rangle = \mu\left(\left((\cos(\theta))\left\langle \hat{X}(0) \right\rangle - \sin(\theta)\left\langle \hat{Z}(0) \right\rangle\right)\cos(\omega_l t) - \left(\left\langle \hat{Y}(0) \right\rangle\right)\sin(\omega_l t)\right) \tag{5.41}.$$

If the initial state of the system is prepared such that population is in the ground state, and there are no coherences present in the system, then the coherent signal in equation (5.41) will be

$$\left\langle \hat{\mu} \right\rangle = \mu\left((\sin(\theta))\cos(\omega_l t)\right) \tag{5.42}.$$

Note that the signal in equation (5.42) is in-phase with the laser (by definition phase is zero) but is in-quadrature with the pulse being applied. The coherent signal in equation (5.42) can be rephased using a π-pulse of zero phase as is usually employed for the observation of photon echoes. Then, the rephased coherent signal will be

$$\left\langle \hat{\mu} \right\rangle = \mu\left((\sin(\theta))\cos(\omega_l t)\right) \tag{5.43}.$$

This coherent echo signal provides a measurement for the rotation angle of the Bloch vector. The pulse sequence needed to realize the measurement scheme is given in Figure 54.

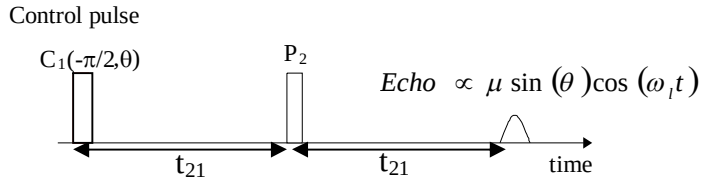

Figure 54: A pulse sequence used to rotate and measure the rotation of the Bloch vector about the y-axis for a single pulse case.

The Bloch Vector Rotation about the Y-axis using the Geometric Phase: Another option is to use a geometric phase and apply a controlled rotation about the y-axis. The expectation is that this method will be robust and will be less influenced by intensity fluctuations compared to the single pulse case. In order to see how the rotation of the Bloch vector around the y-axis can be realized using a geometric phase, we write the decomposition of rotation matrix, R_Y, as

$$R_Y = \begin{pmatrix} \cos\left(\frac{\delta}{2}\right) & \sin\left(\frac{\delta}{2}\right) \\ -\sin\left(\frac{\delta}{2}\right) & \cos\left(\frac{\delta}{2}\right) \end{pmatrix} = \frac{1}{2i}\begin{pmatrix} 1 & i \\ i & 1 \end{pmatrix}\begin{pmatrix} 0 & e^{i\left(\frac{\delta}{2}\right)} \\ e^{-i\left(\frac{\delta}{2}\right)} & 0 \end{pmatrix}\begin{pmatrix} 1 & i \\ i & 1 \end{pmatrix} \quad (5.44).$$

The decomposed rotation matrix shows that there are three sub-rotations which can be realized using three optical pulses having appropriately chosen pulse areas and phases. For this specific decomposition, pulse 1 needs to be a $\pi/2$ pulse with zero phase, pulse 2 needs to be a π pulse with $\pi+\delta/2$ phase, and pulse 3 needs to be a $\pi/2$ pulse with the zero phase to accomplish δ rotation of the Bloch vector around the y-axis.

Detection of the Bloch Vector Rotation about the Y-axis using the Geometric Phase: The detection scheme and the analysis are similar to the case for the Bloch vector rotation with a single pulse. Initially the Bloch vector on the Bloch sphere is given by a position vector as $\vec{r}_0 = \left(\langle \hat{X}(0)\rangle, \langle \hat{Y}(0)\rangle, \langle \hat{Z}(0)\rangle\right)$. If the system is in the ground state and there are no coherences in the system, then the position of the Bloch vector will be $\vec{r}_0 = (0,0,-1)$. Suppose that the first pulse in the sequence of pulses needed to rotate the Bloch vector around the y-axis is applied. Since this pulse has pulse area $\pi/2$ and phase zero, it will rotate the Bloch vector to a new position given by a new position vector, $\vec{r}_1 = (0,1,0)$. The second pulse of pulse area π and phase $\pi+\delta/2$ will rotate the Bloch vector to the new position, $\vec{r}_2 = (\sin(\delta),-\cos(\delta),0)$. The last pulse of $\pi/2$ pulse area and zero phase will rotate the Bloch vector to the position $\vec{r}_2 = (\sin(\delta),0,\cos(\delta))$. We recall equation (5.28) and the position of the Bloch vector and write the coherent emission just after this pulse sequence as $\langle \hat{\mu} \rangle = \mu(\sin(\delta)\cos(\omega_l t))$. Note that the coherent emission in this case is similar to the case of the Bloch vector rotation around the y-axis with a single optical pulse. The coherent signal will dephase after the pulse with a dephasing time that depends on the inhomogeneous broadening of the sample and the material dephasing time. However, this signal can be rephased using a technique often used to obtain a spin and an optical echo as noted in earlier cases. Thus, another π-pulse of zero phase is applied to rephase the coherences, and the rephased coherent signal is obtained as $\langle \hat{\mu} \rangle = \mu((\sin(\delta))\cos(\omega_l t))$.

This coherent echo signal again provides a measurement for the magnitude of the Bloch vector rotation. The pulse sequence to detect the rotation angle is given in Figure 55.

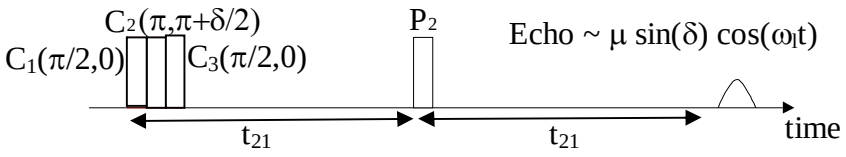

Figure 55: A pulse sequence to rotate and detect the control rotation about the y-axis of the Bloch vector with relative phase control of the optical pulses.

Excitation with the Gaussian Spatial Beam for Single Qubit Operations

As noted in the previous sections, the specific rotation of a Bloch vector requires a certain pulse sequence with definite pulse areas and a relative phase. In the case of excitation with a beam having a Gaussian beam profile, the area of the beam and, hence, the pulse area varies across the beam. This means that the ions in different spatial locations in the beam will experience different pulse areas. Thus, the spatially-distributed ions will also have spatial distributions in their Bloch vectors after the excitation with the Gaussian spatial beam. In this section, the effect of non-uniformity in the intensity of a beam profile on the Bloch vector rotations is analyzed. In this study, it is assumed that the intensity profile of the beam profile follows a Gaussian profile. The effect of the inhomogeneity in the optical beam in the context of rotation with the geometric phase has not been studied before. The aim here is to study the dependence of each rotation on the beam profile. Assume that the center of each pulse has the pulse area needed to impart

correct rotation. This means that the ions interacting with the center part of the beam follow theoretically predicted results for the Bloch vector rotation. Thus, the pulse area for such a pulse can be written as

$$\theta_i(r) \propto \theta_{0i} e^{-\left(\frac{r}{r_0}\right)^2} \tag{5.45},$$

where θ_{0i} is the pulse area of i^{th} pulse at the center of the beam and r_0 is the 1/e width of the field.

The Bloch Vector Rotation about the Z-axis

Recall the pulse sequence needed to rotate the Bloch vector around the z-axis. Now consider beams that have pulse areas $\theta_1(r)$, and $\theta_2(r)$ for the rotation of the Bloch vector around the z-axis. Now we apply the rotation matrix in equation (5.30) and write the detected echo signal for this case as

$$\begin{aligned} Echo \quad \propto & \left(-f_1(x)\sin\left(\frac{\delta}{2}\right) + f_2(x)\sin(\delta) \right)\cos(\omega_l t) \\ & + \left(-g_0(x) - g_1(x)\cos\left(\frac{\delta}{2}\right) + g_2(x)\left(\cos\left(\frac{\delta}{2}\right)\right)^2 \right)\sin(\omega_l t) \end{aligned} \tag{5.46},$$

where the pulse area of each of the control pulses in the center of beam is π, x in units of r_0 is the partial width of the beam, and $f_1(x)$, $f_2(x)$, $g_0(x)$, $g_1(x)$, and $g_2(x)$ are positive-valued functions and can be tabulated for known x as outlined in APPENDIX B. Note that if the echo phase is measured, it will not give the rotation angle, δ, and thus, will have an error in the rotation angle.

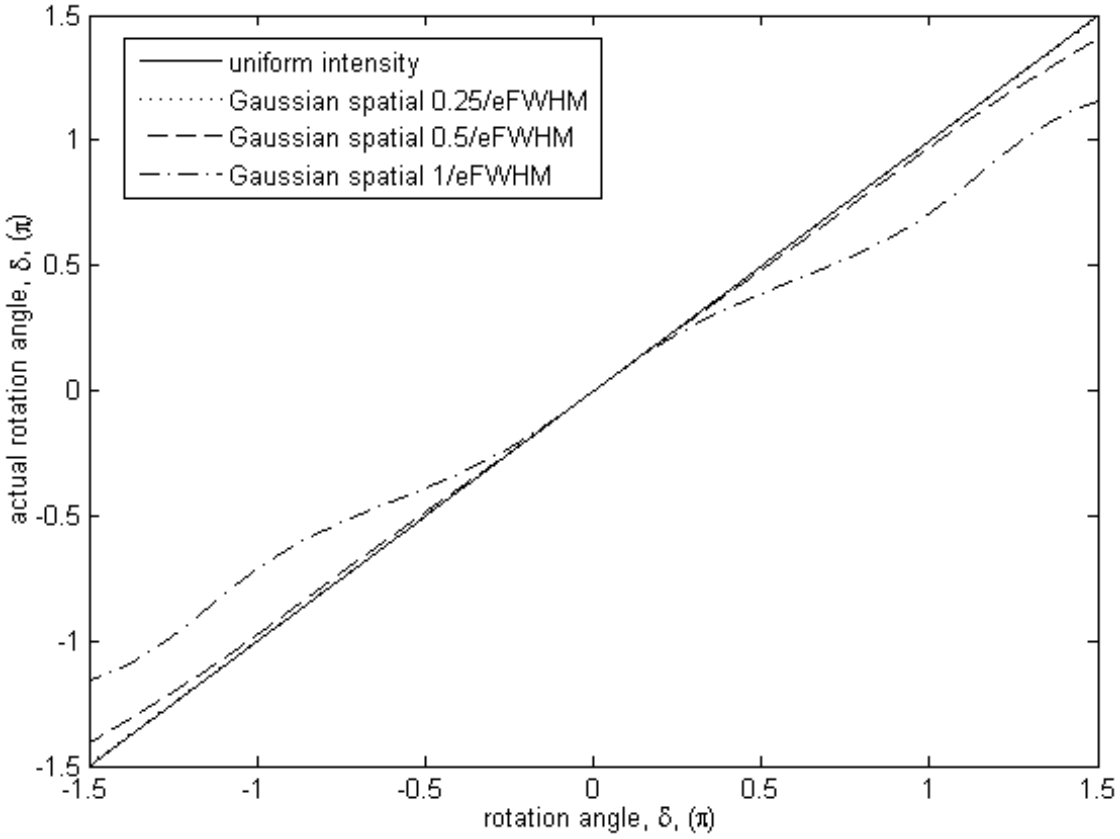

Figure 56: Theoretical results for the Bloch vector rotation around the z-axis using optical pulses having Gaussian spatial beam profiles.

We analyzed the theoretical results further by plotting the components of the Bloch vector for various values of x. In the first plot, we looked at the relation between the actual rotation angle used and the angle of the rotation imparted with the Gaussian spatial beams. The theoretical results in Figure 56 show that the central part of the Gaussian beams is imparting the correct rotation. However, as we move away from the center, the actual rotation imparted by the Gaussian beams differs significantly from the value of the rotation angle used in the control pulses. Thus the ions at different spatial locations in the system undergo a rotation with the different rotation angle.

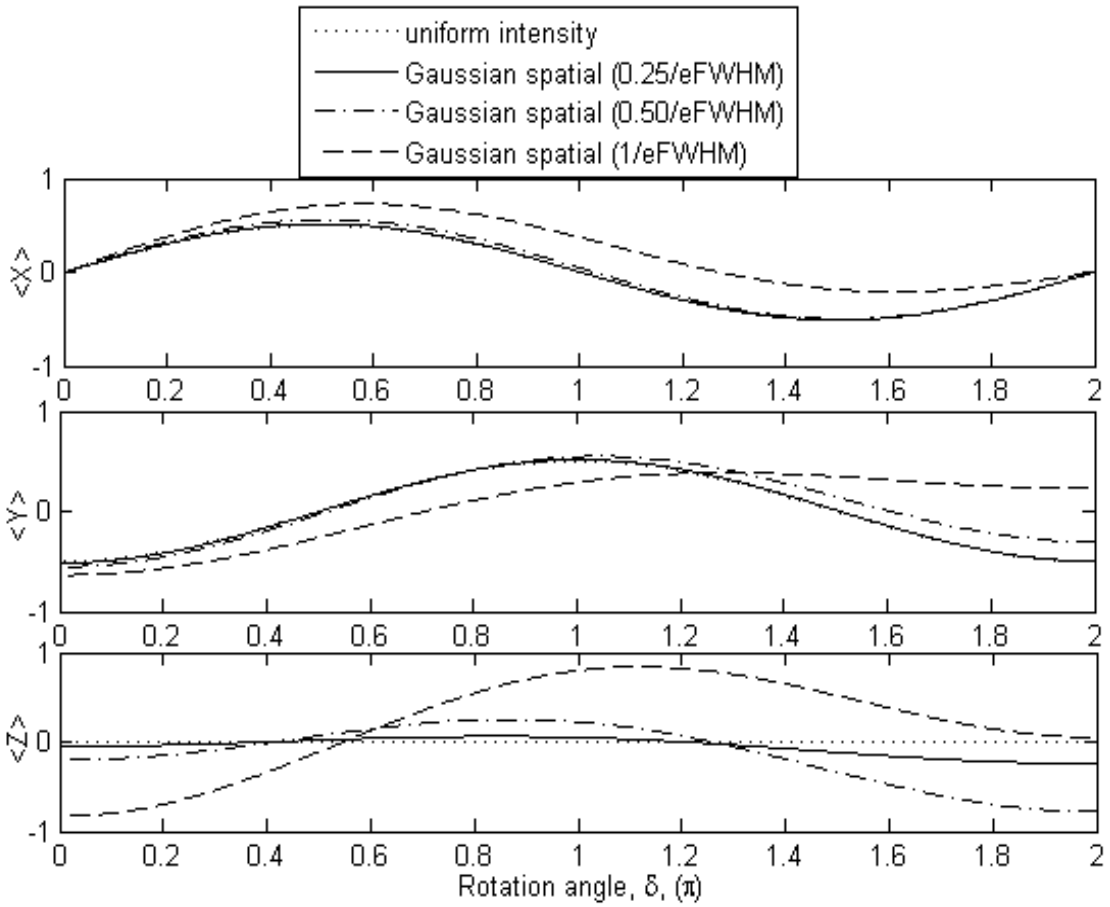

Figure 57: Theoretical results show the components of the Bloch vector for rotation around the z-axis. Here, areas at the center of the uniform intensity and the Gaussian spatial beam are assumed to have ideal values of the pulse areas needed to impart the correct Bloch vector rotation about the z-axis.

Now we need to analyze the rotation axis for ions at different spatial locations in the system. This can be analyzed by plotting the theoretical results for components of the Bloch vector. The z-component of the Bloch vector in Figure 57 shows that the ions at the center of the Gaussian spatial beams rotate along the correct axis (i.e., the z-axis in this case). However, the ions interacting with the off-center part of the Gaussian beams have nonzero z-components. This means that ions at these spatial locations do not rotate along the z-axis. Therefore, we will have a range of spatial distribution for the rotation

axis. The other two components (x and y) of the Bloch vector for rotation with the Gaussian spatial beam also differ significantly from the results of the rotation with the uniform intensity beam. This led us to believe that the rotation of Bloch vector using the Gaussian spatial beam introduces error, not only in the axis of the rotation, but also in the rotation angle.

The Bloch Vector Rotation about the Y-axis

The Bloch Vector Rotation with a Single Optical Pulse: Now we consider the rotation of the Bloch vector around the y-axis where a single pulse is needed to realize the rotation. In this case, instead of using a pulse with uniform intensity, a pulse having a Gaussian spatial profile is applied to the Bloch vector. Consider a pulse with the pulse area $\theta(r)$ that follows a Gaussian profile given in equation (5.45). Then, the echo from the pulse sequence for the Bloch vector rotation about the y-axis will be

$$Echo \propto \left(0.5Si(\theta) - 0.5Si\left(\theta e^{-x^2}\right)\right)\cos(\omega_1 t) \qquad (5.47),$$

where θ is the pulse area of pulse 1, x (in unit of r_0) is the beam width selected, and $Si(y_0) = \int_0^{y_0} \frac{\sin(y)}{y} dy$. Results from equation (5.47) show that the echo intensity does not follow a sinusoidal relation as predicted by the excitation with the uniform intensity beam, but, instead, follows a complicated function (the plot is shown in Figure 58).

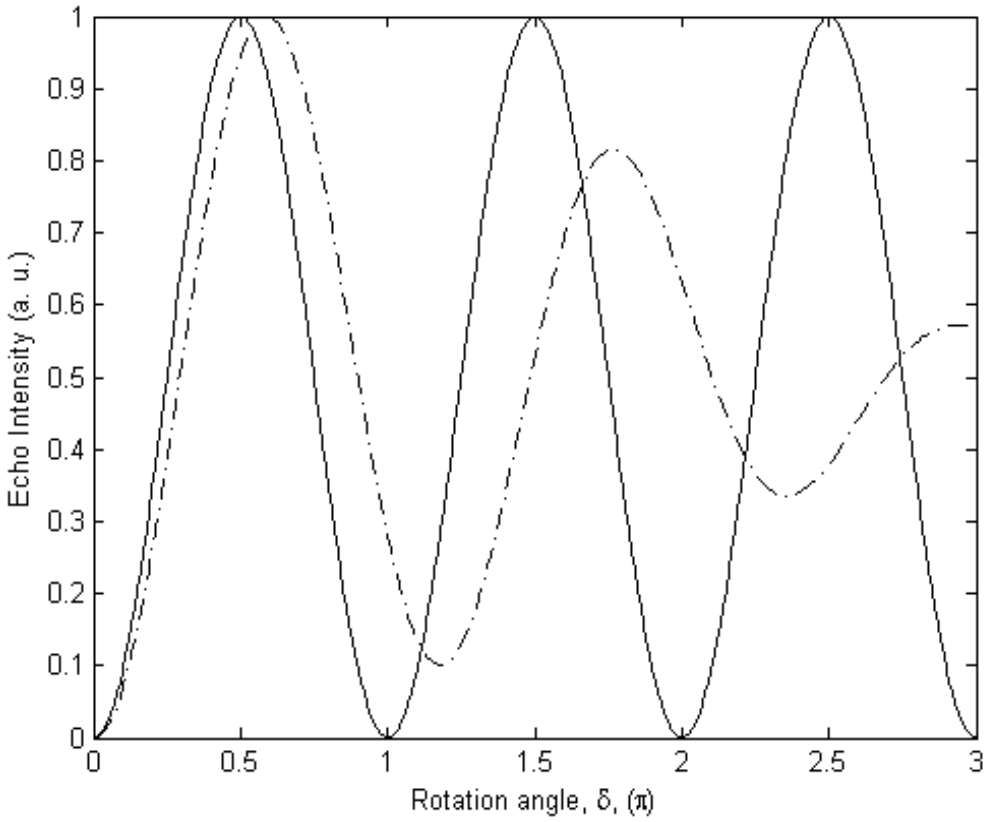

Figure 58: Theoretical results show the dependence of the echo intensity on the pulse area at the center of the beam of the control pulse when the medium is excited with a pulse having a uniform spatial profile (solid line) and Gaussian spatial profile (dotted line) for the Bloch vector rotation around the y-axis.

Figure 58 shows the dependence of echo intensity on the pulse area of the first pulse. As in this case, the rotation angle of the Bloch vector rotation is the same as the area of pulse 1; it again shows deviation of results in a Gaussian spatial beam from the uniform intensity case as the rotation angle of the Bloch vector increases.

The Bloch Vector Rotation about the Y-axis Using Geometric Phase: Now, if the geometric phase is used to realize a controlled rotation of the system about the y-axis, and

each pulse in the sequence has a Gaussian spatial intensity profile, then the detected echo signal will be

$$\begin{aligned} Echo \quad \propto & \left(h_1(x)\sin\left(\frac{\delta}{2}\right) - h_2(x)\sin(\delta) \right)\cos(\omega_l t) \\ & + \left(k_0(x) - k_1(x)\cos\left(\frac{\delta}{2}\right) - k_2(x)\left(\cos\left(\frac{\delta}{2}\right)\right)^2 \right)\sin(\omega_l t) \end{aligned} \tag{5.48},$$

where detuning and any other dephasing mechanism during the pulse are ignored, pulse areas of control pulses in the center of beam are $\pi/2$, π, $\pi/2$, x (in units of r_0) is the partial width of the beam, and $h_1(x)$, $h_2(x)$, $k_0(x)$, $k_1(x)$, and $k_2(x)$ are positive-valued functions and can be tabulated for known x as outlined in APPENDIX C.

The amplitude of the detected echo in Figure 59 is normalized to the maximum value of the echo for each data set. Figure 59 shows that the detected echo deviates from the usual sinusoidal dependence as the rotation angle increases. This is again attributed to the fact that the rotation angle varies across the beam profile of the Gaussian beam with only the center of the beam giving the desired rotation of the Bloch vector.

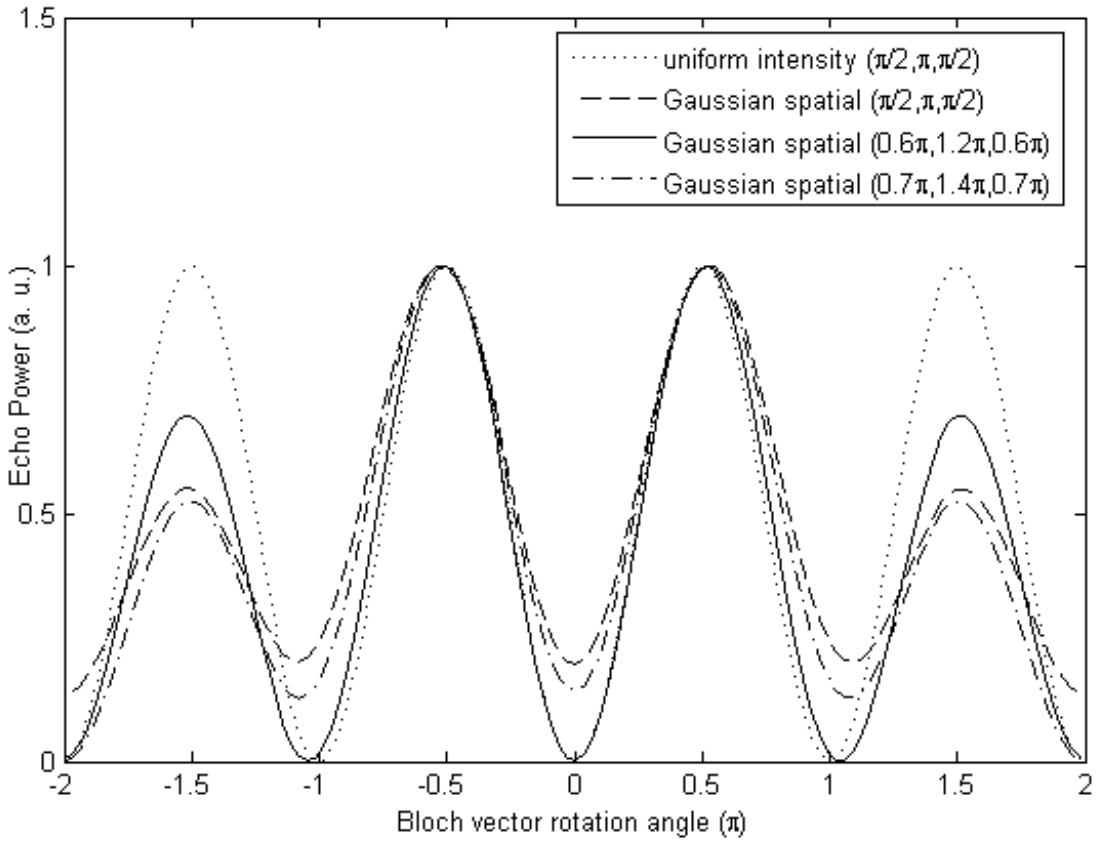

Figure 59: Theoretical results for the detected echo power for the Bloch vector rotation around the y-axis. The echo power strongly depends on the spatial profiles of the control pulses.

Now we plot the components of the Bloch vector for rotation about the y-axis using the excitation pulses having a Gaussian profile. The theoretical results in Figure 60 are obtained using a Gaussian model outlined in APPENDIX C. First, we analyze the y-component of the Bloch vector, as in this case, we are using the pulse sequence to rotate the Bloch vector around the y-axis. The theoretical results in Figure 60 show that the ions interacting with the center part of the Gaussian beams rotate the Bloch vector around the y-axis. However, the ions interacting with the off-center parts of the Gaussian beams undergo a rotation around the axes that are spatially distributed. Note that in this case, the

x-component was responsible for the rephased signal (echo signal) for the uniform intensity beams. The x-component of the Bloch vector in Figure 60 shows significant deviation as we move away from the center of the Gaussian beams. Thus, again, we have an error in the rotation axis and an error in the rotation angle for this case as well.

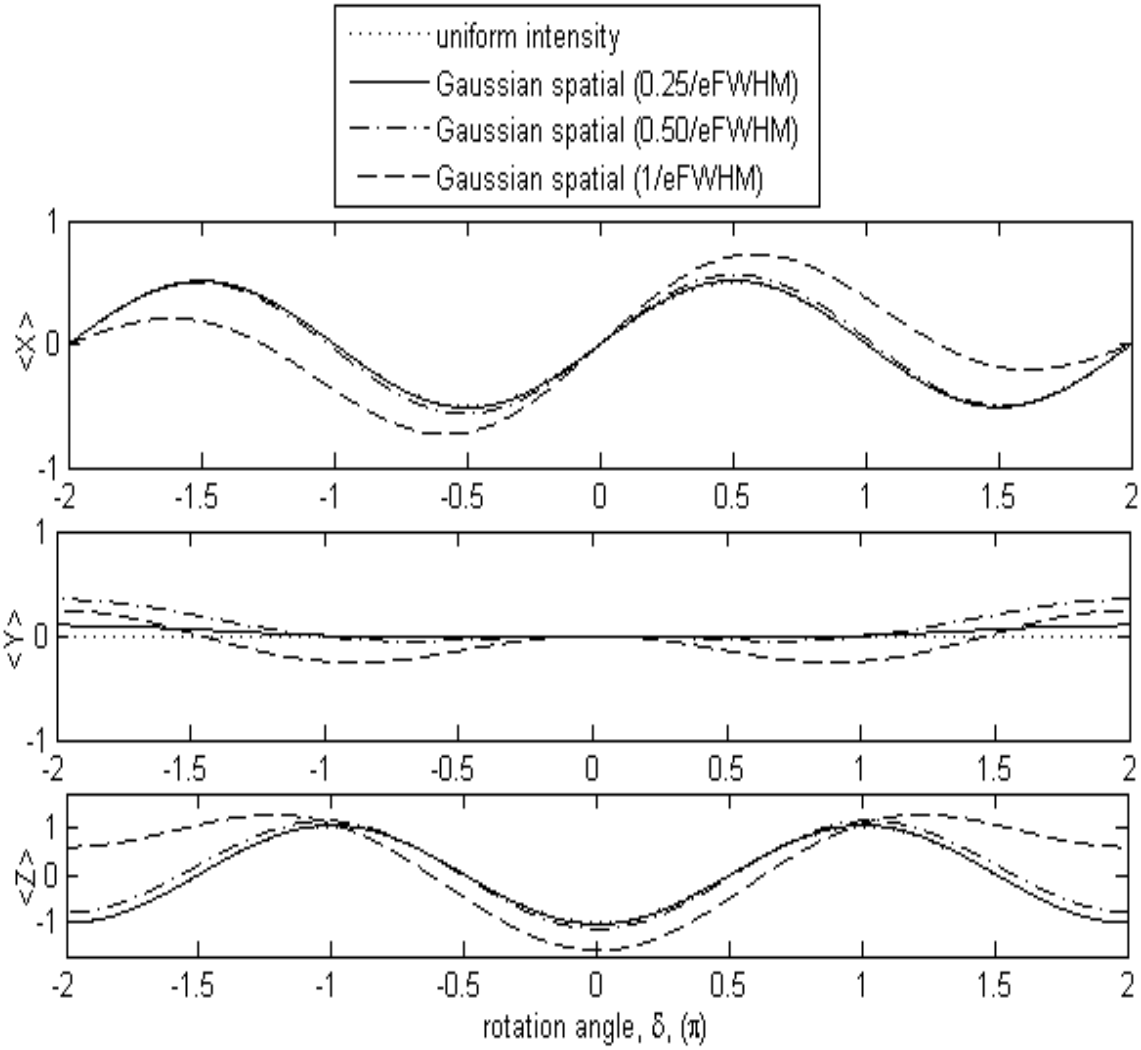

Figure 60: Theoretical results show the components of the Bloch vector for rotation around the y-axis. The areas at the center of each control pulse are ($\pi/2$, π, $\pi/2$) as required by the sequence for ideal Bloch vector rotation around the y-axis (Figure 55).

Qubit State Measurement and the Operation Fidelity

In order to measure the operation fidelity, a framework is needed to measure the state of the qubit, as the operation on a qubit changes the state of the qubit. The operation fidelity then will be a comparison between the initial state and the final state. Where the final state can be mapped with the state measurement process described below. The procedure to measure the state of a qubit is well understood, and we follow the derivation given in [(50), (98)]. Here, a qubit is represented by the ensemble of ions whose state can be controlled with the optical pulses. Consider an ensemble of ions whose initial state is given by the Bloch vector as

$$\vec{r}(0) = (\langle \hat{X}(0) \rangle, \langle \hat{Y}(0) \rangle, \langle \hat{Z}(0) \rangle) \qquad (5.49).$$

Now if we know the components of the Bloch vector, then we know the state of an ensemble. Thus, the process described here is used to measure the components of the Bloch vector. Now, if a measurement is made just after preparing the state of the ensemble as given in equation (5.49) by measuring the free induction decay., The measurement will provide the in-phase with the laser signal as $\langle \hat{X}(0) \rangle$ and will provide the in-quadrature with the laser signal as -$\langle \hat{Y}(0) \rangle$. The system is excited some time later with a π-pulse of zero phase. This pulse rotates the Bloch vector around the x-axis on the Bloch sphere. At the rephasing time, another measurement of the in-phase component provides $\langle \hat{X}(0) \rangle$, while the in-quadrature component provides $\langle \hat{Y}(0) \rangle$. At the same time, another $\pi/2$-pulse with zero phase that is partially overlapped with a rephased signal is

applied, and the free induction decay is measured after the pulse. This time, the measurement of the in-phase component of the laser will give $\left\langle \hat{X}(0) \right\rangle$, and the in-quadrature component will give $\left\langle \hat{Z}(0) \right\rangle$. Thus, the Bloch vector is completely specified and so is the state of the ensemble. This procedure was successfully adopted to measure the state of the ensemble [(50)] and can be adopted for the operation fidelity measurements. As mentioned earlier, the process fidelity will then be the comparison between the experimentally-measured state after the qubit operation and the theoretically-predicted state of the qubit after the qubit operation.

Thus, for this case, the operation fidelity is defined as [(113)]

$$\Im = \frac{1}{2}\left(1 + \vec{R}_{\exp} \cdot \vec{R}_{theory} + \sqrt{\left(1 - \vec{R}_{\exp} \cdot \vec{R}_{\exp}\right)\left(1 - \vec{R}_{theory} \cdot \vec{R}_{theory}\right)}\right) \qquad (5.50),$$

where $\vec{R}_{\exp} = \left(\left\langle \hat{X}_{\exp} \right\rangle, \left\langle \hat{Y}_{\exp} \right\rangle, \left\langle \hat{Z}_{\exp} \right\rangle\right)$, $\vec{R}_{theory} = \left(\left\langle \hat{X}_{theory} \right\rangle, \left\langle \hat{Y}_{theory} \right\rangle, \left\langle \hat{Z}_{theory} \right\rangle\right)$, $\left|\vec{R}_{theory}\right| \le 1$, and $\left|\vec{R}_{\exp}\right| \le 1$ represents the position of the Bloch vector on the Bloch sphere.

Degradation of the Operation Fidelity for Single Qubit Operations

We theoretically analyze the operation fidelity using equation (5.50). Here we compare the rotations of the Bloch vector using a uniform intensity beam and rotation of the Bloch vector using the Gaussian spatial beams. Thus, we start with the same initial state of the qubit. In one case, the final state, $\vec{R}_{uniform}$, of the qubit is obtained after the rotation of the qubit using the pulse sequence, with each pulse having a uniform intensity across the beam. In another case, the final state, $\vec{R}_{Gaussian}$, of the qubit is obtained after the rotation of the qubit using the pulse sequence, with each pulse having the Gaussian beam

profile. Therefore, the fidelity, $\Im(r)$, of the operation is obtained using results in equation (5.50). Note that the uniform intensity beams give us the desired rotation around the desired rotation axis. The operation fidelity for this case will be unity (perfect rotation).

The degradation of the operation fidelity is defined as the difference in the operation fidelities of the qubit operation with the Gaussian spatial and the uniform intensity beams integrated across the Gaussian spatial profile. Thus, the degradation of the fidelity due to intensity variation across the beam will be

$$\langle \Delta\Im \rangle = \frac{\int_0^{r_0} rdre^{-\left(\frac{r}{r_0}\right)^2} \left(1-\Im(r)\right)}{\int_0^{r_0} rdre^{-\left(\frac{r}{r_0}\right)^2}} \qquad (5.51),$$

where $\Im(r)$ is the fidelity of the operation as defined in equation (5.50) and r_0 is the 1/e width of the Gaussian spatial beam.

Operation Fidelity for the Bloch Vector Rotation about the Z-axis: Recall the pulse sequence given in Figure 53 that rotates the Bloch vector around the z-axis. Now, we use that pulse sequence and calculate the components of the Bloch vector for uniform excitation and non-uniform (spatial Gaussian) excitation. Then, the operation fidelity for each case will be given by equation (5.50). Now, we obtain the degradation in the operation fidelity using the formula in equation (5.51). The results are plotted in Figure 61 for the degradation in the operation fidelity. The results show that the degradation in the operation fidelity depends on the rotation angle of the Bloch vector. Results show

that the degradation in the operation fidelity is more than 12% for all rotation angles. The degradation in the operation fidelity is within 12% to 15% for all rotation angles.

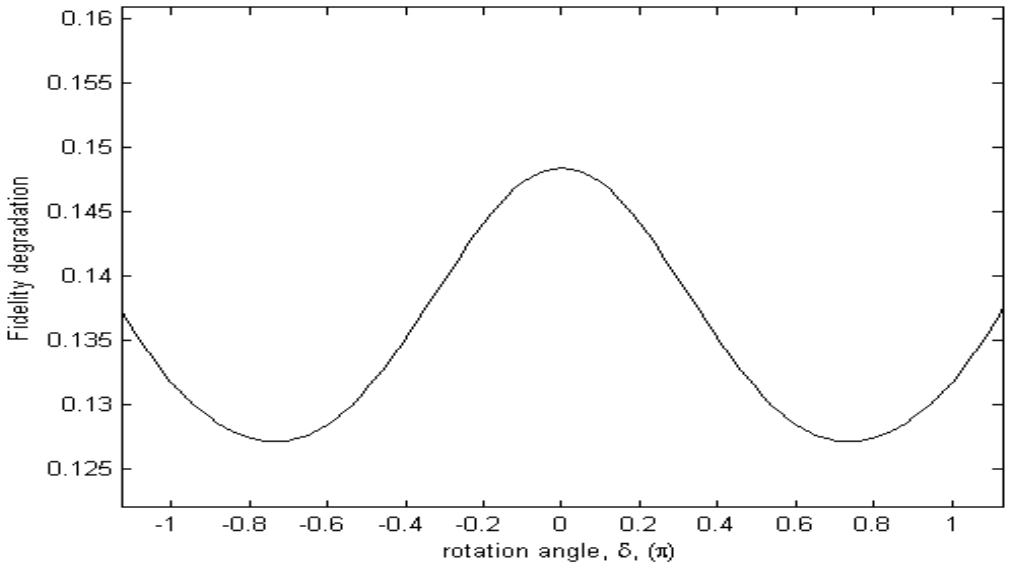

Figure 61: Theoretical results [(5.50), (5.51)] for the fidelity degradation of the z-axis rotation of the Bloch vector with control pulses having Gaussian spatial profiles.

Operation Fidelity for the Bloch Vector Rotation about the Y-axis: In this case, we analyze the degradation of the operation fidelity when the pulse sequence in Figure 55 for the rotation around the y-axis is applied to the ensemble. We again use the operation for uniform excitation and non-uniform excitation using the formula in equation (5.50). Again, the degradation of operation fidelity is calculated using formula (5.51). The theoretical results for the degradation in the operation fidelity are plotted in Figure 62. It again shows degradation in the operation fidelity for all rotation angles. The degradation in the operation fidelity again is negligibly small for a rotation angle of $\pm 0.2\pi$. The degradation in the operation fidelity increases with the rotation angle. For this case, degradation in the operation fidelity reaches a maximum of about 12%.

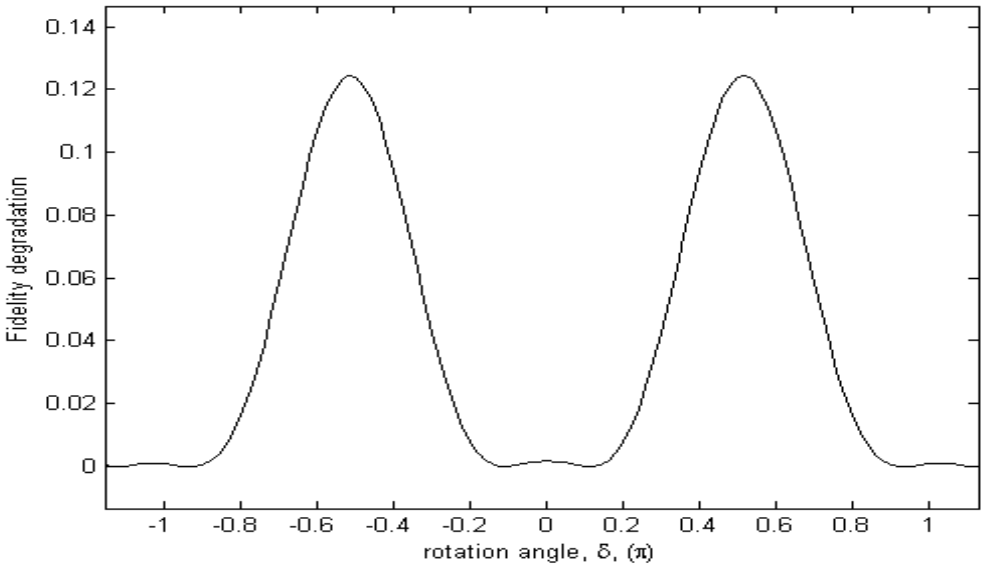

Figure 62: Theoretical results [(5.50), (5.51)] for the fidelity degradation of the y-axis rotation of the Bloch vector with control pulses having Gaussian spatial profiles.

The results for the degradation in the operation fidelity imply that, for non-uniform excitation, the operation fidelity will be less than 80%. Thus, a modified pulse sequence recently suggested may be the best option for high fidelity qubit operations [(114)].

Conclusions

A review of the well-known results shows that any pure and mixed state of a 2-level system can be mapped onto the Bloch sphere. Thus, a change of the state of a 2-level system amounts to a change in the position of the Bloch vector on the Bloch sphere. Review also shows that the position of the Bloch vector depends not only on the area of the applied pulse but also on the phase of the laser pulse. In the later part of the chapter, optical pulses with certain phases and areas were used to predictably change the Bloch vector position on the Bloch sphere. An experimental framework was presented to realize

the two basic rotations of the Bloch vector on the Bloch sphere. Any other rotation on the Bloch sphere can be realized using these two basic sets of rotations. A detection scheme using the two pulse photon echo was presented.

The effects of the non-uniformity in the intensity of the laser beam on the rotation of the Bloch vector were calculated. This is an important investigation since the intensity in the laser beam typically follows a Gaussian profile. In rare-earth quantum computing, an ensemble of ions that is being excited has ions that are usually spatially distributed. Thus, their interaction with a Gaussian beam will result in different positions of their Bloch vectors on the Bloch sphere. The theoretical results for a single qubit operation presented in this chapter will be helpful to analyze the experimental results in Chapter 6.

The effects of the non-uniformity in the beam intensity were further analyzed by analyzing the operation fidelities of single qubit operations. It was noted that the degradation of the operation fidelity for the case of non-uniform excitation is significant for all Bloch vector rotation angles. Therefore, the operation fidelity of the qubit operations obtained using the Gaussian spatial beams will be significantly lower than those obtained using uniform intensity beams.

CHAPTER SIX

QUANTUM COMPUTING: EXPERIMENTAL DEMONSTRATION

Introduction

In this chapter, the experimental results for the ensemble selection and the operation on a single qubit in the thulium-doped crystal are presented. The experiments discussed in this chapter involve an ensemble of ions that contains only those ions that can be addressed uniformly with the optical field. For experimental demonstrations using this selected ensemble of ions, we will follow the scheme mentioned earlier where geometric phase gates can be constructed by application of the laser pulses with the definite areas and phases [(109)]. We experimentally demonstrate that the geometric phase gate can be implemented in such an ensemble of ions. An earlier demonstration of one of the two basic rotations was accomplished in the inhomogeneously broadened medium without selecting an ensemble of ions [(108)]. In this chapter, the experimental demonstration of a single qubit operation involves the implementation of a Bloch vector rotation scheme on the selected ensemble of ions. At the end of the chapter two ensembles of ions were selected. The interaction between two selected ensembles was measured using photon echo experiments.

Ion Selection for a Single Qubit Preparation

Introduction

Since the aim of this chapter is to demonstrate the operation on a single qubit with the laser pulses, the ensemble of ions needed to be selected with the following special properties. First, the laser pulse should be able to address all the ions in the ensemble with a single Rabi frequency so that the Bloch vector for each ion in the ensemble is rotated the same amount on the Bloch sphere. In our theoretical treatment for a single qubit rotation, the detuning during the pulse was neglected. This treatment can only be justified if the inhomogeneous spectral width of the selected ensemble is smaller than the bandwidth of the pulse used to address the ensemble. Therefore, the Rabi frequency and the bandwidth of the optical pulse need to be higher than the spectral width of the ensemble of ions. Note that the rare-earth-doped crystal, (Tm^{3+}:YAG), considered here, has a multi-GHz bandwidth. This means that a laser pulse of multi-GHz Rabi frequency and bandwidth is required to address all ions in the medium uniformly. Therefore, a different approach is needed to realize the qubit operation in the thulium with the laser pulses. This approach involves selecting an ensemble of ions with a reasonable spectral width.

The first experiment to produce a narrowband ensemble of ions in the inhomogeneously broadened absorption profile of the medium used “zero area” pulses [(115)]. This technique was successfully implemented to select a narrowband ensemble of ions and provided the basic idea for selecting an ensemble of ions in the rare-earth-doped crystals. We did not choose to implement this technique in our experiment. This

technique was not suitable for our purpose, where significant spatial inhomogeneity in the optical field is present and the optically dense ($\alpha L \sim 3.0$) material is considered. However, our goal is to implement another technique that was also successfully implemented in other rare-earths ions [(116), (117)]. This technique accomplishes the task of selecting an ensemble of ions in two steps. In the first step, a spectral window in the inhomogeneous absorption profile of the medium is emptied by optically pumping ions to the long-lived levels. In the second step, another optical pulse is used to burn an ensemble of ions with the desired characteristics back in the trench. We have chosen this technique because this technique does not require exact pulse areas and is well-suited for cases where significant spatial inhomogeneity is present and optically thick material is considered. In this scheme, the population is stored in other energy levels with the population lifetime of these population storage levels being much longer than the time scale of the experiment. This means that the selected ensemble can be considered long-lived for the duration of the experiment. In this technique, the bandwidth and the number of ions in the selected ensemble can be varied by varying the parameters of the burn-back pulse. In the case where selected ensemble of ions have low absorption length, i.e., $\alpha L << 1$, the Rabi frequency will not be significantly affected by the absorption in the medium. For this case, the optical pulse with Rabi frequency and bandwidth greater than the spectral width of the selected ensemble will address all the ions in the ensemble uniformly.

Now we consider the important parameters needed to implement this technique in Tm^{3+}:YAG. The most important parameter is the population lifetime of the storage level.

If we consider Tm^{3+}:YAG energy structure without the applied magnetic field, we note that the longest population lifetime available is about 12 ms. In that case, about 90% of the total population will be stored in the long-lived storage level, and there is no possibility of removing the remaining population from the frequency trench. However, if the external magnetic field is applied to the sample, then the hyperfine levels have a population lifetime in excess of 100ms at a 4K sample temperature. The population lifetime can be further increased by decreasing the temperature of the sample. Thus, the unwanted population can be stored in these long-lived levels. Now, we investigate options available for implementation of this scheme in Tm^{3+}:YAG. The important part of this requires emptying a trench in the inhomogeneously broadened absorption profile of the medium. We, first, theoretically investigate the effect of the pumping pulse on the population in each energy level in Tm^{3+}:YAG after the application of the external magnetic field.

Theoretical and Simulation Results: We have previously demonstrated that a secant pumping chirp pulse (equation (6.1)) can invert almost all, 80%, of the ions absorbing light at that frequency in an optically thick sample of Tm^{3+}:YAG [(118)]. Thus, the preferred choice for the current implementation will be the secant pumping chirp pulse given in equation (6.1):

$$E(t)=\begin{cases} E_0\,\mathrm{sech}\left(\dfrac{t-T_0}{T_E}\right)\sin\left(2\pi\left(\omega_0(T_0-t)-\dfrac{B_c}{2}(T_0-t)-\dfrac{B_c}{T_c}T_E^2\ln\left(\cosh\left(\dfrac{T_0-t}{T_E}\right)\right)\right)\right), & 0<t<T_0 \\ E_0\sin\left(2\pi\left(\omega_0(t-T_0)-\dfrac{B_c}{T_c}\left(\dfrac{(t-T_0)^2}{2}-\dfrac{T_c(t-T_0)}{2}\right)\right)\right), & T_0<t<T_c+T_0 \\ E_0\,\mathrm{sech}\left(\dfrac{t-T_0-T_c}{T_E}\right)\sin\left(2\pi\left(\omega_0(t-T_0)+\dfrac{B_c}{2}(t-T_0-T_c)+\dfrac{B_c}{T_c}T_E^2\ln\left(\cosh\left(\dfrac{t-T_0-T_c}{T_E}\right)\right)\right)\right), & T_0+T_c<t<2(T_0+T_c) \end{cases} \quad (6.1),$$

where the time duration of the secant edge, T_0 is 4 μs, the chirp bandwidth, B_c is 5MHz, the chirp time, T_c is 5μs, and T_E = 0.5 μs was used in the experiment.

Now we present the theoretical investigation for pumping the medium with the secant pumping chirp pulse. In simulations with the theoretical model given in Chapter 4, we assume that this chirp inverts the 80% of the population for the direct transition and find the effective pulse area, θ_a, for direct transition for thin medium approximation. This effective pulse area, θ_a, and experimentally-measured value of the cross-transition ratios are used to find the effective pulse area, $\theta_u = (\mu_u/\mu_a)\theta_a$, and hence the population inversion for the cross transition (cf. Equations (4.17-4.20)). Note that the goal is to implement this scheme in the experiment where the orientation of the magnetic field is along $\theta_B = -15^o \pm 1^o$ (the orientation of a high cross-transition ratio for ions at sites 4 and 6 in the crystal). Thus, in this study, we use all the relevant experimentally-measured parameters for this orientation of the magnetic field.

Now, we apply the first secant pumping chirp pulse with a center frequency ω_0 and bandwidth B_c such that $B_c < \delta_g$. The interaction of the pump pulse at ω_0 with various

ions in Tm^{3+}:YAG is shown in Figure 63. We start with the situation where both of the ground state hyperfine levels are equally populated and consider each ion in the group of ions in Figure 63. The population in each level for each ion in Figure 63 can be tracked using the theoretical model given in Chapter 4. For all ions, most of the population in the excited state will decay away after 1ms, as the lifetime of the excited state is 0.6ms [(71), (72), (51)]. The experimental data in the spectral hole burning study in Chapter 4 shows that most of the population, about 75%, will decay to the intermediate level, and the rest will decay back to the ground state manifold. Now, we allow the excited population to decay and apply a series of these secant pumping chirp pulses to the medium. The pulse sequence is shown in Figure 64. We track the population in each level for all ions in Figure 63.

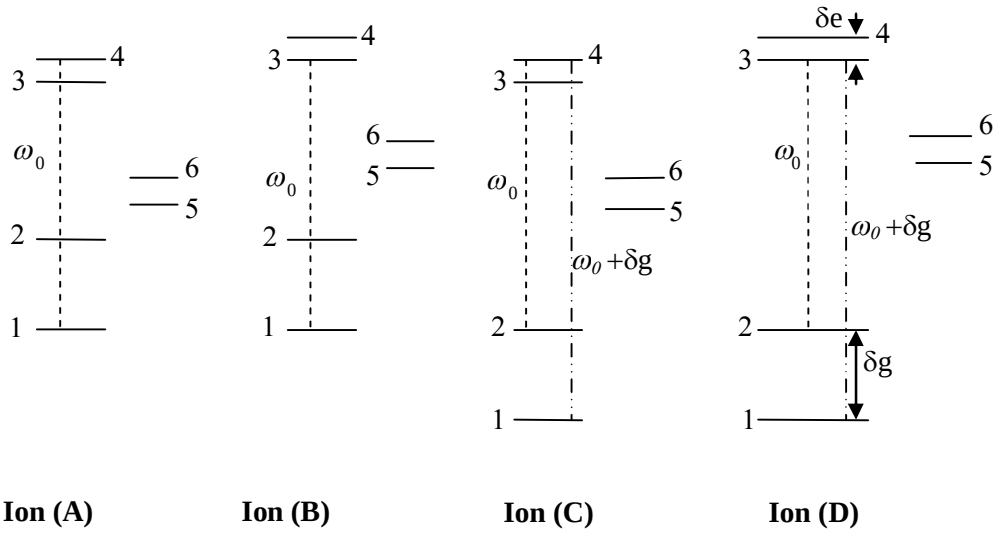

Figure 63: The energy level of ions being addressed with a secant pumping chirp pulse to empty a frequency spectrum around ω_0 in Tm^{3+}:YAG. The hyperfine structure is obtained with an external magnetic field of 440 Gauss which gives hyperfine splitting in the ground state of 11MHz and hyperfine splitting in the excited state of 2MHz

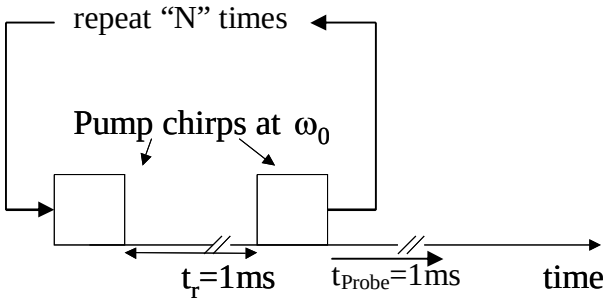

Figure 64: A pulse sequence to empty a spectral trench in the inhomogeneous absorption profile of Tm^{3+}:YAG.

First, we consider the interaction of the secant pumping chirp pulse with the population in ion A. Simulation results are given in Figure 65. As the secant pumping chirp pulse is applied with a repetition rate of 1kHz, the population in ion A is pumped from level 1. The pumped population initially accumulates in levels 2, 5, and 6. As the secant pumping chirp pulse is repeatedly applied to the medium, the population accumulates in level 2. In the meantime, population in the other levels depletes. The population in each level reaches a steady state after about twenty-five repetitions of the secant pumping chirp pulse. Note that level 1 is completely empty after about fifty repetitions of the secant pumping chirp pulse.

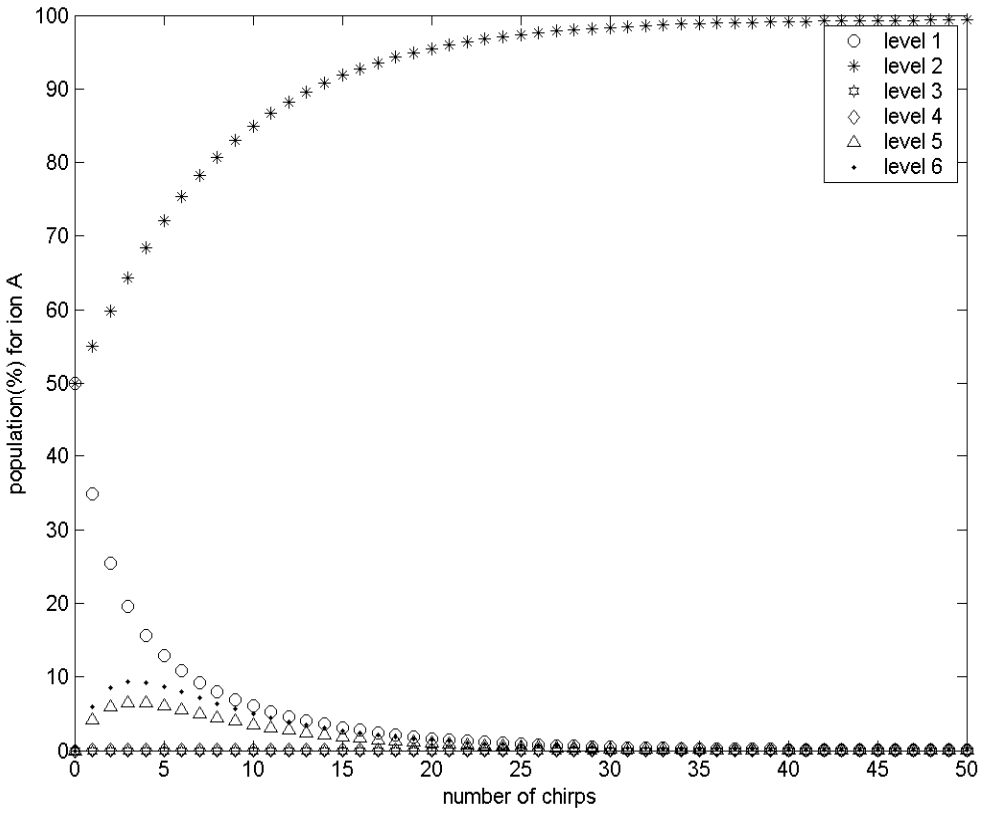

Figure 65: Theoretical results for the population in each energy level for ion A after a 1ms decay from the Nth secant pumping chirp pulse as a function of the number of repeated secant pumping chirp pulses.

Now we track the population in levels for ion B. The population in various levels for ion B shows very similar distribution after a few repetitions (Figure 66), as was the case for ion A. The only difference in this case is the rate of population depletion in level l. In the case of ion B, the rate of population depletion is faster than that of ion A. The reason for the faster population depletion in level 1 is the strength of transition being pumped. The transition strength in the case of ion B is higher than that of ion A. In the case of ion B, the secant pumping chirp pulse is pumping the allowed transition, while in

the case of ion A, the secant pumping chirp pulse is pumping the weakly allowed transition. Again in the case of ion B, after fifty repetitions most of the population is stored in level 2.

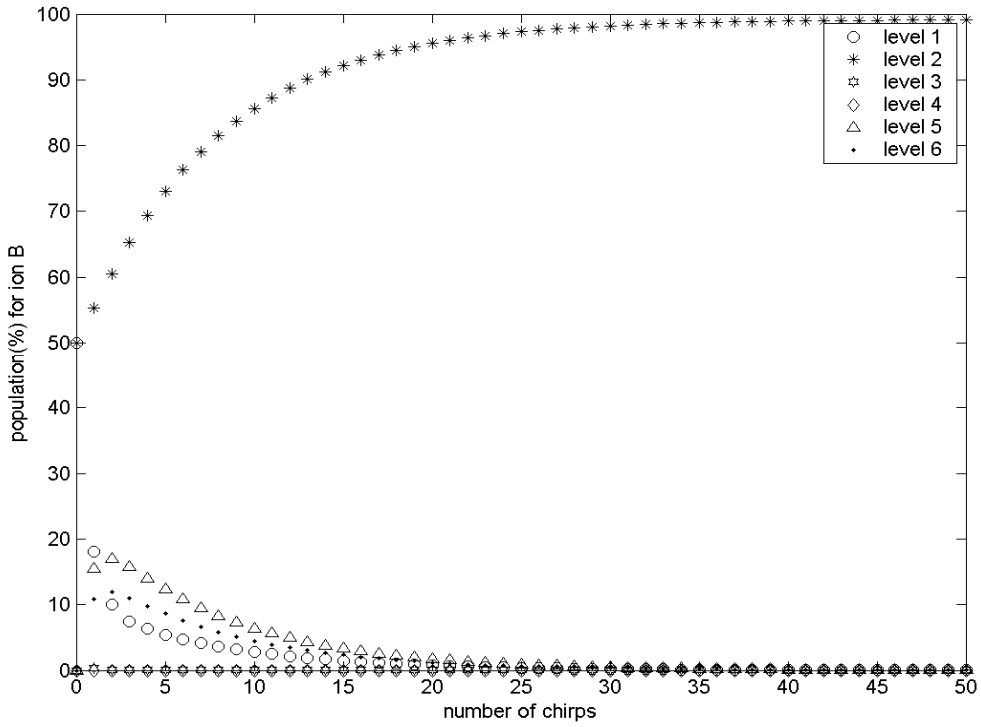

Figure 66: Theoretical results for the population in each level for ion B after a 1ms decay from the Nth secant pumping chirp pulse as a function of the number of repeated secant pumping chirp pulses.

We now consider the population dynamics in various levels for ion C as multiple repetitions of the secant pumping chirp pulse are applied. Simulation results are given in Figure 67. Level 2 of ion C is being pumped with the secant pumping chirp pulse, and this transition is an allowed transition. Thus, the population depletion rate for level 2 is the same as in the case of ion B, but is faster than that of ion A. Again, initially,

population accumulates in level 5 and level 6. The system reaches a steady state after about twenty-five repetitions of the secant pumping chirp pulse. Most of the population is removed from level 2 and is stored in level 1 after fifty repetitions of the secant chirp pulse (Figure 67).

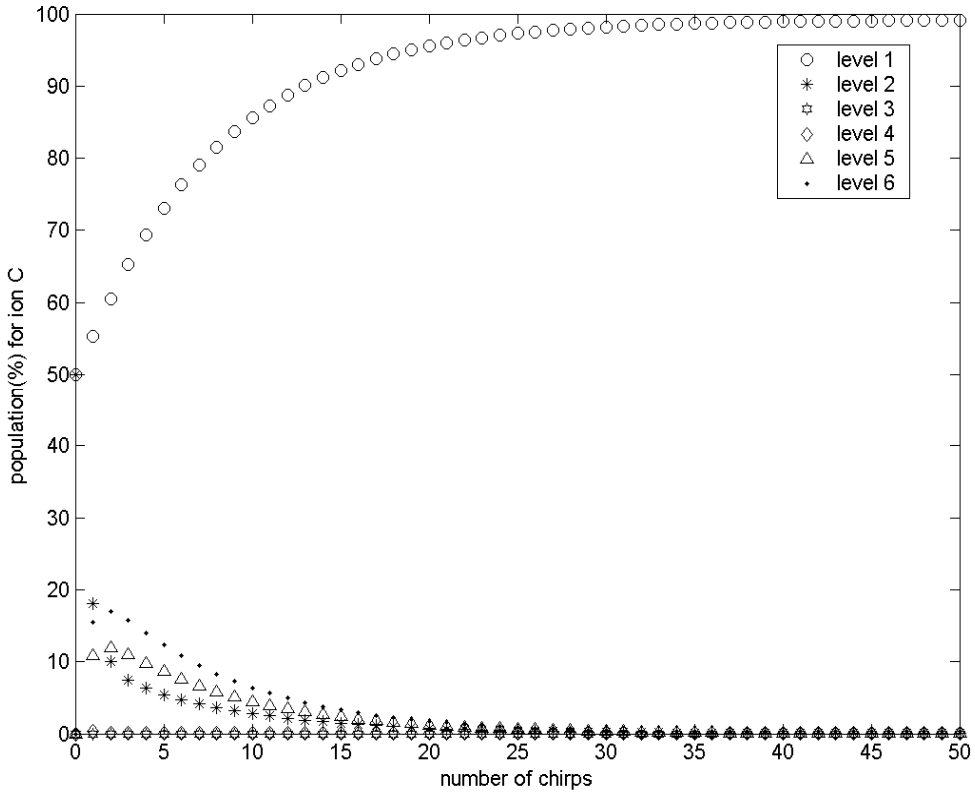

Figure 67: Theoretical results for the population in each level for ion C after a 1ms decay from the Nth secant pumping chirp pulse as a function of the number of repeated secant pumping chirp pulses.

For ion D, levels 2 and 3 are resonant with the secant pumping chirp pulse, and this is a weakly allowed transition. Simulation results in Figure 68 show the population in each level for ion D. In this case, the depletion of the population in level 2 is expected to

be slower. The rate of the population depletion will be similar to that of the case of ion A. The results for ion D follow a similar trend as was the case for ion A, as expected. Again, for this case, after fifty repetitions of the secant pumping chirp, the population from level 2 is removed and is stored in level 1 as shown in Figure 68.

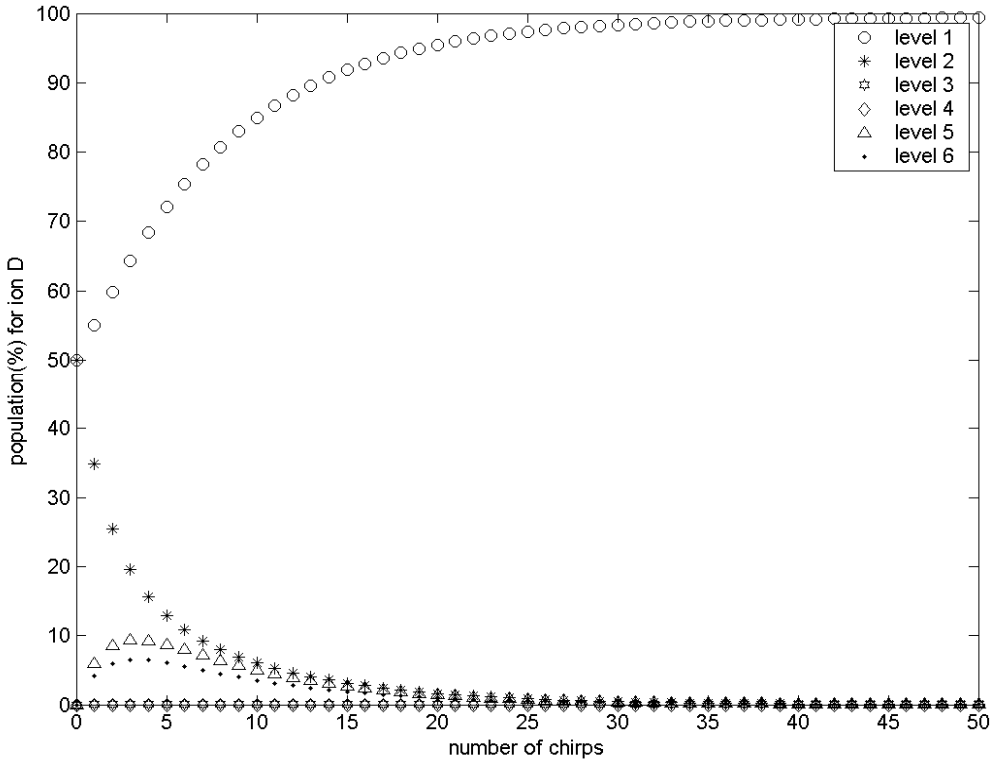

Figure 68: Theoretical results for the population in each level for ion D after a 1 ms decay as from the Nth secant pumping chirp pulse as a function of the number of repeated secant pumping chirp pulses.

Thus, with the chosen secant pumping chirp pulse sequence, we have managed to remove the population from the certain region in the inhomogeneously broadened absorption profile of the medium. The removed population is stored in the hyperfine level that is outside the region of interest. The population lifetime for the ground state

hyperfine levels is about 100 ms at 4K, as measured in Chapter 4. Thus, the population decay between hyperfine levels can be ignored for the time of the experiment.

Another scheme recently proposed pumping the population from the excited state $^3H_4$ to the intermediate level $^3F_4$ with another laser at 1500 nm [(119)]. This scheme will still need to store population in hyperfine levels and will introduce considerable complexity to the system. In our experimental demonstration, we did not use a second laser.

Now, using the results of the simulation (Figure 65-Figure 68), we can estimate the number, N, of secant pumping chirps needed to empty a trench in the inhomogeneously broadened absorption profile of the medium. Note that if the chirp sequence in Figure 64, with N=50, is applied to these levels in Figure 63, then an empty trench can be obtained in the absorption profile of the medium. Before we implement this scheme in the experiment, we first describe the experimental details.

Material and the Frequency Stabilized Laser Source

For all the experiments presented in this chapter, thulium-doped in YAG with 0.1% atm. thulium concentration supplied by Scientific Materials Corporation, Bozeman, MT was used. The peak absorption at 793nm for this concentration is ~0.19/mm. The length of the sample was 20mm. In order to access the transition in the material, a commercial external cavity diode laser from New Focus Vortex laser was used. This diode laser provides us with about 12 mW of laser power, which is insufficient for this experiment. The laser was amplified using a commercial tapered amplifier chip from

Eagleyard. The amplifier chip was custom-mounted. This set-up provided us sufficient power for the experiment, about 300mW. The diode laser was frequency stabilized using a spectral hole burning locking technique [(51)] giving a stability, typically, of about 20kHz over 1ms. The stabilization scheme was the same as described in Chapter 4.

Experimental Set-up

The experimental set-up is shown in Figure 69. Most of the components are similar to those shown in Chapter 4, Figure 15. We have an elaborate detection scheme in this experimental set-up. The elaborate detection scheme is needed because in this experiment, it is required to measure both the phase and the amplitude of the optical pulse. In order to achieve phase and amplitude detection, a heterodyne detection scheme is followed. In this scheme, the laser beam from an amplified frequency stabilized laser source is divided into two beams using a beam splitter with almost 90% of the light used for the experiment and the rest going to a reference beam. The beam used for the experiment goes through two acousto-optics modulators (AOMs), a half-wave plate, a polarizer, and the sample. The reference beam passes through a half-wave plate, a polarizing beam cube, and another half-wave plate. This arrangement for the reference beam allowed continuous control over the power and polarization of the beam. Both beams were combined at a 50/50 beam splitter.

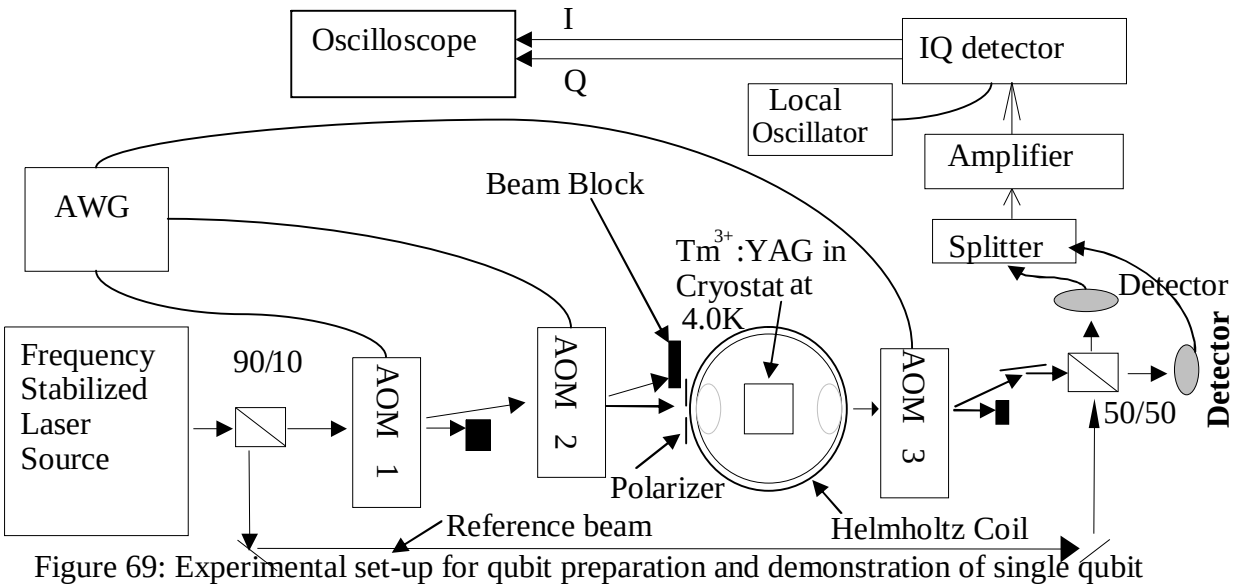

Figure 69: Experimental set-up for qubit preparation and demonstration of single qubit operations.

In the experiment, an arbitrary waveform generator (AWG) provided the radio frequency (RF) source at 210MHz for AOM 1, and the beam with its frequency up-shifted 210MHz from the laser frequency was fed to AOM2. Again, an RF signal from AWG at 120 MHz was used to drive AOM2, and the final beam from both AOMs was 90 MHz up-shifted from the laser beam. This beam was then directed to the sample in the cryostat with a beam waist in the sample of about 100 μm. Another acousto-optics modulator, AOM3, after the sample, allowed us to block the strong signal in the pulse sequence and provided an output beam that was up-shifted 10MHz from the reference beam.

The polarization of the reference beam and the overlap of the two beams at 50/50 beam splitter were adjusted to get maximum amplitude modulation. This beat signal was fed to two amplified silicon detectors (Thorlabs PDA 155) of bandwidth 50 MHz for

balanced detection. Theoretical and experimental analyses show a reduction in noise with the balanced detection scheme as compared to the case of detection with a single detector [(120), (121), (122), (123)].

The output from each detector was combined in a beam splitter/combiner and then was filtered with 10MHz band pass filter of 3MHz bandwidth. The beam splitter/combiner in the current system takes two inputs from both the detectors and imparts a phase of 180^o on one input and then combines both the inputs to give one output signal. The resultant signal from the beam splitter/combiner was amplified. The output from the beam splitter/combiner and the local oscillator signal at 10MHz were fed into Mini-circuits' 2FMIQA-10D I&Q detector. This detector provided two outputs with one in-phase output, I, and another in-quadrature output, Q, with the provided local oscillator signal. These two outputs were used to measure the amplitude and the phase of the signal.

Experiment Results for the Ensemble Selection

In the experiment, a sample of Tm^{3+}:YAG with 0.1% atm. thulium and a material absorption length of 2.87 was vapor-cooled with the liquid helium to 4K. Here the absorption length was smaller than the peak absorption of 3.8, as the laser was detuned from the center of the absorption line. The magnetic field was kept fixed at 400 Gauss. The sample was positioned in the direction with the magnetic field for the highest cross-transition ratio for ions at sites 4 and 6, i.e., $\theta_B = -15^o \pm 1^o$ with the <001> direction. The strength, 400 Gauss, and the orientation, $\theta_B = -15^o \pm 1^o$, of the magnetic field provided

us the hyperfine structure in Tm^{3+}:YAG. The excited state splitting for this case was 2.2MHz, and the ground state splitting for this case was 11MHz.

A secant pumping chirp pulse, given in equation (6.1), of 5MHz bandwidth centered around -11MHz was repeatedly applied to the medium. The power of the secant chirp pulse was the equal to the power of a single frequency pulse having 1MHz Rabi frequency. The chirp rate was set to 1MHz/1μs. The chirp with similar parameters can invert 80% of the population for the optically allowed transition in Tm^{3+}:YAG [(118)]. In the experiment the secant pumping chirp pulse is repeated fifty times at a repetition rate of 1kHz as suggested in Figure 64. The absorption in the medium was probed with a 40MHz/500μs weak probe chirp. The absorption spectrum after the repeated application of the secant pumping chirp pulse, as measured with the probe chirp, is shown in Figure 70.

The scale on the vertical axis in the absorption spectra in all proceeding experimental results was obtained as follows. First the material's initial absorption length, $\alpha_0 L$, was experimentally measured using the absorption measurement. In the next experiment, the medium was scanned with a 40MHz/500μs probe chirp. This measurement gave us $I_1 = I_0 e^{-\alpha_0 L}$. In the next measurement, fifty secant pumping chirps as demanded by Figure 64 were applied to the medium and the medium was again scanned with the weak probe chirp. This second measurement gave us $I_2 = I_0 e^{-\alpha L}$. Using these two measurements, the absorption spectrum was obtained as $\alpha L = \alpha_0 L - \ln(I_2/I_1) = -\ln(I_2/I_0)$.

Note that the bandwidth of the emptied trench is higher than the bandwidth, 5MHz, of the secant pumping chirp pulse. The broadening in the edge of the trench in the spectrum is due to the overlap of side hole spectra with the spectrum of secant pumping chirp pulse. The experimental result for the absorption spectrum of the medium in Figure 70 agree very well with the simulation results in Figure 65 - Figure 68 as both results show that the medium is nearly transparent around -11MHz with 5MHz bandwidth.

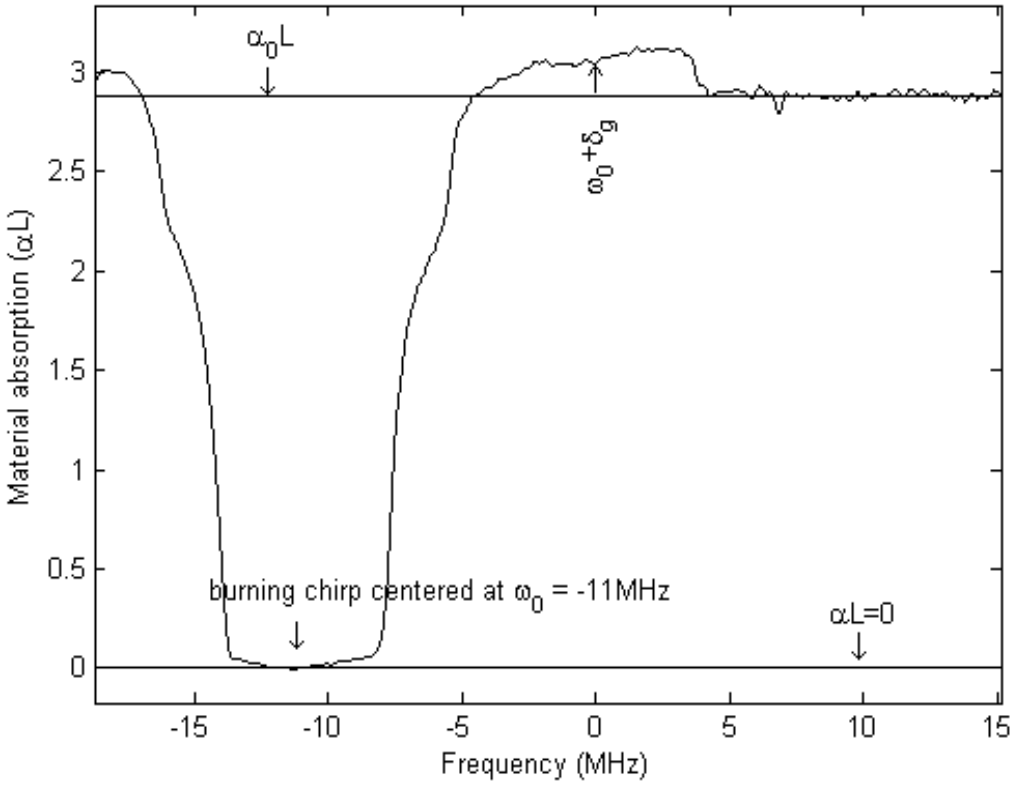

Figure 70: Experimental results for the spectrum of the medium at 4K. The spectrum shows the emptied trench of 5MHz width in the inhomogeneously broadened absorptive medium. The initial absorption in the medium was $\alpha_0 L = 2.87$.

The ions in the emptied trench, shown in Figure 70, around $\omega_0 = -11MHz$ were selected by burning ions back in the trench. The burn-back pulse was used to select an

ensemble of ions in the trench [Figure 70]. This burn-back pulse at $\omega_0 + \delta_g$ is applied to the medium after the coherences in the medium have dissipated. The pulse sequence to achieve that objective is shown in Figure 71. The burn-back pulse at $\omega_0 + \delta_g$ interacts with ions C and D (Figure 63) and two other sets of ions. Apart from ions C and D, the contributions of the two other sets of ions lie outside the region of interest. However, the burn-back pulse does not interact with ions A and B (Figure 63). Therefore, the contributions from ions other than ions C and D are ignored, as those contributions lie outside the region of interest, i. e., the trench at $\omega_0 = -11MHz$. Thus, the burn-back pulse pumps the populations from ions C and D back into the trench at ω_0.

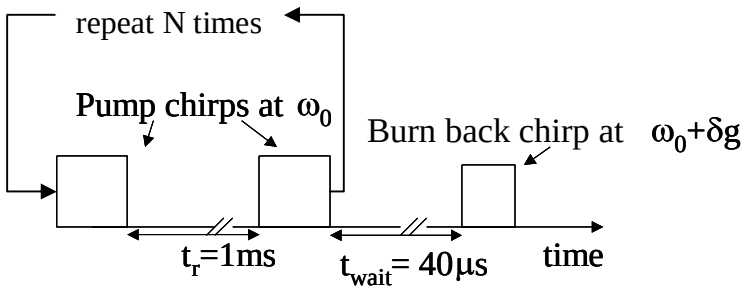

Figure 71: A pulse sequence to select an ensemble of ions. Here δ_g is the hyperfine splitting for the ground state manifold. An ensemble of ions is selected in the emptied trench using a burn-back pulse after N repetitions of the broadband pump chirp pulse.

In the experiment, a 20 μs long narrowband burn-back chirp of bandwidth 500kHz centered around $\omega_0 + \delta_g = 0MHz$ was applied to the medium. This burn-back pulse burned ions back at $\omega_0 = -11MHz$ in the emptied trench. The experimental results in Figure 72 show the spectrum of the medium after the secant pumping chirp and the burn-back pulses are applied to the medium. Note that the absorption feature at $0MHz$ is

broader than the bandwidth of the burn-back pulse. The broadening of the main feature at $0MHz$ is due to the excitation of ions at other sites, in this case ions at site 2, that have splitting such that $\delta_2^e < \delta_{4,6}^e$, for the experimental settings of the strength, 440 Gauss, and orientation, $\theta_B = -15^o \pm 1^o$, of the applied magnetic field. In this case, thulium ions at site 2 in the crystal have 1MHz excited state splitting. Another factor contributing to the broadening at 0MHz is the stray light affecting the zero level of the signal and, hence, giving a wrong normalization factor for the data. However, the broadening of the feature at $\omega_0 + \delta_g = 0MHz$ does not affect the results presented here.

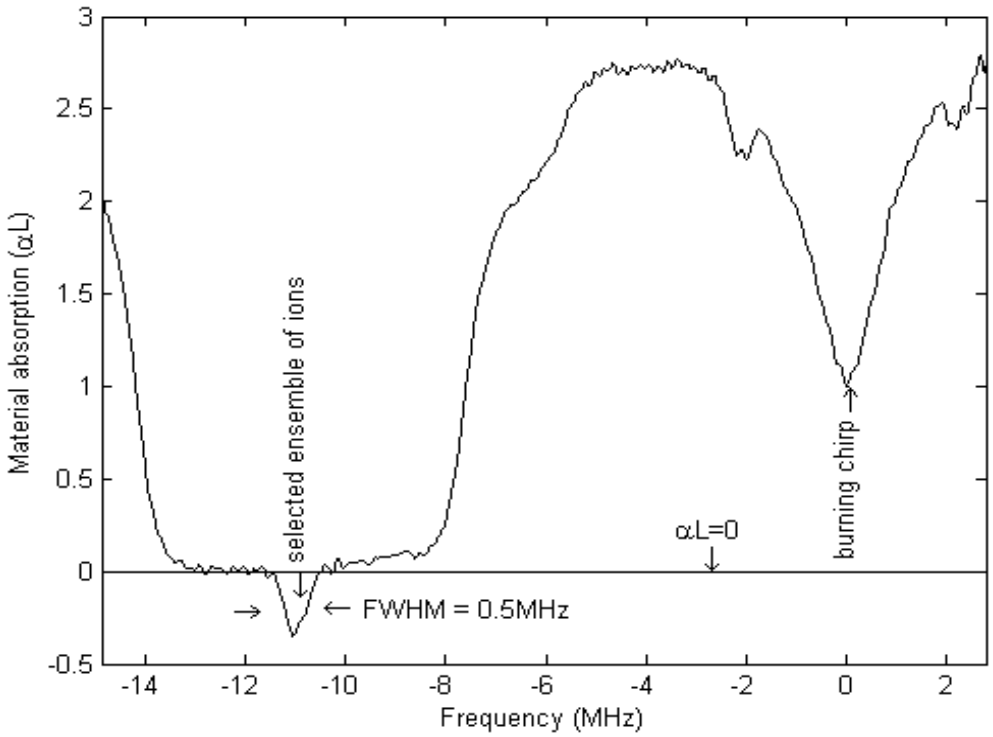

Figure 72: The spectrum of the medium after the application of the pulse sequence in Figure 71. The spectrum shows burned back ions at $\omega_0 = -11MHz$ in the emptied trench with a burn-back chirp applied at $\omega_0 + \delta_g = 0MHz$.

In the current experiment, the inhomogeneous width of the selected ensemble of ions was about $0.5MHz$, which is the same as the bandwidth of the burn-back chirp. The ions in the selected ensemble can be addressed with a single Rabi frequency using a moderate power laser. Note that the bandwidth of the burn-back ions can always be adjusted by choosing the bandwidth of the burn-back pulse. The correlation between the bandwidth of the burn-back pulse and the bandwidth of the selected ensemble of ions was experimentally verified. We noted that the peak of the selected ensemble of ions drops with the drop in the bandwidth of the selected ensemble of ions for constant power and chirp duration.

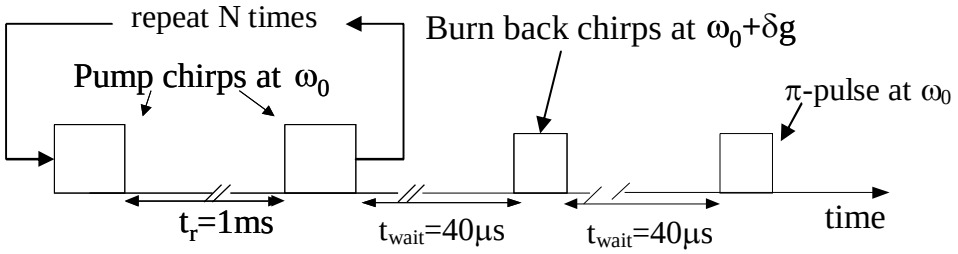

Figure 73: A pulse sequence used to initialize the selected ensemble of ions to the lowest energy Eigen-state for the demonstration of single qubit operations

Note that, these ions in the selected ensemble in Figure 72 are not in the ground state, as is shown by the negative absorption change in the spectrum in Figure 72. However, these ions in the selected ensemble of ions can be initialized to any state using a laser pulse. An optical pulse having Rabi frequency > 500kHz and duration < 2μs will address all the ions in the selected ensemble in Figure 72 uniformly. Now, a single π-

pulse satisfying the conditions for uniform excitation of all ions in the trench is applied to the ensemble at $\omega_0 = -11MHz$. The sequence of pulses needed to initialize the ions in the ensemble is given in Figure 73. The spectrum of the medium, after application of the sequence in Figure 73 is shown in Figure 74. In this spectrum, the selected ensemble of ions has a positive absorption, which signifies that the ions are in the lowest energy Eigen-state.

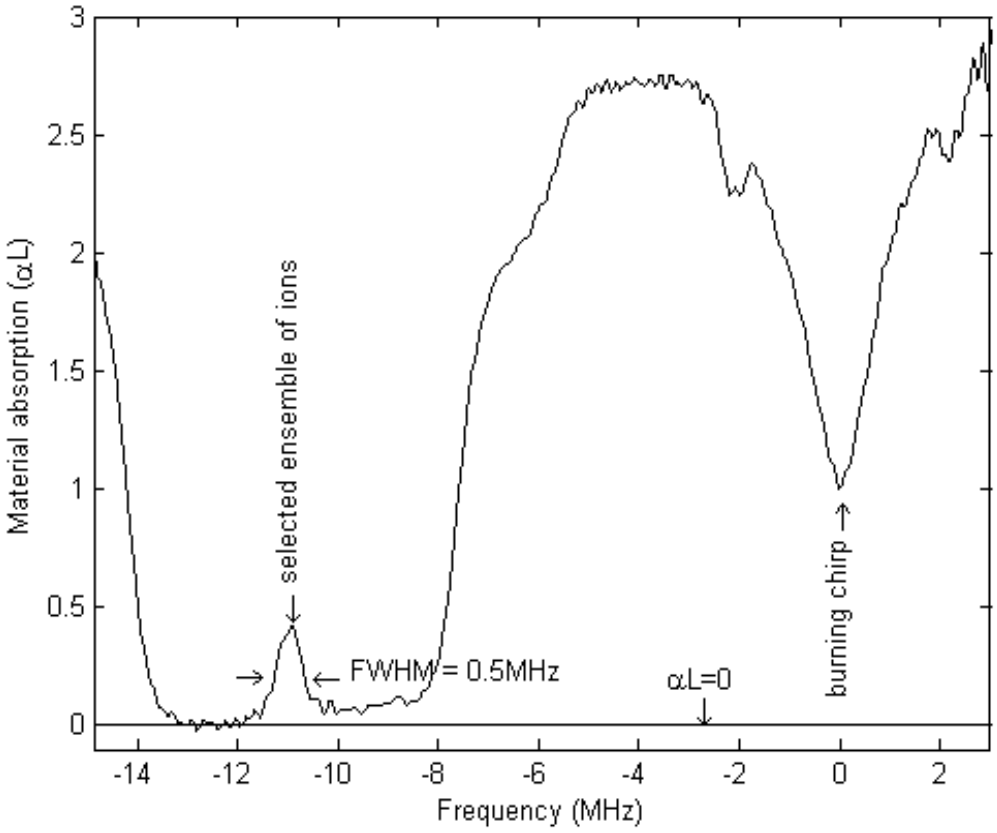

Figure 74: The transmission spectrum from the medium shows the burned back ions in the lowest energy Eigen-state in the emptied frequency. Since the number density of 0.1% thulium-doped in YAG is 10^{19} ions/cm^3, the laser pulse of bandwidth > 0.5MHz with a spot size of about 100μm will be interacting with about 10^{13} ions over a 20mm long sample.

Thus, we have successfully initialized the selected ensemble of ions to the lowest energy state. This also suggests that the optical pulse was addressing all the ions in the ensemble uniformly. This experimentally demonstrates that it is possible to address the selected ensemble of ions uniformly. This experiment verifies that our calibration of $\alpha L=0$ was accurate.

Characterization of the Selected Ensemble of Ions

Uniform Excitation of the Selected Ensemble of Ions

First, the inhomogeneous width of the selected ensemble of ions was measured by scanning the medium with a weak chirp pulse. The experiment was designed to show that an ensemble of ions can be addressed with a single Rabi frequency. This experiment involves the excitation of the selected ensemble with the pulses having definite pulse areas. The experimental results presented in Figure 74 have already demonstrated to some extent that the ions in the selected ensemble can be excited with a single Rabi frequency, as a single π-pulse was able to invert all the ions in the selected ensemble. In the case discussed here, a series of π-pulses are applied to the selected ensemble. The ion selection process was the same as described in Figure 71. Since the selected ensemble has a 500kHz width, a pulse with Rabi frequency and bandwidth > 500kHz will be able to address all the ions in the selected ensemble with a single Rabi frequency. The sequence of the pulses is shown in Figure 75, and the experimental implementation for selecting an ensemble was described earlier in the text.

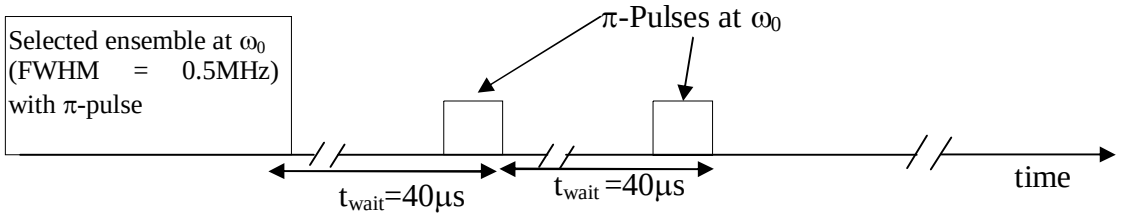

Figure 75: A pulse sequence used to characterize the selected ensemble of ions for its interaction with the optical field.

In the experiment, a sample of 0.1% atm. Tm^{3+}:YAG was vapor-cooled in the cryostat with liquid helium to 4K. The selected ensemble, similar to the one given in Figure 74, was addressed first with a π-pulse having a Rabi frequency 1.3MHz and duration 400ns. The resultant transmission spectrum of the probe pulse reflects the state of ensemble as shown in the Figure 76 (left). The spectrum indicates that almost all the ions are excited uniformly, and these ions are now in the excited state, as indicated by the negative absorption of the selected ensemble. A second π-pulse with the same parameters as the first π-pulse was applied to the ensemble, and all the ions in the ensemble were brought back to the ground state (Figure 76 (right)) as indicated by the positive absorption of the selected ensemble. These results show that it is possible to address all the ions in the selected ensemble with a single Rabi frequency. This shows that all the ions in the selected ensemble of ions can be addressed uniformly. Thus, the ions in the ensemble can form a qubit for the implementation of quantum operations. We were unable to tailor a single 2π pulse that can address all the ions in the ensemble uniformly because of the power limitations.

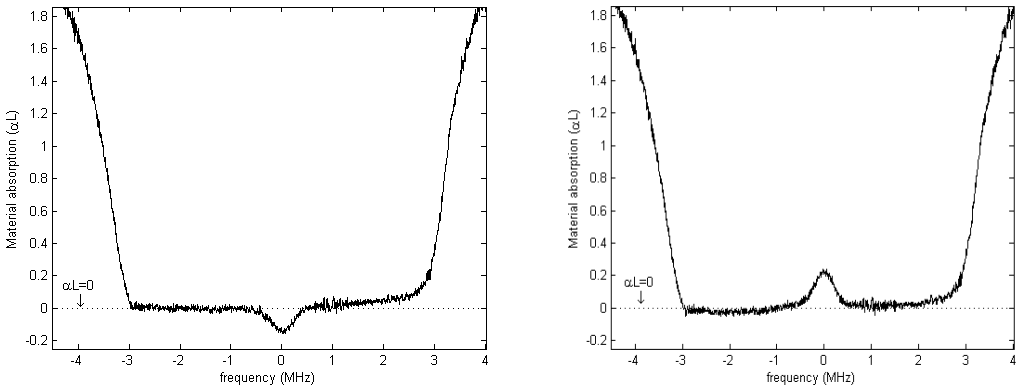

Figure 76: The selected ensemble, in Figure 74, after it was addressed with a single π-pulse (left) and two π-pulses (right). Each π-pulse has a Rabi frequency 1.3MHz at the center of the Gaussian spatial beam, and its pulse width was 400 ns.

Optical Coherence Time of the Selected Ensemble of Ions

The material coherence time for the optical transitions for Tm^{3+}:YAG has been studied [(29)]. The measurements for the material coherence time in reference (29) have shown that de-coherence in the material for optical transitions at a low temperature, 1.5K, is due to the spin fluctuations of nuclei in the host material. Thus, it was anticipated that the coherence time of the selected ensemble in Figure 74 will be the same as the material coherence time. This was experimentally verified by measuring the coherence time of the selected ensemble shown in Figure 74. We used the 2-pulse echo technique to measure the coherence time. In this technique, an interacting pulse creates the coherence in the medium at time t_1. The macroscopic coherence in the medium dephases, as each ion in the medium evolves in time according to its detuning from the laser frequency. However, a second interacting pulse at a later time t_2 can rephase the coherence. This second pulse reverses the frequency of the evolution of each interacting ion in the medium. Consequently, a perfect rephasing in the medium gives a coherent signal at $2*(t_2-t_1)$. This

rephased signal is called a 2-pulse echo (2PE). Note that the maximum rephased signal can be obtained if the area of the first pulse is $\pi/2$, and the area of the second pulse in the 2PE sequence is π. The coherence in the medium is usually measured by measuring the strength of rephased signal at different times. The strength of this 2PE and the separation between the two pulses in 2PE sequence are related as $I_{echo} = I_0 e^{-4^{t_{21}}/T_2}$ [(112)], where $t_{21} = (t_2 - t_1)$ and T_2 is the material dephasing time. Thus, time-dependent measurements of the echo intensity will provide the material dephasing time.

In this experiment, the 0.1% atm. Tm^{3+}:YAG sample was vapor-cooled to 4K. Here, the first pulse in the 2PE sequence has pulse area $\pi/2$ and 250ns, duration while the second pulse in the 2PE sequence has pulse area π and 500ns duration. The Rabi frequency of each pulse was fixed at 1MHz. We first measured the background level in the emptied trench (Figure 70) by applying the 2PE sequence in the trench. We did not get any detectable echo signal from the background ions in the emptied trench. This means that the contribution from the background ions in the trench will be negligible in the echo signal for 2-pulse echo. This is another verification that the background is truly at $\alpha L=0$. The results in Figure 77 (dotted line) show a 2-pulse echo signal just from the background ions in the emptied trench. The results in Figure 77 (dotted line) show that the medium is nearly transparent in the trench. This means that the 2PE sequence will probe the coherence of the selected ensemble. Now, we apply the 2PE sequence to the ions in the selected ensemble given in Figure 74. An example of a 2-pulse echo signal from the ions in the selected ensemble in Figure 74 is shown as a solid line in Figure 77.

Note that the width of a 2-pulse echo signal is about 2μs, which is much longer than the width of the two pulses used to create coherence in the ensemble. However, the width of the echo signal is about the same as the inverse width of the selected ensemble in Figure 74. The correspondence between the two widths provides an alternate way of measuring the spectral width of the selected ensemble.

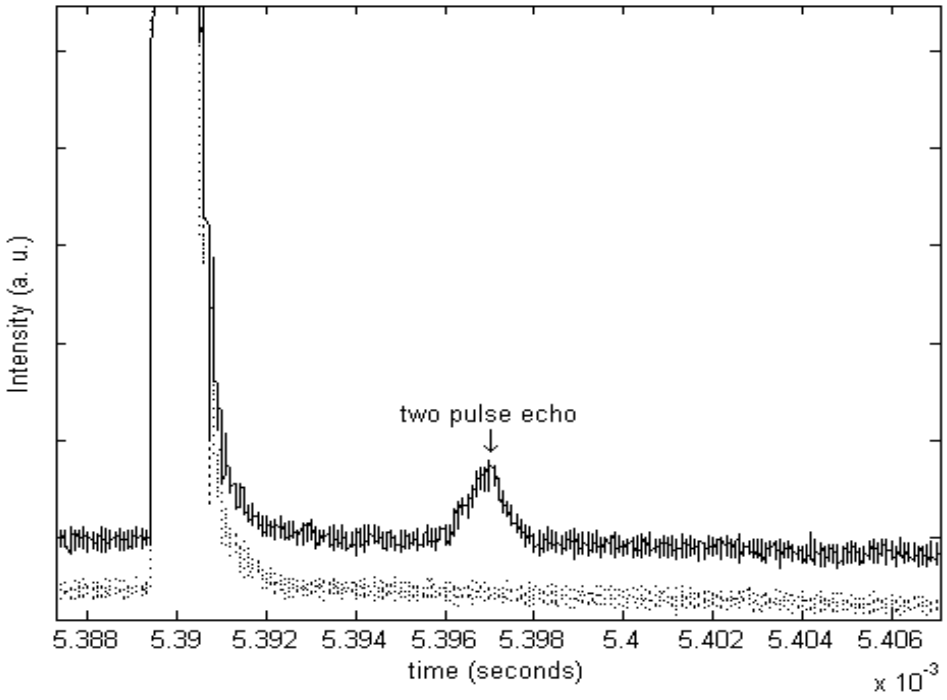

Figure 77: The dotted line is the 2-pulse echo signal from the background ions in the trench in Figure 70. The solid line is the 2-pulse echo signal from the selected ensemble of ions in Figure 74. The vertical scale in the plot is shifted to show two signals.

Now we vary the delay between two pulses in the 2PE sequence and record the intensity of the echo signal. The data for the echo intensity and corresponding delay is plotted in Figure 78. The data set in Figure 78 shows that the echo decays exponentially with the delay between two the pulses in the 2PE sequence. The exponential decay of the

echo gives the material coherence time of $(35 \pm 0.70)\mu s$. This value of the material coherence time is about the same as the coherence time obtained using the full inhomogeneous profile of the medium at 4K [(29)].

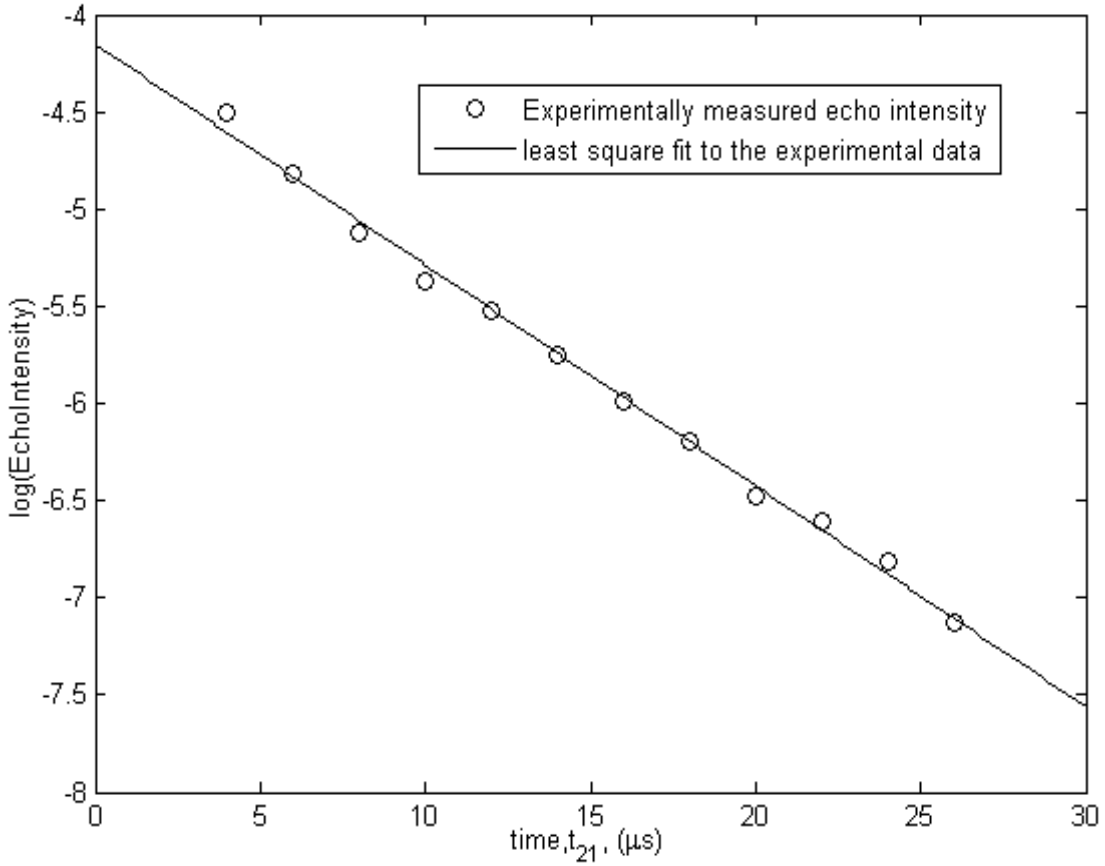

Figure 78: Experimental results for the measured echo intensity as a function of the delay between the two pulses in 2PE sequence. The least square fit to the experimental data gives a coherence time of $(35 \pm 0.70)\mu s$ at 4K.

Now we know the basic characteristics, including the line-width, the coherence time, and the peak absorption of the selected ensemble. The next step will be to use this selected ensemble of ions as a test-bed and implement the single qubit operations.

Single Qubit Operations Using an Ensemble of Ions

The selected ensemble of ions, as per Figure 74, is used to demonstrate two basic rotations of the Bloch vector, as discussed in Chapter 5. The experimental demonstrations of the Bloch vector rotation of the selected ensemble were performed using 0.1% atm. Tm^{3+}:YAG. The experimental set-up and the detection system are the same as given in Figure 69. In all the experimental demonstrations, the selected ensembles of ions were similar, as shown in Figure 74, with a fixed bandwidth 0.5MHz and peak absorption 0.3. Before we implement the single qubit operation on the selected ensemble of ions, we first present the results for the calibration of our detection system.

Calibration of the Detection System

Detecting the Phase of a Laser Pulse: Initially the stability of the detection scheme was tested with a single laser pulse that was not interacting with the medium. The phase of the laser pulse was varied using an arbitrary waveform generator (AWG), while the amplitude of the pulse was kept fixed. The in-phase and in-quadrature components of the signal were detected using the I & Q detection scheme, as outlined earlier. The error in the measured phase versus the input phase sets the lower limit on the error in our detection scheme. We postulate that the error is due to the vibrations in the system.

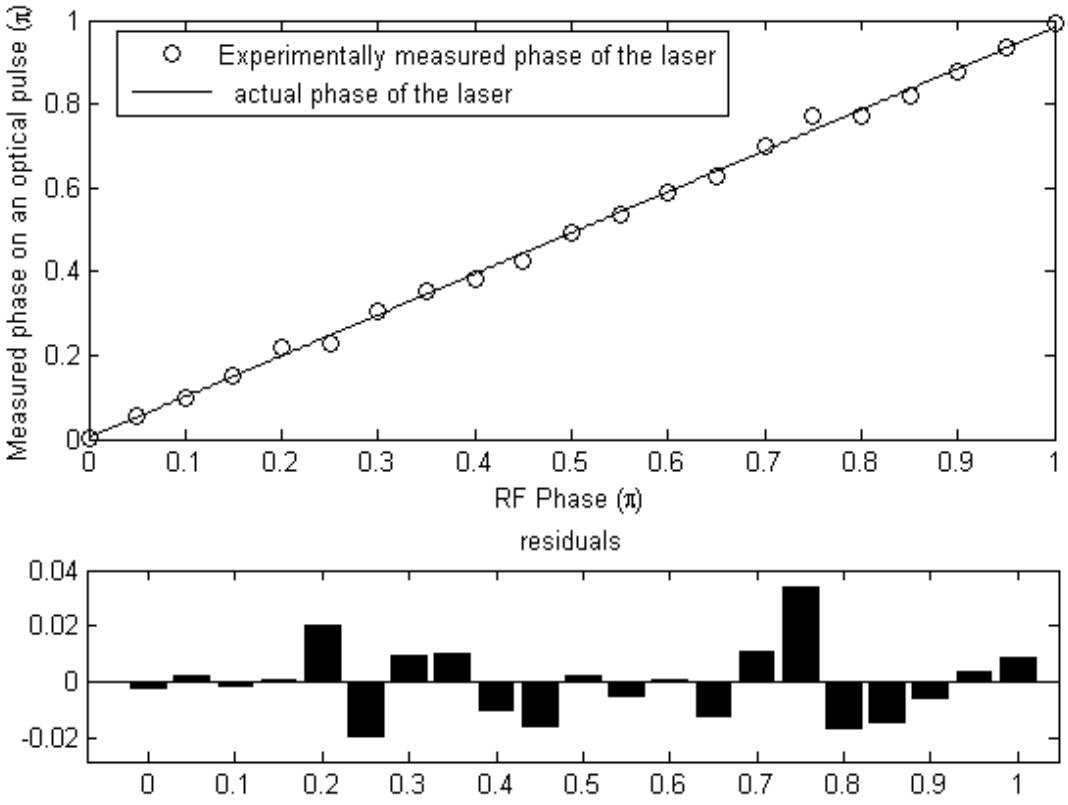

Figure 79: The calibration results of the phase detection set-up used to measure the phase of an optical signal. The lower plot shows the residual error in each measurement with a maximum error of about 0.03π.

The results in Figure 79 show the measured phase is in quite good agreement with the input phase. We varied the power of the optical pulse, and a series of single shot measurements were performed to calibrate the detection system. The standard deviation in the phase detection of all those single shot measurements was 0.013π . The calculated signal-to-noise-ratio (SNR) of about 640 would predict a root mean square of 0.0125π. There are a few other possible sources of the excess phase error in this measurement. One source of error in the measurement is the jitter in the clock of the RF source used for local

oscillator. Other possible sources may be the vibrations in mirrors, thermal noise. This experiment defines the error inherent in our detection system, which will always be present in our phase detection measurements.

Detecting the Phase of the 2-Pulse Echo: In another experiment, the performance of the phase detection set-up was tested by detecting the phase of the 2PE in a coherent transient experiment. In this case, 0.1% atm. Tm^{3+}:YAG was vapor-cooled to 4K, and the two pulses required by the 2PE sequence were applied to the selected ensemble, shown in Figure 74, whose inhomogeneous width was 500kHz. The pulse length of each pulse in the 2PE sequence was 500 ns, and powers of both pulses were optimized to give a maximum 2-pulse echo signal. In the experiment, the phase of pulse 2 was fixed at 0 and the phase of pulse 1 was varied.

Theoretical results show that for such a pulse sequence, the phase of the 2-pulse echo changes linearly with the change in the phase of pulse 1. Experimental results (circles) in Figure 80 show that the phase of the 2-pulse echo changes linearly. The spread in data points in the experimental data is attributed to a low signal-to-noise ratio. This can be seen by considering only the additive noise in signal, $n(t)$, and its influence on the phase error, $\varphi_N(t)$, as $n(t)+A'(t)\cos(\omega_l t+\varphi_0)=A_0\cos(\omega_l t+\varphi_0+\varphi_N)$ where $\varphi_N << \pi$ ω_l is the laser frequency, $A'(t)$ is the amplitude of the signal, $A_0(t)$ is the measured amplitude of the signal, and φ_0 is the phase of the signal. To the first order, $A'(t)$ does not affect the phase noise and the root mean square of the phase noise, σ_{noise}, can be written as

$$\left(\sigma_{noise}\right) \cong \sqrt{\frac{\left\langle n(t)^2 \right\rangle}{\left\langle A_0{}^2 \right\rangle}} = \sqrt{\frac{P_N}{P_A}} \equiv \frac{1}{\sqrt{SNR}} .$$

This result shows that, the root mean square of the phase noise will be higher for the case that has a lower SNR.

Now, we analyze the results for 2PE experiment in Figure 80. Note that the measurements (Figure 80) for 2PE experiment indicate that the error is much higher in these measurements as compared to the inherent error in the phase detection system (Figure 79). The standard deviation in the phase measurement for single shot measurements for four different experimental data sets are 0.13π, 0.12π, 0.097π, and 0.08π, while corresponding SNR for these data sets are 100, 180, 250, and 270. These data show that the lower SNR corresponds to the higher phase error in the measurements. The SNR in these data sets are lower than the case in Figure 79 for which the SNR for the data set (640) was higher. Other possible sources of error are jitter in the mirrors, thermal noise, and also vibration of the sample in the cryostat. The error due to the laser instability was discounted, as the frequency of the laser was stabilized using the spectral hole locking technique [(51)]. This locking technique gave us the frequency stability of the laser about 20kHz over a millisecond. The stability of the laser was confirmed by burning a 20kHz and scanning the medium after a millisecond. This provided us a higher frequency stability of the laser than the required stability, 100kHz over 1ms, in the laser at 4K.

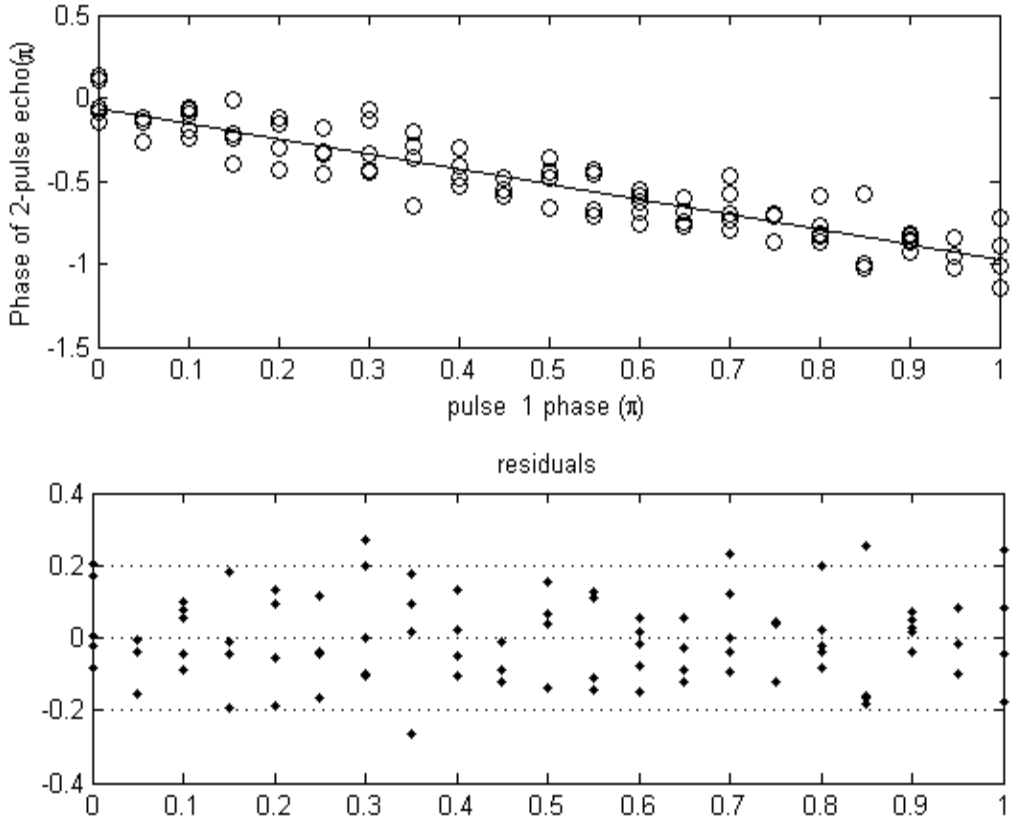

Figure 80: Experimental results (circles) of phase detection system for the 2PE sequence. Here, the phase of the second pulse in the 2PE sequence was fixed, and the phase of the first pulse was varied. The circles represent six single experimental acquisitions; the solid line is the expected theoretical result. The bottom plot shows the error in the experimental data compare to the theoretical result.

Now we use the single experimental acquisitions and find the average results for the measured phase of the echo in the 2PE experiments. The results of such an average are shown in Figure 81. The results show that the error in the averaged data is reduced. The reduction in the error for this case implies that the error is random. This discounts the possibility of a systematic error in the detection system. The standard deviation in the phase measurements is 0.098π, as calculated from the averaged data in Figure 81. The higher standard deviation in the phase measurements for the 2PE experiment is attributed

to lower SNR for this case, as compared to the case when a single detection pulse was used (cf. Figure 79).

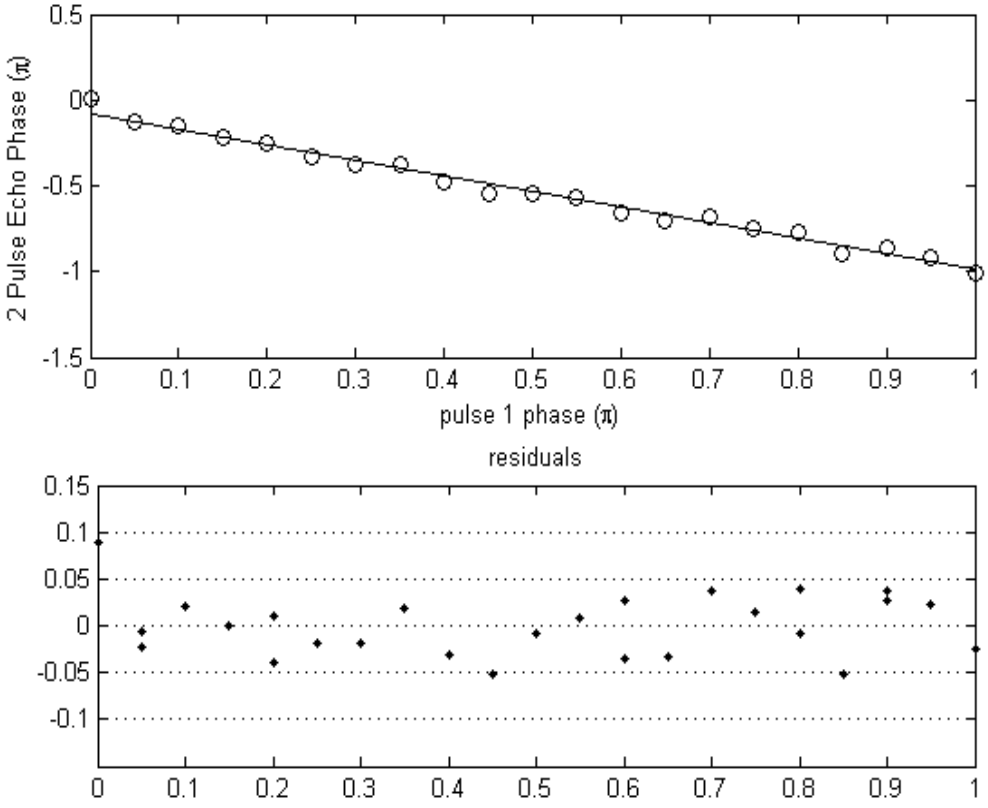

Figure 81: The average (circles) of the experimental data in Figure 80 and the expected theoretical result (solid line). The bottom plot is the comparative error.

Now, we implement the single qubit operation in the selected ensemble and use the well-characterized detection system for the measurements.

Demonstration of the Bloch Vector Rotation about the Z-axis

The selected ensemble of ions used for the demonstration of the two Bloch vector rotations is shown in Figure 74. We first present the results for the implementation of rotation about the z-axis. As explained in Chapter 5, this rotation can be detected by

using a photon echo experiment. All characteristics of the selected ensemble are the same as outlined previously (Figure 74). The optical pulse sequence required to detect the rotation of the Bloch vector is outlined in Figure 82, while the experimental procedure for the detection of the phase and the amplitude of the optical signal has been explained earlier in the text. Each pulse in the sequence has a 1MHz Rabi frequency at the center of the beam, each π-pulse was 500 ns long, and each π/2 pulse was 250 ns long. The phases of all pulses, except the control pulse C_2, were set to zero. The phase of the control pulse C_2 was varied from 0 to π, and the phase of the echo was measured using the I&Q detection scheme.

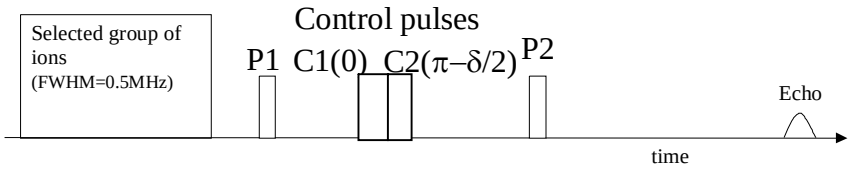

$$Echo \propto \mu(\cos(\omega_l t)\sin(\delta) + \sin(\omega_l t)\cos(\delta))$$

Figure 82: The pulse sequence to demonstrate the geometric rotation about the z-axis. Here C_1 and C_2 are the control pulses of area π and phase difference π–δ/2. P_1 and P_2 are part of the detection pulses, with areas π/2 and π and zero phases.

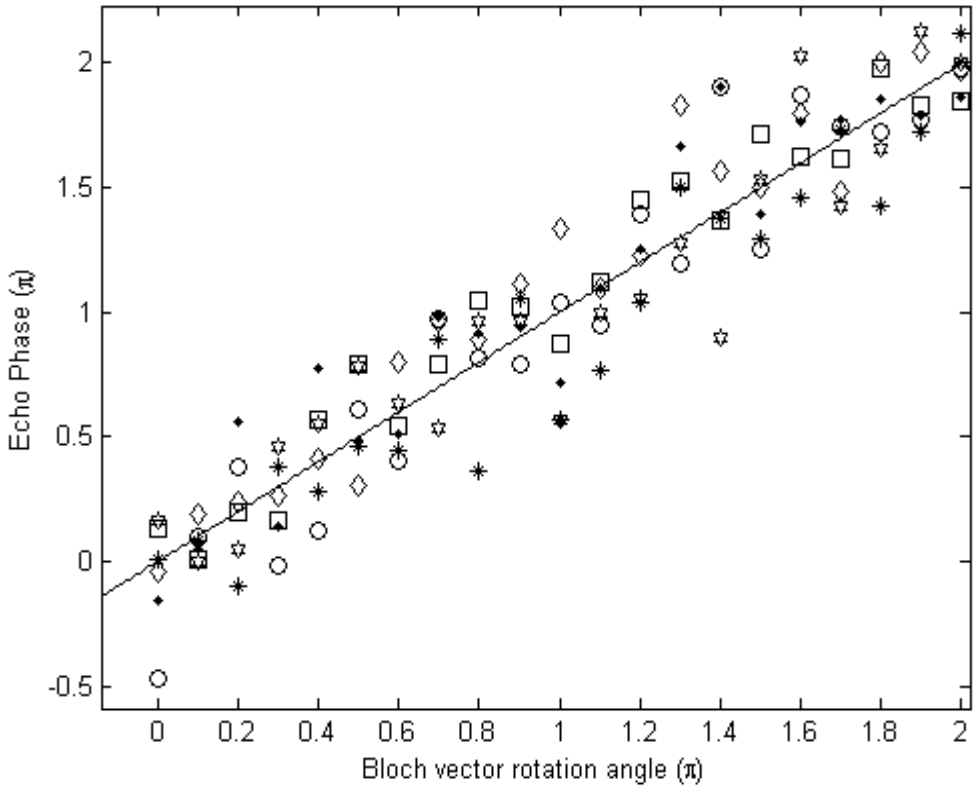

Figure 83: The experimental demonstration of the geometric rotation about the z-axis. The rotation angle was measured through photon echoes. The solid line is the expected theoretical results, and the experimental data points are six single acquisitions of the experiment taken on different days with no averaging performed on each data point.

Note that the phase of the detected echo changes linearly with the rotation angle for this rotation as explained in Chapter 5. The data (points) for each single experimental acquisition are presented in Figure 83. The experimental data (points) in Figure 83 show that the phase of the detected echo signal changes linearly. The experimental data (points) also compare favorably with the theoretically-predicted phase of the echo (solid line) as shown in Figure 83. However, the error in each of the single experimental acquisitions is significant. The standard deviation in the phase measurement for single shot

measurements for four different experimental data sets are 0.13π, 0.14π, 0.17π, and 0.18π, while corresponding SNR for these data sets are 150, 100, 86, and 80. These data show that the lower SNR corresponds to the higher phase error in the measurements, as expected. Again, in this case values of SNR, for all the data sets, are lower than the case in Figure 79 for which the value of SNR (640) was higher. In this case, we again average the data in all six single experimental acquisitions. The results of the average are shown in Figure 84. The results again show the reduction in the error in the experimental data. The results of the average show that there is no systematic error in the detection system, and the error is random, which is due to a low signal-to-noise ratio (SNR). The standard deviation of the experimental results for phase measurements from the theory is calculated to be 0.15π for an average of 6 experimental acquisitions.

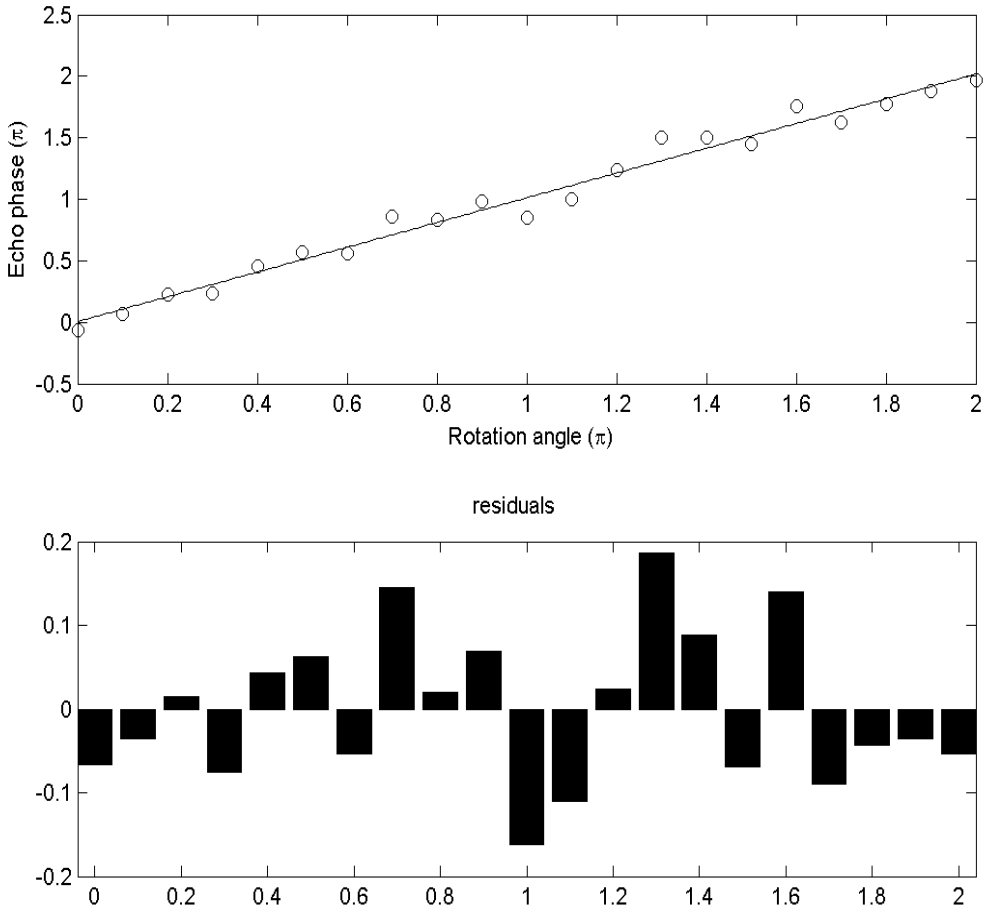

Figure 84: The averaged experimental data (circles) showing the phase of the detected echo for the rotation about the z-axis. The expected rotation angle is represented as a solid line. The error bars in the lower plot show deviation from the expected value of the rotation.

Now, the fidelity of the rotation about the z-axis is calculated with the definition given in equation (5.50). The results, in Figure 61, for degradation in the operation fidelity suggest that fidelity degradation, for Gaussian spatial beam, will be within 13% to 15%. Thus, the single qubit operation with the Gaussian spatial beam results in, at most, 85% operation fidelity. In the current experiment, we could only measure two components (x and y) of the Bloch vector and could not measure all three components of

the Bloch vector. This means that we cannot measure the actual fidelity of the operation. However, we can estimate the operation fidelity as described next. We first assume that there was no change in the initial z-component of the Bloch vector (not a good assumption, but it can provide a rough estimates on the operation fidelity); then we can use equation (5.50), and the fidelity of the operation can be estimated. The results for such a calculation are plotted in Figure 85. Data in Figure 85 show about 60% operation fidelity for small rotations, and essentially, after a 0.2π rotation, we can not call it a rotation about the z-axis (error in the rotation axis).

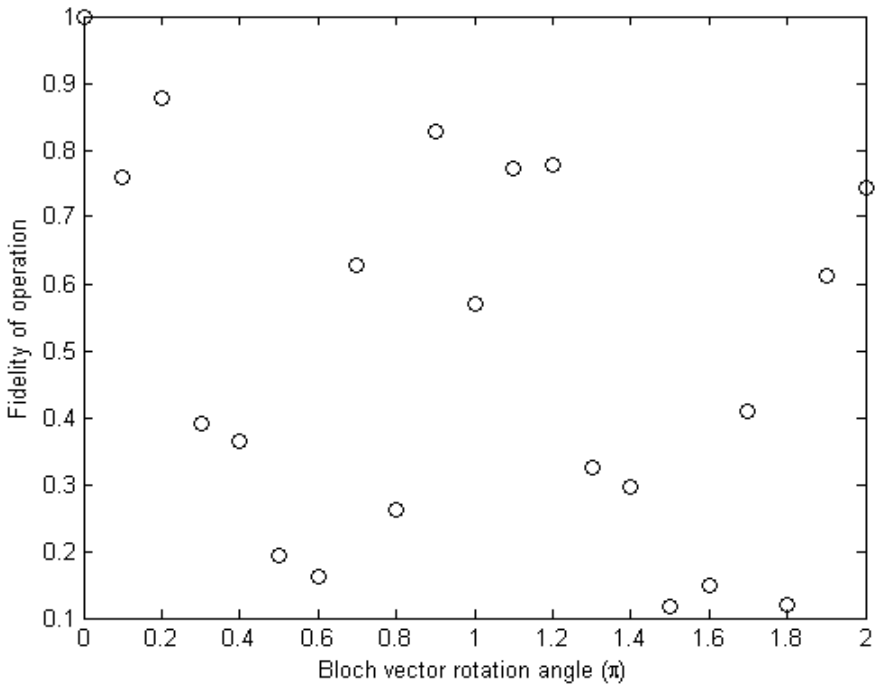

Figure 85: Estimate of the fidelity of single qubit operation for rotations around the z-axis using equation (5.50).

The results of this experimental investigation reinforce the conclusion drawn in Chapter 5, that the uniform intensity beam or a modified pulse sequence similar to the

one suggested recently [(114)] is required for high fidelity quantum operation. Now in the next section, we experimentally investigate the second of the two rotations of the Bloch vector.

Demonstration of the Bloch Vector Rotation about the Y-axis

In this section, the rotation of the Bloch vector around the y-axis is investigated using two different techniques. As noted in Chapter 5, the direct rotation of the Bloch vector around the y-axis for a selected ensemble can be realized with a single laser pulse. In the current notation it can be seen that an optical field with a phase $-\pi/2$ can rotate the Bloch vector around the y-axis. In this case, the rotation angle of the Bloch vector is given by the pulse area of the optical pulse.

Later, the rotation of the Bloch vector around the y-axis for a selected ensemble is realized with geometric phase involving multiple pulses, where the rotation angle of the Bloch vector is controlled by the relative phases of the optical pulses.

Finally, these two techniques of realizing the Bloch vector rotation around the y-axis will be compared. Both of these methods are implemented on the identical ensemble of ions, as given in Figure 74. The experimental set-up is similar to that depicted in Figure 69, with the detection system explained earlier in the text.

Bloch Vector Rotation about the Y-axis with a Single Optical Pulse: Here, the experimental results for rotation of the Bloch vector with a single optical pulse are presented. The pulse area, θ, is expected to be the rotation angle of the Bloch vector.

In the experiment, the maximum Rabi frequency for the available power, 300mW, and beam size, 100μm, was about 1MHz at the center of the Gaussian spatial beam.

The rotation of the Bloch vector is detected by using a second pulse of pulse area π and zero phase. The pulse area of the first pulse (a control pulse) was varied by changing the duration of the pulse. The area of the detection pulse, pulse 2 in the sequence (Figure 86), was fixed with a 1MHz Rabi frequency at the center of the Gaussian spatial beam and 500 ns duration.

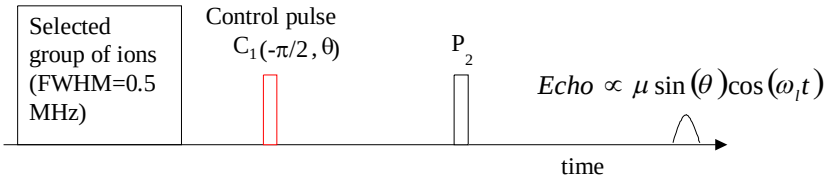

Figure 86: A pulse sequence to realize and detect the rotation around the y-axis with a single control pulse, C_1.

The intensity of the detected echo for a uniform intensity beam is expected to be $\sin^2\theta$, as shown by the solid line in Figure 87. Experimental results (squares) in Figure 87 show the detected echo intensity as a function of the area of pulse 1. The theoretical results are obtained by noting that the Bloch vector rotation angle, δ, and the pulse areas, θ, are the same as defined in Chapter 5. The theoretical results obtained using equation (5.47) and the experimental data are normalized to the maximum echo power.

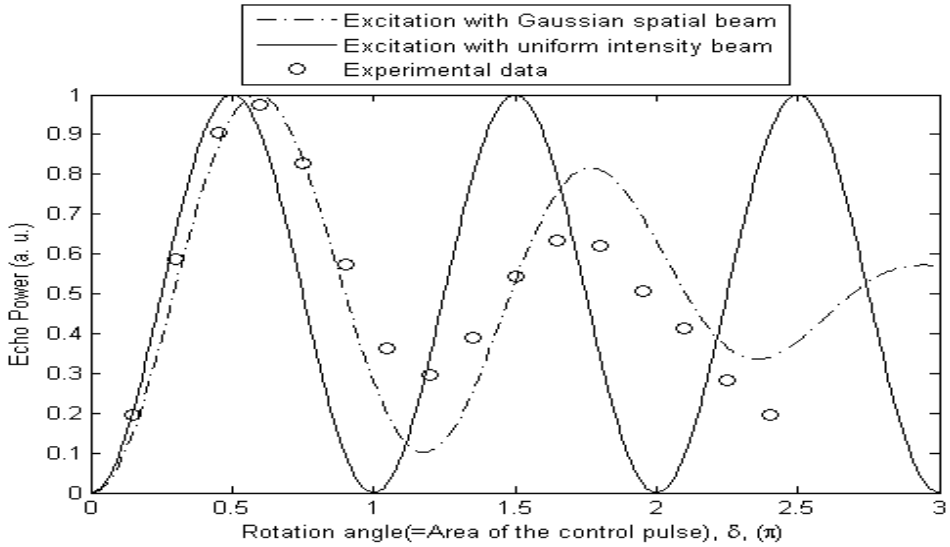

Figure 87: Intensity of the experimentally-detected echo after the Bloch vector around the y-axis with a single optical pulse. The experimental (circles) and theoretical results (solid and dot-dashed lines) are normalized to the maximum echo power.

The experimental results (circles in Figure 87) deviate significantly from the theoretically predicted results for the uniform intensity beam after the rotation angle of about 0.5π. However, these experimental results match pretty well with the theoretically-predicted results (dot-dashed line) for the Gaussian spatial beam (dotted line) up to the Bloch vector rotation angle of π. Again, after π rotation, the experimental results start to deviate from the Gaussian beam model. The reason is that the area of the pulse being used to drive the Bloch vector is not uniformly addressing all of the ions in the ensemble. The reason for this is the way the area of the driving pulse is increased. There are two ways the area of a pulse can be increased (decreased); one way is to increase (decrease) the Rabi frequency, and the other is to increase (decrease) the duration of the pulse. The best option is to increase the Rabi frequency of the pulse and keep the condition for the

uniform excitation of ions in the ensemble fulfilled. However, limited power is available in the laboratory. In the laboratory, the maximum available laser power and the beam size gave us 1MHz Rabi frequency. Note that the estimate for the transition dipole moment, $5.03\times10^{-21} esu\cdot cm$, agrees with the data obtained earlier [(67)]. Thus, the available option is to increase the pulse duration in order to increase the pulse area. As the duration of the control pulse is increased, the bandwidth of the control pulse is decreased. This causes the non-uniform interaction of the control pulse with the ensemble of ions. In the current experiment, the pulse was unable to uniformly address all ions in the ensemble when its duration was greater than 2000 ns. Therefore, the control pulse, with the pulse area > 4π, was unable to uniformly address all the ions in the ensemble. Therefore, the experimental results significantly deviate from the theoretical results in Figure 87 for higher duration control pulse. Therefore, it may be practical to use a technique to rotate the Bloch vector that is less dependent on the laser power. In the next section, we will focus on the rotation of the Bloch vector around the y-axis using the geometric phase.

Bloch Vector Rotation about the Y-axis Using the Geometric Phase: The rotation with a single pulse, described earlier, is simple, but it suffers from drawbacks. One drawback in that case is the dependence of the rotation of the Bloch vector on the exact pulse area of the control optical pulse. The other drawback is the need for higher laser power to uniformly address the ions in the ensemble. As discussed earlier, another way to achieve this rotation is to use the relative phases of the optical pulses as is required for rotation using geometric phase.

In the experimental implementation of this scheme, again, the ensembles of ions having similar characteristics, as given in Figure 72 and Figure 74, were used. Recall, the results in Chapter 5. Note that, three pulses with pulses areas $\pi/2$, π, and $\pi/2$ and phases 0, $\pi+\delta/2$, and 0 are needed to rotate the Bloch vector around the y-axis. The pulse sequence for rotation and detection using an ensemble of ions is given in Figure 88.

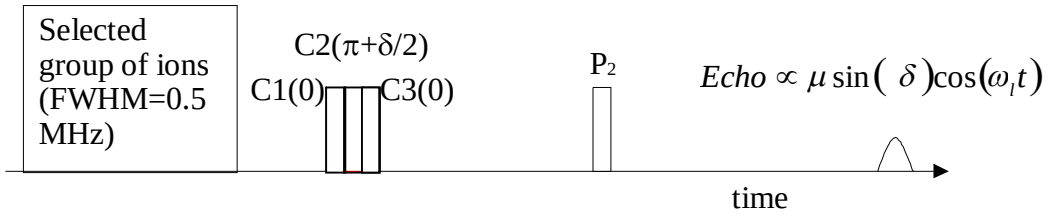

Figure 88: A pulse sequence used in the experiment to demonstrate the Bloch vector rotation around the y-axis. Here, the control pulse sequence has pulses C_1, C_2, and C_3, while P_2 is the detection pulse.

In the first experiment, an ensemble of ions initially in the excited state with the identical characteristics, as in Figure 72, is selected. Each $\pi/2$-pulse in the sequence has a 1MHz Rabi frequency and 250 ns duration. Each π-pulse in the sequence has the same value of Rabi frequency as the $\pi/2$-pulse and the duration of each π-pulse was twice as long as that of the $\pi/2$-pulse. Again, we use the photon echo technique to detect the effect of the Bloch vector rotation around the y-axis. For the uniform intensity beam, the theoretical results for the expected echo power are given by the dotted line in Figure 89. The experimental results (circles) for the detected echo power in Figure 89 show significant deviation from the theoretical results for the uniform intensity beam. This means that rotation angle for the Bloch vector rotation is not the same for these two cases. The analysis in Chapter 5 has shown that this is to be expected. Now, we compare

the theoretical results (solid line in Figure 89) for excitation with the Gaussian spatial beam having the pulse areas at the center of each Gaussian beam as $\pi/2$, π, and $\pi/2$ with the experimental data (circles in Figure 89). For Gaussian spatial excitation, the theoretical results were obtained using equation (5.48). These theoretical results, (solid line in Figure 89) for excitation with Gaussian spatial beam, agree very well with the experimental results (circles in Figure 89). This means that the rotation of the Bloch vector obtained in the experiment is similar to the rotation with the Gaussian spatial beam. The experimental data and the theoretical results were normalized using a Bloch vector rotation of $-\pi/2$. Error in the normalization of the data point was ± 0.01 while the SNR in this experiment was about 2000. Note that, the theoretical results and the experimental data were normalized independently.

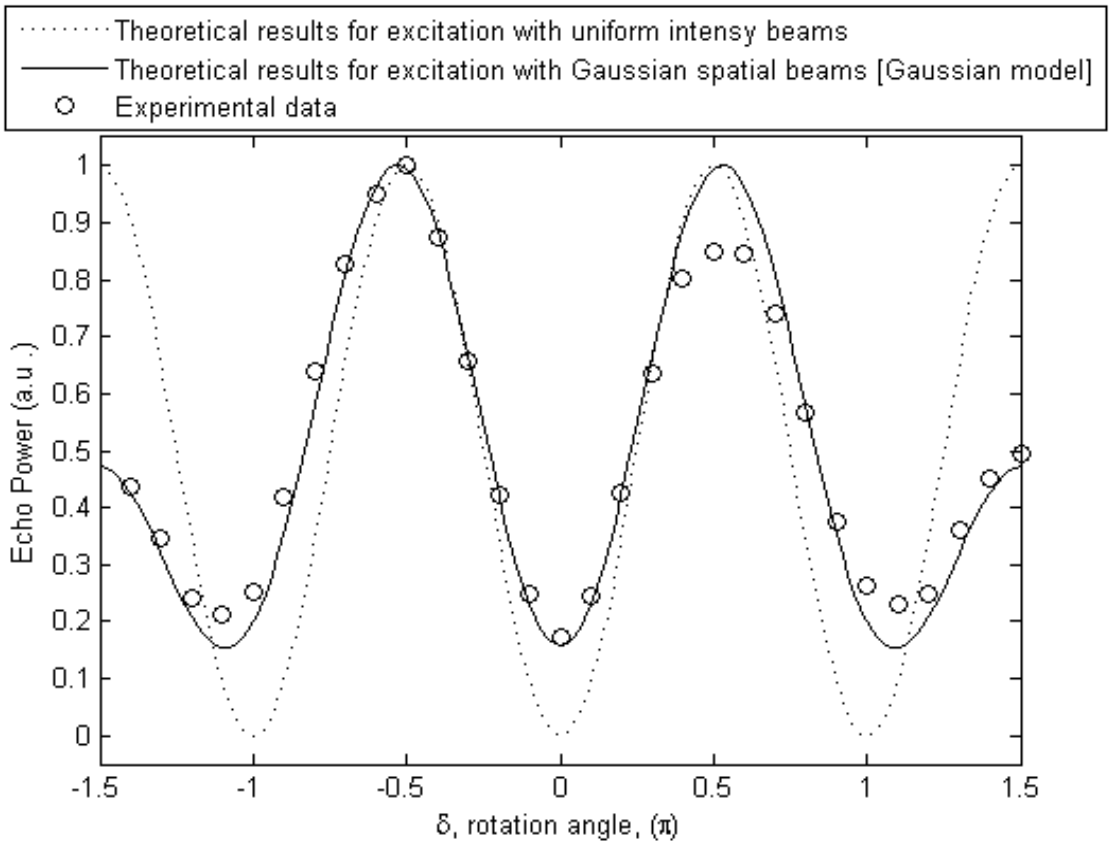

Figure 89: Results for the rotation about y-axis with the control pulse sequence when the selected ensemble was initialized to the excited state. Results show the measured intensities of the detected echo and their dependence on the rotation angles for the Bloch vector rotation around the y-axis. Each pulse in the sequence has ideal intensities $(\pi, \pi/2, \pi)$ at the center of the Gaussian spatial beam.

In the second measurement, an ensemble of ions initially in the ground state was selected. This ensemble has similar properties as that of the ensemble of ions in Figure 74. Again, the same pulse sequence, as described in the previous case was applied to the selected ensemble. Here, the selected ensemble of ions is initialized to the ground state. The experimental (circles) and theoretical results (dotted and solid lines) are presented in Figure 90. These results again show that the expected change in the echo intensity for the uniform intensity beam does not agree well with the experimental results as expected.

However, the Gaussian beam model (equation (5.48)), with the same parameters as were used in the experiment, shows a good agreement with the experimental results. Therefore, the rotation of the Bloch vector in the experiment can be characterized with the Gaussian beam model given in Chapter 5.

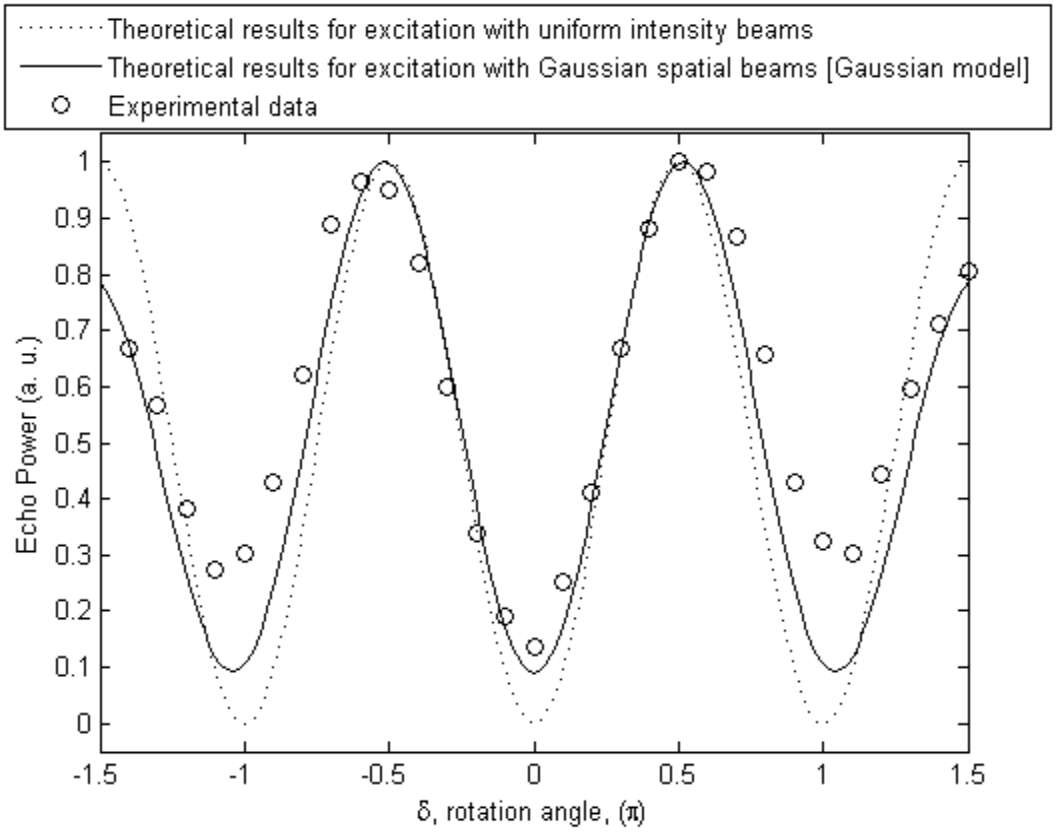

Figure 90: Results for the rotation about y-axis with the control pulse sequence when the selected ensemble was initialized to the ground state. Results show the measured intensities of the detected echo and their dependence on the rotation angles for the Bloch vector rotation around the y-axis. Each pulse in the sequence has ideal intensities (π, $\pi/2$, π) at the center of the Gaussian spatial beam

Again, for this case, the theoretical results in Chapter 5 for the degradation of the operation fidelity show that the degradation in the operation fidelity will be about 12% (Figure 62). Now, if the phase error and the intensity fluctuation are taken into account,

then the degradation in fidelity will be even higher. Therefore, the operation fidelity for a single qubit operation will be even lower than 88%. This suggests that the uniform intensity laser beam or the modified pulse sequence [(114)] is needed to reduce the degradation in the operation fidelity.

Ion-Ion Interaction

In the previous section, it was demonstrated that an ensemble of ions can be selected with the characteristics required for a single qubit. The next step would be to select two ensembles, with each ensemble having the same characteristics as a single ensemble. These selected ensembles should be able to communicate with each other in a controlled fashion. This kind of communication can be used to build the two-qubit quantum gates, like the controlled NOT (CNOT) gate [(124), (125)]. The main requirement of this communication is that one must be able to turn on or off the communication between the qubits as desired.

One way to control the interactions between the two ensembles of ions is to use the effect of the excitation induced frequency shift (EIFS) [(124), (126)]. Excitation induced frequency shift was first observed in NMR systems, where the precession of the spin of ions was affected by the excitation of the spin of neighboring ions [(127)]. Later, EIFS was also observed in many rare-earth-doped crystals [(128), (129), (130), (131), (132), (133)]. Controllable excitation induced frequency shift was also demonstrated in Pr^{3+}, Nd^{3+}, and Eu^{3+} doped in Y_2SiO_3 [(134)].

In EIFS, as the name suggests, if one ensemble is excited from its initial state, then this influences the neighboring ensemble, which usually manifests itself as a change in the resonant frequency of the neighboring ensemble. As the optical field excites an ensemble of ions, it essentially changes the environment of the neighboring ions; this causes their resonant frequencies to shift. The phenomenon of EIFS is governed by the dipole-dipole interactions between the ions [(28)].

In the case of an inhomogeneously broadened ensemble, like rare-earth-doped crystals, each ion in the ensemble has a different transition frequency due to its unique local environment. In EIFS, if an ion in the local environment is excited, then the resonance frequency of the neighboring ion is shifted. The EIFS depends on the ion concentration, bandwidth of the excitation pulse, intensity of excitation pulse, and the local separation between the ions.

There are two techniques being used to measure the excitation induced frequency shift. In one technique, first, an ensemble of ions is selected with an inhomogeneous width comparable to or smaller than the anticipated increase in the inhomogeneous width due to the excitation induced frequency shift. The comparison of the inhomogeneous widths of the selected ensemble of ions with and without excitation of the neighboring selected ensemble of ions provides a direct measure for the change in the inhomogeneous width due to the excitation induced frequency shift [(126)]. In another technique, the decay of the photon echo, from the selected ensemble of ions with and without excitation of the neighboring selected ensemble of ions, is measured [(128), (129)]. The idea that the echo dephasing time is influenced by the instantaneous spectral diffusion was

developed by Mims [(135)]. Note that, in the 2-pulse echo sequence, if the excitation pulse is applied before the two pulses in the echo sequence, then there will be no excess dephasing in the echo, as the detuning during dephasing and rephasing time is exactly the same. However, if the perturbing pulse is applied between the two pulses in 2PE sequence, then there will be excess dephasing in the echo, as the detuning during the dephasing and rephasing times is not be the same. Therefore, the comparison of the amplitudes and the decays of the echo in each case will provide information about the excess dephasing in the material due to the EIFS. This technique is more sensitive and can be useful in a material where the excitation induced frequency shift causes small dephasing. The earlier investigations of EIFS were motivated to minimize the dephasing caused by EIFS [(128), (129), (130), (131), (132), (133)], as demanded for optical processing and storage applications. However, recently, it has been proposed to put EIFS to use in quantum computing applications for building the multi-qubit quantum gate [(124), (125)]. These proposed schemes in rare-earth-doped crystals use the EIFS caused by dipole-dipole interaction to achieve entanglements between two qubits. Recently, the EIFS caused by the dipole-dipole interaction was successfully used to implemented the controlled NOT gate in rare-earth ions, Eu^{3+} [(48)]. The main advantage of these schemes, that use dipole-dipole interaction, is that the dipole-dipole coupling in rare-earth materials is generally stronger than the spin-spin interaction. Therefore, the dipole-dipole interaction between selected ensembles of ions does not strongly affect the coherence in the hyperfine levels. Hence, the coherence time for the hyperfine levels remains the same, and the state of the qubit remains well-isolated. In order to consider the EIFS to

implement in the multi-qubit operation in Tm^{3+}:YAG, we need first to quantify the effect arising from the EIFS in Tm^{3+}:YAG.

The results from previous studies indicate that the broadening due to the excitation induced frequency shift (EIFS) for 0.1% atm. Tm^{3+}:YAG is about 1.2kHz per excitation density of $10^{15} cm^{-3}$ [(136)], and the broadening due to the EIFS for 0.5% atm. Tm^{3+}:YAG is about 3kHz per excitation density of $5\times10^{15} cm^{-3}$ [(126)]. In our experimental study, we will study the interaction specifically between two selected ensembles and quantify the interaction between these two ensembles. This should provide information for interaction between the ensembles of ions to implement the multi-qubit operation in Tm^{3+}:YAG. Therefore, the first step was to select two ensembles of ions in the inhomogeneously broadened absorption profile of the medium (Tm^{3+}:YAG).

The Selection of Two Ensembles

Introduction: The method to select two ensembles of ions employed here is similar to the one explained in the case of a selection of a single ensemble. First, a secant pumping chirp pulse creates a trench in the inhomogeneous spectrum of the medium by pumping almost all of the ions to the long-lived hyperfine level, as described in the beginning of this chapter. After the pumping secant chirp pulse, two burn-back pulses, instead of a single burn-back pulse, are applied to the medium. These two pulses are separated in frequency and time. These two pulses burn ions back from the inhomogeneous profile of the medium at two different frequency locations in the emptied trench. The pulse sequence to implement this scheme is given in Figure 91.

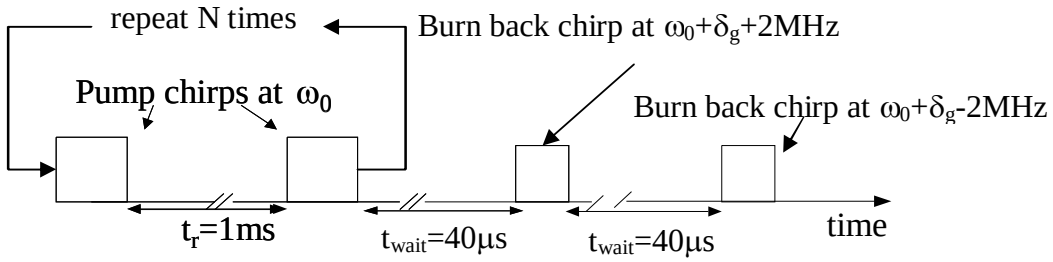

Figure 91: A pulse sequence to select two ensembles of ions in the inhomogeneously broadened absorption profile in Tm:YAG.

Experiment: The material parameters in this experiment were identical to those used to select a single ensemble of ions in Figure 74. The main differences are described below. In this experiment fifty repetitions of a 10MHz secant pumping chirp pulse were applied to the medium with a repetition rate of 1.0kHz, as shown in Figure 91.

Each burn-back pulse in the sequence of two burn-back pulses has a 500kHz bandwidth. The other parameters of these burn-back pulses were similar to those used for the single burn-back pulse for the single ensemble selection. These two burn-back pulses have center frequencies that are 4MHz apart. The temporal separation between these two burn-back pulses was 40μs as shown in Figure 91.

The resultant absorption spectrum of the medium showing the two selected ensembles of ions after the application of the pulse sequence is shown in Figure 92. Note that in this case, the emptied pit is not flat, which is due to some population relaxation between the hyperfine levels. The relaxation between hyperfine levels can be minimized by lowering the sample temperature and thus increasing the relaxation time between the hyperfine levels. In the current experiment, the sample was cooled to 4K. It would be

better to decrease the sample temperature further. However, note that in the absorption spectrum (Figure 92), each selected ensemble still shows up as a negative absorption peak. This means that the population for these selected ensembles is in the excited state.

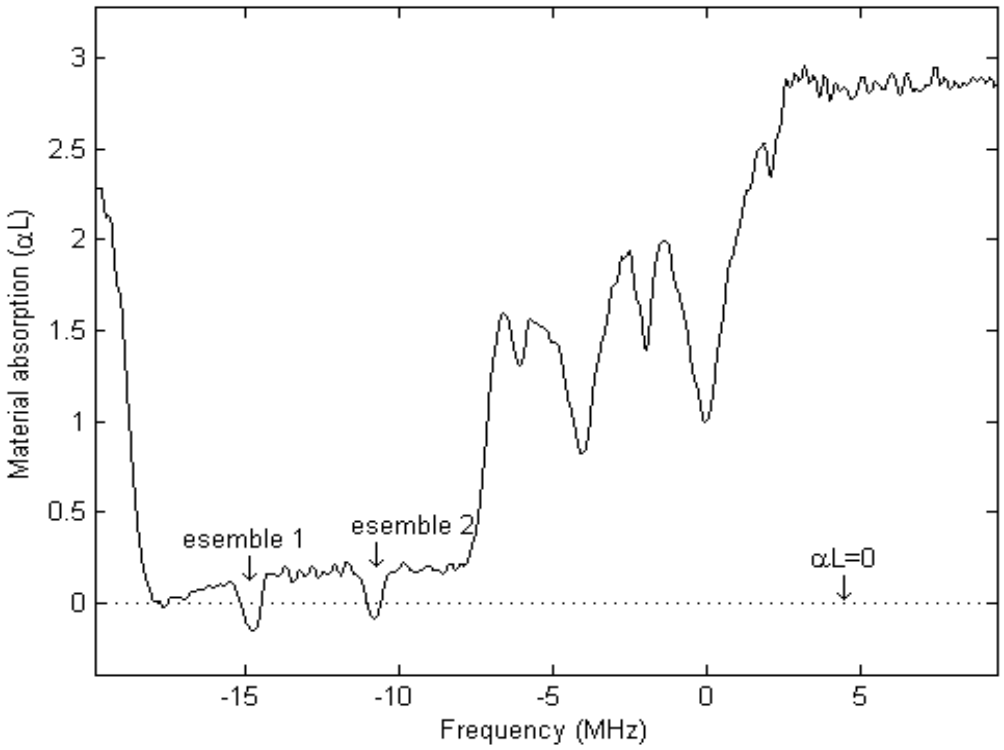

Figure 92: The experimentally-measured absorption spectrum of the material after excitation with the pulse sequence in Figure 91. The experimental result demonstrated the isolation of the two ensembles at 4MHz apart in the inhomogeneous absorption profile of the medium with the ions in each ensemble in the excited state.

Note that in this experiment, two narrowband, 500kHz, burn-back pulses having center frequencies $\omega_{c1} = \omega_0 + \delta_g + 2MHz$ and $\omega_{c2} = \omega_0 + \delta_g - 2MHz$ were applied to the medium. Another choice would be to use narrowband (500kHz) burn-back pulses with center frequencies at $\omega_{c1} = \omega_0 + \delta_g + 0MHz$ and $\omega_{c2} = \omega_0 + \delta_g - 4MHz$, and the experimental results obtained here will still hold. The condition on choosing the center

frequencies of the burn-back pulses is $\omega_0 + \delta_g - 0.5B_c < \omega_{ci} < \omega_0 + \delta_g + 0.5B_c$, where ω_{ci}, i=1 and 2 are the center frequencies of burn-back pulses and B_c is the bandwidth of the secant pumping chirp pulse having a center frequency ω_0. In this experiment, the bandwidth of the secant pumping chirp pulse was 10MHz; therefore, the condition on the choice of the center frequencies of the burn-back pulses was easily satisfied.

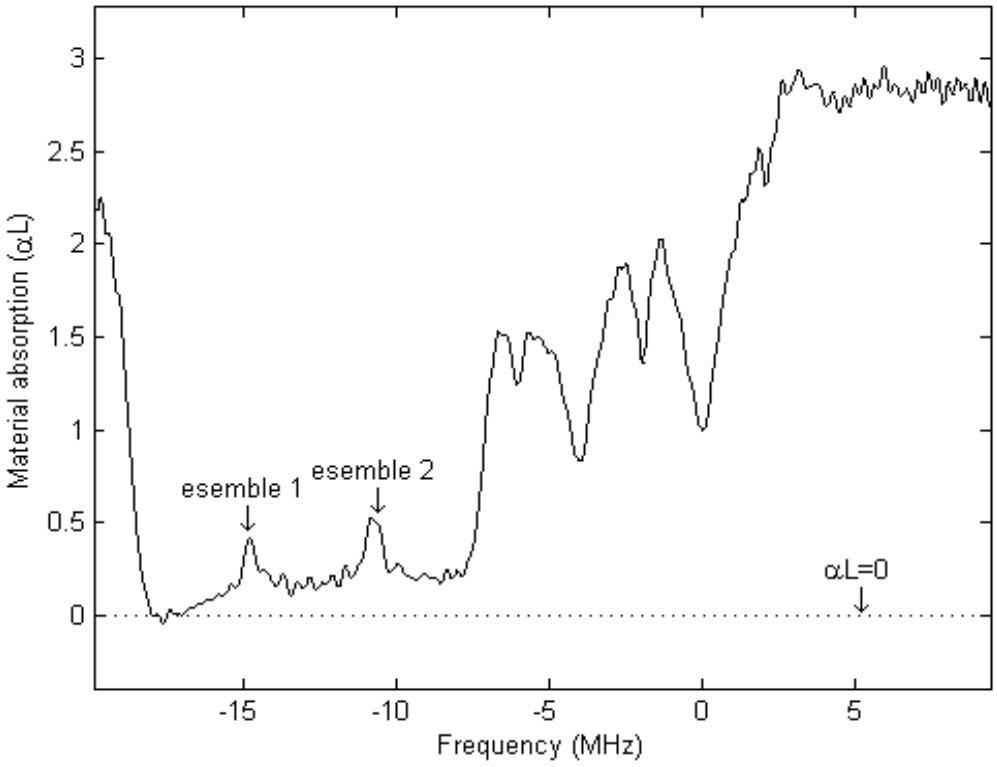

Figure 93: The experimentally-measured absorption spectrum of the material. The results demonstrate the initialization of the two selected ensembles (ensemble 1 and ensemble 2) of ions to the ground state.

Now, the two selected ensembles in Figure 92 are initialized to the ground state with the application of two π pulses instead of a single π pulse. The two π pulses, having

center frequncies $\omega_{c1} = \omega_0 + \delta_g + 2MHz$ and $\omega_{c2} = \omega_0 + \delta_g - 2MHz$ and satisfying the conditions of uniform excitation of the two selected ensembles, are applied. Note that, each π pulse initializes the corresponding ensemble to the ground state as can be seen from the positive absorption of each selected ensemble (Figure 95). The experimental result for the absorption spectrum of the medium after the initialization of both selected ensembles of ions is shown in Figure 93. Note that the two selected ensembles in 10MHz pit (Figure 92) have broader pedestals. The broader pedestal, in each selected ensemble of ions, is due to the background ions being excited with the inverting π-pulse of 2MHz bandwidth. Note that, the spectral width of the pedestal for each selected ensemble is broader than the spectral width of each selected ensemble of ions. However, the spectral width (about 2MHz) of each pedestal is comparable to the bandwidth of the inverting π-pulse. This indicates that the inverting π-pulse is indeed exciting the background ions in the 10MHz trench. As mentioned earlier, the effect from the background ions can be minimized by further lowering the sample temperature. However, in our investigations we used these two selected ensembles of ions and studied the interaction between these two selected ensembles of ions using the photon echo technique.

Interaction between Two Selected Ensembles

Introduction: In this section, an ensemble is excited with an optical field, and the change in the inhomogeneous broadening of the neighboring ensemble is measured using a 2PE sequence. The idea employed here is similar to the one employed in rare-earth-doped crystals in the earlier studies [(128), (129)]. In our study, the experiment is

performed using two selected ensembles of ions instead of the full inhomogeneously broadened absorption profile [(136)]. Author could not find a study in Tm^{3+}:YAG where two selected ensembles of ions were used to study the EIFS. First, two spectrally-separated (about 4MHz) ensembles of ions (Figure 93) are prepared. The ions in both of these selected ensembles in Figure 93 can be addressed uniformly using a moderate power laser. In this experiment, the Rabi frequency and the bandwidth of each pulse in the 2PE sequence were also kept higher than the spectral width of each selected ensemble of ions. Similarly, the Rabi frequency and the bandwidth of each pulse in the excitation sequence were kept also higher than the spectral width of each selected ensemble of ions. The pulses with these characteristics were able to uniformly excite all the ions in their respective ensembles, and they did not excite the ions in the neighboring ensemble.

Experiment: In this experiment, the set-up was similar to the one given in Figure 69, with only difference in the detection system. For this experiment, the I&Q detection system was not needed, and instead, the intensity of the optical field was detected. In the first experiment, the 2PE was applied on one selected ensemble of ions, while no perturbing pulse was applied to the neighboring ensemble. This experiment enabled us to measure the coherence time of the selected ensemble using the same process as described earlier in the chapter. The measured coherence time was $(35 \pm 0.70)\mu s$ (circles in Figure 95) and is the same as measured earlier for the single selected ensemble of ions. In the second experiment, the 2PE is applied on one selected ensemble of ions, and the perturbing pulse was applied on the neighboring ensemble of ions as shown in Figure 94.

The time between the perturbing pulse and the pulse 1 in the 2PE sequence was such that $t_{31} = 0.5t_{21}$.

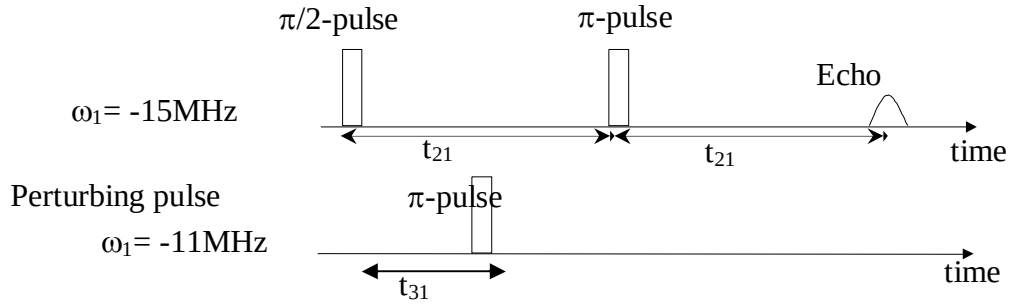

Figure 94: A pulse sequence used to measure ion-ion interaction. Each pulse has a 1MHz Rabi frequency. The π/2-pulse has 250ns duration, and the π-pulse was twice as long in duration. The perturbing pulse was always kept in the center of the 2PE sequence, and echo decay was measured as a function of the delay between the two pulses in the 2PE sequence.

Again, the coherence time of the selected ensemble is measured for this case by varying t_{21} and measuring the 2-pulse echo intensity. In this case, again, the echo intensity exponentially decreased with an increase in the separation between the two pulses in the 2PE sequence. The measured coherence time in this case was $(30 \pm 0.40)\mu s$ (asterisk in Figure 95), which is smaller than in the case not containing any perturbing pulse. Since the 2PE decay is exponential, most of the contribution in the excitation induced frequency shift is due to the diagonal interactions between the two ensembles, and the off-diagonal interactions are negligible [(132)]. This decrease in the coherence time is attributed to the excess dephasing caused by the broadening caused by the excitation induced frequency shifts of individual ions. The contribution of the EIFS in the excess dephasing can be calculated [(135)] as $\Delta\Gamma_{EIFS} = \frac{1}{\pi}\left(\frac{1}{T_2} - \frac{1}{T_2^0}\right)$, where T_2^0 is the

coherence time without any perturbing pulse and T_2 is the coherence time with the perturbing pulse. The number density of ions excited that contribute to EIFS, $\Delta\Gamma_{EIFS}$, for 0.1% atm. Tm^{3+}:YAG and 100% excitation, can be calculated as

$$\rho_{excit} = \rho_0 \left(\frac{\int_{-\Gamma_{excited}/2}^{\Gamma_{excited}/2} d\omega\, \alpha_{ensemble}(\omega)}{\int_{-\Gamma_{inh}/2}^{\Gamma_{inh}/2} d\omega\, \alpha(\omega)} \right),$$

where $\rho_0 = 1.39 \times 10^{19}\, cm^{-3}$ is the density of thulium ions in YAG, $\Gamma_{inh} = 20GHz$ is the inhomogeneous line-width, $\Gamma_{excited} = 2MHz$ is the bandwidth of the excitation pulse, $\alpha(\omega)$ is the Gaussian line shape of the inhomogeneously broadened medium, and $\alpha_{ensemble}(\omega)$ is the line shape of the selected ensemble, including the pedestal in Figure 93. Therefore, in the current case, the EIFS will amount to $(1.7 \pm 0.3)kHz$ per $10^{15}\, cm^{-3}$ ions excited.

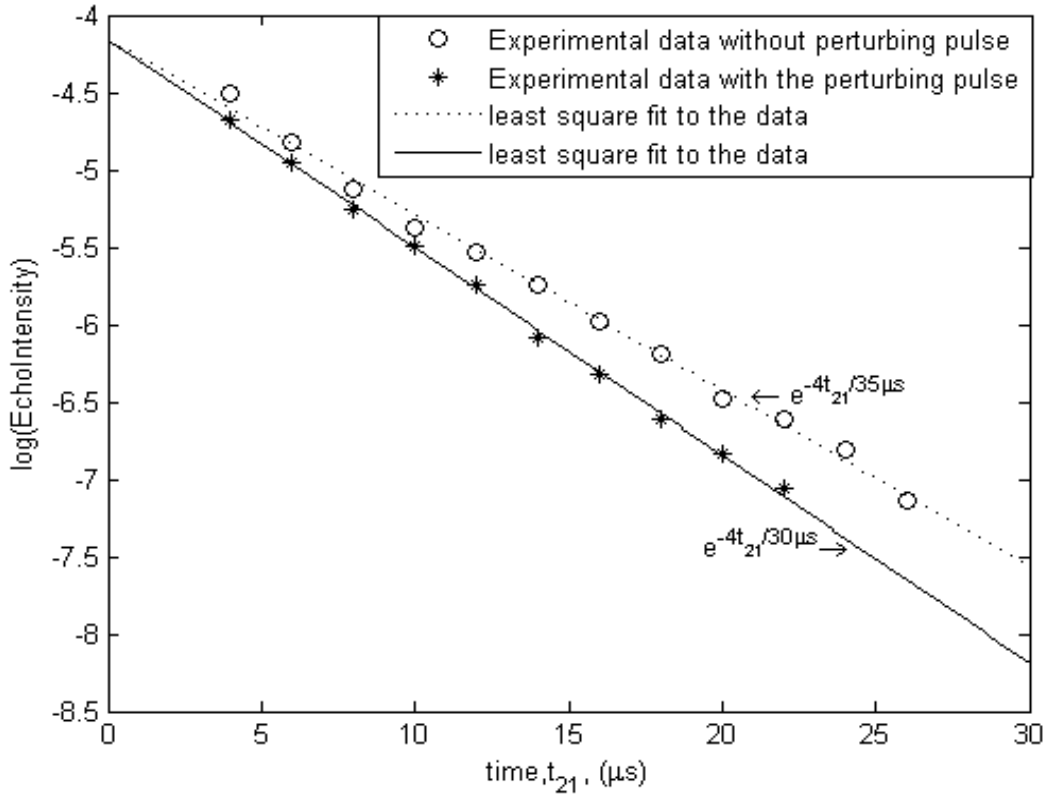

Figure 95: The experimentally-measured decay of the 2-pulse echo as a function of the delay between two pulses in the 2PE sequence.

Results obtained here give a higher excitation induced frequency shift than quoted earlier, $1.2kHz$ per $10^{15} cm^{-3}$ ions excited [(136)]. This leads us to believe that we are not measuring the correct background level of the ions in the selected ensemble, and the emptied pit might have a higher number of ions than that of our estimate.

Now, we consider the current schemes proposed for two qubit operations that use the EIFS [(114), (124)]. These schemes can be divided into two categories: one scheme in reference [(124)], after qubit distillation, uses a single pulse in each single qubit quantum gate for the two qubit controlled NOT gate. The other scheme, in reference [

(114)], after following a slightly modified distillation scheme, uses composite pulses in each single qubit quantum gate for the implementation of the controlled NOT gate. The scheme in reference [(124)] requires that the EIFS should be large enough so that the broadening of the selected ensemble due to the EIFS should be larger than the width of the ensemble. Current experimental investigations of EIFS in 0.1% atm. Tm^{3+}:YAG show that it is not possible in 0.1% atm. Tm^{3+}:YAG to implement the scheme in reference (124) as the broadening due to the EIFS is too small, and the distillation process in the scheme [(124)] will not leave enough ions (at least $5\times10^{15}cm^{-3}$) for the implementation of a meaningful two-qubit operation. The scheme can only be implemented in Tm^{3+}:YAG if we can significantly increase (more than 50 times) the excitation induced frequency shift (EIFS). Therefore, there is very little hope to implement the scheme involving a single pulse [(124)] in 0.1% atm. Tm^{3+}:YAG or in 0.5% atm. Tm^{3+}:YAG.

However, the composite pulse scheme [(114)] requires the EIFS only to be larger than the homogeneous line-width of the material ions. This scheme offers a hope for implementation of a two qubit operation in Tm^{3+}:YAG, which has a homogeneous line-width of 5kHz at 2K [(29)]. The estimated radiative line-width would be 10kHz. This scheme was successfully implemented in the europium doped yttrium orthosilicate for the demonstration of a controlled NOT gate [(48)]. A similar scheme using the geometric phase can be implemented in which each π-pulse is replaced with three pulses of total pulse area 2π [(108)]. The operating temperature can be increased by increasing the EIFS. Experimental results indicate that the EIFS is three times higher for 0.5% than for 0.1% atm. in Tm^{3+}:YAG [(126)]. Further studies are needed to investigate the EIFS and

its dependence on thulium concentration in YAG. Additional research is also needed to investigate the dependence of the homogeneous line-width on the thulium concentration in YAG.

Conclusions

It is shown that an ensemble of ions, required to implement the qubit operations, can be prepared using a spectral hole burning technique. A single ensemble of ions was obtained by storing the unwanted ions in the long-lived hyperfine level and then burning back ions with desired characteristics. It was demonstrated that the selected ensemble of ions can be addressed uniformly with the optical pulses. This selected ensemble provided us with the test-bed for the implementation of a quantum operation using the geometric phase technique. However, the problem of preparing a completely isolated ensemble remains, as the current pumping and burn-back schemes fail to completely eliminate ions in the background. In these schemes, there will always be some fraction of the ions in the background as some stored ions will always relax back. In our study of single qubit operation, the contribution of the background ions to the signal was negligible.

The selected ensemble of the ions was characterized using spectral hole burning and photon echo techniques. The optical coherence time of the selected ensemble was measured to be the same as the material coherence time. It was also demonstrated that the ensemble can be initialized using the appropriate optical pulses.

Two basic qubit operations for the Bloch vector rotation were applied on this selected ensemble, and the photon echo technique, as outlined in Chapter 5, was used to

detect the effect of these rotations. The analysis of these results for a single qubit operations shows that the Gaussian beams are not suitable for high fidelity quantum operations. A uniform intensity beam or a modified pulse sequence is needed for high fidelity qubit operations.

Preliminary experimental results for investigations of the interaction between two selected ensembles for the application of two-qubit quantum operations were also presented. In order to study the interaction between two ensembles, we isolated two ensembles of ions in the inhomogeneously broadened absorption profile of Tm^{3+}:YAG. The broadening due to EIFS in 0.1% atm. Tm^{3+}:YAG was about $(1.7 \pm 0.3) kHz$ per $10^{15} cm^{-3}$ ions excited. It is noted that the broadening due to EIFS in 0.1% Tm^{3+}:YAG is smaller than the widths of the interacting ensembles. Based on these observations, it is concluded that method in the reference (124), which requires greater broadening due to EIFS than the widths of the two ensembles cannot be implemented in 0.1% atm. Tm^{3+}:YAG to build two-qubit quantum gate. However, an alternate method, that requires the broadening due to EIFS to be greater than the homogeneous line-width of the material ions and involves composite optical pulses, can be used to implement to build two-qubit quantum gate [(114), (108)].

CHAPTER SEVEN

SUMMARY

Investigations have been carried out to study the suitability of rare-earth-doped crystals, specifically Tm^{3+}:YAG, for quantum computing applications. Even though thulium is a spin ½ system, it still poses a significant challenge for characterization due to the presence of thulium ions at magnetically inequivalent sites in YAG. Adjustment in the polarization of the optical field was used to selectively address various ions in the crystal. The control on the optical polarization selection and the confinement of the magnetic field in the (1-10) plane resulted in distinct ions at three different sites in the crystal. In that case, ions at two different sites were magnetically equivalent. The ions at third site were magnetically inequivalent with ions at the other two sites.

Our initial spectral hole burning experiment provided us with the experimental data for calculating the magnetic anisotropy in the medium. This allowed us to map the cross-transition ratios for various orientations of the magnetic field and for ions at different sites in the crystal. Two magnetic orientations yielding high cross-transition ratios for ions at certain sites were selected for further investigations. It was also noted that the hyperfine splittings for these particular orientations of the magnetic field were accessible with the available magnetic field.

In further analysis, the spectral hole burning technique was used to experimentally measure the population lifetimes of hyperfine levels for these two orientations. In the case where cross-transition was high, the population lifetime of hyperfine levels in excess

of 100 ms was measured. For ions showing negligibly small cross-transition ratio, the population lifetime of hyperfine levels in excess of 1s was observed. The difference in the population lifetime of hyperfine levels for these cases was attributed to the different coupling of thulium ions with the host's (aluminum) spin for these two orientations of the magnetic field. It was noted that the population lifetime of hyperfine levels for ions at different sites strongly depends on the orientation of the magnetic field.

The dynamics of the relaxation parameters were also modeled theoretically. Time-dependent measurements using the spectral hole burning technique provided us with the experimental data, which was used in theoretical results to map out relaxation dynamics. This measurement also provided us with the direct measurement of cross-transition ratio, about 0.15. The theoretical model employed for exploring the cross-transition ratio and other relaxation parameters for one orientation of magnetic field can also be used to explore other magnetic fields' orientations as well. The theoretical model for relaxation dynamics developed in Chapter 4 also helped us to prepare the isolated ensemble of ions for quantum computing applications.

Later on, two different techniques were used to probe the coherences between hyperfine levels. Again the two orientations of magnetic field giving us high cross-transitions were used for hyperfine coherence time explorations. One method involves using a coherent Raman beats experiment. The estimated coherence time, using experimental results of this experiment, was greater than 0.020 ms at 4K. The results for the hyperfine splittings from this experiment also agreed very well with the results obtained using the spectral hole burning experiment. We also positively identified the

contributions in the coherent Raman beat signal from the ions at two different sites in the crystal. The second experimental method uses two bi-frequency pulses, with each pulse satisfying two photon resonance conditions. The beat signal was obtained using the Raman forward scattering technique. The decay of the beat signal was used to measure a coherence time of 0.070ms at 2K. The coherence time was found to be the same as the optical coherence time. It was noted that the coherence time is limited due to induced spin flip-flop by the aluminum in the host crystal.

In Chapter 5 we first summarized the basic theory for implementing the single qubit operation in rare-earth-doped crystals. It was noted that if the optical field's intensity is not uniform, then the fidelity of the qubit operation will be 10-20% lower. Therefore, a uniform intensity beam is critical for the high fidelity qubit operations.

In Chapter 6, the insight gained from the material characterization allowed us to select the best possible strategy for demonstrating the quantum operation on a single qubit. First step to demonstrate a single qubit operation involved the selection of an isolated ensemble of ions that can be addressed uniformly with the optical pulse. Using the theoretical model and relaxation parameters, it was shown that the best option involves the storing the unwanted population in one of the hyperfine levels. This can be seen from the fact that the population lifetime of hyperfine levels is about 10 times higher than any other storage level in the thulium. The population storage in the long-lived level reduced the leakage of unwanted ions in the emptied pit. This allowed us to create a pit with zero background. The zero background is important for isolating the ensemble of ions. The isolated selected ensemble is the pre-requisite for high fidelity quantum

operations. The ensemble of ions of required spectral width was selected by burning back ions in the empty pit from other spectral location in the inhomogeneously broadened absorption profile of Tm^{3+}:YAG. We used photon echo to characterize the ensemble of ions in the pit. Any contribution in echo signal from unwanted ions in the background was not measurable, thus suggesting an insignificant effect on the signal from these unwanted ions. A series of optical pulses were applied to the selected ensemble. These pulses were able to address the ensemble of ions uniformly across their spectra, though Gaussian beam profile resulted in the non-uniform excitation across the beam profile. This provided us with the test-bed to investigate the single qubit operations. It was also shown that the selected ensemble was initialized in the desired state through the application of a series of optical pulses. The optical coherence properties of the selected ensemble were probed using the photon echo technique. The value of optical coherence time for the selected ensemble was the same as the material coherence time (35μs at 4K).

The single qubit operations, as defined in Chapter 5, were applied to the selected ensemble of ions. Two basic single qubit operations were studied and the fidelities of the operations were analyzed. The experimental results show that the phase of the detected echo for the Bloch vector rotation about the z-axis was not affected by the non-uniformity in the beam but the fidelity of the operation was still affected. The experimental results for the Bloch vector rotation around the y-axis show that the amplitude of the detected echo follows the theoretical result predicted by the Gaussian model. Since the Gaussian beam is driving the Bloch vector, the fidelity of the single qubit operation is lower as was

predicted in Chapter 5. It was concluded that a uniform intensity beam or modified pulse is required for high fidelity quantum operations.

Finally, two ensembles at two different frequencies in the inhomogeneous absorption profile of the medium (Tm^{3+}:YAG) were selected. In this case, the unwanted ions in the background were significantly higher. The problem of unwanted ions in the background can be reduced by lowering the sample temperature, since the population relaxation rate between the hyperfine levels critically depends on the sample temperature. However, in general for this ensemble selection scheme, it is impossible to get rid of all the unwanted ions. These two selected ensembles of ions were used to study the ion-ion interaction. The 2-pulse echo technique was used to measure the broadening due to EIFS in 0.1% atm. Tm^{3+}:YAG as $(1.7 \pm 0.3) kHz$ per $10^{15} cm^{-3}$ ions excited. Two different methods, in context of implementing a two-qubit quantum gate in Tm^{3+}:YAG, were discussed. It was noted that the method in reference (124) can not be used to implement the two-qubit quantum operation in 0.1% atm. Tm^{3+}:YAG as the EIFS results in a much smaller broadening than the widths of the selected ensembles. However, an alternate method, which requires the broadening due to EIFS to be greater than the homogeneous line-width of the material ions, can be used to implement the two-qubit quantum operation [(114), (108)].

Future Directions

Based on our exploration of thulium for suitability as a test-bed for basic quantum operation, it is possible to build a V-system in Tm^{3+}:YAG. However, in order to tailor a Λ–system, one has to come up with a new technique to store unwanted ions. It is possible to demonstrate a system with three or maybe four qubits in Tm^{3+}:YAG. In order to achieve these goals, one has to improve or modify the following:

1. Selection of the Isolate ensemble of ions
    a. Use material with a preselected ensemble of ions, i.e. use Stoichiometrically doped materials [(137), (138)].
    b. Improve existing enabling techniques i.e. use lower temperature or use other orientation of the magnetic field that gives longer population lifetime.
2. Interaction between ensembles of ions
    a. Improve ensemble selection technique so that ensemble bandwidth is homogeneous line-width limited. Then use the Stark effect to get an inhomogeneously broadened ensemble [(139)].
    b. Implement composite pulse sequence for CNOT demonstration [(114)].
    c. Increase the thulium concentration.
    d. Search other host material for thulium that can provide higher excitation induced frequency shift.
3. Investigate other host material for thulium with weaker/zero magnetic interactions with the thulium ions.

It is tempting to implement quantum operation in thulium because it has the convenient transition that can be accessed with commercially available diode lasers. Thus one option would be to investigate new host material for thulium that can provide an

environment for thulium such that it has higher cross-transition ratio, longer coherence time and longer population lifetime of hyperfine levels, and also have about 5 to 10 times higher ion-ion interaction than in Tm^{3+}:YAG.

REFERENCE CITED

1. Turing, A. M. Proceedings of the London Mathematical Society, Series 2. 1936, Vol. 41, pp. 230-267.

2. Church, Alonzo. American Journal of Mathematics. 1936, Vol. 58, pp. 345-363.

3. Feynman, R. P. Int. J. Theor. Phys. 1982, Vol. 21, p. 467.

4. Deutsch, D. Proc. R. Soc. Lond. A. 1985, Vol. 400, pp. 97-117.

5. D. Deutsch, and R. Jozsa. Proc. R. Soc. London A. 1992, pp. 439-553.

6. Algorithms for quantum computation: discrete logarithms and factoring. Shor, P. W. Los Alamitos, CA : IEEE Press, 1994. 35th Annual Symposium on Foundations of Computer Science.

7. Shor, P. W. SIAM J. Comp. 1997, Vol. 26, 5, pp. 1484-1509.

8. Simon, D. R. SIAM J. Comp. 1997, Vol. 26, 5, pp. 1474-1483.

9. Grover, L. K. Phys. Rev. Lett. 1997, Vol. 79, 2, p. 325.

10. DiVincenzo, David P. arXiv:quant-ph/0002077 v3 13 Apr 2000.

11. ARDA. Quantum Computing Road Map. http://qist.lanl.gov/qcomp_map.shtml. 2004.

12. Shoemaker, R. L. Coherent Transient Infrared Spectroscopy. [ed.] Jeffrey I. Steinfeld. Laser Coherence Spectroscopy. New York : Plenum Press, 1978.

13. Rabi, I. I. Phys. Rev. . 1937, Vol. 51, pp. 452-454.

14. L. Allen and J. H. Eberly. Optical resonance and two-level atoms . Mineola, N.Y. : Dover Publications, Inc., 1987.

15. Hahn, E. L. Phys. Rev. 1949, Vol. 77, 2, pp. 297-298.

16. Richard G. Brewer and E. L. Hahn. Phys. Rev. A. 1973, Vol. 8, 1, pp. 464-472.

17. Richard G. Brewer and E. L. Hahn. Phys. Rev. A. 1975, Vol. 11, 5, pp. 1641-1649.

18. Tilo Blasberg, Dieter Suter. J. Lumm. 1995, Vol. 65, pp. 199-209.

19. Hartmann, S. R. IEEE Journal of Quantum Electronics. 1963, Vols. QE-4, 11, pp. 802-807.

20. R. L. Shoemaker and R. G. Brewer. Phys. Rev. Lett. 1972, Vol. 28, 22, pp. 1430-1433.

21. R.M. Shelby, A.C.Tropper, R.T.Harley, and R.M.Macfarlane. Optics Letters. 1983, Vol. 8, 6, pp. 304-306.

22. Babbitt, W. R. The response of inhomogeneously broadened optical absorbers to temporally complex light pulses. [Ph.D. thesis]. s.l. : Harvard University, 1987.

23. Annabel L. Alexander, Jevon J. Longdell, and Mathew J. Sellars. J. Opt. Soc. Am. B. 2007, Vol. 24, 9, pp. 2479-2482.

24. John A. Hoffnagle and C. Michael Jefferson. Applied Optics. 2000, Vol. 39, 30, pp. 5488-5499.

25. Tilo Blasberg and Dieter Suter. Phys. Rev. B. 1995, Vol. 51, 10, pp. 6309-6318.

26. A. Louchet, Y. Le Du, F. Bretenaker, T. Chaneliere, F. Goldfarb,I. Lorgere, and J.-L. Le Gouet. Private Communication. 2007.

27. R. W. Equall, Y. Sun, R. L. Cone, and R. M. Macfarlane. Phys. Rev. Lett. 1994, Vol. 72, 14, pp. 2179-2182.

28. R. W. Equall, R. L. Cone, and R. M. Macfarlane. Phys. Rev. B. 1995, Vol. 52, 6, pp. 3963-3969.

29. Macfarlane, R. M. Optics Letters. 1993, Vol. 18, 22, pp. 1958-1960.

30. P. H. Lee and M. L. Skolnick. Appl. Phys. Lett. 1967, Vol. 10, p. 303.

31. A. A. Gorokhovskii, R. K. Kaarli, and L. A. Rebane. JETP Lett. 1974, Vol. 20, p. 216.

32. B. M. Kharlamove, R. I. Personov, and L. A. Bykovskaya. Opt. Comm. 1974, Vol. 12, p. 191.

33. N. Bloembergen, E.M. Purcell, and R.V. Pound. Phys. Rev. . 1948, Vol. 73, 7, pp. 679-712.

34. P.H. Lee and M.S. Skolnick. Applied Physics Letters. 1967, Vol. 10, 11, pp. 303-305.

35. Szabo, A. Phys. Rev. B. 1975, Vol. 11, 11, pp. 4512-4517.

36. H. deVries and D.A. Wiersma. Phys. Rev. Lett. 1976, Vol. 36, 2, pp. 91-94.

37. R.M. Macfarlane and R.M. Shelby. Spectroscopy of Solids Containing Rare Earth Ions. [book auth.] R.M. Macfarlane A.A. Kaplyanskii. Spectroscopy of Solids Containing Rare Earth Ions. Amsterdam : North Holland, 1987.

38. Erickson, L.E. Phys. Rev. B. 1977, Vol. 16, 11, pp. 4731-4736.

39. Macfarlane, R.M. Optics Letters. 1993, Vol. 18, 10, pp. 829-831.

40. K. D. Merkel and W. R. Babbitt. Optics Letters. 1998, Vol. 23, 7, pp. 528-530.

41. K. D. Merkel and W. R. Babbitt. Optics Letters. 1999, Vol. 24, 3, pp. 172-174.

42. T. Wang, H. Lin and T. W. Mossberg. Optics Letters. 1995, Vol. 20, 24, pp. 2541-2543.

43. K. D. Merkel and W. R. Babbitt. Optics Letters. 1996, Vol. 21, 1, pp. 71-73.

44. Janus H. Wesenberg, Klaus Mølmer, Lars Rippe, and Stefan Kröll. Phys. Rev. A. 2007, Vol. 75, 1, pp. 012304-012310.

45. O. Guillot-Noel, Ph. Goldner, E. Antic-Fidancev, A. Louchet, J.L. Le Gouet,F. Bretenaker, and I. Lorgere. Journal of Luminescence. 2007, Vols. 122-123, pp. 526-528.

46. B. Kraus, W. Tittel,N. Gisin, M. Nilsson, S. Kröll, and J. I. Cirac. Phys. Rev. A. 2006, Vol. 73, 2, pp. 020302-020305.

47. E. Fraval, M. J. Sellars, and J. J. Longdell. Phys. Rev. Lett. 2004, Vol. 92, 7, pp. 077601-077604.

48. J. J. Longdell, M. J. Sellars, and N. B. Manson. Phys. Rev. Lett. 2004, Vol. 93, 13, pp. 130503-130506.

49. L. Rippe, B. Julsgaard, A. Walther, Yan Ying, and S. Kroll. Phys. Rev. A. 2008, Vol. 77, pp. 022307-022311.

50. J. J. Longdell and M. J. Sellars. Phys. Rev. A. 2004, Vol. 69, 3, pp. 032307-032311.

51. N. M. Strickland, P. B. Sellin, Y. Sun, J. L. Carlsten, and R. L. Cone. Phys. Rev. B. 2000, Vol. 62, 3, pp. 1473-1476.

52. Nicklas Ohlsson, Mattias Nilsson, Stefan Kroll, and R. Krishna Mohan. Optics Letters. 2003, Vol. 28, 6, pp. 450-452.

53. A. Abragam and B. Bleaney. Electron paramagnetic resonance of transition ions. Oxford : Clarendon Press, 1970.

54. Abragam, A. The principles of nuclear magnetism. London : Oxford university press, 1961.

55. O. Guillot-Noël, Ph. Goldner, and E. Antic-Fidancev. Phys. Rev. B. 2005, Vol. 71, 17, pp. 174409-174423.

56. F. de Seze, A. Louchet, V. Crozatier, I. Lorgeré, F. Bretenaker, J.-L. Le Gouët, O. Guillot-Noël, and Ph. Goldner. Phys. Rev. B. 2006, Vol. 73, 8, pp. 085112-085122.

57. A. Louchet, J. S. Habib, V. Crozatier, I. Lorgeré, F. Goldfarb, F. Bretenaker, J.-L. Le Gouët, O. Guillot-Noël, and Ph. Goldner. Physical Review B. 2007, Vol. 75, 3, pp. 035131-035139.

58. R. W. P. Drever, J. L. Hall, F. V. Kowalski, J. Hough, G. M. Ford, A. J. Munley, and H. Ward. Appl. Phys. B: Photophys. Laser Chem. 1983, Vol. 31, p. 97.

59. M. Zhu and J. L. Hall. J. Opt. Soc. Am. B. 1993, Vol. 10, p. 802.

60. Bubble Level Specifications. [Online] www.rdso.gov.in/machine/Spec/TM_28.doc.

61. S. Geller and M. A.Gilleo. Journal of Physics and Chemistry of Solids. 1957, Vol. 3, 30, pp. 30-36.

62. John B. Gruber, Marian E. Hills,Roger M. Macfarlane, Clyde A. Morrison, Gregory A. Turner, Gregory J. Quarles, Gregory J. Kintz, and Leon Esterowits. Phys. Rev. B. 1989, Vol. 40, 14, pp. 9464-9478.

63. A. Lupei, C. Tiseanu and V. Lupei. Phys. Rev. B. 1993, Vol. 47, 21, pp. 14084-14092.

64. Kramers, H. A. Proc. Amsterdam Acad. 1930, Vol. 33, p. 959.

65. G. F. Koster, J. O. Dimmock, R. G. Wheeler, and H. Statz. Properties of the 32 Point Groups. Cambridge : M. I. T. Press, 1963.

66. James R. Bolton and John E. Wertz. Electron Spin Resonance: Elementry Theory and practical Applications. New York : McGraw-Hill Book Inc., 1972.

67. Y. Sun, G. M. Wang, R. L. Cone, R. W. Equall, and M.J.M. Leask. Phys. Rev. B. 2000, Vol. 62, 23, pp. 15443-15451.

68. Orbach, R. Proc. Roy. Soc. A. 1961, Vol. 264, pp. 458-484.

69. Orbach, R. Proc. Roy. Soc. A. 1961, Vol. 264, pp. 485-495.

70. Stapleton H. J., Orbach R. Electron Spin-Lattice Relaxation. [ed.] S. Geschwind. Electron Paramagnetic Resonance. New York : Plenum Press, 1972.

71. Caird, John A. IEEE Journal of Quantum Electronics. 1975, Vols. QE-11, 11, pp. 874-881.

72. Roger M. Macfarlane and Mathew J. Dejneka. Optics letters. 2001, Vol. 26, 7, pp. 0429-0431.

73. B. S. Ham, P. R. Hemmer, and M. S. Shahriar. Opt. Comm. 1997, Vol. 144, pp. 227-230.

74. B. S. Ham, P. R. Hemmer, and M. S. Shahriar. Phys. Rev. A. 1999, Vol. 59, 4, pp. R2583-R2586.

75. A. V. Turukhin, V. S. Sudarshanam, M. S. Shahriar, J. A. Musser, B. S. Ham, and P. R. Hemmer. Phys. Rev. Lett. 2002, Vol. 88, 2, pp. 023602-023605.

76. J. Mlynek, N. c. Wong, R. G. DeVoe, E. S. Kintzer, and R. G. Brewer. Phys. Rev. Lett. 1983, Vol. 50, 13, pp. 993-996.

77. N. C. Wong, E. S. Kintzer, J. Mlyneck, R. G. DeVoe, and R. G. Brewer. Phys. Rev. B. 1983, Vol. 28, 9, pp. 4993-5010.

78. Neil B. Manson and Ann J Silversmith. J. Phys. C: Solid State Phys. 1987, Vol. 20, pp. 1507-1517.

79. P. Hu, S. Geschwind and T. M. Jedju. Phis. Rev. Lett. 1976, Vol. 37, 20, pp. 1357-1360.

80. N. W. Carlson, W. R. Babbitt, Y. S. Bai, and T. W. Mossberg. J. Opt. Soc. Am. B. 1985, Vol. 2, 6, pp. 908-914.

81. Tilo Blasberg and Dieter Suter. Optics Comm. 1995, Vol. 120, pp. 55-62.

82. Erickson, L. E. Phys. Rev. B. 1985, Vol. 32, 1, pp. 31-35.

83. Erickson, L. E. Phys. Rev. B. 1989, Vol. 39, 10, pp. 6342-6347.

84. Erickson, L. E. J. Phys. C: solid state phys. 1987, Vol. 20, pp. 291-298.

85. K. K. Sharmat and L. E. Erickson. J. Phys. C: Solid State Phys. 1985, Vol. 18, pp. 2935-2942.

86. Y. Takahashi, K. Ishikawa, Y. Fukuda, T. Yabuzaki, and T. Hashi. Phys. Rev. B. 1991, Vol. 43, 10, pp. 7527-7537.

87. Michio Matsushita, Akiko Mutoh, and Tatsuhisa Kato. Phys. Rev. B. 1998, Vol. 58, 21, pp. 14372-14382.

88. J. J. Longdell, M. J. Sellars, and N. B. Manson. Phys. Rev. B. 2002, Vol. 66, 3, pp. 035101-035106.

89. A. Louchet, J.S. Habib, F. Bretenaker, F. Goldfarb, I. Lorgere, and J.-L. Le Gouet. Journal of Luminescence. 2007, Vol. 127, pp. 89-93.

90. J. J. Longdell, A. L. Alexander, and M. J. Sellars. Phys. Rev. B. 2006, Vol. 74, 19, pp. 195101-19507.

91. V. Hugo Schmidt and E. D. Jones. Phys. Rev. B. 1970, Vol. 1, 5, pp. 1978-1986.

92. Y. S Bai and R. Kachru. Opt. Lett. 1993, Vol. 18, 14, pp. 1189-1191.

93. X. A. Shen and R. Kachru. Opt. Lett. 1993, Vol. 18, 22, pp. 1967-1969.

94. X. A. Shen, E. Chiang, and R. Kachru. Opt. Lett. 1994, Vol. 19, 16, pp. 1246-1248.

95. R. Yano, M. Mitsunaga, and N. Uesugi. Opt. Lett. 1991, Vol. 16, 23, pp. 1884-1886.

96. B. S. Ham, M. S. Shahriar, M. K. Kim, and P. R. Hemmer. Phys. Rev. B. 1998-II, Vol. 58, 18, pp. R11825-R11828.

97. G. M. Wang, R. W. Equall, R. L. Cone, M. J. M. Leask, K. M. Godfrey, and F. R. Wondre. Opt. Lett. 1996, Vol. 21, 11, pp. 818-820.

98. M. A. Nielsen and I. L. Chuang. Quantum computation and quantum information. Cambridge : Cambridge University Press, 2000.

99. Jonathan A. Jones, Vlatko Vedral, Arthur Ekert, Giuseppe Castagnoli. Nature. 2000, Vol. 403, pp. 869-871.

100. Berry, M.V. Proc. R. Soc. Lond. A. 1984, Vol. 392, pp. 45-57.

101. X. Wang and K. Matsumoto. J. Phys. A: Math. Gen. 2001, Vol. 34, pp. L631-L634.

102. A. Ekert, M. Ericsson, P. Hayden, H. Inamori, J. A. Jones, D. K. L. Oi, and V. Vedral. J. Mod. Opt. 2000, Vol. 47, 14-15, pp. 2501-2513.

103. L. M. Duan, J. I. Cirac, P. Zoller. Science. 2001, Vol. 292, pp. 1695-1697.

104. A. Recati, T. Calarco, P. Zanardi, J. I. Cirac, and P. Zoller. Phys. Rev. A. 2002, Vol. 66, pp. 032309-032321.

105. J. Pachos and S. Chountasis. Phys. Rev. A. Vol. 62, pp. 052318-052326.

106. Giuseppe Falci, Rosario Fazio, G. Massimo, and Jens Siewert. Nature. 2000, Vol. 407, pp. 355-358.

107. D. Leibfried, B. DeMarco, V. Meyer, D. Lucas, M. Barrett, J. Britton, W. M. Itano, B. Jelenkovic, C. Langer, T. Rosenband, and D. J. Wineland. Nature. 2003, Vol. 422, pp. 412-415.

108. Mingzhen Tian, Zeb W. Barber, Joe A. Fischer, and Wm. Randall Babbitt. Phys. Rev. A. 2004, Vol. 69, 5, pp. 050301-050304.

109. Mingzhen Tian, Randy R. Reibel, Zeb W. Barber, Joe A. Fischer, and Wm. Randall Babbitt. Phys. Rev. A. 2003, Vol. 67, 1, pp. 011403-011406.

110. Bloch, F. Phys. Rev. 1946, Vol. 70, 7-8, pp. 460-474.

111. N. A. Kurnit, I.D. Abella, and S. R. Hartmann. Phys. Rev. Lett. 1964, Vol. 13, 19, pp. 567-568.

112. Hahn, E. L. Phys. Rev. 1950, Vol. 80, 4, pp. 581-594.

113. Jozsa, Richard. Journal of Modern Optics. 1994, Vol. 41, 12, pp. 2315-2323.

114. J. Wesenberg and K. Molmer. Phys. Rev. A. 2003, Vol. 68, pp. 012320-012324.

115. G. J. Pryde, M. J. Sellars, and N. B. Manson. Phys. Rev. Lett. 2000, Vol. 84, 6, pp. 1152-1155.

116. M. Nilsson, L. Rippe, S. Kroll, R. Kieber, and D. Suter. Phys. Rev. B. 2004, Vol. 70, pp. 214116-214126.

117. Lars Rippe, Mattias Nilsson, Stefan Kroll, Robert Klieber, and Dieter Suter. Phys. Rev. A. 2005, Vol. 71, 6, pp. 062328-062339.

118. Ijaz Zafarullah, Minghzen Tian, Tiejun Chang, and W. Randall Babbitt. J. of Lumm. 2007, Vol. 127, pp. 158-163.

119. G. Gorju, A. Louchet, D. Paboeuf, F. Bretenaker, F. Goldfarb,T. Chaneliere, I. Lorgere, J-L LeGouet, O. Guillot-Noel, and Ph. Goldner. J. Phys.: Condens. Matter 19 (2007) 386226 (10pp). 2007, Vol. 19, pp. 386226-38235.

120. G. L. Abbas, V. W. S. Chan, and T. R. Yee. Opt. Lett. 1983, Vol. 8, 8, pp. 419-421.

121. Horace P. Yuen and Vincent W. S. Chan. Opt. Lett. 1983, Vol. 8, 3, pp. 177-179.

122. M. J . Collett, R . Loudon, and C . W. Gardiner. J. of Mod. Opt. 1987, Vol. 34, 6-7, pp. 881-902.

123. Shapiro, J. H. IEEE Journal of Quantum Electronics. 1985, Vols. QE-21, 3, pp. 237-250.

124. N. Ohlsson, R. K. Mohan, and S. Kroll. Opt. Commun. 2002, Vol. 201, 1-3, pp. 71-77.

125. M. S. Shahriar, P. R. Hemmer, S. Lloyd, P. S. Bhatia, and A. E. Craig. Phys. Rev. A. 2002, Vol. 66, pp. 032301-032306.

126. M. Nilsson, L. Levin, N. Ohlsson, T. Christiansson, and S. Kroll. Physica Scripta. 2002, Vol. T120, pp. 178-185.

127. J. R. Klauder and P. w. Anderson. Phys. Rev. 1962, Vol. 125, 3, pp. 912-932.

128. Jin Huang, J. M. Zhang, A. Lezama, and T. W. Mossberg. Phys. Rev. Lett. 1989, Vol. 63, 1, pp. 78-81.

129. G. K. Liu and R. L. Cone. Phys. Rev. B. 1990, Vol. 41, 10, pp. 6193-6200.

130. Masaharu Mitsunaga, Toshihide Takagahara, Ryuzi Yano, and Naoshi Uesugi. Phys. Rev. Lett. 1992, Vol. 68, 21, pp. 3216-3219.

131. Jiamin Zhang and T. W. Mossberg. Phys. Rev. B. 1993, Vol. 48, 10, pp. 7668-7671.

132. Felix R. Graf, Alois Renn, Gert Zumofen, and Urs P. Wild. Phys. Rev. B. 1998, Vol. 58, 9, pp. 5462-5478.

133. X. A. Shen and R. Kachru. Applied Optics. 1997, Vol. 36, 26, pp. 6692-6695.

134. S. B. Altner, M. Mitsunaga, G. Zumofen, and U. P. Wild. Phys. Rev. Lett. 1996, Vol. 76, 10, pp. 1747-1750.

135. Mims, W. B. Electron Spin Echoes. [ed.] S. Geschwind. Electron Paramagnetic Resonance. New York : Plenum Press, 1972.

136. Sun, Y. Internal report.

137. R. M. Shelby and R. M. Macfarlane. Phys. Rev. Letts. 1980, Vol. 45, 13, pp. 1098-1101.

138. M. J. Sellars, E. Fraval, and J. J. Longdell. Journal of Luminescence. 2004, Vol. 107, pp. 150-154.

139. Macfarlane, Roger M. Journal of Luminescence. 2007, Vol. 125, pp. 156-174.

APPENDICES

APPENDIX A

FITTING ROUTINE USED TO OBTAIN LINEAR FIT TO THE DATA

```
% FITTING ROUTINE USED TO OBTAIN LINEAR FIT TO THE DATA
%This routine takes the experimental data and provides a linear fit to the data
% it also gives the standard error in the fitting parameters

N=length(data(:,1)); % length of data set need to be analyzed
xD=data(:,1); % independent variable obtained from the experimental data
yD=log((data(:,4))); % dependent variable obtained from the experimental data
P1D=polyfit(xD,yD,1); % Linear fit to the experimental data
x1=min(xD(:,1))-10:0.01*xD(1,1):max(xD(:,1))+10; % assign range to the figure
y1=P1D(1)*x1+P1D(2); % Line obtained using least square fitting parameters from the
%experimental data
ypred=polyval(P1D,xD);% predictions
dev=yD-mean(yD);% deviations - measure of the spread in the data
SST=sum(dev.^2);% total variation in the data
resid=yD-ypred;% residuals - measure of mismatch with data
SSE=sum(resid.^2);% variation NOT accounted with the linear fit model
normr=sqrt(SSE);% residual norm% the 2-norm of the vector of the residuals
            % for the fit
Rsq = 1 - SSE/SST        % R2 Error The closer that Rsq is to 1, the more completely
                % the fitted model "explains" the data.
chi2=sum((yD-P1D(1)*xD-P1D(2)).^2); % goodness of the fit
S=N;
Sx=sum(xD); %sum of the independent variable in the data points
Sxx=sum((xD).^2);%sum of the squares of the independent variables in the data points
Sy=sum(yD); %sum of the dependent variable in the data points
Sxy=sum(xD.*yD); %sum of the product of independent and dependent variable in the data points
Delta=Sxx*S-Sx.*Sx; %N time the square of the standard deviation of the independent variable
a=P1D(2);b=P1D(1);
sig_a=sqrt((chi2/(N-2))*Sxx/Delta);% standard error in measuring the slope
sig_b=sqrt((chi2/(N-2))*S/Delta); % standard error in measuring the intercept
plot(xD,yD,'sk',x1,y1,'--k')
```

APPENDIX B

MATLAB CODE FOR ROTATION AROUND Z-AXIS WITH THE GAUSSIAN SPATIAL BEAMS

```
%MATLAB CODE FOR ROTATION AROUND Z-AXIS WITH GAUSSIAN SPATIAL BEAMS
% In this case it is assumed that medium is optically thin dephasing phenomena during the pulse
%are ignored
%This routine calculates the in-phase and in-quadrature components of the coherent signal after
%medium is excited with Gaussian spatial beams
%Beam sequence is the sequence required to get Bloch vector rotation around z-axis
%The input parameters are the phases, amplitudes in units of pi, at the center of the Gaussian
%beam, and 1/e width of the field of the Gaussian beam
%output from the routine is the in-phase and in-quadrature components of the coherent signal

I=sqrt(-1);
syms x;
syms phi theta1 theta2 theta3 theta4 phi2 r real;
% pulse areas of pulse 1 is theta1
% pulse areas of pulse 2 is theta2
% pulse areas of pulse 3 is theta4
% pulse areas of pulse 4 is theta5
% control phase is phi2
u(1,1)=cos(x/2);u(2,2)=cos(x/2);u(1,2)=I*exp(I*phi)*sin(x/2);
u(2,1)=I*exp(-I*phi)*sin(x/2);% evolution matrix for evolution of the Bloch vector due to each pulse
rho(1,1)=1;rho(2,2)=0;rho(1,2)=0;rho(2,1)=0;%initial population
rho11=subs(u*rho*inv(u),{x,phi},{'theta1',0});% density matrix after pulse 1
rho22=subs(u*rho11*inv(u),{x,phi},{'theta2',0}); %density matrix after pulse 2
rho33=subs(u*rho22*inv(u),{x,phi},{'theta3','phi2'});% density matrix after pulse 3
rho44=subs(u*rho33*inv(u),{x,phi},{'theta4',0}); % density matrix after pulse 4
r0=1.0; %1/e width of the field for Gaussian spatial beam
a=1.0% area in units of pi or pi/2 at the center of Gaussian beam
rho441sG=subs(rho44(1,2),{theta1},{a*pi/2*exp(-r^2)});
rho442sG=subs(rho441sG(1,2),{theta2},{a*pi*exp(-r^2)});
rho443sG=subs(rho442sG(1,2),{theta3},{a*pi*exp(-r^2)));
rho44sG=subs(rho443(1,2),{theta4},{a*pi*exp(-r^2)});
%Coherence created in the medium with Gaussian spatial beams
% rho44pG=subs(rho44(2,2)-rho44(1,1),{theta1,theta2,theta3,theta4}
% ,{a*pi/2*exp(-r^2),a*pi*exp(-r^2),a*pi*exp(-r^2),a*pi*exp(-r^2)});
%population change after excitation with Gaussian spatial beams
InPhaseG=real(rho44sG);%in-phase component of the coherent signal
InQuadG=imag(rho44sG);%in-quadrature component of the coherent signal
InPhaseGD=simplify((int(InPhaseG*2*r,r,0,r0))/(int(exp(-r^2)*2*r,r,0,r0)));%in-phase component of
%the coherent signal detected at detector
InQuadGD=simplify((int(InQuadG*2*r,r,0,r0))/(int(exp(-r^2)*2*r,r,0,r0))); %in- quadrature
%component of the coherent signal detected at detector
powerG=simplify(InPhaseGD.^2+InQuadGD.^2); % %detected Echo power
```

APPENDIX C

MATLAB CODE FOR ROTATION AROUND Y-AXIS WITH THE GAUSSIAN SPATIAL BEAMS

```
%MATLAB CODE FOR ROTATION AROUND Y-AXIS WITH GAUSSIAN SPATIAL BEAMS
% In this case it is assumed that medium is optically thin dephasing phenomena during the pulse
%are ignored
%This routine calculates the in-phase and in-quadrature components of the coherent signal after
%medium is excited with Gaussian spatial beams
%Beam sequence is the sequence required to get Bloch vector rotation around Y-axis
%The input parameters are the phases, amplitudes in units of pi, at the center of the Gaussian
%beam, and 1/e width of the field of the Gaussian beam
%output from the routine is the in-phase and in-quadrature components of the coherent signal

%Rotation around y-axis with Gaussian spatial beams
I=sqrt(-1);
syms x;syms phi theta1 theta2 theta3 theta4 phi2 r real;
% pulse areas of pulse 1 is theta1
% pulse areas of pulse 2 is theta2
% pulse areas of pulse 3 is theta4
% pulse areas of pulse 4 is theta5
% control phase is phi2
% rotation angle is delta=-2+2phi
u(1,1)=cos(x/2);u(2,2)=cos(x/2);u(1,2)=I*exp(I*phi)*sin(x/2);
u(2,1)=I*exp(-I*phi)*sin(x/2);%Evolution matrix for evolution of the Bloch vector for evolution due to
%each pulse
rho(1,1)=1;rho(2,2)=0;rho(1,2)=0;rho(2,1)=0;
%initial population
rho11=subs(u*(rho*inv(u)),{x,phi},{'theta1',0});
% density matrix after pulse 1
rho22=subs(u*(rho11*inv(u)),{x,phi},{'theta2','phi2'});
%density matrix after pulse 2
rho33=subs(u*(rho22*inv(u)),{x,phi},{'theta3',0});
% density matrix after pulse 3
rho44=subs(u*rho33*inv(u),{x,phi},{'theta4',0});
% density matrix after pulse 4

r0=1.0; %1/e width of the field for Gaussian spatial beam
a=1; % pulse area in units of pi or pi/2
rho441sG=subs(rho44(1,2),{theta1},{a*pi/2*exp(-r^2)});
rho442sG=subs(rho441sG(1,2),{theta2},{a*pi*exp(-r^2)});
rho443sG=subs(rho442sG(1,2),{theta3},{a*pi/2*exp(-r^2)));
rho44sG=subs(rho443(1,2),{theta4},{a*pi*exp(-r^2)});
%Coherence created in the medium with Gaussian spatial beams
% rho44pG=subs(rho44(2,2)-rho44(1,1),{theta1,theta2,theta3,theta4},
% {a*pi/2*exp(-r^2),a*pi*exp(-r^2),a*pi/2*exp(-r^2),a*pi*exp(-r^2)});
%population change after excitation with Gaussian spatial beams
InPhaseG=real(rho44sG);%in-phase component of the coherent signal
InQuadG=imag(rho44sG);%in-quad component of the coherent signal
```

```
InPhaseGD=simplify((int(InPhaseG*2*r,r))/(int(exp(-r^2)*2*r,r)));
% in-phase detected signal at the detector
InQuadGD=simplify((int(InQuadG*2*r,r))/(int(exp(-r^2)*2*r,r)));
%in-quadrature detected signal at the detector

PowerG=simplify(InPhaseGD.^2+InQuadGD.^2); %detected Echo powe
```